Doctoral Dissertation

博士論文

Control scheme for a Fabry–Pérot type interferometric space gravitational wave antenna

(Fabry–Pérot 型宇宙重力波望遠鏡の
制御手法に関する研究)

A Dissertation Submitted for the Degree of Doctor of Philosophy

令和元年 12 月博士（理学）申請

December 2019

Department of Physics, Graduate School of Science,
The University of Tokyo
東京大学 大学院理学系研究科 物理学専攻

Koji Nagano
長野 晃士

Abstract

Control scheme for a Fabry–Pérot type interferometric space gravitational wave antenna

by Koji Nagano

Supervisor: Takashi Uchiyama

A gravitational wave is a ripple of space time. The existence of gravitational wave was predicted by Albert Einstein, who developed general relativity. The first observation of gravitational waves from a black-hole binary with Advanced Laser Interferometer Gravitational-Wave Observatory (aLIGO) started a new era of gravitational wave physics, astronomy, and cosmology.

The observation frequency of the current ground-based gravitational wave observatory, such as aLIGO, is limited between ~ 10 Hz and a few kHz. The lower frequency limit is mainly determined by the seismic motion. Even below 10 Hz, some observational targets are predicted. One target is the coalescence of the intermediate-mass black holes with masses in the range between $\sim 10^3\ M_\odot$ and $\sim 10^6\ M_\odot$. The intermediate-mass black holes typically emit the gravitational waves in the frequency range between $\sim 10^{-3}$ Hz and ~ 1 Hz. The coalescence of the intermediate-mass black holes is considered to be a candidate of the origin of the super massive black hole that has been discovered at the galactic center. Another target is the early Universe. The quantum fluctuation is considered to cause the gravitational waves in the wide frequency range, for example, between $\sim 10^{-17}$ Hz and $\sim 10^4$ Hz. The observations of the gravitational waves from the coalescence of the intermediate-mass black holes and the early Universe provide new physical and astronomical information. Therefore, some space gravitational wave observatories are proposed to avoid the seismic motion.

In order to observe the gravitational waves in the frequency range between ~ 0.1 Hz and ~ 10 Hz, DECi-hertz Interferometer Gravitational Wave Observatory (DECIGO) and its precursor mission, B-DECIGO, have been proposed. The final goal of DECIGO is the observation of the gravitational waves from the early Universe. DECIGO and B-DECIGO are Fabry–Pérot type space gravitational wave antennas. Their sensitivities are enhanced by a Fabry–Pérot cavity while it requires sub-μm precision ranging for interferometer operation. This requirement level is significantly more stringent than that for other type of the space antennas such as Laser Interferometer Space Antenna (LISA). LISA utilizes an optical transponder configuration and the requirement for the ranging precision is about 10 m. Therefore, in order to operate Fabry–Pérot type space gravitational wave antennas, new advanced control scheme for precise ranging is necessary. Specifically, control topology and a longitudinal sensing scheme have to be considered.

The control topology of the Fabry–Pérot type space gravitational wave antennas should be addressed for the following reasons: First, the drag-free control of satellites to suppress the effect of dragging force is necessary. It was not clear whether the drag-free control can be engaged with all degrees-of-freedom control of the cavity. The second reason is a lack of natural reference for the

control while, in ground-based detectors, the ground is a stable reference. Third, a feedback system introduces additional noises through the feedback loop. Thus, the control system has to be carefully designed, especially in the observation frequency band.

In addition, for the gravitational wave observation, a sensing method, i.e. an interferometer configuration, is also important. DECIGO and B-DECIGO utilize dual-pass Fabry–Pérot cavities to form a triangular shaped interferometer to obtain the redundancy with minimum number of the test masses. In the dual-pass Fabry–Pérot cavity, laser light is injected from both sides of one Fabry–Pérot cavity and the relative frequency of the two lasers cannot be controlled independently. This is a new interferometer configuration for DECIGO and B-DECIGO. In this interferometer configuration, since the Fabry–Pérot cavities are coupled with each other, a new scheme to obtain the longitudinal signal of all the interferometers is necessary. Therefore, the operation of the dual-pass Fabry–Pérot cavity has to be demonstrated for DECIGO and B-DECIGO.

In this thesis, the control scheme of the Fabry–Pérot type space gravitational wave antenna is studied. First, the control topology is considered with the numerical model of the Fabry–Pérot type antenna including a mechanical and opto-mechanical response, a sensing and actuation scheme, external disturbances, and sensing noises. The new model is named a *full DECIGO interferometer model*. This new model reveals that the interferometer control and drag-free control can be engaged at the same time by separating the controlled degrees of freedom with each control, and the mirror position can be used as a reference of the control. Using the model, a solution of DECIGO parameters with interferometer control achieving the target strain sensitivity of 10^{-23} $/\sqrt{\mathrm{Hz}}$ is also found. In addition, more than one-day stability is also achieved. With the sensitivity of 10^{-23} $/\sqrt{\mathrm{Hz}}$, for example, the model of the phase transition at the electroweak scale in the early Universe can be tested. Second, the dual-pass differential Fabry–Pérot interferometer is formulated and is constructed in a ground laboratory with the 55-cm-long Fabry–Pérot cavity. The operation of the dual-pass differential Fabry–Pérot interferometer is demonstrated for the first time. Moreover, it is confirmed that cavity detuning can be reduced by the cavity length adjustment as predicted by the formulation. The cavity detuning reduction is essential to minimize a laser intensity noise, which would be a major noise source in DECIGO. These results indicate that the dual-pass differential Fabry–Pérot interferometer is correctly understood with the new formulation.

This work helps conduct the detailed design of DECIGO and B-DECIGO and is an essential basis for opening the window of gravitational wave physics and astronomy in the decihertz band, especially for the observation of the early Universe.

要旨

Fabry–Pérot 型宇宙重力波望遠鏡の制御手法に関する研究

長野　晃士

指導教員: 内山　隆

重力波とは、時空の歪みが波となって伝わる現象である。重力波の存在は、一般相対性理論を考案した Albert Einstein によって指摘された。Advanced Laser Interferometer Gravitational-Wave Observatory (aLIGO) による、ブラックホール連星合体からの重力波の初検出により、重力波物理学、天文学、そして宇宙論の新しい時代が始まった。

現在の aLIGO などの地上重力波望遠鏡の観測帯域は、重力波の周波数で約 10 Hz から数 kHz に限られている。この低周波帯域は、主に地面振動に起因する雑音で決まっている。しかし、より低い周波数帯域でも、いくつかの観測目標が予言されている。一つの観測目標が、太陽質量の約 $10^{3\text{-}6}$ 倍の質量を持ち、中間質量ブラックホールの合体である。中間質量ブラックホール合体は、典型的に約 10^{-3} Hz から 1 Hz の重力波を放出する。この中間質量ブラックホール合体は、銀河中心の超巨大ブラックホールを形成過程の候補であると考えられている。また、初期宇宙も観測目標の一つである。初期宇宙の量子ゆらぎは、約 10^{-17} Hz から 10^{4} Hz の幅広い重力波を生成すると考えられている。これらの中間質量ブラックホール合体や、初期宇宙由来の重力波観測により、新しい物理的・天文学的知見を得ることができる。したがって、地面振動の影響を避け、より低い周波数の重力波を観測するための宇宙重力波望遠鏡が提案されている。

約 0.1-10 Hz の間の重力波を観測することを目指して、DECi-hertz Interferometer Gravitational Wave Observatory（DECIGO）プロジェクトが提案されている。また、DECIGO の前哨ミッションとして、B-DECIGO プロジェクトも計画されている。DECIGO の最終的な科学目標は、宇宙誕生直後の姿の直接観測である。DECIGO と B-DECIGO は、Fabry–Pérot 型宇宙重力波望遠鏡である。これらの望遠鏡では、Fabry–Pérot 共振器により最高感度は向上するが、干渉計の動作のためにサブ μm の精度の測距が要求される。この要求精度は、他の方式の宇宙重力波望遠鏡より遥かに厳しく、例えば、光トランスポンダ方式を採用している、Laser Interferometer Space Antenna での干渉計動作に必要な測距の精度は 10 m 程度である。したがって、Fabry–Pérot 型宇宙重力波望遠鏡のためには、測距・測角のための新しい精密制御手法を開発する必要がある。特に、制御トポロジーと精密測距手法を検討する必要がある。

Fabry–Pérot 型宇宙重力波望遠鏡の制御トポロジーの開発は、以下の 3 つの理由のために必要である。1 つ目の理由は、レーザー干渉計制御と、外力雑音の影響を低減するための衛星のドラッグ・フリー制御が共存可能かどうかを確認する必要があるからである。ドラッグ・フリー制御と、Fabry–Pérot 共振器の全自由度制御が、同居できるかは確認する必要があった。2 つ目の理由は、制御のための自明な基準点がないためである。DECIGO のような宇宙重力波望遠鏡では、地上重力波望遠鏡のように地面を基準として制御を行うことはできない。3 つ目の理由は、制御による雑音の混入である。DECIGO の感度を落とさないような制御が設計可能かどうかを確認する必要がある。

また、重力波観測のためには、測定手法も、つまり干渉計方式も重要である。特に、DECIGO と B-DECIGO では、双方向 Fabry–Pérot 共振器と呼ばれる干渉計方

式を用いて、三角形型の干渉計を構成する予定である。双方向 Fabry–Pérot 共振器を用いると、最少数の鏡で冗長性を持つことができる。双方向 Fabry–Pérot 共振器では、一つの Fabry–Pérot 共振器に両側からレーザー光を入射させる。そのため、2つのレーザー光の周波数を独立に制御する事ができない。この双方向 Fabry–Pérot 共振器は、DECIGO と B-DECIGO のための新しい干渉計方式である。この方式では、複数の Fabry–Pérot 共振器が互いに影響を与え合うため、すべての干渉計の信号を同時に得るための新しい手法が必要である。そのため、DECIGO と B-DECIGO のためには、双方向 Fabry–Pérot 共振器の動作を確認する必要がある。

本論文では、Fabry–Pérot 型宇宙重力波望遠鏡の制御に関する研究を行った。まず、Fabry–Pérot 型宇宙重力波望遠鏡の、機械的および光学機械的応答、センサーとアクチュエーター、外力雑音、そしてセンサー雑音を含む新しい数値的モデルを構築し、制御トポロジーを検討した。このモデル化により、干渉計制御とドラッグ・フリー制御は、制御自由度を分けることにより、共存可能であることが示された。また、宇宙重力波望遠鏡の制御においては、試験質量の位置を基準にすることで制御が可能であることも示された。また、構築されたモデルと制御トポロジーを用いて、DECIGO における現実的な外乱や測定の雑音を考慮しても、目標感度である 10^{-23} $1/\sqrt{\mathrm{Hz}}$ というひずみ感度と 1 日以上の安定性を持つ、DECIGO の干渉計制御の成立解を確立した。この感度が達成されれば、初期宇宙の電弱相転移モデルの検証などが可能になる。次に、双方向差動 Fabry–Pérot 干渉計を定式化するとともに、実際に地上の実験室に 55 cm の基線長を持つセットアップを構築し、その動作を世界で初めて実証した。さらに、DECIGO の主要な雑音源となりうるレーザー強度雑音の原因となる、共振器の共振点からのずれが、共振器長さを調整することで低減されることを確認した。これらの結果は、今回新たに行った定式化により、双方向差動 Fabry–Pérot 干渉計の挙動を正しく理解できることを示している。

この研究は、DECIGO と B-DECIGO の詳細な設計に資するものであり、将来の 0.1 Hz 帯での重力波観測、特に宇宙誕生直後の姿の直接観測にむけた重要な基礎となるものである。

Contents

List of Figures

List of Tables

Glossary

Symbols

i	imaginary unit $i = \sqrt{-1}$
c	speed of light $c = 299792458$ m/s
$\hbar$	reduced Planck constant $\hbar = 1.054 \times 10^{-34}$ J s
e	elementary charge $e = 1.602 \times 10^{-19}$ C
λ	wavelength of laser light
ν	frequency of laser light ($\nu = c/\lambda$)
ω_{l}	angular frequency of laser light ($\omega_{\mathrm{l}} = 2\pi\nu$)
ω_{GW}	angular frequency of gravitational wave
h	strain of gravitational wave
k_{B}	Boltzmann constant $k_{\mathrm{B}} = 1.38 \times 10^{-23}$ m^2 kg/(s^2 K)
d_{L}	luminosity distance
z	red shift
r	amplitude reflectiveity
t	time, or amplitude transmissivity
$l,\ \xi$	length of interferometer
L	length of cavity
$\mathcal{F}$	finesse
G	gravitational constant $G = 6.67 \times 10^{-11}$ m^3/kg s^2
m, M	mass
I	moment of inertia
H_0	Hubble constant
$M_\odot$	solar mass
E_{inc}	incident electric field
P_{inc}	incident laser power
$R^{\mu}{}_{\nu\delta\sigma}$	Riemann tensor
$R_{\mu\nu}$	Ricci tensor
R	scalar curvature
R_c	radius of curvature of mirror
T	temperature
$T_{\mu\nu}$	energy-momentum tensor
$\Omega_{\mathrm{GW}}(f)$	energy per unit logarithmic interval frequency of stochastic gravitational wave

(for indices)

$\mu, \nu, \delta, ...$	0, 1, 2, 3
$i, j, k, ...$	1, 2, 3

Abbreviations

AdVirgo	Advanced Virgo
aLIGO	Advanced LIGO
AOM	acousto-optic modulator
ASC	alignment sensing and control
BBO	Big Bang Observer
BD	beam dump, or Brans–Dicke
BS	beam splitter
CAST	CERN Axion Solar Telescope
CE	Cosmic Explorer
CBC	compact-binary coalescence
DC	direct current
DECIGO	DECi-hertz Interferometer Gravitational Wave Observatory
EOM	electro-optic modulator
ETM	end test mass
FI	Faraday isolator
FP (FPC)	Fabry–Pérot (Fabry–Pérot cavity)
FSR	free spectral range
FWHM	full width at half maximum
GRB	gamma-ray burst
GW	gravitational wave
HWP	half-wave plate
ISCO	inner most stable circular orbit
ITM	input test mass
LIGO	Laser Interferometer Gravitational-Wave Observatory
LISA	Laser Interferometer Space Antenna
LS	local sensor
M	mirror
MI	Michelson interferometer
NS	neutron star
OC	optical circulator
PBS	polarizing beam splitter
PD	photo detector
PDH	Pound–Drever–Hall
PSR	pulser
PZT	piezoelectric transducer
QPD	quadrant photo detector
SAT	satellite
SN	supernova
STM	steering mirror
TM	test mass
UTC	coordinated universal time
UGF	unity gain frequency
WFS	wavefront sensor

Chapter 1

Introduction

Gravitational wave is a ripple of spacetime. The existence of the gravitational wave was predicted in 1916 by Albert Einstein [1], who pointed out that gravity is a curvature of spacetime in general relativity. General relativity predicts several new gravitational phenomena, such as apsidal precession [2], gravitational lensing [3–5], black holes [6, 7], and gravitational waves [1]. The gravitational wave is one of the most important predictions. Therefore, many studies for detecting gravitational waves have been performed after the Einstein's predication [8–10]. Especially, astronomical objects are main targets of the study.

The observation of gravitational waves is motivated by two major scientific objectives. The first motivation is the test of general relativity [11, 12]. Since general relativity is the most reliable theory of gravity so far, most of the physical studies on the Universe are based on general relativity. Thus, testing general relativity leads to improving our knowledge about the Universe. The second motivation is astronomical one [13, 14]. To gravitational waves, almost everything is highly transparent. Although electro-magnetic waves are used in conventional astronomy, they can be absorbed and/or scattered by normal matter and much information is lost. Accordingly, gravitational waves provide essentially new astronomical information, such as mechanism of gamma ray bursts [15] and supernovae [16,17]. With the gravitational observation, the mass and the dynamics of the astronomical event can be observed.

The first but indirect evidence of the gravitational wave was found by Russell Alan Hulse and Joseph Hooton Taylor, Jr., who observed an orbital period of the binary pulsar, PSR B1913+16 [18]. They found that the orbital period of the binary pulsar was getting short and it was consistent with the predication of general relativity. This result indicates that the binary pulsar loses a part of its energy with gravitational wave emissions as predicted by general relativity and the existence of the gravitational wave. However, the dynamics of strain of space-time cannot be observed in the binary pulsar observation since, in the observation of the orbital period, just the energy of the binary system can be measured.

For the direct observation of strain of space-time, laser interferometric gravitational wave detectors are widely used. The laser interferometric gravitational wave detecters are based on a Michelson interferometer [19]. The Michelson interferometer transduces the phase difference of two splitted laser lights into

the laser intensity variation. Therefore, by using the Michelson interferometer, the optical path length fluctuation due to the gravitational waves can be observed. In addition, a Fabry–Pérot cavity is implemented in the base-line of the Michelson interferometer to enhance the gravitational wave signal [20, 21]. For now, several km-class ground-based laser interferometric gravitational wave detectors are in operation all over the world, such as Advanced Laser Interferometer Gravitational-Wave Observatory (aLIGO) in US [22], Advanced Virgo (AdVirgo) in Italy [23], GEO600 in Germany [24–26], and KAGRA in Japan [27, 28]. The observation frequency of these observatory is from $\sim$ 10 Hz to a few kHz. The lower limit of the frequency is determined by the seismic motion.

In 2015, aLIGO observed the first gravitational wave event, which is called GW150914 [29]. GW150914 is the gravitational wave from binary black holes of which masses are 36 $M_\odot$ and 29 $M_\odot$ ($M_\odot$ is the solar mass) at redshift $z = 0.09$. After GW150914, more than 10 black hole binaries including GW150914 were detected [30]. By using these events (and a neutron star binary event explained later), general relativity was tested while no inconsistency with general relativity was found [31, 32].

In addition to the black hole binaries, the neutron star binary has been observed with aLIGO and AdVirgo in 2017. The neutron star binary event is called GW170817 [33]. In GW170817, besides the gravitational wave observation, electro-magnetic follow-up observations were also performed [34]. Especially, there was coincidence between the gravitational wave event and the short gamma-ray burst event GRB 170817A [35]. This multi-observation strongly indicates that the short gamma-ray burst is caused by the neutron star binary coalescence. According to these black hole and neutron star events, it can be said that a new era of the gravitational wave and multi-messenger physics and astronomy has started.

Although the observational frequency range of the ground-based laser interferometric gravitational wave observatory is from $\sim$ 10 Hz to $\sim$ 1000 Hz, some observational targets outside the range of the frequency band are predicted. One target is the coalescence of the intermediate-mass black holes, i.e. the black holes with masses in the range between $\sim 10^3\ M_\odot$ and $\sim 10^6\ M_\odot$, which typically emit the gravitational waves in the frequency range between $\sim 10^{-3}$ Hz and $\sim$ 1 Hz. The coalescence of the intermediate-mass black holes is considered to be a candidate of the origin of the super massive black hole that has been discovered at the galactic center [36, 37]. Another target is the early Universe [38, 39]. The quantum fluctuation is considered to cause the gravitational waves in the wide frequency range, for example, between $\sim 10^{-17}$ Hz and $\sim 10^4$ Hz [40]. The observations of the gravitational waves from the coalescence of the intermediate-mass black holes and the early Universe provide new physical and astronomical information.

Therefore, for further expansion of gravitational wave physics and astronomy, it is important to expand the observation frequency range. The observation of lower frequency gravitational waves (< 10 Hz) than those have been observed allows us to study various sciences, such as distinction of the formation scenario of super-massive black holes in galactic centers [36, 37, 41], study on the evolution

of the compact binary stars, such as white dwarf binaries [42], precise test of the modified gravity theories [43, 44] and so on. Especially in 0.1-Hz range, there is a possibility to observe the gravitational waves generated in the early Universe [38, 39] and to verify the inflation theory [40, 45, 46].

So far, two types of the next generation laser interferometric gravitational wave detectors are proposed for further expansion of the gravitational wave science: 10-km-class ground-based detectors and space detector with 100-km to 2.5-Gm scale interferometer. Examples of the former type detectors are Einstein Telescope [47] and Cosmic Explorer [48]. They are aimed to observe relatively high frequency gravitational waves in between 5 Hz and $\sim$ kHz. For example, gravitational waves in that frequency range are caused by stellar mass compact binaries. Examples of the latter type detectors are Laser Interferometer Space Antenna (LISA) [49], Big Bang Observer (BBO) [50], TianQin [51], Taiji [52], TianGO [53], DECi-hertz Interferometer Gravitational Wave Observatory (DECIGO) [54], and B-DECIGO are proposed. Since the low frequency sensitivity of the ground based detectors are limited by ground motion [55, 56], space detectors are necessary for low frequency gravitational wave observation.

Space gravitational wave detectors are classified into mainly two types: optical transponder type (LISA, BBO, TianQin, and Taiji) and Fabry–Pérot type detectors (DECIGO and B-DECIGO). By using the Fabry–Pérot cavity, the laser beam is circulated in the cavity. In other words, the time for the interaction of the laser interferometer and the gravitational waves is enhanced with the cavity. As a result, the highest sensitivity of the laser interferometer can be improved. Consequently, DECIGO can be so sensitive that it has a possibility to observe the gravitational wave background generated in the inflation era of the early Universe [38, 39].

The Fabry–Pérot type space gravitational wave detectors, however, need precise control system since the Fabry–Pérot cavity has small linear range shorter than the laser wavelength. In gravitational wave detectors, laser with a wavelength of $\sim \mu$m is used[*1] so that sub-μm level control is necessary. Although the precise control of $\sim 10^{-11}$ m has been achieved in the current ground-based gravitational wave detectors, new control scheme is necessary for space detectors since they have a number of challenges that are not in the ground-based detectors. One of the challenges is lack of natural reference for the control while, in ground-based detectors, the ground is a stable reference. Another challenge is the necessity of drag-free control that is not used in the ground-base detectors. The drag-free control is the control of a satellite to follow a test mass. The test mass floats in the satellite and is isolated from the dragging force, such as solar radiation pressure, applied to the satellite [57]. It was not clear whether the drag-free control can be engaged simultaneously with all the degrees-of-freedom control of the Fabry–Pérot cavity. Moreover, a feedback system for precise control introduces additional noises through feedback loops. The additional noise could disturb the gravitational wave observation. Therefore, the control system has to be carefully designed especially in the observation frequency band [58, 59].

[*1] This wavelength is used for the gravitational wave observatory due to the technical reason. There is a stable and powerful laser with a wavelength of ~ 1 μm, for example 1.064 μm.

In addition, for gravitational wave observation, a sensing method to measure the length of cavity, i.e. an interferometer configuration, is also important. DECIGO and B-DECIGO (and most of the other space detectors) adopt a triangular shaped interferometer geometry for improving calibration precision, false alarm ratio, and sensitivity to polarizations of gravitational waves [60, 61]. These features are important to improve the accuracy of the parameter estimation of the gravitational wave sources from the observation and the reliability of the gravitational wave detection. DECIGO and B-DECIGO utilize a dual-pass Fabry–Pérot cavity to form the triangular shaped interferometer. One advantage of this configuration is that the redundancy can be obtained with minimum number of the test masses. This is a new interferometer configuration. In the dual-pass Fabry–Pérot cavity, laser light is injected from both sides of one Fabry–Pérot cavity and the relative frequency of the two lasers cannot be controlled independently. In this interferometer configuration, since the Fabry–Pérot cavities are coupled with each other, we need a new scheme to obtain the longitudinal signal of all the interferometers while the Fabry–Pérot cavity is widely used in optics field, e.g. spectroscopy, optical quantum computing, laser telecommunications. Therefore, the operation of the dual-pass Fabry–Pérot cavity should be demonstrated for DECIGO and B-DECIGO.

In this thesis, in order to realize the Fabry–Pérot type space gravitational wave detectors, such as DECIGO and B-DECIGO, and expand the gravitational wave physics and astronomy, the control scheme of the Fabry–Pérot type space gravitational wave detectors is addressed. Specifically, we investigate the control topology of the Fabry–Pérot type space gravitational wave detectors and experimentally construct the dual-pass Fabry–Pérot interferometer for demonstration.

This thesis is organized as follows: Chapter 1 is this chapter. Chapter 2 introduces features of the gravitational wave from general relativity, sources of the gravitational wave, and scientific cases with the observation of the gravitational waves. Chapter 3 shows a review of the laser interferometric gravitational wave detectors and comparison among the ground-based detectors and space detectors (LISA, the optical transponder type; DECIGO, Fabry–Pérot type). Chapter 4 explains the scientific objectives and overall concept of DECIGO and B-DECIGO. Chapter 5 describes the study of control scheme of DECIGO and B-DECIGO. The result of the study includes the confirmation of the control stability and noise performance of feedback control. Chapter 6 provides the result of the experimental demonstration of the dual-pass Fabry–Pérot cavity. Chapter 7 concludes the study of the control scheme of the Fabry–Pérot type space gravitational wave detectors.

Chapter 2

Gravitational wave

Gravitational waves are ripples in space-time. They were predicted in general relativity by Einstein [1]. Hulse and Taylor proved the existence of the gravitational wave indirectly via a reduction in the revolution cycle of the binary pulsar, PSR B1913+16 [18]. Their observation indicated that reduction in the energy of the binary pulsar was able to be explained with general relativity. In other words, the ripple in space-time was not detected in Hulse and Taylor observation.

Afterward, research toward the direct observation of the gravitational wave was conducted. Subsequently, aLIGO detected the gravitational wave from a binary black hole on Sep. 14, 2015 (UTC) for the first time [29]. This event is called GW150914. After GW150914, more than 10 gravitational wave events have been detected. Among them, a neutron star binary event, GW170817, was also detected [33]. In GW170817, many electro-magnetic observatories detected afterglow of the neutron binary coalescence [34]. These gravitational wave events led to many scientific results, such as the test of general relativity [31, 32], and opening the gravitational wave physics and astronomy era.

In this chapter, we linearize Einstein equation for understanding the gravitational waves. From the linearized Einstein equation, the gravitational wave is derived. Then, we introduce a number of gravitational wave sources that can be or is expected to be detected. Finally, expected sciences with gravitational waves are reviewed.

2.1 Linearized Einstein Equation

In general relativity, time and space are represented in four dimensions (one time coordinate and three space coordinates). In the four-dimensional space-time, two very near events, x^μ [*1] and $x^\mu + dx^\mu$, have a gap, ds, which is expressed in quadratic form as

$$ds^2 = g_{\mu\nu} dx^\mu dx^\nu, \tag{2.1}$$

where $g_{\mu\nu}$ is a metric tensor, which is often abbreviated simply as a metric [62].[*2] Equation (2.1) shows that, in general relativity, nature of space-time is repre-

[*1] In this thesis, x^0, and (x^1, x^2, x^3) indicate time coordinate (ct) and space coordinate, respectively. Also, Greek indices (Roman indexes) take the value of 0, 1, 2, 3 (1, 2, 3).

[*2] In this thesis, we follow Einstein summation convention.

sented by the metric tensor. In addition, equation (2.1) indicates that $g_{\mu\nu}$ is a symmetric tensor.

When matter exists, the metric tensors follow the Einstein equation,

$$R_{\mu\nu} - \frac{1}{2}g_{\mu\nu}R = \frac{8\pi G}{c^4}T_{\mu\nu}, \tag{2.2}$$

where $R_{\mu\nu}$ is a Ricci tensor, R is scalar curvature, G is the gravitational constant, c is the speed of light, $T_{\mu\nu}$ is an energy-momentum tensor. [*3] The left and right hand side of Einstein equation (2.2) correspond to space-time and matter field, respectively. In other words, Einstein equation indicates that matter makes curvature of space-time, i.e. gravitational field. In addition, Einstein equation shows that moving matter varies the gravitational field.

In the range well far from the source of the gravitational field, we can understand the nature of the space-time considering the perturbation from the flat space-time. When a Minkowski metric, $\eta_{\mu\nu}$, is expanded with small perturbation, $h_{\mu\nu}$, and we drop the second order term of $|h_{\mu\nu}|$, the metric, $g_{\mu\nu}$, under the existence of matter is represented as

$$g_{\mu\nu} = \eta_{\mu\nu} + h_{\mu\nu}, \tag{2.3}$$

$$\eta_{\mu\nu} = \begin{pmatrix} -1 & 0 & 0 & 0 \\ 0 & 1 & 0 & 0 \\ 0 & 0 & 1 & 0 \\ 0 & 0 & 0 & 1 \end{pmatrix}, \quad |h_{\mu\nu}| \ll 1. \tag{2.4}$$

This kind of treatment is known as the linearized theory.

From here, we drives Einstein equation in linearized theory. First, we define

$$h \equiv \eta^{\mu\nu}h_{\mu\nu}, \tag{2.5}$$

$$\bar{h}_{\mu\nu} \equiv h_{\mu\nu} - \frac{1}{2}\eta_{\mu\nu}h. \tag{2.6}$$

When we inversely define $\bar{h} \equiv \eta^{\mu\nu}\bar{h}_{\mu\nu} = h - 2h = -h$, the metric can be represented as,

$$h_{\mu\nu} = \bar{h}_{\mu\nu} - \frac{1}{2}\eta_{\mu\nu}\bar{h}. \tag{2.7}$$

[*3] In this thesis, Christoffel symbol, $\Gamma^{\rho}_{\mu\nu}$, Riemann tensor, $R^{\mu}{}_{\nu\delta\sigma}$, Ricci tensor, $R_{\mu\nu}$, scalar curvature, R, are defined as follows [63]

$$\Gamma^{\rho}_{\mu\nu} = \frac{1}{2}g^{\rho\sigma}(\partial_\mu g_{\sigma\nu} + \partial_\nu g_{\sigma\mu} - \partial_\sigma g_{\mu\nu}) \quad \left(\partial_\mu \equiv \frac{\partial}{\partial x^\mu}\right),$$

$$R^{\mu}{}_{\nu\delta\sigma} = \partial_\rho\Gamma^{\mu}_{\nu\sigma} - \partial_\sigma\Gamma^{\mu}_{\nu\rho} + \Gamma^{\mu}_{\alpha\rho}\Gamma^{\alpha}_{\nu\sigma} - \Gamma^{\mu}_{\alpha\sigma}\Gamma^{\alpha}_{\nu\rho},$$

$$R_{\mu\nu} = R^{\alpha}{}_{\mu\alpha\nu},$$

$$R = g^{\mu\nu}R_{\mu\nu}.$$

Ricci tensor, $R_{\mu\nu}$, and scaler curvature, R, is denoted as,

$$R_{\mu\nu} = -\frac{1}{2}(\Box\bar{h}_{\mu\nu} - \partial^\rho\partial_\mu\bar{h}_{\rho\nu} - \partial^\rho\partial_\nu\bar{h}_{\rho\mu} - \frac{1}{2}\eta_{\mu\nu}\Box\bar{h}), \tag{2.8}$$

$$R = -\frac{1}{2}(-\Box\bar{h} - 2\partial^\rho\partial^\mu\bar{h}_{\rho\mu}), \tag{2.9}$$

where $\Box \equiv \eta_{\mu\nu}\partial^\mu\partial^\nu = \partial_\mu\partial^\mu$. Consequently, Einstein equation (equation (2.2)) is expressed as,

$$\frac{1}{2}\left(\Box\bar{h}_{\mu\nu} + \eta_{\mu\nu}\partial^\rho\partial^\sigma\bar{h}_{\rho\sigma} - \partial^\rho\partial_\nu\bar{h}_{\mu\rho} - \partial^\rho\partial_\mu\bar{h}_{\nu\rho}\right) = -\frac{8\pi G}{c^4}T_{\mu\nu}. \tag{2.10}$$

Finally, when we apply Lorenz gauge,

$$\partial^\nu\bar{h}_{\mu\nu} = 0, \tag{2.11}$$

equation (2.10) is denoted as

$$\Box\bar{h}_{\mu\nu} = -\frac{16\pi G}{c^4}T_{\mu\nu}. \tag{2.12}$$

This equation is the linearized Einstein equation. The linearized equation can be used to understand gravitational field in linearized theory.

With equation (2.11), 10 degrees of freedom of symmetry tensor, $h_{\mu\nu}$, is reduced to 6. In addition, with equations (2.11) and (2.12), the energy-momentum tensor is represented as

$$\partial^\nu T_{\mu\nu} = 0. \tag{2.13}$$

This equation corresponds to the law of conservation of the energy and momentum.

As the end of this section, we show that Lorenz gauge can be applied anytime. First, let's consider coordinate transformation, $x^\mu \to x'^\mu = x^\mu + \xi^\mu(x)$, where $|\partial_\mu\xi_\nu|$ is the same order of magnitude as $|h_{\mu\nu}|$. Then, $\bar{h}_{\mu\nu}$ and its derivatives are transformed as

$$\bar{h}_{\mu\nu}(x) \to \bar{h'}_{\mu\nu}(x') = \bar{h}_{\mu\nu}(x) - \partial_\mu\xi_\nu(x) - \partial_\nu\xi_\mu(x) + \eta_{\mu\nu}\partial_\rho\xi^\rho(x). \tag{2.14}$$

$$\partial^\nu\bar{h}_{\mu\nu}(x) \to (\partial^\nu\bar{h}_{\mu\nu})'(x') = \partial^\nu\bar{h}_{\mu\nu}(x) - \Box\xi_\mu(x) \tag{2.15}$$

Thus, if ξ_μ meeting the equation

$$\Box\xi_\mu(x) = \partial^\nu\bar{h}_{\mu\nu}(x) \tag{2.16}$$

exists anytime, Lorenz gauge can be applied anytime. Since we can denote $\partial^\nu\bar{h}_{\mu\nu}(x) = f_\mu(x)$ using a function $f_\mu(x)$, equation (2.16) is expressed as

$$\Box\xi_\mu(x) = f_\mu(x). \tag{2.17}$$

Then, the answer of equation (2.17) can be denoted with Green function $G(x)$ meeting

$$\Box G(x-y) = \delta^4(x-y), \tag{2.18}$$

as

$$\xi_\mu(x) = \int d^4y \; G(x-y) f_\mu(y). \tag{2.19}$$

Since $\xi_\mu(x)$ in the left hand side of equation (2.19) formally exists always, there is an answer of equation (2.16) anytime. It means that Lorenz gauge can be applied anytime.

2.2 Derivation of gravitational waves and their nature

In vacuum, that is the region where $T_{\mu\nu} = 0$, equation (2.12) is denoted as

$$\Box \bar{h}_{\mu\nu} = 0. \tag{2.20}$$

This is a wave equation for $\bar{h}_{\mu\nu}$ and shows that $\bar{h}_{\mu\nu}$, which is perturbation from the Minkowski metric, is propagated at the speed of light. This $\bar{h}_{\mu\nu}$ is a gravitational wave.

From here, we investigate the nature of the gravitational wave. In the range far enough from the gravitational wave source, Einstein equation can be represented in a simple form using Lorenz gauge, equation (2.11). However, Lorenz gauge does not decide the gauge form completely. In other words, even with Lorenz gauge, we can still perform coordinate transformation. In fact, according to equation (2.15), when we transform the coordinate, x^μ, meeting Lorenz gauge as

$$x^\mu \to x'^\mu = x^\mu + \xi^\mu, \tag{2.21}$$

$$\Box \xi_\mu = 0, \tag{2.22}$$

Lorenz gauge is invariant. When $\Box \xi_\mu = 0$, $\Box \xi_{\mu\nu} = 0$, where

$$\xi_{\mu\nu} \equiv \partial_\mu \xi_\nu + \partial_\nu \xi_\mu - \eta_{\mu\nu} \partial_\rho \xi^\rho, \tag{2.23}$$

is also valid since $\Box$ and ∂_μ can be commutated. Equation (2.14) indicates that, under the coordinate transformation as equation (2.21), equation (2.20) is invariant. Therefore, by using equation (2.22), degrees of freedom of $\bar{h}_{\mu\nu}$ can be reduced by four. As a result, according to this symmetry and Lorenz gauge, the degree of freedoms of $\bar{h}_{\mu\nu}$ is two.

To denote $\bar{h}_{\mu\nu}$ with two degrees of freedom, we deform equations (2.11) and (2.22). First, ξ^0 is chosen to make trace zero, that is $\bar{h} = 0$. Notice that, when $\bar{h} = 0$, $\bar{h}_{\mu\nu} = h_{\mu\nu}$. Second $\xi^i(x)$ is chosen to make $h^{0i}(x) = 0$. Then, since $\bar{h}_{\mu\nu} = h_{\mu\nu}$, from Lorenz gauge, equation (2.11), with $\mu = 0$,

$$\partial^0 h_{00} + \partial^i h_{0i} = 0, \tag{2.24}$$

and $h_{0i} = 0$, $\partial^0 h_{00}$ is denoted as

$$\partial^0 h_{00} = 0. \tag{2.25}$$

This indicates that h_{00} is temporally constant. From physical point of view, the time independent term, h_{00}, represents static gravitational field, i.e. Newtonian potential of the gravitational wave source. Since gravitational waves are time dependent, $\partial^0 h_{00} = 0$ means $h_{00} = 0$ when we consider gravitational waves. Consequently, $h^{0i}(x) = 0$. Therefore, only spacial components, h_{ij}, which meet Lorenz gauge ($\partial^j h_{ij} = 0$) and traceless condition ($h^i{}_i = 0$) are left. In summary, $h_{\mu\nu}$ is donated as,

$$h^{0\mu} = 0,\ h^i{}_i = 0,\ \partial^j h_{ij} = 0, \tag{2.26}$$

which are called a transverse-traceless gauge (TT gauge). Since equation (2.26) is composed of eight formulas, 10 degrees of freedom of $h_{\mu\nu}$ are reduced to be two. Hereafter, the metric in TT gauge is written as h_{ij}^{TT}.

Note that TT gauge is not valid in gravitational wave sources since $\Box\bar{h}_{\mu\nu} \neq 0$. In the gravitational wave sources, once Lorenz gauge is applied, the degree of freedom of $\Box\xi_\mu = 0$, i.e. $\Box\xi_{\mu\nu} = 0$, remains. However, we cannot make the components of $\bar{h}_{\mu\nu}$ to meet $\Box\bar{h}_{\mu\nu} \neq 0$, zero even by subtracting $\xi_{\mu\nu}$ meeting $\Box\xi_{\mu\nu} = 0$.

Equation (2.20) has a plane wave solution, $h_{ij}^{\mathrm{TT}}(x) = e_{ij}(\boldsymbol{k})e^{ikx}$, where $kx = k^\mu x_\mu$, $k^\mu = (\omega_{\mathrm{GW}}/c, \boldsymbol{k})$, $\omega_{\mathrm{GW}}/c = |\boldsymbol{k}|$, $e_{ij}(\boldsymbol{k})$ is a polarization tensor, and ω_{GW} is angular frequency of the gravitational wave. When a monochromatic plane wave that is denoted with a wave-number vector, $\boldsymbol{k}$, equation (2.26) indicates that non-zero components of h_{ij}^{TT} is orthogonal to the propagation direction vector of the gravitational wave, $\hat{\boldsymbol{n}} = \boldsymbol{k}/|\boldsymbol{k}|$. This is because in the plane wave, $\partial^j h_{ij} = 0$ means $n^j h_{ij} = 0$, i.e. the transverse wave. When $\hat{\boldsymbol{n}}$ is chosen along z axis, because of equation (2.26) and the symmetry analysis of h_{ij}^{TT}, the metric is written as,

$$h_{ij}^{\mathrm{TT}}(t,z) = \begin{pmatrix} h_+ & h_\times & 0 \\ h_\times & -h_+ & 0 \\ 0 & 0 & 0 \end{pmatrix}_{ij} \cos[\omega_{\mathrm{GW}}(t - z/c)], \tag{2.27}$$

or simply,

$$h_{ab}^{\mathrm{TT}}(t,z) = \begin{pmatrix} h_+(t) & h_\times(t) \\ h_\times(t) & -h_+(t) \end{pmatrix}_{ab}, \tag{2.28}$$

where $h_+(t) \equiv h_+ \cos[\omega_{\mathrm{GW}}(t - z/c)]$, $h_\times(t) \equiv h_\times \cos[\omega_{\mathrm{GW}}(t - z/c)]$, and $a, b = 1, 2$. $h_+(t)$ and $h_\times(t)$ are called plus mode (+ mode) and cross mode ($\times$ mode), respectively. By using them, a square of the infinitesimal world line, ds^2 is denoted as

$$ds^2 = -c^2dt^2 + dz^2 + [1 + h_+(t)]dx^2 + [1 - h_+(t)]dy^2 + 2h_\times(t)dxdy. \tag{2.29}$$

Figure 2.1 shows time variation of the free particle swarm motion caused by plus- and cross-mode gravitational waves.

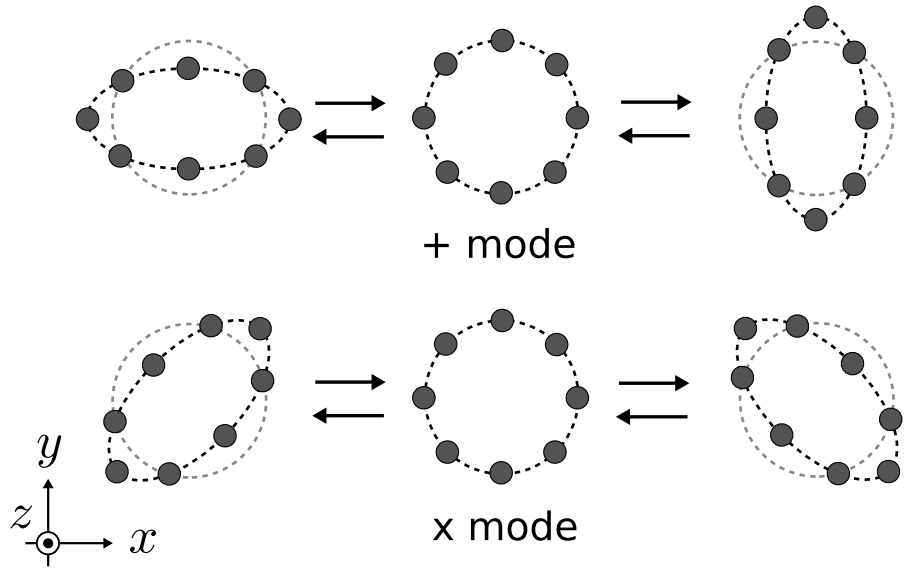

Figure 2.1: Time variation of the free particle swarm's motion caused by plus- and cross-mode gravitational waves. Here, gravitational waves are assumed to propagate along z-axis.

2.3 Generation of gravitational waves and their sources

2.3.1 Generation of gravitational waves

Using the linearized Einstein equation (equation (2.12)), generation of the gravitational wave can be understood. When the source, i.e. the energy-momentum tensor, generating gravitational waves is locally distributed, the solution of equation (2.12) is denoted as

$$\bar{h}_{\mu\nu}(t, \boldsymbol{x}) = \frac{4G}{c^4} \int \frac{T^{\mu\nu}(t - |\boldsymbol{x} - \boldsymbol{x'}|/c, \boldsymbol{x'})}{|\boldsymbol{x} - \boldsymbol{x'}|} d^3\boldsymbol{x'}. \tag{2.30}$$

Moreover, if the size of the gravitational wave source is much smaller than the wave length of the gravitational wave generated by the source and an observer is in far from the source, equation (2.30) is written as

$$\bar{h}_{ij}(t, \boldsymbol{x}) = \frac{2G}{c^4 r_\mathrm{o}} \ddot{Q}_{ij}(t - r_\mathrm{o}/c), \tag{2.31}$$

where r_o is a distance between the gravitational wave source and the observer, and Q_{ij} is a quadrupole momentum of the source, which is defined as

$$Q_{ij}(t - r_\mathrm{o}/c) \equiv \int \rho(t - r_\mathrm{o}/c, \boldsymbol{x'}) \left(x'_i x'_j - \frac{1}{3} \delta_{ij} x'^i x'^j \right) d^3\boldsymbol{x'}. \tag{2.32}$$

Equation (2.31) indicates that the lowest degree of the gravitational wave generation is quadrupole. Using equation (2.31), the amount of the gravitational wave generated by its source is evaluated.

2.3.2 Sources of the gravitational wave

Compact-binary coalescence

All gravitational waves detected by ground-based detectors by the end of 2017 are generated by compact-binary coalescences, known as CBC, [30]: binary black holes, and binary neutron stars. Other compact-binary-coalescence candidates that have not been detected directly are a neutron-star-black-hole binary [64, 65],[*4] a binary white dwarf [66], a white-dwarf-neutron-star [67] and white-dwarf-black-hole binary [68], and so on. Strain equivalent amplitude, $h_{\rm CBC}(t)$, of gravitational waves from equal-mass compact-binary coalescences during inspiral, i.e. the evolution phase of the compact binary of which orbital radius decreases gradually before the merging, is written as [63], in the detector frame,

$$h_{\rm CBC}(t) \simeq \frac{4}{d_{\rm L}} \left(\frac{GM_{\rm CBC}}{2^{1/5}c^3}\right)^{5/3} \left(\frac{\pi f_{\rm GW}(\tau)}{c}\right)^{2/3} \cos(2\pi f_{\rm GW}(\tau)t + \phi_0), \tag{2.33}$$

$$f_{\rm GW}(\tau) = \frac{1}{\pi}\left(\frac{5}{256}\frac{1}{\tau}\right)^{3/8} \left(\frac{GM_{\rm CBC}}{2^{1/5}c^3}\right)^{-5/8} \quad (\tau \equiv t_{\rm coal} - t), \tag{2.34}$$

where $M_{\rm CBC}$ is the mass of the source object, $d_{\rm L}$ is the luminosity distance, $f_{\rm GW}$ is the frequency of the gravitational wave, ϕ_0 is a phase factor, and $t_{\rm caol}$ is the time at coalescence. Equation (2.34) indicates that the frequency of the gravitational wave is gradually increasing during the inspiral and is the largest at coalescence. This characteristic signal of the gravitational wave is called a chirp signal. Strain equivalent amplitude in frequency space, $h_{\rm CBC}(f)$ [1/Hz], is written as [63], in detector frame,

$$h_{\rm CBC}(f) \simeq \frac{1}{\pi^{2/3}}\left(\frac{5}{24}\right)^{1/2} \frac{c}{d_{\rm L}} \left(\frac{GM_{\rm CBC}}{2^{1/5}c^3}\right)^{5/6} f^{-7/6}. \tag{2.35}$$

The inspiral is finished at the innermost stable circular orbit. The gravitational wave frequency at the innermost stable circular orbit is given by

$$f_{\rm ISCO} = \frac{1}{6\sqrt{6}(2\pi)} \frac{c^3}{GM_{\rm CBC}}. \tag{2.36}$$

Let us consider the amplitude of the gravitational wave during inspiral from compact-binary coalescences, especially black-hole binaries. From

[*4] There is a probable neutron-star-black-hole-binary event in Observational Run 3 of aLIGO and AdVirgo, so called S190814bv, which is publicly alerted in GraceDB (https://gracedb.ligo.org) while detailed parameters have not been published yet.

equations (2.35) and (2.36),

$$h_{\rm CBC}(f) \simeq 4 \times 10^{-21} \left(\frac{M}{10^4\ M_\odot}\right)^{5/6} \left(\frac{100\ {\rm Gpc}}{d_{\rm L}}\right) \left(\frac{f}{f_{\rm ISCO}}\right)^{-7/6}, \tag{2.37}$$

$$f_{\rm ISCO} \simeq 0.2 \left(\frac{10^4\ M_\odot}{M}\right)\ [{\rm Hz}]. \tag{2.38}$$

Supernova

It is possible to detect gravitational waves from core collapse of supernovae if there is a mass asymmetry in the core collapse [17]. By using numerical simulation, amplitude and frequency of gravitational waves from supernova is estimated. Typically the amplitude is $h \sim 10^{-22} - 10^{-21}$ and the frequency is ~ 1 kHz in 10 kpc far from the supernova [69].

Isolated pulsar

A pulsar is an astronomical object emitting periodic electromagnetic pulse in gamma ray, X-ray, radio wave, and visible light [70]. The pulsar is considered to be spinning magnetized neutron star that is a supernova remnant [70]. If these pulsars have a slight mountain or valley because of the deformation or the fluid oscillation, they can generate continuous gravitational wave [71]. For example, mili-second pulsars that have 1 ms or a few 10 ms duration emit gravitational waves in the frequency range between 10 Hz and 1000 Hz. The amplitude of the gravitational waves from the isolated pulsar is given by [63]

$$h_{\rm pulsar} \simeq \frac{16\pi^2 G f_{\rm rot}^{3/2}}{c^4 d_{\rm L}} \epsilon I, \tag{2.39}$$

where $f_{\rm rot}$ is the rotation frequency of the pulsar, ϵ is the ellipticity of the pulsar, and I is the momentum inertial along the rotation axis of the pulsar. If the Crab Pulsar (PSR J0534+2200), which is 2 kpc away from the Earth, has ellipticity $\epsilon \sim 10^{-5}$, the gravitational wave of which amplitude is estimated to be $h \sim 10^{-26}$ at the Earth is considered to be generated [63]. Although this amplitude is relatively small compared with the amplitude of the gravitational waves from compact-binary coalescences, the gravitational waves from the pulsars can be amplified by integrating the signal for long time since they are continuous. Therefore, the pulsar is one of the promising astronomical objects generating detectable gravitational waves.

Early Universe

During inflation in the early Universe, the quantum fluctuation of the space-time, i.e. the tensor metric, can generate stochastic gravitational waves called stochastic gravitational wave background [38, 39]. Since the quantum fluctuation is considered to be scale invariant, the generated gravitational wave is also scale invariant. In other words, the power of the generated gravitational wave is frequency independent. In addition to the space-time fluctuation, cosmic

strings [72, 73], domain walls [74, 75], and preheating of the Universe after inflation [76] in the early Universe are considered to be the sources of the stochastic gravitational wave background. The stochastic gravitational wave background is characterized with its energy per unit logarithmic interval of frequency, $\Omega_{\rm gw}(f)$, and its power spectral density is written as

$$S_{\rm SGWB}(f) = \frac{3H_0^2}{4\pi^2 f^3}\Omega_{\rm gw}(f), \tag{2.40}$$

where H_0 is the Hubble constant [63] (the definition of the power spectral density is shown in Appendix B).

2.4 Gravitational wave physics and astronomy

So far, aLIGO and AdVirgo have been operated for two Observational Runs and 10 black hole binaries and one neutron star binary have been detected [30]. Here, we review the scientific results of the two Observational Runs. Notice that although the third Observational Run started from April, 2019, and many gravitational waves were detected, the results are not explained here since the detailed parameters of the events have not been published yet. In addition to the current result, future prospect of the gravitational wave physics and astronomy are shown, too.

2.4.1 Test of general relativity

One of the most important objectives of the gravitational wave physics is testing general relativity [31,32]. The simplest way to do the test is comparing the waveform predicted from general relativity to that observed with the real detectors. This method is called parameterized test [77, 78]. Another way is comparing the parameters of the gravitational wave source estimated from two durations, for example, inspiral and ringdown modes [79]. Since gravity in the ringdown modes is much stronger than that in the inspiral, the gravitational effect beyond general relativity is considered to be visible in the ringdown modes. Although contradiction of general relativity has not been found yet, many modified gravitational theories are proposed [80–82]. One of the major predictions of modified theories is gravitational wave of vector and/or scalar mode in addition to the conventional tensor mode [83]. The additional mode affects the waveform of the gravitational waves or the result of the parameter estimation. The number of gravitational wave modes that can be tested is in principle equal to or less than the effective number of the detectors. Thus, further observation with more detectors is necessary [84, 85].

2.4.2 Source of the gamma-ray burst

In the neutron star binary observation, GW170817, not only gravitational wave but also electro-magnetic signals were observed [86]. Especially, the short gamma-ray burst, GRB 170817A, is coincident to the gravitational wave

event [35]. Although the gamma-ray burst is discovered in 1960s [87], its source and mechanism are not fully concluded [88]. Joint observation of gravitational wave and gamma-ray burst was considered to be promising method to address the mechanism of the gamma-ray burst [89]. The observations of GW170817 and GRB 170817A indicate that the neutron star binary can be the source of the short gamma-ray burst. However, there is an unresolved point in this event: the observed gamma-ray bust is much weaker and closer than the typical event. The observed luminosity distance and the flux of GW170817 and GRB 170817A is 42.9 Mpc and 2×10^{47} erg, respectively, while the nearest and weakest gamma-ray burst except for GRB 170817A is about 400 Mpc away from the Earth and 2×10^{49} erg [35]. Thus, it has not been concluded if GRB 170817A is the same type of gamma-ray burst as the other events or not and further observations are still necessary for the final conclusion.

2.4.3 Synthesis of heavy nuclei

Multi-messenger astronomy related with GW170817 provided important information about the synthesis of heavy nuclei. In the follow-up electro-magnetic observation, a kilonova was found [86]. The spectra of the kilonova afterglow observed by various observatories with electro-magnetic waves, such as infra red, visible, ultra violet, and X-rays, indicate that the r-process occurred in the neutron star binary merger and heavy nuclei were generated [90]. However, it has not been qualitatively concluded that the amount of heavy nuclei is enough to explain the current amount of that in the Universe. If more events are observed, we can investigate the synthesis of heavy nuclei in more quantitative way.

2.4.4 Verifying inflation

If the gravitational wave from the early Universe is observed, its nature, for example, inflation mechanism [91, 92], can be directly investigated. Gravitational waves from the early Universe is expanded by the inflation. Since spectra of the stochastic gravitational wave background is frequency invariant, there are wide frequency range observation and measurement. In very low frequency (10^{-18}-10^{-16} Hz), manifold microwave telescopes are trying to detect B mode of cosmic microwave background that is characteristic signal generated by the stochastic gravitational wave background [93, 94]. Observations in the frequency range between 10^{-9} Hz and 10^{-3} Hz were performed pulsar timing array [95–97] and doppler tracking using Cassini [98]. Between 1 Hz and 10^3 Hz, the ground-based interferometric gravitational wave detectors provided the upper limits [99–101]. The gravitational waves at very high frequency (100 MHz-1 GHz) were searched for with a special laser interferometer, called synchronous recycling interferometer [102,103], and magnon detectors [104]. Although no observation has detected stochastic gravitational wave background, cosmic microwave background observation gave the most strict upper limit to $\Omega_{\rm gw}(0.2\ {\rm Hz})$ of $\sim 10^{-16}$ [105].

2.5 Multi-band gravitational wave physics and astronomy

It is worth noting that there are advantages of the multi-band gravitational wave physics and astronomy.

2.5.1 Precise Characterization of the compact binary

As shown in equations (2.33) and (2.34), the frequency of the gravitational wave increases with time. If the gravitational wave is observed from the low frequency, we can observe the gravitational wave event from the early phase. Thus, the multi-frequency band observation of the compact binaries leads to the long observation duration. For example, the 30-30 $M_\odot$ binary black hole can be observed for ~ 2 years if the observation band is between 0.01 and 1000 Hz. Such a long observation provides the high signal-to-noise ratio observation. As a result, the compact binary can be precisely characterized. Consequently, early alerts before the coalescence for the electromagnetic observatories and the precise test of general relativity can be conducted [106–108]. For example, if there is an observatory with the strain sensitivity of $\sim 10^{-22}$ $/\sqrt{\mathrm{Hz}}$ between 0.1 Hz and 10 Hz (this corresponds to the B-DECIGO sensitivity explained later), the coalescence time can be estimated with statistic error with in 5 s in six days before the coalescence [108].

2.5.2 Mass distribution of the black hole

One of the astrophysically important questions is the way the super-massive black hole ($\sim 10^8$ $M_\odot$) in the galactic center is formed. There are a number of scenarios proposed to the formation mechanism. One scenario is so-called hierarchical scenario [36]. In this scenario, a lot of seed black holes of which masses are $\sim 10^3$ $M_\odot$ merge and form relatively heavy black holes ($\sim 10^6$ $M_\odot$). These black holes having masses between $\sim 10^3$ $M_\odot$ and $\sim 10^6$ $M_\odot$ are called intermediate-mass black holes. Subsequently, the coalescences of the intermediate-mass black holes produce the super-massive black hole. This formation scenario predicts the existence of the black holes with wide mass range. In order to distinguish the formation scenario, we need to investigate the mass distribution of the black hole in the Universe. As shown in equation (2.36), the frequency of the gravitational wave from the black hole binary varies depending on the black hole mass. Therefore, the multi-band observation is necessary to obtain the mass distribution of the black hole.

2.5.3 Observing the structure of the stochastic gravitational wave background

Another important target of the multi-band gravitational wave observation is the examination of the stochastic gravitational wave background. It is a main target of multi-band gravitational wave observation since the energy of stochastic

gravitational wave background from the inflation is considered to be frequency independent as explained in Subsection 2.3.2. Actually, the multi-band observation of the stochastic gravitational wave background is important even more as described below. In addition to the energy of stochastic gravitational wave background, its spectrum shape is used to probe the evolution of the early Universe [109]. For example, after the inflation, the Universe was considered to be reheated [110]. The reheating makes a cut-off frequency in the spectrum of the stochastic gravitational wave background depending on the duration of reheating. This is because the expansion law of the Universe during the reheating is the same as that during the matter-dominant phase where $\Omega_{\rm gw}(f)$ is reduced. The observation of cut-off frequency provides a direct evidence of the reheating [111, 112]. Moreover, there are other proposed models predicting different spectra of the stochastic gravitational wave background [113, 114]. Therefore, by observing the stochastic gravitational wave background in the wide frequency range, the proposed models can be tested.

Chapter 3

Interferometric gravitational wave detector

In this chapter, we summarize the feature of laser interferometers: a Michelson interferometer and a Fabry–Pérot cavity. Then the designed sensitivity of ground-based and space gravitational wave detectors are shown. In the end, two space gravitational wave detectors, LISA and DECIGO, are compared.

3.1 Overview of interferometric gravitational wave detectors

For direct detection of gravitational waves, it is necessary to measure the strain between two free masses, at least, of $h \sim 10^{-21}$ caused by gravitational waves. This tiny space-time ripple was detected with aLIGO for the first time. aLIGO is a laser interferometric gravitational wave detector [22]. Most of the gravitational wave detectors that are under operation, such as AdVirgo [23], KAGRA [27,28], and GEO600 [24–26] are also laser interferometers. Moreover, future space gravitational wave detectors, such as DECIGO [54], LISA [49], BBO [50], TianQin [51], Taiji [52], and TianGO [53] are interferometric detectors.

Laser interferometric gravitational wave detectors are based on a Michelson interferometer [19]. The Michelson interferometer converts the variation of two arms length, i.e. phase variation, to the variation of intensity. Since a wavelength of laser light (~ 1 μm) is used as a reference of the arm length, length change can be measured precisely. However, if we use a simple Michelson interferometer, optimal arm length of the response to the gravitational waves at 100 Hz (0.1 Hz) is 750 km (750 Mm). Such long interferometer cannot be constructed on the Earth. Therefore, the Fabry–Pérot cavity is used as a base-line of the interferometer to obtain an effective long arm by circulating the laser in the cavity as shown in figure 3.1 [21]. Another way to obtain long arm interferometer is constructing the interferometer in space. For example, LISA will have 2.5×10^9-m arms without cavities to detect 1-mHz gravitational waves [49]. DECIGO will have 1000-km-long Fabry–Pérot cavity with finesse, i.e. the number of the roundtrips of laser in the cavity (defined in equation (3.35) later), of 10 to detect

gravitational waves in 0.1-10 Hz [54].

Laser interferometers are prevented from detecting gravitational waves by various noise sources, such as quantum noise caused by the quantum mechanics of laser [115, 116], thermal noise due to the brownian motion of the mirror and suspension systems [117–122], a noise caused by seismic motion [123, 124], Newtonian force applied to the mirror [55, 125, 126], and so on. We need to reduce the effect of all noise sources below that of the gravitational waves to detect them.

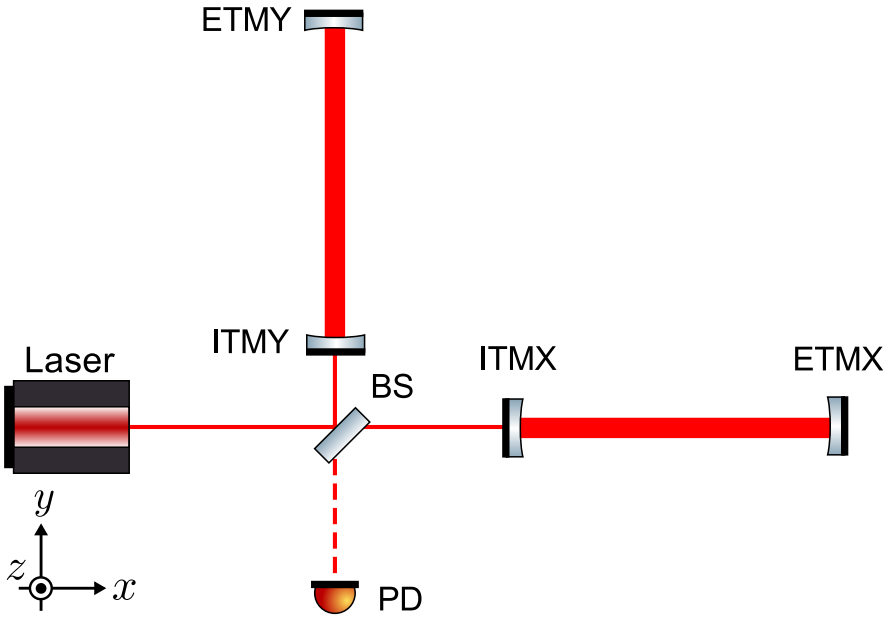

Figure 3.1: Schematic of the Michelson interferometer with the Fabry–Pérot arm cavity, called a Fabry–Pérot Michelson interferometer. BS is beam splitter, ITMX(Y) and ETMX(Y) are input and end test masses, and PD is a photodetector.

3.2 Michelson interferometer

3.2.1 Electric field response of Michelson interferometer

Schematic view of a Michelson interferometer is shown in figure 3.2. Laser light is emitted from the source and the electric field injected to the beam splitter, E_{inc}, is expressed as [127]

$$E_{\mathrm{inc}} = E_0 e^{i\omega_{\mathrm{l}} t}, \tag{3.1}$$

where E_0 is amplitude of the electric field, and ω_{l} is angular frequency of the laser light. When amplitude reflectivity and transmissivity of the beam splitter is $\frac{1}{\sqrt{2}}$, and that of the two end mirrors is unity, the electric field of the laser light received by the photodetector, E_{PD}, is written as

$$E_{\mathrm{PD}} = \frac{1}{2} E_0 e^{i\omega_{\mathrm{l}} t} \left(e^{-2i\phi_X} - e^{-2i\phi_Y} \right), \tag{3.2}$$

where $2\phi_X$ and $2\phi_Y$ are phase shifts due to the round trip in arm along x- and y-axis, respectively.[*1]

Laser power, $P(\boldsymbol{x})$, at $\boldsymbol{x}$ can be expressed by the following relation:

$$P(\boldsymbol{x}) = \alpha |E(\boldsymbol{x})|^2, \quad \alpha \equiv \epsilon_0 \mathcal{A} c, \tag{3.3}$$

where $E(\boldsymbol{x})$ is the electric field at that place, ϵ_0 is vacuum permittivity, and $\mathcal{A}$ is an effective cross section of the laser light along its propagation direction. Thus, laser power received by the photodetector, P_{PD}, is

$$P_{\mathrm{PD}} \equiv \alpha |E_{\mathrm{PD}}|^2 = \frac{1}{2} P_{\mathrm{inc}} (1 - \cos 2\phi_-), \tag{3.4}$$

where $\phi_- \equiv \phi_X - \phi_Y$, and $P_{\mathrm{inc}} \left(\equiv \alpha |E_{\mathrm{inc}}|^2 = \alpha |E_0|^2\right)$ is a laser power injected to the beam splitter. Equation (3.4) indicates that the Michelson interferometer transforms the phase difference between the two arms to the laser power on the photodetector.

3.2.2 Michelson interferometer response to gravitational waves

To understand the response of the Michelson interferometer shown in figure 3.2, let's consider a plus-mode gravitational wave comes from z-axis ($z > 0$), i.e. gravitational wave expressed in equation (2.29) with $h_+(t) = h(t)$ and $h_\times(t) = 0$. In this condition, the response of photon in the Michelson interferometer is considered [128]. The square of the infinitesimal world line ds^2 meets

$$ds^2 = -c^2 dt^2 + [1 + h(t)] dx^2 = 0. \tag{3.5}$$

If $|h(t)| \ll 1$ and $\frac{dx}{dt} > 0$, it is denoted as

$$\left[1 - \frac{1}{2} h(t)\right] c\, dt = dx. \tag{3.6}$$

When we integrate both sides of equation (3.6) with time from $t - \Delta t_X$ to t,

$$\Delta t_X = \frac{2\xi_X}{c} + \frac{1}{2} \int_{t - \Delta t_X}^{t} h(t') dt' \tag{3.7}$$

where Δt_X is the time for round trip of photon between the beamsplitter and the end test mass, and ξ_X is a length of the x-arm. By recursively substituting equation (3.7) for the Δt_X in the right-hand side of equation (3.7), we obtain the following equation:

$$\Delta t_X = \frac{2\xi_X}{c} + \frac{1}{2} \int_{t - 2\xi_X/c}^{t} h(t') dt'. \tag{3.8}$$

[*1] There is a phase shift occurring during traveling from the beamsplitter to the photodetector and the factor should be in the right-hand side of equation (3.2). However, we can set the factor to be unity without losing generality.

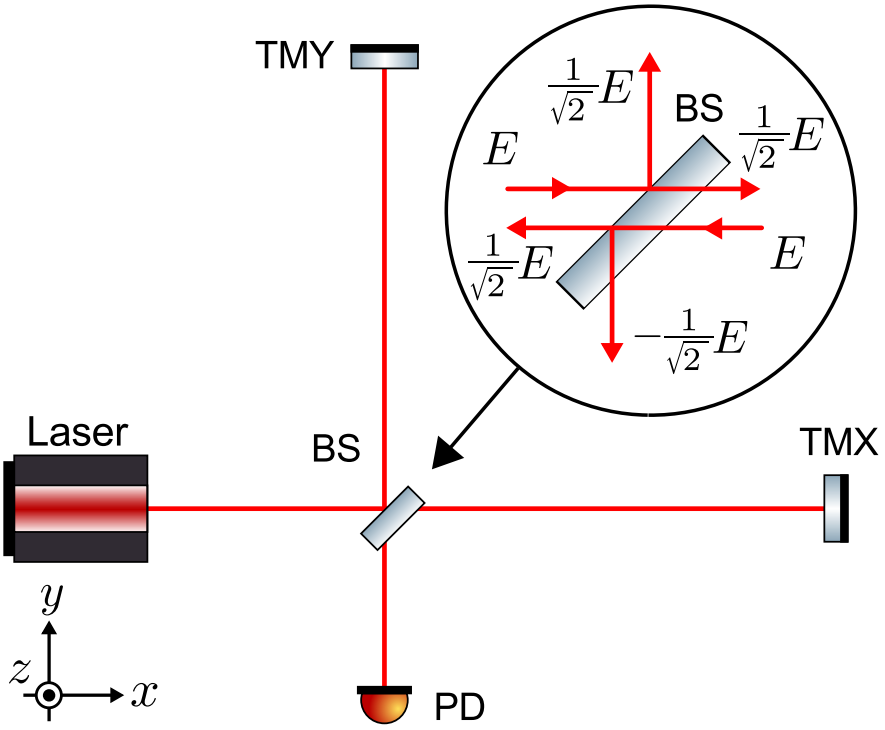

Figure 3.2: Schematic of a Michelson interferometer. Base lines along x-axis and y-axis are called x-arm and y-arm, respectively. TMX and TMY are end test masses (mirrors). In the panel on top right, transformation of the electric field, E, when it is reflected and transmitted by the beamsplitter, is shown. Note that the phase of the electric field is flipped when it is injected from the substrate side of the beamsplitter.

Therefore, the phase shift of that photon receives during round trip in the x-arm, $2\phi_X(t)$, is expressed as

$$2\phi_X(t) = \omega_\mathrm{l}\Delta t_X \tag{3.9}$$

$$= \frac{2\xi_X\omega_\mathrm{l}}{c} + \frac{\omega_\mathrm{l}}{2}\int_{t-2\xi_X/c}^{t} h(t')dt'. \tag{3.10}$$

In the same manner, we obtained the formula about the phase shift of which photon receives during round trip in the y-arm, $2\phi_Y(t)$, as

$$2\phi_Y(t) = \frac{2\xi_Y\omega_\mathrm{l}}{c} - \frac{\omega_\mathrm{l}}{2}\int_{t-2\xi_Y/c}^{t} h(t')dt', \tag{3.11}$$

where ξ_Y is a length of the y-arm. When both arms are almost the same but have a bit different length, i.e. $\xi_X \simeq \xi_Y \simeq l$ and $l_- \equiv \xi_X - \xi_Y \neq 0$, the difference

of the phase shift that occurs in both arms, $2\phi_-(t)$, is written as,

$$2\phi_-(t) = \frac{2l_-\omega_\mathrm{l}}{c} + \omega_\mathrm{l}\int_{t-2l/c}^{t} h(t')dt' \tag{3.12}$$

$$\equiv \frac{2l_-\omega_\mathrm{l}}{c} + \delta\phi_\mathrm{GW}(t). \tag{3.13}$$

The first and second terms of equation (3.13) indicate the static phase shift just due to the length difference between the beamsplitter and two end mirrors and the dynamical phase variation due to the gravitational waves, respectively.

From here, we consider the frequency response of the Michelson interferometer. When we perform Fourier transform of $h(t)$,

$$h(t) = \int_{-\infty}^{\infty} h(\omega)e^{i\omega t}d\omega, \tag{3.14}$$

from equation (3.13), $\delta\phi_\mathrm{GW}(t)$ is written as

$$\begin{aligned}\delta\phi_\mathrm{GW}(t) &= \omega_\mathrm{l}\int_{t-2l/c}^{t} h(t')dt' \\ &= \int_{-\infty}^{\infty} H_\mathrm{MI}(\omega)h(\omega)e^{i\omega t}d\omega,\end{aligned} \tag{3.15}$$

where we define

$$H_\mathrm{MI}(\omega) \equiv \frac{2\omega_\mathrm{l}}{\omega}\sin\left(\frac{\omega l}{c}\right)e^{-i\frac{\omega l}{c}}. \tag{3.16}$$

On the other hand, Fourier transform of $\delta\phi_\mathrm{GW}(t)$ is

$$\delta\phi_\mathrm{GW}(t) = \int_{-\infty}^{\infty} \delta\phi_\mathrm{GW}(\omega)e^{i\omega t}d\omega. \tag{3.17}$$

By comparing equations (3.15) and (3.17), we obtain the following relationship:

$$\delta\phi_\mathrm{GW}(\omega) = H_\mathrm{MI}(\omega)h(\omega). \tag{3.18}$$

This equation indicates that $H_\mathrm{MI}(\omega)$ is the (angular) frequency response of the Michelson interferometer to the gravitational wave at angular frequency of ω.

The gain of the frequency response of the Michelson interferometer, $|H_\mathrm{MI}(\omega)|$, is maximized at

$$\omega = \frac{\pi}{2}\frac{c}{l}. \tag{3.19}$$

This means that the sensitivity of the Michelson interferometer cannot be improved by making long arm length at high frequency region. This is because the phase variation caused by gravitational waves is cancelled while the photon travels in the arm of the Michelson interferometer. For example, the optimal arm length for the gravitational wave at 100 Hz (0.1 Hz) is 750 km (750 Mm). Such long interferometers cannot be constructed on the Earth. In space, very long arm interferometers are planned, such as LISA, which has 2.5×10^9-m-long arms to detect gravitational wave below 0.01 Hz [49].

3.3 Fabry–Pérot cavity

As explained in the previous section, the response of the simple Michelson interferometer on the Earth to gravitational waves at 0.1 Hz or 100 Hz is not optimized for its length limit. To solve this problem, the Fabry–Pérot cavity as shown in figure 3.3 is used to obtain an effective long arm interferometer, i.e. large response to the gravitational waves [21]. The current ground-based observatories have a few kilometer-long cavities that make effectively about 1000 km arms.[*2] Also, Fabry–Pérot type space gravitational wave antennas are planned, such as DECIGO and B-DECIGO. The detail of these detector is explained later. In this section, the feature of the Fabry–Pérot cavity is reviewed.

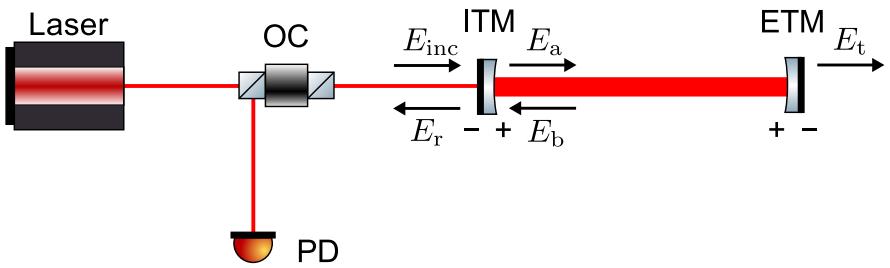

Figure 3.3: Schematic of the Fabry–Pérot cavity. OC is an optical circulator, ITM and ETM are input and end test masses (mirrors), respectively. When the light coming from the substrate side is reflected by the mirror, the phase of electric field is sign flipped.

3.3.1 Electric field response of the Fabry–Pérot cavity

Schematic of the Fabry–Pérot cavity is shown in figure 3.3. From here, we discuss electric fields in the cavity, $E_{\rm a}$ and $E_{\rm b}$, incident electric field, $E_{\rm inc}$, reflected and transmitted electric fields, $E_{\rm r}$ and $E_{\rm t}$. Without losing generality, the incident electric field is written as

$$E_{\rm inc} = E_0 e^{i\omega_{\rm l} t}. \tag{3.20}$$

The amplitude reflectivity and transmissivity of ITM (ETM) are defined as $r_{\rm i}$ and $t_{\rm i}$ ($r_{\rm e}$ and $t_{\rm e}$), respectively. We assume that there is no optical loss in the cavity, unless otherwise stated. The intracavity electric field is expressed as

$$E_{\rm a} = E_{\rm inc} t_{\rm i} \sum_{n=0}^{\infty} (r_{\rm i} r_{\rm e})^n e^{-2i\phi n}, \tag{3.21}$$

$$E_{\rm b} = t_{\rm e} E_{\rm a} e^{-2i\phi}, \tag{3.22}$$

[*2] GEO600 utilizes a folded Michelson configuration.

where 2ϕ is the phase shift that photon receives during one round trip. By taking summation, these equations are denoted as

$$E_{\mathrm{a}} = E_0 e^{i\omega_{\mathrm{l}} t} \frac{t_{\mathrm{i}}}{1 - r_{\mathrm{i}} r_{\mathrm{e}} e^{-2i\phi}}, \tag{3.23}$$

$$E_{\mathrm{b}} = E_0 e^{i\omega_{\mathrm{l}} t} \frac{t_{\mathrm{i}} r_{\mathrm{e}} e^{-2i\phi}}{1 - r_{\mathrm{i}} r_{\mathrm{e}} e^{-2i\phi}}. \tag{3.24}$$

Consequently, the reflected and transmitted electric fields are written as

$$E_{\mathrm{r}} = E_0 e^{i\omega_{\mathrm{l}} t} \frac{-r_{\mathrm{i}} + ({r_{\mathrm{i}}}^2 + {t_{\mathrm{i}}}^2) r_{\mathrm{e}} e^{-2i\phi}}{1 - r_{\mathrm{i}} r_{\mathrm{e}} e^{-2i\phi}}, \tag{3.25}$$

$$E_{\mathrm{t}} = E_0 e^{i\omega_{\mathrm{l}} t} \frac{t_{\mathrm{i}} t_{\mathrm{e}} e^{-i\phi}}{1 - r_{\mathrm{i}} r_{\mathrm{e}} e^{-2i\phi}}. \tag{3.26}$$

Using equations (3.23), (3.25), and (3.26), the intracavity power, P_{a}, reflected power, P_{r}, and transmitted power, P_{t}, are written as,

$$P_{\mathrm{a}} \equiv \alpha |E_{\mathrm{a}}|^2 = \frac{{t_{\mathrm{i}}}^2}{1 + (r_{\mathrm{i}} r_{\mathrm{e}})^2 - 2 r_{\mathrm{i}} r_{\mathrm{e}} \cos 2\phi} P_{\mathrm{inc}}, \tag{3.27}$$

$$P_{\mathrm{r}} \equiv \alpha |E_{\mathrm{r}}|^2 = \frac{{r_{\mathrm{i}}}^2 + [({r_{\mathrm{i}}}^2 + {t_{\mathrm{i}}}^2) r_{\mathrm{e}}]^2 - 2({r_{\mathrm{i}}}^2 + {t_{\mathrm{i}}}^2) r_{\mathrm{i}} r_{\mathrm{e}} \cos 2\phi}{1 + (r_{\mathrm{i}} r_{\mathrm{e}})^2 - 2 r_{\mathrm{i}} r_{\mathrm{e}} \cos 2\phi} P_{\mathrm{inc}}, \tag{3.28}$$

$$P_{\mathrm{t}} \equiv \alpha |E_{\mathrm{t}}|^2 = \frac{(t_{\mathrm{i}} t_{\mathrm{e}})^2}{1 + (r_{\mathrm{i}} r_{\mathrm{e}})^2 - 2 r_{\mathrm{i}} r_{\mathrm{e}} \cos 2\phi} P_{\mathrm{inc}}. \tag{3.29}$$

The example of the transmitted power, P_{t}, is illustrated in figure 3.4.

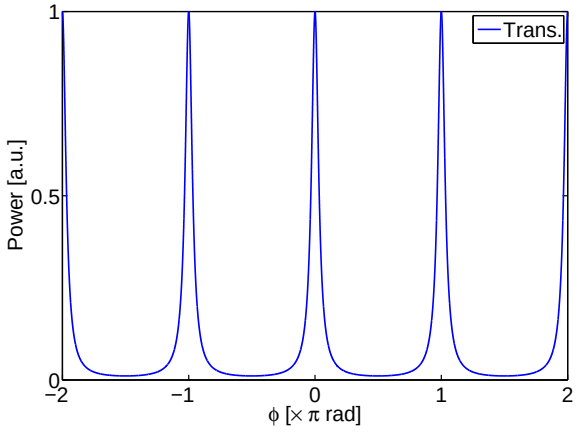

Figure 3.4: Example of the transmitted power of the Fabry–Pérot cavity. In this figure, the case of the cavity with finesse, $\mathcal{F}$, of 15 is shown.

The intracavity power is maximized at $2\phi = 2\pi n$ ($n \in \mathbb{N}$, $\mathbb{N}$ is a set of natural numbers). This condition is called resonance. The resonance condition is denoted as

$$\frac{2L\omega_{\mathrm{l}}}{c} = 2\pi n, \tag{3.30}$$

where L is the cavity length. The resonance frequency, i.e. resonance condition in terms of frequency, is written as

$$\nu_{\mathrm{res}} = n\frac{c}{2L} \equiv n\nu_{\mathrm{FSR}}, \tag{3.31}$$

where ν_{FSR} is called the free spectral range.

When the cavity is composed of high reflectivity ($\gtrsim 0.9$) mirrors, the cavity has the peak of the intracavity power around resonance frequency. Using equation (3.27), the full width at half maximum of the peak, $2\phi_{1/2}$, meets

$$\cos 2\phi_{1/2} = \frac{-1 + 4r_{\mathrm{i}}r_{\mathrm{e}} - (r_{\mathrm{i}}r_{\mathrm{e}})^2}{2r_{\mathrm{i}}r_{\mathrm{e}}}. \tag{3.32}$$

If $\left|\frac{\phi_{1/2}}{\pi}\right| \ll 1$, $2\phi_{1/2}$ is denoted as

$$\phi_{1/2} = \frac{1 - r_{\mathrm{i}}r_{\mathrm{e}}}{2\sqrt{r_{\mathrm{i}}r_{\mathrm{e}}}}. \tag{3.33}$$

The half width at half maximum is also written in terms of frequency as

$$\nu_{1/2} = \frac{1 - r_{\mathrm{i}}r_{\mathrm{e}}}{2\sqrt{r_{\mathrm{i}}r_{\mathrm{e}}}}\frac{c}{2\pi L}. \tag{3.34}$$

$\nu_{1/2}$ is called the cavity pole frequency. Here, the ratio of the free spectral range (ν_{FSR}) to the full width at half maximum of the peak ($2\nu_{1/2}$) is finesse, which represents the sharpness of the resonance peak. Specifically, the finesse, $\mathcal{F}$, is written as

$$\mathcal{F} \equiv \frac{\nu_{\mathrm{FSR}}}{2\nu_{1/2}} = \frac{\pi\sqrt{r_{\mathrm{i}}r_{\mathrm{e}}}}{1 - r_{\mathrm{i}}r_{\mathrm{e}}}. \tag{3.35}$$

With equation (3.25), the complex reflectivity of the Fabry–Pérot cavity, r_{FP}, is denoted as

$$r_{\mathrm{FP}} = \frac{-r_{\mathrm{i}} + ({r_{\mathrm{i}}}^2 + {t_{\mathrm{i}}}^2)r_{\mathrm{e}}e^{-2i\phi}}{1 - r_{\mathrm{i}}r_{\mathrm{e}}e^{-2i\phi}}. \tag{3.36}$$

Figure 3.5 shows that absolute value and phase of r_{FP}.

3.3.2 Response of the Fabry–Pérot cavity to the mirror motion

We will consider the response of the Fabry–Pérot cavity to the mirror motion [128]. The time for laser to make n-times round trips, which is Δt_n, is denoted as,

$$\Delta t_n \simeq \frac{2L}{c}n + \frac{2}{c}\sum_{m=1}^{n}\delta L(t - (2m-1)L/c), \tag{3.37}$$

where $\delta L(t)$ ($|\delta L(t)| \ll L$) is the cavity length variation, i.e. mirror motion. By performing Fourier transformation of $\delta L(t)$,

$$\delta L(t) = \int_{-\infty}^{\infty}\delta L(\omega)e^{i\omega t}d\omega, \tag{3.38}$$

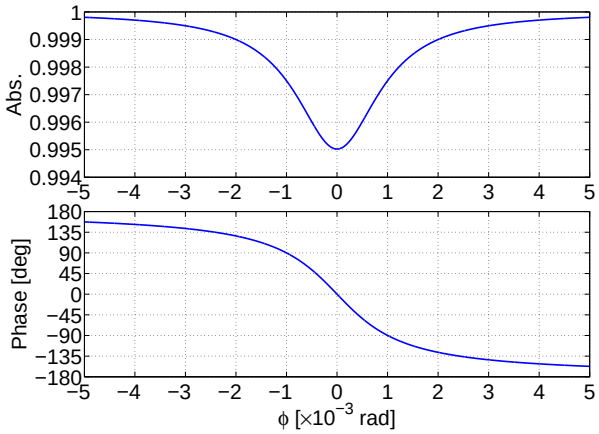

Figure 3.5: Complex reflectivity of the Fabry–Pérot cavity. Here, we adopt $r_\mathrm{i} = 0.998$, $t_\mathrm{i} = 0.063$, and $r_\mathrm{e} = 0.999995$.

Δt_n is written as

$$\Delta t_n \simeq \frac{2L}{c} n + \frac{2}{c} \int_{-\infty}^{\infty} \delta L(\omega) \frac{1 - e^{-2i\gamma(\omega)n}}{e^{i\gamma(\omega)} - e^{-i\gamma(\omega)}} e^{i\omega t} d\omega, \tag{3.39}$$

where $\gamma(\omega) \equiv \frac{L\omega}{c}$.

In the same way as equation (3.21), when the cavity length is fluctuating, the intracavity electric field of the cavity, $E_\mathrm{a}^{(L)}$, is written as

$$E_\mathrm{a}^{(L)} = E_\mathrm{inc} t_\mathrm{i} \sum_{n=1}^{\infty} (r_\mathrm{i} r_\mathrm{e})^{n-1} e^{-2i\Delta t_n \omega_\mathrm{l}}. \tag{3.40}$$

By substituting equation (3.39) for equation (3.40) and using $|\delta L| \ll L$, we obtain the intracavity electric field as,

$$\frac{E_\mathrm{a}^{(L)}}{E_\mathrm{inc}} = \frac{t_\mathrm{i}}{1 - r_\mathrm{i} r_\mathrm{e} e^{-2i\phi}} - i \frac{t_\mathrm{i}}{1 - r_\mathrm{i} r_\mathrm{e} e^{-2i\phi}} \int_{-\infty}^{\infty} \frac{2\omega_\mathrm{l}}{c} \frac{e^{-i\gamma(\omega)}}{1 - r_\mathrm{i} r_\mathrm{e} e^{-2i(\phi + \gamma(\omega))}} \delta L(\omega) e^{i\omega t} d\omega \tag{3.41}$$

$$\equiv \frac{t_\mathrm{i}}{1 - r_\mathrm{i} r_\mathrm{e} e^{-2i\phi}} - i \frac{t_\mathrm{i}}{1 - r_\mathrm{i} r_\mathrm{e} e^{-2i\phi}} \int_{-\infty}^{\infty} H_\mathrm{FP}^{(L)}(\phi, \omega) \delta L(\omega) e^{i\omega t} d\omega, \tag{3.42}$$

wehre

$$H_\mathrm{FP}^{(L)}(\phi, \omega) \equiv \frac{2\omega_\mathrm{l}}{c} \frac{e^{-i\gamma(\omega)}}{1 - r_\mathrm{i} r_\mathrm{e} e^{-2i(\phi + \gamma(\omega))}}. \tag{3.43}$$

This $H_\mathrm{FP}^{(L)}(\phi, \omega)$ is the response of the Fabry–Pérot cavity to the mirror motion. When $\omega/(2\pi) \ll \nu_\mathrm{FSR}$ and $2\phi = 2\pi n$, the response can be approximately presented as

$$H_\mathrm{FP}^{(L)}(\omega) = \frac{2\omega_\mathrm{l}}{c} \frac{2\mathcal{F}}{\pi} \frac{1}{1 + i\omega/(2\pi\nu_{1/2})}. \tag{3.44}$$

In the same manner as the intracavity case, the formula of the reflected electric field, $E_{\mathrm{r}}^{(L)}$, is obtained as

$$E_{\mathrm{r}}^{(L)} = -r_{\mathrm{i}} E_{\mathrm{inc}} + t_{\mathrm{i}} r_{\mathrm{e}} E_{\mathrm{a}}^{(L)} e^{-2i\phi}. \tag{3.45}$$

As a result, the response of the reflected electric field is denoted as

$$\frac{E_{\mathrm{r}}^{(L)}}{E_{\mathrm{inc}}} = \frac{-r_{\mathrm{i}} + r_{\mathrm{e}} e^{-2i\phi}}{1 - r_{\mathrm{i}} r_{\mathrm{e}} e^{-2i\phi}} - i \frac{{t_{\mathrm{i}}}^2 r_{\mathrm{e}} e^{-2i\phi}}{1 - r_{\mathrm{i}} r_{\mathrm{e}} e^{-2i\phi}} \int_{-\infty}^{\infty} H_{\mathrm{FP}}^{(L)}(\phi, \omega) \delta L(\omega) e^{i\omega t} d\omega. \tag{3.46}$$

Equations (3.42) and (3.46) indicate that, in addition to the electric field at angular frequency of ω_{l}, the electric field at angular frequency of $\omega_{\mathrm{l}} \pm \omega$ is generated by the mirror motion at angular frequency of ω. The electric field at angular frequency of ω_{l} and $\omega_{\mathrm{l}} \pm \omega$ are called a carrier and a side-band light, respectively.

In the end, we consider the amplification of the phase variation with the Fabry–Pérot cavity. Here, we assume $r_{\mathrm{i}} \ll r_{\mathrm{e}}$ to compare the response of the cavity with that of just the end mirror ($r_{\mathrm{i}} = 0$). Note that the Fabry–Pérot cavity is usually used on a condition that the end mirror is more reflective than the input mirror ($r_{\mathrm{i}} \ll r_{\mathrm{e}}$, over-coupled cavity) or the end mirror is as reflective as the input mirror ($r_{\mathrm{i}} = r_{\mathrm{e}}$, critically-coupled cavity). The response of the cavity is different from when it is in resonance condition or anti-resonance condition. Anti-resonance condition is given by

$$2\phi = 2\pi \left(n + \frac{1}{2} \right). \tag{3.47}$$

At anti resonance, the intracavity power is the weakest. When we consider the frequency range meeting $|\gamma(\omega)| \ll 1$ or $|\delta L(\omega)| \ll 1$, the reflected electric fields at resonance and anti resonance are written as

$$\frac{E_{\mathrm{r}}^{(L,\mathrm{reso})}}{E_{\mathrm{inc}}} = 1 - 2i \int_{-\infty}^{\infty} \left(\frac{2}{\pi} \mathcal{F} \right) \frac{2\omega_{\mathrm{l}}}{c} \delta L(\omega) e^{i\omega t} d\omega \quad \text{(resonance)}, \tag{3.48}$$

$$\frac{E_{\mathrm{r}}^{(L,\mathrm{anti})}}{E_{\mathrm{inc}}} = -1 + 2i \int_{-\infty}^{\infty} \left(\frac{\pi}{2} \frac{1}{\mathcal{F}} \right) \frac{2\omega_{\mathrm{l}}}{c} \delta L(\omega) e^{i\omega t} d\omega \quad \text{(anti resonance)}. \tag{3.49}$$

The electric filed just reflected by the end mirror without the input mirror is expressed as

$$\frac{E_{\mathrm{r}}^{(L,\mathrm{NC})}}{E_{\mathrm{inc}}} = 1 - 2i \int_{-\infty}^{\infty} \frac{2\omega_{\mathrm{l}}}{c} \delta L(\omega) e^{i\omega t} d\omega \quad \text{(no cavity)}. \tag{3.50}$$

Here, we compare the phase quadrature, i.e. imaginary part, of each case. They

are denoted as

$$\mathrm{Im}\left[\frac{E_{\mathrm{r}}^{(L,\mathrm{reso})}}{E_{\mathrm{inc}}}\right] = -2\int_{-\infty}^{\infty}\left(\frac{2}{\pi}\mathcal{F}\right)\frac{2\omega_{\mathrm{l}}}{c}\delta L(\omega)e^{i\omega t}d\omega \quad \text{(resonance)}, \tag{3.51}$$

$$\mathrm{Im}\left[\frac{E_{\mathrm{r}}^{(L,\mathrm{anti})}}{E_{\mathrm{inc}}}\right] = 2\int_{-\infty}^{\infty}\left(\frac{\pi}{2}\frac{1}{\mathcal{F}}\right)\frac{2\omega_{\mathrm{l}}}{c}\delta L(\omega)e^{i\omega t}d\omega \quad \text{(anti resonance)}, \tag{3.52}$$

$$\mathrm{Im}\left[\frac{E_{\mathrm{r}}^{(L,\mathrm{NC})}}{E_{\mathrm{inc}}}\right] = -2\int_{-\infty}^{\infty}\frac{2\omega_{\mathrm{l}}}{c}\delta L(\omega)e^{i\omega t}d\omega \quad \text{(no cavity)}. \tag{3.53}$$

These equations show the phase variation of the electric field reflected by the cavity is $^{2\mathcal{F}}/_{\pi}$ times larger at resonance than that of just the end mirror, while $^{2\mathcal{F}}/_{\pi}$ times smaller at anti resonance. In other words, the photons in the Fabry–Pérot cavity make $^{2\mathcal{F}}/_{\pi}$-times round trips on average in the resonance condition. Therefore, to obtain the effective long interferometer, we need to keep the Fabry–Pérot cavity at the resonance. For this purpose, Pound–Drever–Hall technique is often used [129]. Notice that the right hand side of equations (3.51) and (3.52) for the critically-coupled cavity is obtained by modifying $\frac{4}{\pi}\mathcal{F} \to \frac{1}{\pi}\mathcal{F}$.

3.3.3 Response of the Fabry–Pérot cavity to the gravitational waves

We consider the response of the Fabry–Pérot cavity to the gravitational wave [128]. Here, gravitational wave, $h(t)$, making space fluctuation along the cavity axis. The time for laser to make n-times round trips is $\Delta t_n^{(h)}$, which is denoted as,

$$\Delta t_n^{(h)} \simeq \frac{2L}{c}n + \int_{t-2Ln/c}^{t} h(t')dt'. \tag{3.54}$$

By performing Fourier transformation of $h(t)$ (equation (3.14)),

$$\Delta t_n^{(h)} \simeq \frac{2L}{c}n + \frac{1}{2}\int_{t-2Ln/c}^{t}\frac{1-e^{2i\gamma(\omega)}}{i\omega}h(\omega)d\omega. \tag{3.55}$$

In the same manner as consideration of the response to the mirror motion, the intracavity and reflected electric fields are written as

$$\frac{E_{\mathrm{a}}^{(h)}}{E_{\mathrm{inc}}} = \frac{t_{\mathrm{i}}}{1-r_{\mathrm{i}}r_{\mathrm{e}}e^{-2i\phi}} - i\frac{t_{\mathrm{i}}}{1-r_{\mathrm{i}}r_{\mathrm{e}}e^{-2i\phi}}\int_{-\infty}^{\infty}H_{\mathrm{FP}}^{(h)}(\phi,\omega)h(\omega)e^{i\omega t}d\omega, \tag{3.56}$$

$$\frac{E_{\mathrm{r}}^{(h)}}{E_{\mathrm{inc}}} = \frac{-r_{\mathrm{i}}+r_{\mathrm{e}}e^{-2i\phi}}{1-r_{\mathrm{i}}r_{\mathrm{e}}e^{-2i\phi}} - i\frac{{t_{\mathrm{i}}}^2 r_{\mathrm{e}}e^{-2i\phi}}{1-r_{\mathrm{i}}r_{\mathrm{e}}e^{-2i\phi}}\int_{-\infty}^{\infty}H_{\mathrm{FP}}^{(h)}(\phi,\omega)h(\omega)e^{i\omega t}d\omega, \tag{3.57}$$

where

$$H_{\mathrm{FP}}^{(h)}(\phi,\omega) \equiv \frac{\omega_{\mathrm{l}}}{\omega}\frac{\sin[\gamma(\omega)]e^{-i\gamma(\omega)}}{1-r_{\mathrm{i}}r_{\mathrm{e}}e^{-2i(\phi+\gamma(\omega))}}. \tag{3.58}$$

This $H_{\mathrm{FP}}^{(h)}(\phi,\omega)$ corresponds to the frequency response of the Fabry–Pérot cavity to the gravitational wave.

When $H_{\rm FP}^{(h)}(\phi,\omega)$ is compared with $H_{\rm FP}^{(L)}(\phi,\omega)$, we obtain the relation, in the frequency range of $\omega \ll 1$, as

$$H_{\rm FP}^{(h)}(\phi,\omega) = \frac{c\sin[\gamma(\omega)]}{2\omega} H_{\rm FP}^{(L)}(\phi,\omega) \tag{3.59}$$

$$\simeq \frac{L}{2} H_{\rm FP}^{(L)}(\phi,\omega). \tag{3.60}$$

Thus, the cavity response to the gravitational wave with amplitude of h is equivalent to the response to the length fluctuation of $Lh/2$.

3.3.4 Pound–Drever–Hall technique

Here, Pound–Drever–Hall technique is reviewed [129]. Pound–Drever–Hall technique is used to obtain the phase fluctuation signal of the cavity by modulating the phase of the incident laser as follows:

$$E_{\rm inc}^{\rm PDH} = E_0 e^{i(\omega_{\rm l} t + \beta \sin\omega_{\rm s} t)} \tag{3.61}$$

$$\simeq E_0 e^{i\omega_{\rm l} t} + \frac{\beta}{2} E_0 e^{i(\omega_{\rm l}+\omega_{\rm s})t} - \frac{\beta}{2} E_0 e^{i(\omega_{\rm l}-\omega_{\rm s})t}, \tag{3.62}$$

where $\omega_{\rm s}$ is the modulation frequency that is typically a few tens MHz and β is the modulation index that is typically ~ 0.1. In the second equality of the above equation, we assumed $|\beta| \ll 1$. Normally, $\omega_{\rm s}$ is chosen for the second and third terms of equation (3.62) to be off the resonance, i.e. to be just reflected by the input mirror. Consequently, from equation (3.25), the reflected electric field is written as

$$E_{\rm r}^{\rm PDH} = \frac{-r_{\rm i} + r_{\rm e} e^{-2i\phi}}{1 - r_{\rm i} r_{\rm e} e^{-2i\phi}} E_0 e^{i\omega_{\rm l} t} - \frac{\beta}{2} E_0 e^{i(\omega_{\rm l}+\omega_{\rm s})t} + \frac{\beta}{2} E_0 e^{i(\omega_{\rm l}-\omega_{\rm s})t} \tag{3.63}$$

$$\simeq E_0 e^{i\omega_{\rm l} t} \left[\frac{r_{\rm e} - r_{\rm i}}{1 - r_{\rm i} r_{\rm e}} - i \left(\frac{1 - r_{\rm i}}{1 - r_{\rm i} r_{\rm e}} \frac{2\mathcal{F}}{\pi} 2\Delta\phi + \beta \sin\omega_{\rm s} t \right) \right]. \tag{3.64}$$

Here, we assume $2\phi = 2\pi n + 2\Delta\phi$ and $|\Delta\phi| \ll 1$. The power of the reflected electric field at angular frequency of $\omega_{\rm s}$ is

$$P_{\rm r}^{\rm PDH}(\omega_{\rm s}) = 2\alpha \left| E_0 e^{i\omega_{\rm l} t} \right|^2 \frac{1 - r_{\rm i}}{1 - r_{\rm i} r_{\rm e}} \frac{2\mathcal{F}}{\pi} (2\Delta\phi) \beta \sin\omega_{\rm s} t \tag{3.65}$$

$$= 2P_{\rm inc} \frac{1 - r_{\rm i}}{1 - r_{\rm i} r_{\rm e}} \frac{2\mathcal{F}}{\pi} (2\Delta\phi) \beta \sin\omega_{\rm s} t. \tag{3.66}$$

By demodulating this signal at the angular frequency of $\omega_{\rm s}$ and applying a low pass filter to the demodulated signal, we obtain the linear signal to $\Delta\phi$ as

$$P_{\rm r,demod}^{\rm PDH} \propto 2P_{\rm inc} \frac{1 - r_{\rm i}}{1 - r_{\rm i} r_{\rm e}} \frac{2\mathcal{F}}{\pi} (2\Delta\phi). \tag{3.67}$$

This can be used to measure the cavity phase signal and to keep resonance of the cavity.

3.3.5 Effect of the frequency and intensity fluctuation of the incident beam to the Fabry–Pérot cavity

In the measurement with the Fabry–Pérot cavity, the frequency and intensity fluctuation of the injected beams are noise sources.

First, how the frequency fluctuation of the incident laser affects the obtained demodulated signal of the Pound–Drever–Hall technique is considered. The phase variation, $\Delta\phi$, is decomposed to the cavity length and frequency fluctuation into two terms,

$$2\Delta\phi = \frac{2L\omega_\mathrm{l}}{c}\left(\frac{\Delta L}{L} + \frac{\Delta\omega_\mathrm{l}}{\omega_\mathrm{l}}\right). \tag{3.68}$$

This equation indicates that, with the Pound–Drever–Hall technique, the difference of the normalized cavity length from the normalized laser frequency cannot be distinguished. In other words, when we measure the cavity length, the frequency fluctuation behaves as noise,

$$\Delta L^{(\mathrm{freq})} = L\frac{\Delta\omega_\mathrm{l}}{\omega_\mathrm{l}}. \tag{3.69}$$

and vice versa for frequency measurement.

Second, we will consider the effect of the laser power fluctuation, ΔP. Here, we assume that there is some detuning of the cavity, i.e. $\Delta\phi \to \phi_0 + \Delta\phi$. In this case, the demodulated signal of the Pound–Drever–Hall technique is denoted as

$$P^{\mathrm{PDH}}_{\mathrm{r,\ demod}} \propto (P_\mathrm{inc} + \Delta P)(\phi_0 + \Delta\phi) = P_\mathrm{inc}\phi_0 + P_\mathrm{inc}\Delta\phi + (\Delta P)\phi_0. \tag{3.70}$$

In the second equality, the second order term, $|\Delta P\Delta\phi|$, is ignored. In the right hand side, the first term corresponds to the DC term that does not affect fluctuation measurement, the second term is the signal term, and the third term is the noise term due to the power fluctuation. This means that the noise due to the power fluctuation increases depending on the detuning ϕ_0.

3.3.6 Alignment sensing with the Fabry–Pérot cavity

With the Fabry–Pérot cavity, not only the length (or frequency) fluctuation but also alignment signal, e.g. the difference of the cavity axis from the injected axis of laser, or miscentering from the center of mass of the mirrors, can be measured. The spatial translation or tilt of laser axis is expressed with higher-order Hermite–Gauss mode expansion as explained in Appendix F. If the translation (tilt) of the laser axis is small, it is written with 10/01-modes of Hermite–Gauss mode [130]. The cavity axis can be expressed in the same way as the laser axis since the laser light in the cavity passes the centers of the curvature of the mirrors. Therefore, by measuring the 10/01-modes, we can perform the alignment sensing and control of the cavity. For example, a number of methods of alignment sensing have been proposed, such as dither technique [131], transmission beam monitoring [132], and wave front sensing method [133, 134].

Table 3.1: Summary of detector configuration and parameters. FPC, Fabry–Pérot cavity; MI, Michelson interferometer.

Detector	**DECIGO**	LISA	Advanced LIGO
Interferometer	FPC	MI (Transponder)	FPC + MI
Location	Space	Space	Ground
Flying scheme	Formation flying	Constellation flying	N/A
Baseline	1000 km	2.5×10^6 km	4 km
Frequency	10^{-1}-10^{1} Hz	10^{-4}-10^{-1} Hz	10^{1}-10^{3} Hz
Major noise sources	• Quatnum (10^{-1}-10^{1} Hz)	• Force ($< 10^{-3}$ Hz) • Quantum ($> 10^{-3}$ Hz)	• Seismic ($< 10^{1}$ Hz) • Thermal (10^{1}-10^{2} Hz) • Quantum ($> 10^{2}$ Hz)
Displacement noise requirement	$\sim 10^{-18}$ m/$\sqrt{\text{Hz}}$	$\sim 10^{-11}$ m/$\sqrt{\text{Hz}}$	$\sim 10^{-20}$ m/$\sqrt{\text{Hz}}$
Force noise requirement	$\sim 10^{-16}$ N/$\sqrt{\text{Hz}}$	$\sim 10^{-14}$ N/$\sqrt{\text{Hz}}$	$\sim 10^{-13}$ N/$\sqrt{\text{Hz}}$

3.4 Sensitivity of various detectors

The interferometric gravitational wave detector can be understood by the combination of the Michelson interferometer and the Fabry–Pérot cavity. Here, the configurations of various detectors and their principal noises are summarized, especially for DECIGO and LISA as examples of space detectors and aLIGO as an example of the ground-based detector. Table 3.1 shows the summary of the detectors. aLIGO (and most of the other ground-based detectors) has a combined interferometer of Michelson interferometer and Fabry–Péort cavity [21, 135]. Similarly, DECIGO uses the Fabry–Pérot cavity to enhance the response to the gravitational waves. The configuration of LISA is a kind of Michelson interferometer. The arm length of LISA is so long that diffraction loss is large and just reflecting the laser by the mirror producing too much signal loss. Thus, LISA measures the phase of the transmitted laser once and transmits the laser with the same phase after amplifying the signal. This configuration is called optical transponder configuration.

The designed sensitivity of DECIGO, LISA, and aLIGO is shown in figure 3.6 (the detailed explanation of noise source is presented in Appendix C). The lower frequency limit of aLIGO (and other ground-based detectors) is ~ 10 Hz due to the seismic motion and Newtonian force noise. As explained in Section 2.3.2, in order to observe heavier mass black holes, we have to go to lower frequency band that can be achieved with space detectors.

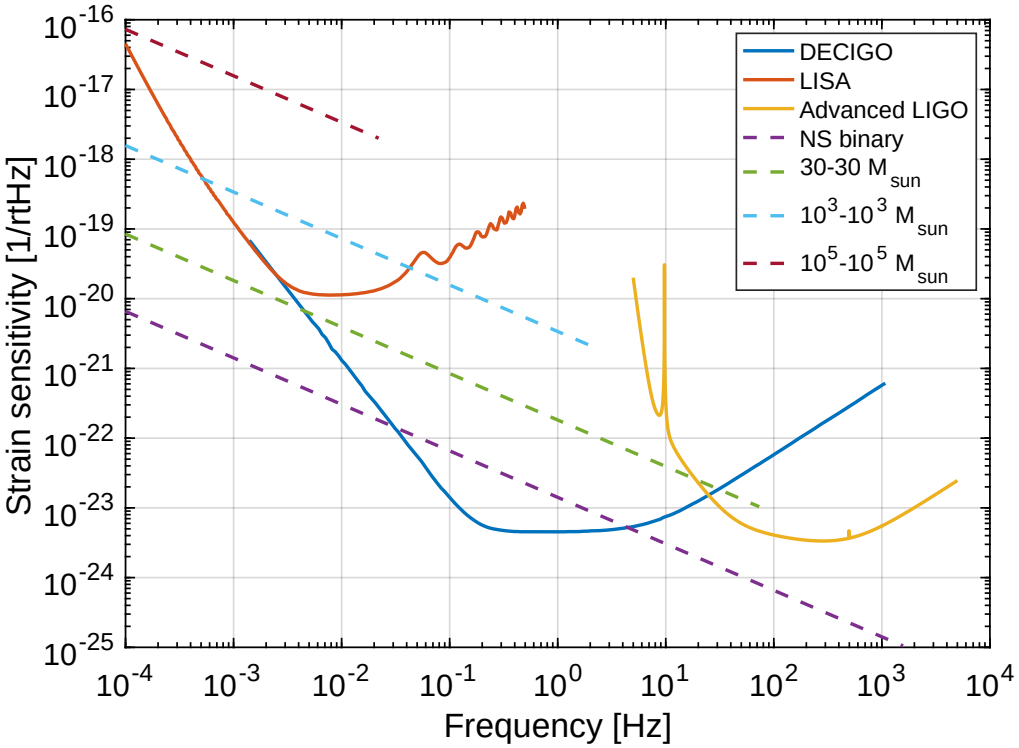

Figure 3.6: Sensitivity cases of interferometric gravitational wave detectors (solid curves): DECIGO [54], LISA [136], and aLIGO [137]. Dashed lines indicate inspiral signals from neutron star binary (1.4-1.4 $M_\odot$) and black hole binaries (30-30 $M_\odot$, 10^3-10^3 $M_\odot$, and 10^5-10^5 $M_\odot$) at redshift $z = 1$. The upper frequency of the inspiral signal is set at the innermost stable circular orbit frequency, $f_{\rm ISCO}$.

3.5 Comparison of space gravitational wave antennas

For now, most of the interferometric space gravitational wave antenna are classified into two types: a Fabry–Pérot type and an optical transponder type[*3]. Fabry–Pérot type is represented by DECIGO and B-DECIGO, whereas optical transponder type is represented by LISA, BBO, Taiji, and TianQin. Here, we compare the two type configurations by taking DECIGO and LISA as examples.

DECIGO and LISA have satellites that include two test masses. The relative position and angle of the satellite to the test mass are controlled with thrusters of the satellite. This control is called a drag-free control [138,139]. The drag-free control is an essential technique for space detectors for reducing noise introduced by the satellite motion [140] that is caused by the thruster noise [141–143] or solar radiation pressure fluctuation [142,144].

One of the major differences between DECIGO and LISA is the base-line

[*3] TianGO [53] adopts a Michelson type configuration.

length. DECIGO has 1000-km-long arms while LISA has 2.5×10^6-km-long arms. The arm length corresponds to the observational frequency band. Although longer arm makes the response to the gravitational wave better, the diffraction loss becomes larger and signal becomes smaller. As a result, by changing the arm length, we can change the frequency band depending on the scientific objectives as shown in figure 3.6. The arm length also varies the noise requirement as shown in table 3.1.

With the short arm length, i.e. the small diffraction loss, the Fabry–Pérot cavity can be applied to enhance the highest sensitivity by enlarging the response to the gravitational waves. DECIGO utilizes Fabry–Pérot type interferometer configuration that is another difference from LISA. LISA uses optical transponder configuration because of its large diffraction loss. This difference leads to the difference of the highest strain sensitivity as shown in figure 3.6.

One challenge with Fabry–Pérot type space gravitational wave antenna is necessity of the precise control. Specifically, the combined control of the laser interferometer and the satellite including drag-free control and formation flying of the satellite is necessary. This is because the Fabry–Pérot cavity has a small linear range that is shorter than the wavelength of the laser as explained in Section 3.3.2. LISA does not require the formation flying and LISA style is constellation flying, i.e. a kind of the flying with rough formation. Therefore, for the Fabry–Pérot type space gravitational wave antenna, we need to develop precise control scheme including sensing scheme and feedback topology.

Chapter 4

Space gravitational wave antenna: DECIGO and B-DECIGO

DECIGO is a proposed space gravitational wave antenna using the Fabry–Pérot arm cavities as shown in figure 4.1 [54]. B-DECIGO, which is a proposed precursor mission to DECIGO, is a relatively small detector while it has almost the same system as DECIGO. B-DECIGO aims to observe the gravitational wave in the same frequency band, i.e. 0.1-10 Hz, as DECIGO. Compared with the other pursued space antennas, LISA, TianQin, Taiji, and TianGO, DECIGO and B-DECIGO have better sensitivity in relatively high frequency range thanks to the Fabry–Pérot arm cavity. BBO has somewhat similar design sensitivity to DECIGO by increasing laser power and telescope size without the Fabry–Pérot cavity. The arm cavity requires precise formation flight. Therefore, we need to develop a new control scheme as explained in Chapter 5.

In this chapter, we review the science targets of DECIGO and B-DECIGO first. Then, their designs are described.

4.1 Scientific objectives

The target sensitivity of DECIGO and B-DECIGO is shown in figure 4.2 (the detailed parameters to obtain the sensitivity is explained later). Once this sensitivity is achieved, fruitful scientific insights are obtained.

4.1.1 Verifying and charactering inflation and thermal history after the inflation

When DECIGO has a sensitivity of 10^{-23} $/\sqrt{\mathrm{Hz}}$ at 0.1 Hz, the stochastic gravitational wave background equivalent to $\Omega_{\mathrm{GW}} \sim 1 \times 10^{-16}$ can be observed by taking the correlation of the two clusters (see Section 4.3.4) with 3-year observation [63]. $\Omega_{\mathrm{GW}} \sim 1 \times 10^{-16}$ is comparable to the current limit of the slow roll model inflation [105]. A number of inflation models that predict this power level of the stochastic gravitational wave background can be verified with the observation with DECIGO [40, 45, 46]. Moreover, in certain parameters, the cut-off frequency due to reheating of the Universe after inflation could be around

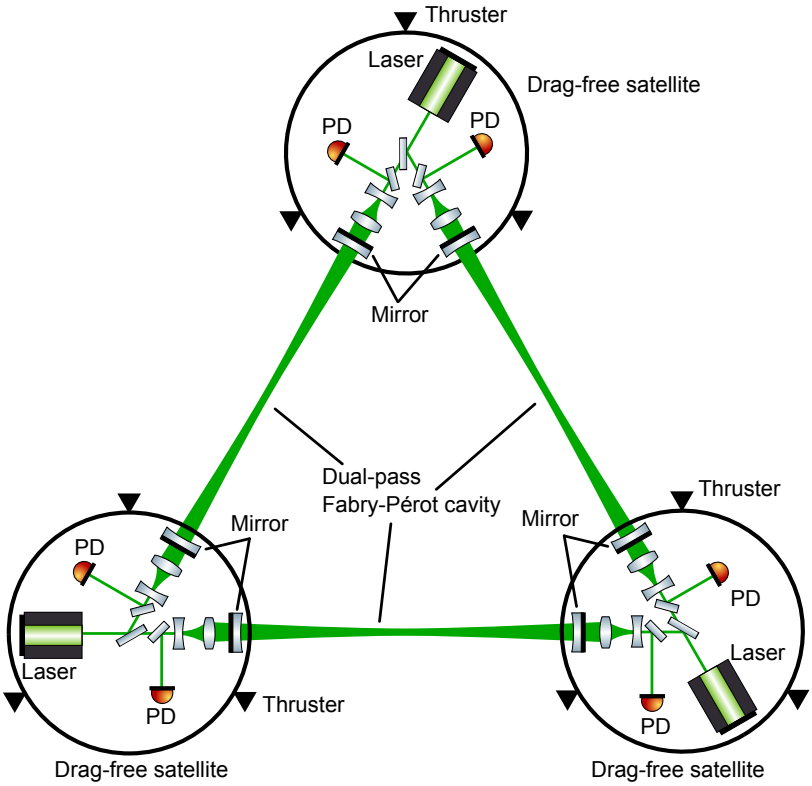

Figure 4.1: Pre-conceptual concept of DECIGO and B-DECIGO.

0.1 Hz. If DECIGO observes the frequency structure of the gravitational wave background spectrum, the thermal history of the Universe is characterized [145].

For the observation of the stochastic gravitational wave background, the compact binary coalescences that cannot be resolved as a single event make the stochastic gravitational wave foreground noise [146, 147]. Especially, galactic white dwarfs [66] and extra-galactic white dwarfs [148] are considered to be the sources of the foreground noise. Since their effect is expected to be small above 0.1 Hz [148], the lower frequency band of DECIGO is 0.1 Hz although the stochastic gravitational wave signal is larger in the lower frequency. One of the objectives of B-DECIGO is characterization of the number of the white dwarf to understand the feature of the foreground noise for the future DECIGO observation for the gravitational wave background. By understanding the foreground noise, we can develop the technique to reduce the effect of the foreground noise.

4.1.2 Early alert to other electromagnetic and gravitational wave observatories

One of the most important abilities of B-DECIGO (and DECIGO) is to alert other electromagnetic and gravitational wave observatories about the astrophysical event well in advance. For example, B-DECIGO can typically detect the neutron star binary at $z = 0.1$ in signal-to-noise ratio of ~ 30 about one week before the merger [108]. Approximately, this leads to the sky localization of

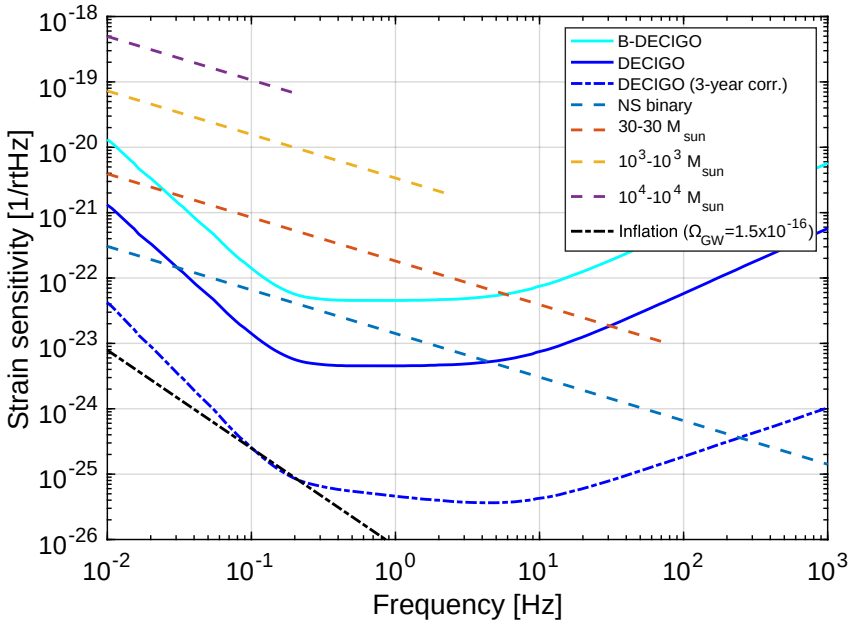

Figure 4.2: Sensitivity of DECIGO and B-DECIGO and their observational targets. Solid lines are B-DECIGO and DECIGO sensitivities. The blue dot-dashed line is DECIGO sensitivity for stochastic gravitational wave with 3-year correlation of two clusters. The dashed lines indicate inspiral signals from the neutron star binary (1.4-1.4 $M_\odot$) and black hole binaries (30-30 $M_\odot$, 10^3-10^3 $M_\odot$, and 10^4-10^4 $M_\odot$) at redshift $z = 1$. The upper end of the frequency of the inspiral signal is set at the innermost stable circular orbit frequency, $f_{\rm ISCO}$. The black dot-dashed line is spectrum of the stochastic gravitational wave background with $\Omega_{\rm GW} = 1.5 \times 10^{-16}$.

$\sim$ 1 deg^2 and coalescence time prediction of $\sim$ 10 s. Using these estimations, B-DECIGO raises an alert. If the moment of the astrophysical transient is observed, totally new information, such as the mechanism of the gamma-ray burst, can be provided [149].

4.1.3 Hubble constant measurement

When the sensitivity shown in figure 4.2 is achieved, DECIGO and B-DECIGO can observe inspiral of neutron star binaries in signal-to-noise ratio of $\sim$ 300 and $\sim$ 30 at redshift, $z = 0.1$, respectively [108]. As a result, the luminosity distance of the source is estimated precisely. In addition, the source can be localized so precisely that the host galaxies can be identified for many gravitational wave events. Such a precise parameter estimation with the gravitational-wave observation provides enough information for the electro-magnetic observatories to measure the redshift. Since the luminosity distance can be estimated from general relativity and the redshift can be measured from the electro-magnetic wave spectrum and its Doppler shift, the Hubble constant is expected to be mea-

sured with small systematic error that will be determined by the instrumental systematic error [150].

DECIGO has an ability to measure the Hubble constant in another way only with the gravitational wave observation [151]. DECIGO can observe the neutron star inspiral for several years if the inspiral is observed from 0.1 Hz to 10 Hz. During the observation, the phase of the inspiral signal is gradually shifted from the waveform predicted without Universe expansion. The waveform of the neutron star binary inspiral can be given by general relativity and the redshift of the neutron star can be determined by investigating the discrepancy from the predicted waveform. Thus, the Hubble constant can be measured from the luminosity distance and the redshift measured with the gravitational wave observation. The precision of the waveform prediction is determined by the statistical error of the parameter estimation of the observed neutron star binary. The precision is expected to be around the inverse of the signal-to-noise ratio of the neutron star binary observation. The Hubble constant is expected to be measured in this precision. This measurement provides totally new information of the Hubble constant even without conventional electro-magnetic observation.

4.1.4 Dark matter search

Primordial black holes are candidates of the cold dark matters. The primordial black holes with masses of $M_{\rm PBH}$ are generated in the very early Universe via gravitational collapse if the quantum density fluctuation is larger than $\sim \frac{M_{\rm PBH}}{(cH^{-1})^3}$, where cH^{-1} is the horizon scale [152]. Since the quantum fluctuation is considered to have a white spectrum, the primordial black hole masses can be widely distributed between $10^{-38}\ M_\odot$ and $10^{3}\ M_\odot$. When DECIGO and B-DECIGO have the sensitivity shown in figure 4.2, the primordial black holes with masses in the range between $10^{-13}\ M_\odot$ and $10^{-7}\ M_\odot$ can be observed [153]. Although this mass region has been limited by the gravitational micro lensing effect [154], the gravitational wave observation provides the independent information about the primordial black hole dark matter.

DECIGO and B-DECIGO are sensitive instruments for another dark matter candidate, axion dark matter. Axion is a pseudo-scalar field which is originally proposed a half-century ago and high energy physics also predicts manifold of axion-like particles. From cosmological point of view, axion or axion-like particle is considered to be a candidate of dark matter. Axion dark matter varies the velocities of the phase of the circular-polarized light. This phase velocity variation can be measured precisely with the Fabry–Pérot cavity [155]. DECIGO and B-DECIGO can improve the current upper limit of the axion-photon coupling constant provided by the haloscope observation by three orders or so. This new scheme was proposed by the researchers including the author of this thesis as a leading person and is explained in detail in Appendix A.

4.1.5 Distinguish formation scenario of supermassive black holes

B-DEICGO (and DECIGO, of course) observes numerous black hole binary coalescences even at very high redshift that corresponds to the age of the Universe of the first star formation. For example, when the strain sensitivity of 10^{-22} $/\sqrt{\mathrm{Hz}}$ is achieved with B-DECIGO, it can detect 30-30 $M_\odot$ black hole binary at $z = 10$, which corresponds to the age of the Universe of the first star formation [156]. Also the intermediate-mass black hole binaries having mass of $\sim 1000\ M_\odot$ at $z = 10$ can be observed with signal-to-noise ratio of 100. These various mass black hole observations allow us to distinguish formation scenario of the supermassive black holes, which are observed in galactic centers [36, 37].

4.1.6 Testing the modified gravitational theory

Using DECIGO and B-DECIGO, the modified gravitational theories can be tested precisely. Although only tensor modes of the gravitational waves are allowed in general relativity, the other modes of vector and scalar can exist in the alternative modified gravity theories [83]. For example, Brans–Dicke theory, which is the simplest tensor-scalar theory, predicts the existence of scalar mode in addition to tensor mode [80]. DECIGO and B-DECIGO have an ability to probe Brans–Dicke theory with the observation of intermediate mass ratio inspiral, e.g. neutron star and black hole binaries with 1.4-10 $M_\odot$ [44]. The inspiral evolution in Brans–Dicke theory differs from that predicted by general relativity because of the scalar dipole radiation. Since the observable number of inspiral cycle of the neutron star and black hole binaries is large in DECIGO and B-DECIGO, the Brans–Dicke parameter, ω_{BD}, which is the characteristic parameter of Brans–Dicke theory, can be tested precisely. The current limit, $\omega_{\mathrm{BD}} > 4 \times 10^4$, provided by the doppler tracking with Cassini [157] can be improved by four orders with DECIGO. In addition to the Brans–Dicke theory, other modified gravitational theory can be tested with DECIGO and B-DECIGO [158–160].

4.1.7 Probing for Type Ia supernova progenitor

Type Ia supernovae are considered to be related with the carbon-oxygen white dwarfs although there is no direct observational evidence. Among the white dwarf related events, white dwarf binary merging is one promising candidate of the Type Ia supernova progenitor. White dwarf binary merges typically between 0.05 and 0.1 Hz, which is almost in the DECIGO and B-DECIGO band, i.e. [161]. Given the event rate of the Type Ia supernovae, DECIGO (B-DECIGO) can observe white dwarf binaries of $\sim$ 20000 ($\sim$ 20) per one year. Since the three-dimensional localization volume of the white dwarf binary is estimated to be about 500 Mpc^3 with DECIGO, a host galaxy can be identified for many events. Even with B-DECIGO, the nearby but rare event could be associated with its host galaxy. If the coincidence of the white dwarf binary and Type Ia supernova is observed with DECIGO or B-DECIGO, the progenitor of the Type Ia supernova may be able to be probed.

4.2 Interferometer design

According to the scientific objectives explained above, the strain sensitivity of DECIGO is required to be better than 10^{-23} $/\sqrt{\mathrm{Hz}}$ between 0.1 and 10 Hz. B-DECIGO aims to achieve the strain sensitivity of 10^{-22} $/\sqrt{\mathrm{Hz}}$ in the same frequency range. Here, we explain the interferometer design of DECIGO and B-DECIGO to meet their sensitivity requirement, at least, in terms of the principal noise discussed in Appendix C. The summary of this section is shown in table 4.1. Notice that the design in this chapter is mainly considered just with the longitudinal things and simple control scheme. For more detailed design, we need to consider the control scheme of all degrees of freedom and control scheme as shown in Chapter 5.

4.2.1 Interferometer configuration

DECIGO and B-DECIGO are Fabry–Pérot type gravitational wave antennas. The pre-conceptual design is shown in figure 4.1. DECIGO and B-DECIGO are constructed as a triangular shaped interferometer. DECIGO (B-DECIGO) has a 1000-km-long (100-km-long) arm cavity of which finesse is 10 (100). DECIGO and B-DECIGO have shorter arms than LISA. This is because of constructing the cavity by reducing the optical loss due to the diffraction, i.e. divergence of the laser light [127]. As a result, DECIGO and B-DECIGO have a better shot noise level than LISA.

Compared with the L-shaped interferometer such as the current ground-based detectors, the triangular shaped interferometer has the following advantages. First, the calibration and false alarm ratio are improved by constructing null-streams, which are time-series data where the gravitational wave signals are cancelled, from the linear combination of each interferometer output [61]. Since the instruments are limited in space detectors, in-situ calibration method is important. Second advantage is the improvement of the sensitivity to the polarization of gravitational waves [60,61]. As discussed above, detection of non-tensor gravitational waves leads to the test of the modified gravity theories. Third, the triangular shaped interferometer provides the redundancy which is important for space gravitational wave detectors.

In DECIGO and B-DECIGO, the laser lights from two satellites are injected one arm cavity from both sides and its length can be measured with the two lasers. This type of the interferometer is called dual-pass Fabry–Pérot interferometer. The dual-pass Fabry–Pérot interferometer leads to the redundancy with minimum number of the main mirrors. However, since the dual-pass Fabry–Pérot interferometer is new configuration for DECIGO and B-DECIGO, we need to develop it.

In order to achieve the DECIGO and B-DECIGO interferometers, two-type concepts as shown in figure 4.3 have been proposed up to now. Notice that the Fabry–Pérot Michelson interferometer similar to the ground-based detector is not effective in DECIGO and B-DEICGO since it is difficult to implement

Table 4.1: Specification and requirement of DECIGO and B-DECIGO in *dual-pass differential Fabry–Pérot interferometer*. Spectrum items are defined at 0.1 Hz.

Items	Specification/Requirement		Limiting factor
	DECIGO	B-DECIGO	
Arm cavity			
Arm length L [km]	10^3	10^2	Sensitivity
Finesse $\mathcal{F}$	10	100	Diffraction loss
Wavelength λ [nm]	515	515	
Mirror mass m [kg]	100	30	Sensitivity
Mirror diameter [cm]	166	70	Diffraction loss
Mirror thickness [cm]	2	4	
Radius of curvature [km]	607	60.7	Angular optical anti-spring
Pre stabilized laser			
Output power P_0 [W]	> 10	> 0.02	Sensitivity
Relative intensity noise $\delta P/P_0$ [$/\sqrt{\text{Hz}}$]	$< 2 \times 10^{-9}$	$< 10^{-8}$	Sensitivity
Frequency noise δf [Hz$/\sqrt{\text{Hz}}$]	< 1	< 1	Sensitivity
Interferometer sensing and actuation			
Actuator noise δF_{act} [N$/\sqrt{\text{Hz}}$]	$< 2 \times 10^{-17}$	$< 2 \times 10^{-17}$	Sensitivity
Actuator range $F_{\text{act}}^{(\text{max})}$ [μN]	> 2	> 0.06 (> 6)	Depend on orbit design
Satellite			
Mass m_{SAT} [kg]	1000	1000	
Cross section [m^2] (typical)	2	2	
Coupling from sat. disp. to mirror acc. K [/s^2]	$< 5 \times 10^{-7}$	$< 5 \times 10^{-7}$	Sensitivity
Drag-free control			
Local sensor noise δx_{LS} [m$/\sqrt{\text{Hz}}$]	$< 10^{-12}$	$< 10^{-12}$	Sensitivity
Control gain of satellite at 0.1 Hz	> 250	> 250	Sensitivity
Control gain of mass at 0.1 Hz	$< 10^{-6}$	$< 10^{-6}$	Sensitivity
Thruster			
Thruster noise $\delta F_{\text{thruster}}$ [N$/\sqrt{\text{Hz}}$]	$< 1 \times 10^{-7}$	$< 1 \times 10^{-7}$	Sensitivity
Thruster range $F_{\text{thruster}}^{(\text{max})}$ [μN]	> 100	> 100 (> 200)	Depend on orbit design

so-called recycling techniques in space [21, 135]. The left and right concepts in figure 4.3 are called a single-source and a two-source concepts, respectively. The advantages and disadvantages of these two concepts are summarized in table 4.2. In the two-source concept, there is a major concern about the detection instrument, i.e. phase meter [162, 163]. To achieve the shot-noise-limited sensitivity, a new low noise phase meter should be developed, especially for DECIGO sensitivity. On the other hand, in the single-source concept, the shot-noise-limited measurement can be achieved with Pound–Drever–Hall technique similarly to the ground-based gravitational wave detectors [164, 165]. Thus, we focus on the single-source concept in this thesis and this concept is called a *dual-pass differential Fabry–Pérot interferometer*. Note that the two lasers confronting in the cavity have orthogonal polarization for decoupling the dual-pass interferometer.

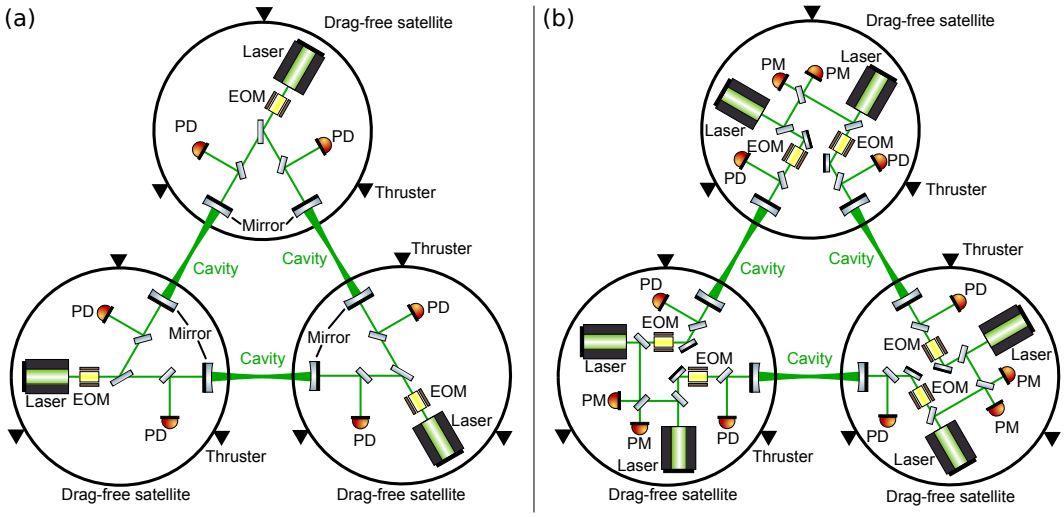

Figure 4.3: Two proposed concepts of the Fabry–Pérot type space gravitational wave antennas. PM means phase meter.

The dual-pass differential Fabry–Pérot interferometer can be divided into three arm-cavity pairs as shown in figure 4.4. In the interferometer (1), one cavity is kept to resonate with the feedback control of the laser frequency and the resonance of the other cavity is kept by controlling the mass position. This kind of interferometer is called a differential Fabry–Pérot interferometer (or locked Fabry–Pérot interferometer), which was used in the ground-based gravitational wave detectors [166, 167]. The interferometer (2) can be operated as another differential Fabry–Pérot interferometer same as the interferometer (1). The interferometer (3) is not simple. Since the length of Cavity b is determined by the interferometer (1), the mass position cannot be controlled arbitrarily. In addition, the laser frequencies are shifted for each other for decoupling the three interferometers. Therefore, in order to resonate Cavity b for both lasers of interferometer (1) and (3) simultaneously, we need to adjust the length of Cavity a and b. They can be adjusted, for example, with auxiliary ranging instruments explained in Section 4.3.5. For more detail, see Chapter 6 also.

Table 4.2: Comparison of the two concepts of the proposed Fabry–Pérot type space gravitational wave antennas.

Concept type	Single source	Two sources
Advantage	• Simple configuration, • Shot noise limited sensitivity can be achieved with the state-of-the-art interferometer technique.	• Three arms can be regarded independently, • Mass control is not necessary (in length control), i.e. mass actuator noise does not matter.
Disadvantage	• To obtain length signals of three arms, absolute length should be adjusted, • Low noise mass actuator is necessary, • Three arms should be controlled in phase.	• To obtain shot noise limited sensing, new low noise sensing technique should be developed, • Doubled space and electric power are necessary for two laser sources.

4.2.2 Arm cavity design

DECIGO has 1000-km-long arm cavities. The finesse of the cavity is 10 and corresponds to the amplitude reflectivity of the mirrors of 0.84. The test masses that float in the satellites are made of fused silica and each test mass weighs 100 kg. The geometry of the test mass is as follows: the diameter, 166 cm; the thickness, 2 cm; the radius of curvature of high reflectivity surface, 607 km. The diameter is designed to receive enough amount of light to reduce diffraction loss in terms of optical power less than 6%. The radius of curvature is designed to obtain stable cavity and to weaken the optical angular anti-spring effect, known as Sidles–Sigg effect [168], as explained in Section 5.2.2. B-DECIGO cavity is 100 km and its finesse is 100. The mirror diameter is 70 cm to make diffraction loss less than 0.6%. Above parameters and the others are summarized in table 4.1.

4.2.3 Pre stabilized laser

The seed laser source of DECIGO and B-DECIGO is the Yb-doped fiber distributed feedback laser of which wave length is 1030 nm [169]. The seed laser is injected to a second harmonic generator and converted to the green light, 515 nm. The laser has to be stabilized and amplified in order to meet the requirement of DECIGO ($P_0 = 10$ W, $\delta P/P_0 = 2 \times 10^{-9}$ $/\sqrt{\text{Hz}}$, $\delta f = 1$ Hz$/\sqrt{\text{Hz}}$) and B-DECIGO ($P_0 = 0.02$ W, $\delta P/P_0 = 10^{-8}$ $/\sqrt{\text{Hz}}$, $\delta f = 1$ Hz$/\sqrt{\text{Hz}}$), which are summarized in table 4.1.

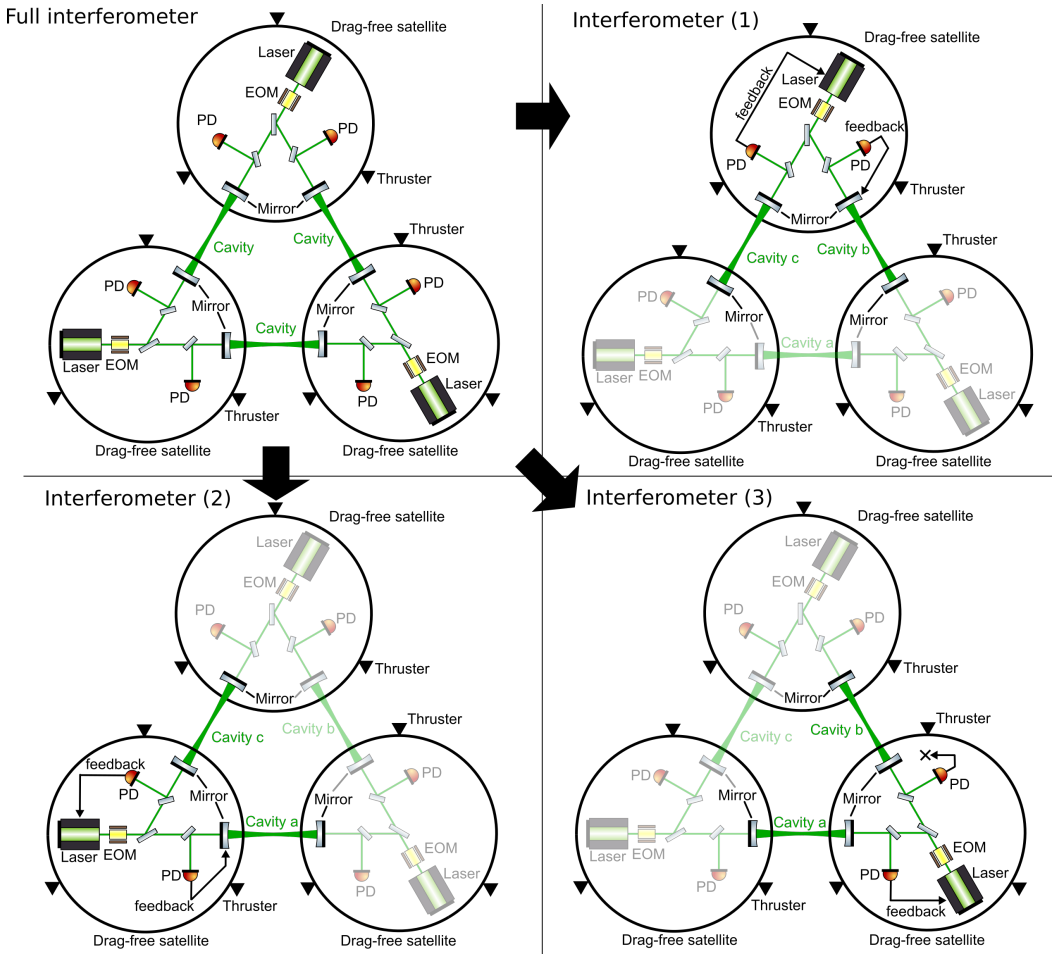

Figure 4.4: Schematic of division of the DECIGO or B-DECIGO interferometer into three pairs of the arm cavities.

For the power amplification to meet the B-DECIGO requirement, the seed laser is amplified with Yb doped fiber amplifier in 1030 nm using master oscillator power amplifier technique. Although the way to amplify the laser to 10 W has not been decided, the coherent combing scheme, which is used in the ground-based gravitational wave detector [170, 171], is one candidate to meet the requirement of DECIGO.

The laser intensity is stabilized with feedback control [169]. The amplified laser is splitted into two paths. One beam goes to the main interferometer and the other is received by the photodetector. The latter signal is fed back to the current of the laser diode used as a pump laser for the above power amplification. As a result, the intensity of the laser introduced to the main interferometer is stabilized.

The frequency stabilization is performed with the iodine cell [169]. In general, stable frequency reference is necessary for the frequency stabilization. In the frequency stabilization with the iodine cell, the saturated absorption line is used as frequency reference. The laser frequency fluctuation is stabilized better than 1 $\mathrm{Hz}/\sqrt{\mathrm{Hz}}$. Since this stability is not enough to detect gravitational wave, the laser

is more stabilized with main arm cavity. For this purpose, as shown in figure 4.5, the laser before the iodine cell is introduced to the acousto-optic modulator, which can shift the laser frequency proportional to the applied voltage. With this scheme, the laser frequency can be controlled with the main interferometer signal [172]. Hereafter, we call the pre-stabilized laser just the laser source unless otherwise noted.

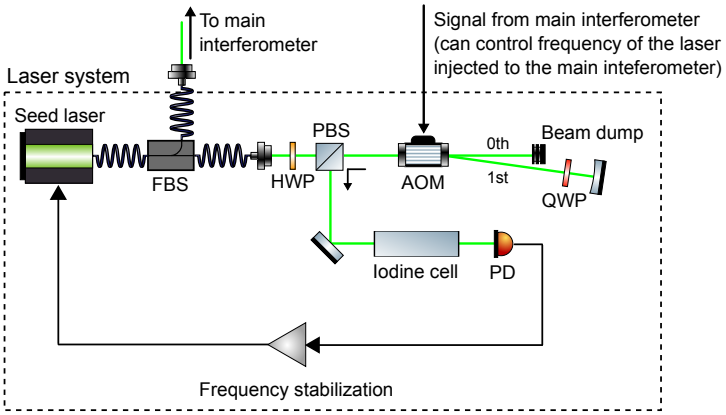

Figure 4.5: Schematic of the frequency stabilizing system with double-pass acousto-optic modulator scheme. FBS is a fiber beam splitter; QWP is a quarter wave plate.

It is important to note that the central frequencies of the three laser sources in each satellite are shifted for each other by a few hundred MHz for decoupling the dual-pass interferometers. Without the frequency shifting, the relative motion of the laser source, i.e. the satellite, makes large phase noise due to Doppler shift. However, this frequency shift requires the absolute cavity length adjustment to operate the three dual-pass interferometers as explained in Chapter 6.

4.2.4 Sensing and actuation

In DECIGO and B-DECIGO, the same sensing method is planned to be used. The longitudinal signal of the cavity is obtained with the Pound–Drever–Hall method [129]. The absolute length of the cavity is measured with the beatnote frequency of the two dual-pass laser resonating in the same cavity as shown in figure 4.6. The absolute cavity length, L, and the beatnote frequency, $\Delta\nu$, have a relationship as

$$L = \frac{Nc}{2\Delta\nu}, \tag{4.1}$$

where N is the number of the beatnote frequencies in terms of the free spectral range. Since N can be determined from the independent measurement, e.g. see [173], the absolute length of the cavity can be determined from equation (4.1) [174, 175]. The precision is wavelength level, i.e. sub-μm or so. The alignment signals are obtained with the wave front sensing method [133, 134] and the dithering method [131]. In addition to these global sensings, in the satellite, the local Michelson interferometer to measure differential optical path

fluctuation is also implemented. The differential optical path fluctuation could be a noise source due to the differential Doppler shift. In order to suppress the Doppler noise, the local Michelson interferometer should have better sensitivity than $2.4\times10^{-15}(^{0.1\ \mathrm{Hz}}/_{f})\ \mathrm{m}/\sqrt{\mathrm{Hz}}$ for DECIGO and $2.4\times10^{-14}(^{0.1\ \mathrm{Hz}}/_{f})\ \mathrm{m}/\sqrt{\mathrm{Hz}}$ for B-DECIGO.

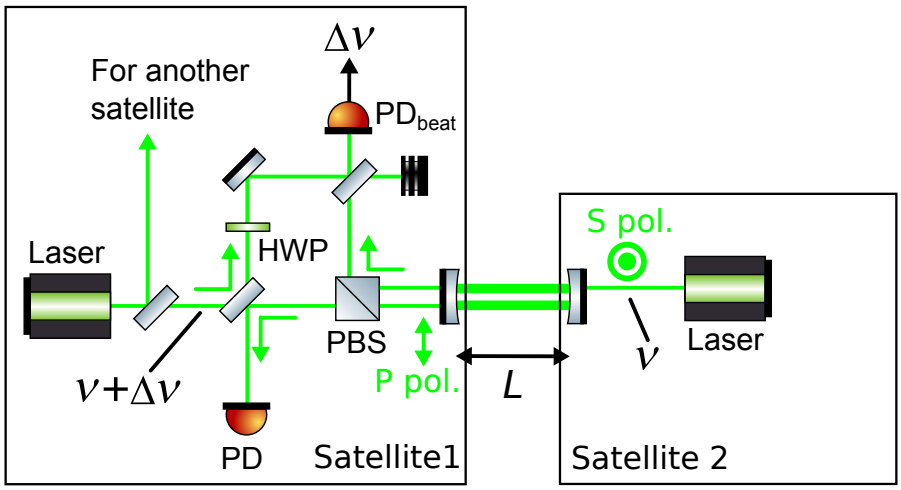

Figure 4.6: Schematic of measuring the beatnote, $\Delta\nu$, of the lasers from two satellites. $\mathrm{PD_{beat}}$ is the photodetector for the beatnote measurement. HWP is the half wave plate, and PBS is the polarizing beam splitter. The half wave plate is used to adjust the polarization and make interference between the lasers from Satellite 1 and 2. Note that the two laser lights in the arm cavity are shifted in the illustration while they are overlapped in fact.

The actuator for cavity control is the frequency actuator in the laser source and the displacement actuator on the test mass. The frequency actuator in the laser is the acousto-optic modulator and has to have lower noise than $1\ \mathrm{Hz}/\sqrt{\mathrm{Hz}}$. For the test mass actuator, electro-static actuator [176,177] is planned to be used and its requirement of noise is better than $2\times10^{-17}\ \mathrm{N}/\sqrt{\mathrm{Hz}}$ for DECIGO and B-DECIGO.

The actuator range is designed to have force enough to compensate relative acceleration to the test masses. In the space detectors, the main causes of the force generating the relative acceleration are the laser radiation pressure and the gravity from the satellite and the Earth. The amount of the force varies by the detector configurations. In DECIGO, the laser radiation pressure is dominant to be 0.1 μN. When B-DECIGO is in heliocentric orbit, gravity from the satellite causes dominant noise which is given by

$$G\frac{(\Delta m)m_{\mathrm{TM}}}{(\Delta r)^2}, \tag{4.2}$$

where Δm is the mass asymmetry and Δr is the distance between the test mass and the mass asymmetry. Since we assume $\Delta m = 3$ kg and $\Delta r = 1$ m, the test mass of B-DECIGO feels the static force of about 6×10^{-9} N. Note that

the laser radiation pressure in B-DECIGO is about 2 nN which is subdominant force. When B-DECIGO is in geocentric orbit, gravity from the Earth causes the major force that is about 0.6 μN as discussed in Section 4.3.4. Consequently, the requirements for the actuators of DECIGO and B-DECIGO in heliocentric orbit is $> 1 \times 10^{-6}$ N and $> 6 \times 10^{-8}$ N, respectively. We assume the safety factor of 10 in terms of the maximum force range of the actuator. For B-DECIGO in geocentric orbit, actuator range should be $> 6 \times 10^{-6}$ N. Again, we assumed the safety factor of 10. In order to achieve the dynamic range of the mass actuator for DECIGO and B-DECIGO in geocentric orbit, we need to design frequency dependent actuation efficiency: low gain and low noise in observation frequency (0.1-10 Hz), high gain and large noise below observation frequency ($\ll 0.1$ Hz). Actually, since actuators with these values are too weak to achieve the cavity resonance at first moment, known as lock acquisition, stronger actuators (more noisy) will be used during the lock acquisition stage. For alignment actuation, steering mirrors are implemented in each optical path.

For the DECIGO and B-DECIGO operation, the control scheme, i.e. how to use the sensed signal and actuators, is important. This will be discussed in detail in Chapter 5.

4.2.5 Input and output optics

After the laser is output from the laser source, the laser is transferred to the optical bench via optical fiber. During the transfer, phase modulation is applied with an electro-optic modulator for the Pound–Drever–Hall method and the wave front sensing method. In the optical bench, the light is divided into two paths for two arm cavities and the polarization is adjusted for discrimination of the dual-pass interferometer. Note that most of the optics are fixed on the optical bench monolithically [178] except for a few steering mirrors, and so on. Then, the light is expanded with telescope system before injected to the arm cavity. The telescope system is one of the components that should be newly developed since the very long cavity requires precise adjustment of the spacial mode of the incident laser. The reflected light is contracted in reversing way. The reflected light and the transmitted light coming from the other satellite are distinguished with the polarization and frequency as explained in Section 4.2.1 and Section 4.2.3.

Using the laser distinguished with the polarization and frequency, the noise caused by the other laser can be reduced. The noise due to the other laser is mainly caused by the intensity fluctuation and is written as

$$h_{\rm laser} \sim \frac{\alpha\lambda}{\beta L\mathcal{F}} \frac{\delta P(\Delta\nu)}{P_0} \frac{1}{\sqrt{1+\left(\frac{\Delta\nu}{\nu_{1/2}}\right)^2}}, \tag{4.3}$$

where α is the amplitude of the non-desired polarized electric field normalized by the amplitude of the desired polarized electric field, and β is the modulation index of the laser for the Pound–Drever–Hall technique. When we design $\Delta\nu \sim 50$ MHz, the typical intensity fluctuation is $\frac{\delta P(\Delta\nu)}{P_0} \sim 10^{-7}\ /\sqrt{\rm Hz}$ [179, 180]. As

a result, the noise caused by the other laser is estimated to be $h_{\rm laser} \sim 10^{-28}$ $/\sqrt{\rm Hz}$ and is 10^5 (10^6) times smaller than the target sensitivity of DECIGO (B-DECIGO). Here, we assume $\alpha = 0.01$ and $\beta = 0.1$. For λ, L, and $\mathcal{F}$, the values shown in table 4.1 are used. $\nu_{1/2}$ can be calculated to be 7.5 Hz from L and $\mathcal{F}$.

4.3 Satellite system design

4.3.1 Overview of satellite

Each satellite is equipped with two test masses, their actuators, a pre-stabilized laser, and local input/output optics. In addition, local sensors around masses, thrusters, auxiliary sensors, data acquisition/processing/transfer systems, and power suppling system are also incorporated into the satellite. The latter two are not discussed in this thesis.

The summary of the satellite parameters is shown in table 4.1. The mass of satellite will be around 1000 kg and the typical cross section will be about 2 $\rm m^2$. To avoid generating mechanical vibration noise, movable components, e.g. momentum wheel, are used as little as possible. Since the mast system can weaken the structure of the satellite and enlarge a mechanical vibration noise, the solar cell will be mounted on the body.

The test mass is stored in the satellite without any mechanical connection. However, there is a small coupling from the satellite motion to the test mass acceleration because of gravitational force or electromagnetic force. The coupling factor, K [$/\rm s^2$], strongly depends on the geometry of the test mass and satellite while it is estimated to be 10^{-6} $/\rm s^2$, at most [140]. In DECIGO and B-DECIGO, K is designed to be less than 5×10^{-7} $/\rm s^2$ with a geometry management.

4.3.2 Drag-free satellite

The drag-free control is the relative motion and angle control of the satellite following the test mass [57]. The drag-free control minimizes the dragging force effect to the test mass [139,140,181,182]. In DECIGO and B-DECIGO, main objective is reduction of solar radiation pressure fluctuation effect. In the drag-free control, local sensor to measure the relative motion/angle between the satellite and the mirror and low noise thrusters are used and their noise level and range are important. The contribution from the satellite motion is written as

$$\delta a_{\rm TM}^{\rm DF} = K \delta x_{\rm SAT}^{\rm DF} \tag{4.4}$$

$$= K \left(\frac{G^{\rm DF}}{1+G^{\rm DF}} \delta x_{\rm LS} + \frac{1}{1+G^{\rm DF}} \frac{\delta F_{\rm thruster}}{m_{\rm SAT}\omega^2} \right), \tag{4.5}$$

where $\delta a_{\rm TM}^{\rm DF}$ is the acceleration of the test mass due to the drag-free control, $\delta x_{\rm SAT}^{\rm DF}$ is the displacement of the satellite, and $G^{\rm DF}$ is the open loop transfer function of the drag-free control (about the open loop transfer function, see Appendix B).

As the local sensor, interferometric sensors are planned to be used for DECIGO and B-DECIGO while LISA will use electro static sensors [177,183]. The

ultimate specification of drag-free control is limited by the sensor noise. The requirement for drag-free control is more strict in DECIGO and B-DECIGO than that of LISA because of the force noise requirement difference. Interferometric sensor has low noise level, $\sim 10^{-12}$ m/$\sqrt{\text{Hz}}$, which meets the DECIGO and B-DECIGO requirement [184, 185]. About the range, orthogonal quadratures type interferometer has a wide range [185].

The thruster for the drag-free control should have low noise although its noise can be suppressed by the drag-free control. Lower noise thrusters make the lower requirement for the control gain of the drag-free control. In addition, the thruster should be continuously variable for the precise drag-free control. Otherwise, quantization noise could be a problem. If the thruster noise is 1×10^{-7} N/$\sqrt{\text{Hz}}$, the control gain should be larger than 250 at 0.1 Hz. There are various thruster candidates which can meet the above features [186], e.g. cold-gas jet, ion thruster, and field-emission electric propulsion. However, they have not been fully characterized and some of them have not been tested in space. Therefore, the design will be finalized after further study.

The largest force applied to the satellite is solar radiation pressure in heliocentric orbit and gravity of the Earth in geocentric orbit. Since the typical solar radiation power density is 1360 W/m^2 [140, 144], the solar radiation pressure force is estimated to be $\sim$ 10 μN. Here, we assume that the typical satellite cross section is 2 m^2. To compensate this amount of force, the low noise thruster should have maximum force larger than 100 μN in heliocentric orbit when we use safety factor of 10. The gravity from the Earth in geocentric orbit is about 20 μN as discussed in Section 4.3.4. This leads to the requirement for the thruster range in geocentric to be larger than 200 μN with safety factor of 10.

Considering that the three-dimensional mechanical degree of freedom of the satellite is six and that of the two test masses is 12 in total,[*1] we cannot control all the relative motions and angles between the satellite and the two test masses only with the drag-free control. Thus, one test mass should be controlled to follow the satellite with the test mass actuators, i.e. electro static actuators.[*2] However, if the control band width is as high as the observation band, the sensitivity can be easily contaminated. To avoid it, the test mass control gain is designed to be less than 10^{-6} at 0.1 Hz. The detailed discussion is described in Chapter 5.

4.3.3 Test mass housing

The test mass is placed in the housing in the satellite. The housing includes electrostatic actuators, interferometric local sensors, vacuum system, discharging system [187], and launch locking system. Here, they are explained briefly. The former two are mentioned above. The vacuum system is necessary in DECIGO and B-DECIGO to reduce noise caused by the molecular gas around the test mass. The molecules stochastically hit the test mass and make the test mass fluctuate. This noise is called residual gas thermal noise. To obtain enough small

[*1] The satellite and the mirror are each considered to be a rigid body.

[*2] There is other choice of which degrees of freedoms are used for the drag-free control. For example, the motion of two test masses $(3+3)$ can be followed by the satellite [139, 182].

residual gas thermal noise, the vacuum level should be better than 10^{-10} Pa. The discharging system is practically important to operate the interferometer stably. Since the test mass does not touch anywhere mechanically, it is gradually charged by the cosmic rays. When the charge of the test mass is large, its coupling to the electrostatic actuator gets strange. Therefore, the test mass should be discharged occasionally with, e.g., ultraviolet light and so on. The launch lock system protects the test mass from the large vibration during launch. The test mass will be softly released after the satellite arrives proper position.

4.3.4 Orbit

DECIGO is planned to be in the heliocentric orbit as shown in figure 4.7. DECIGO is composed of the four clusters, i.e. 12 satellites [188]. Two of four clusters are overlapped in opposite shape to take correlation for the stochastic gravitational wave background. Using the four clusters, we can observe the multi-mode gravitational waves, i.e. not only tensor mode gravitational wavs but also vector/scalar mode gravitational waves, for testing the modified gravitational theories.

B-DECIGO orbit will be heliocentric orbit or geocentric orbit as shown in figure 4.7. In geocentric orbit a bit far or near orbit from geostationary orbit is considered for now. In contrast to DECIGO, B-DECIGO will have one cluster. Note that even with one cluster, we can localize gravitational wave events considering the time variation of the angular response of the detector, called antenna pattern discussed in Appendix G, during the event. For example, it is expected that one neutron star inspiral is typically in B-DECIGO observation band in ~ 1 year.

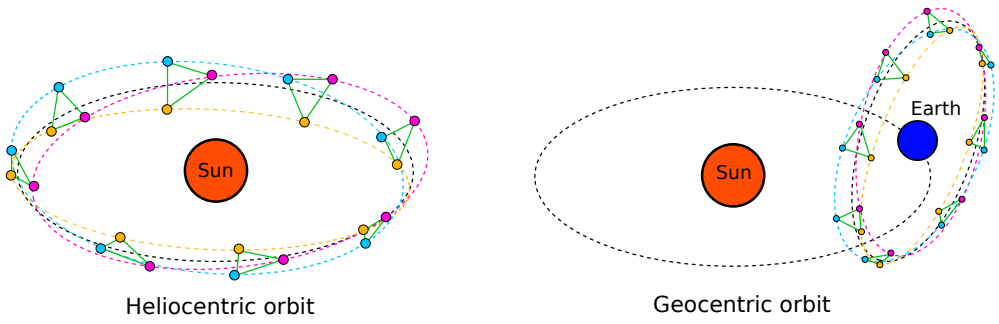

Figure 4.7: Schematic of the heliocentric and geocentric orbit.

In geocentric orbit, the gravity of the Earth, especially its J_2 term, limits the range of actuator and thruster. J_2 term is an ellipticity measure of the Earth and makes a differential acceleration of the two masses, a_{J2}, given by

$$a_{J_2} \simeq J_2 \frac{3GM_E r_E^2}{2r_D^4} = 8.2 \times 10^{-6} \left(\frac{42000 \text{ km}}{r_D} \right)^4 \left[\text{m/s}^2 \right], \tag{4.6}$$

where, $J_2 (= 1.08263 \times 10^{-3})$ is the J2 constant, G is gravity constant, M_E is the mass of the Earth, r_E is the radius of the Earth, and r_D is orbital radius of

B-DECIGO. The differential acceleration between two masses in distance of L is written as

$$\Delta a_{\mathrm{J}_2} \simeq \frac{L}{r_{\mathrm{D}}} a_{\mathrm{J}_2} = 1.9 \times 10^{-8} \left(\frac{L}{100 \text{ km}} \right) \left(\frac{42000 \text{ km}}{r_{\mathrm{D}}} \right)^5 \left[\mathrm{m/s^2} \right] . \tag{4.7}$$

4.3.5 Auxiliary sensors and thrusters

Auxiliary sensors

In addition to the main interferometer, DECIGO and B-DECIGO have various auxiliary sensors. For example, star trackers, beam scanning systems with an acousto-optic deflector, sun sensors, global positioning systems, microwave ranging systems [189], and so on. They are used for rough ranging in orbit before interferometer lock acquisition [190]. During observation, their signals are used for the calibration of satellite position and orientation. The calibration precision affects the systematic error of the gravitational wave localization. For example, typical star tracker has the angular resolution ~ 10 arcsec and it corresponds to $\sim 10^{-5}$ deg^2, which is much better than the statistic localization error while relative calibration of the star tracker and interferometer axis is necessary.

Thrusters

In addition to the low noise thruster, two types of auxiliary strong thrusters will be incorporated. The first one is bipropellant catalytic hydrazine thruster (N_2O_4/N_2H_4) for apogee kick. The thruster has typically 500-N thrust force. The second one is 1-N-class cold gas jets. They are used for orbital control which will be performed when we need to move the satellite a lot, e.g. during interferometer lock acquisition. These two strong thrusters are turned off during observation for avoiding causing the vibration noise.

Chapter 5

Control scheme of DECIGO and B-DECIGO

DECIGO and B-DECIGO are currently designed to be unique space gravitational wave antennas with Fabry–Pérot arm cavities and drag-free satellites. Each technique has been independently demonstrated, e.g. the former in ground-based detectors, and the latter in LISA path finder [139, 182], while the combination of them has been neither demonstrated nor considered. Actually, although the two controls can be regarded almost independently in LISA configuration [191], they are strongly related to DECIGO and B-DECIGO configurations. Therefore, the control topology in which the interferometer and drag-free control should be developed for DECIGO and B-DECIGO. Moreover, feedback control system introduces additional noise through the feedback loop. The additional noise could disturb the gravitational wave observation. Therefore, control system should be carefully designed especially in observation frequency band [58, 59].

In this chapter, we study on the control topology of DECIGO type space detector and construct the numerical control model. Moreover, using the model, the detailed requirements including control design, the stability, and the sensitivity of DECIGO and B-DECIGO are considered.

This chapter is organized as follows: In Section 5.1, we show the setup and basis definition used in this chapter. From Section 5.2 to Section 5.4, as a preparation of the numerical model construction, we newly modeled the mechanical and opto-mechanical response, and sensing and actuation scheme in DECIGO and B-DECIGO. This modeling clarifies which degrees of freedom should be controlled in the interferometer control or the drag-free control. In Section 5.5, dominant sources of noise and instability are shown. In Section 5.6, using the result prepared in the above sections, we design the control topology of DECIGO and B-DECIGO. After that, in Section 5.7, the numerical control model of DECIGO and B-DECIGO is constructed with the designed control topology. The model is the new model including full responses of the Fabry–Pérot type space antenna and is named a *full DECIGO interferometer model*. Subsequently, in Section 5.8, using the full DECIGO interferometer model, we consider the detailed requirement including control design for DECIGO and B-DECIGO, and investigate the performance of the design control scheme. Especially, the sta-

bility of the control and the interferometer operation, and noise performance of DECIGO and B-DECIGO are investigated. Finally in Section 5.9, the obtained results are discussed.

5.1 Setup and basis definition

The setup that we consider is shown in figure 5.1. Note that not all components of DECIGO and B-DECIGO are shown here. For example, the electro-optic modulator is not shown. All components except for the test masses are fixed on the satellite. Hereafter, we assume all test masses have the same mass $m_{\rm TM}$, reflectivity r, and the radius of curvature R_c and the optical loss of the cavity is negligible. The length of each cavity is $L_{\rm a(b,c)}$ and they are macroscopically the same ($L \simeq L_{\rm a,b,c}$). Each laser frequency is represented as $f_{1(2,3)}$.

The basis with which we consider the interferometer and satellite motion and angle is shown in figure 5.1-(b). Hereafter, we assume that the center of mass and geometry of the satellite are located at the same position, and the satellites and the test masses are rigid bodies when we consider the control topology. The origin of each basis is defined at initial position of the center of satellite mass for the satellites, and the center of mass for the test mass. The optical basis origin is defined at the initial waist position that is located at the center of the cavity since the cavity is composed of the mirror having the same radius of curvature.

The mechanical position and angle vector of Test Mass $i\alpha$ and Satellite i are represented as $\boldsymbol{x}_{i\alpha} \equiv (x_{i\alpha}, y_{i\alpha}, z_{i\alpha}, \theta_{{\rm rol},i\alpha}, \theta_{{\rm pit},i\alpha}, \theta_{{\rm yaw},i\alpha})^\top$ and $\boldsymbol{x}_{{\rm SAT}i} \equiv (x_{{\rm SAT}i}, y_{{\rm SAT}i}, z_{{\rm SAT}i}, \theta_{{\rm rol,SAT}i}, \theta_{{\rm pit,SAT}i}, \theta_{{\rm yaw,SAT}i})^\top$ ($i = 1, 2, 3$, and $\alpha =$ a,b,c). The optical alignment of Cavity α and incident beam from Satellite i are expressed as $\boldsymbol{x}_{i\alpha}^{{\rm cav}\alpha} \equiv (x^{{\rm cav}\alpha}, y^{{\rm cav}\alpha}, z^{{\rm cav}\alpha}, \theta_{\rm rol}^{{\rm cav}\alpha}, \theta_{\rm pit}^{{\rm cav}\alpha}, \theta_{\rm yaw}^{{\rm cav}\alpha})^\top$ and $\boldsymbol{x}^{{\rm inci}\alpha} \equiv (x^{{\rm inci}\alpha}, y^{{\rm inci}\alpha}, z^{{\rm inci}\alpha}, \theta_{\rm rol}^{{\rm inci}\alpha}, \theta_{\rm pit}^{{\rm inci}\alpha}, \theta_{\rm yaw}^{{\rm inci}\alpha})^\top$. In terms of Satellites 1(2,3) basis, test mass TM1b(2c,3a) is at $(a\cos(\pi/6), a\sin(\pi/6), 0)^\top$ and test mass TM1c(2a,3b) is at $(a\cos(\pi/6), -a\sin(\pi/6), 0)^\top$. The force and torque applied to the Test mass $i\alpha$ and Satellite i are expressed as $\boldsymbol{F}_{i\alpha} \equiv (F_{x_{i\alpha}}, F_{y_{i\alpha}}, F_{z_{i\alpha}}, T_{\theta_{{\rm rol},i\alpha}}, T_{\theta_{{\rm pit},i\alpha}}, T_{\theta_{{\rm yaw},i\alpha}})^\top$ and $\boldsymbol{F}_{{\rm SAT}i} \equiv (F_{x_{{\rm SAT}i}}, F_{y_{{\rm SAT}i}}, F_{z_{{\rm SAT}i}}, T_{\theta_{{\rm rol,SAT}i}}, T_{\theta_{{\rm pit,SAT}i}}, T_{\theta_{{\rm yaw,SAT}i}})^\top$, respectively.

5.2 Cavity and satellite

5.2.1 Mechanical property

Table 5.1 shows the mechanical property of the test masses and satellites. They are regarded as rigid bodies in the consideration of control. The satellite is assumed to be cylindrical shaped along z-axis and to have uniform density. In addition, we assume that they are damped with the surrounding gas of which pressure is 10^{-10} Pa and damping ratio is the same for all degrees of freedom as 10^{11} Hz. As a result, the equations of motion of the test mass and the satellite

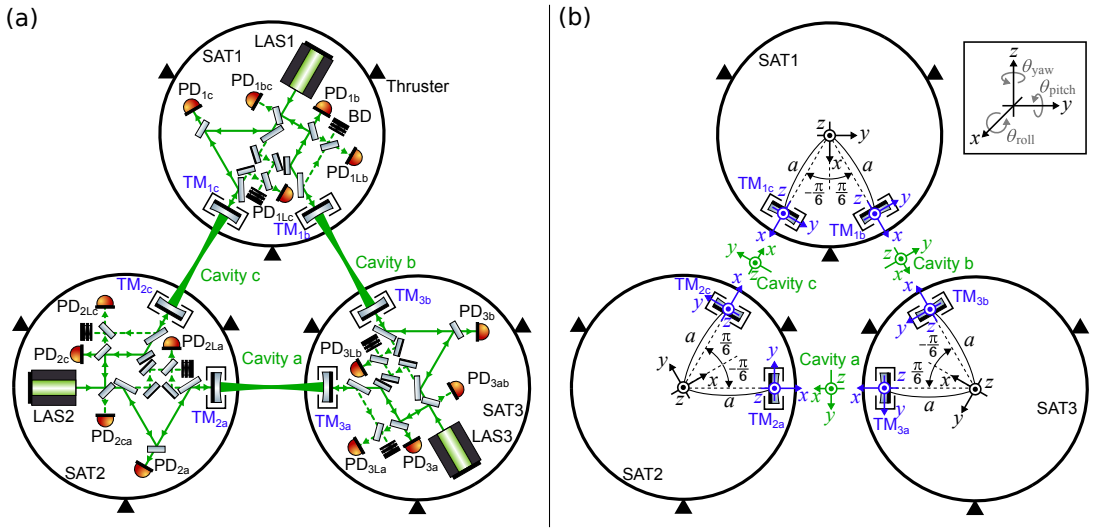

Figure 5.1: (a) Setup for control topology consideration. PD is photodetector, LAS is laser, SAT is satellite, TM is test mass, and BD is beam dump. The photodetector is composed of the photodetector and quadrant photodetectors that are used for length and alignment sensing although the quadrant photodetectors are not explicitly shown in the figure. The mirrors located between the beamsplitter just in front of the laser source and each test mass are used as steering mirrors. The black boxes around the test masses are each their housing including actuators and local sensors. Note that not all components on DECIGO and B-DECIGO are shown here. (b) Basis of each component. Black and blue colors indicate the bases for satellites and test masses, respectively. Green color indicates the basis for the optical axis for cavity and injected beam. The top right subpanel shows the definition of six degrees of freedom of the basis.

are given by

$$\boldsymbol{M}_{\rm TM}(\ddot{\boldsymbol{x}}_{i\alpha} + \boldsymbol{\gamma}_{\rm TM}\dot{\boldsymbol{x}}_{i\alpha}) = \boldsymbol{F}_{i\alpha}, \tag{5.1}$$

$$\boldsymbol{M}_{\rm SAT}(\ddot{\boldsymbol{x}}_{{\rm SAT}i} + \boldsymbol{\gamma}_{\rm SAT}\dot{\boldsymbol{x}}_{{\rm SAT}i}) = \boldsymbol{F}_{{\rm SAT}i}, \tag{5.2}$$

where $\boldsymbol{M}_{i\alpha} \equiv {\rm diag}(m_{\rm TM}, m_{\rm TM}, m_{\rm TM}, I_{\rm TM,rol}, I_{\rm TM,pit}, I_{\rm TM,yaw})$ and $\boldsymbol{M}_{\rm SAT} \equiv {\rm diag}(m_{\rm SAT}, m_{\rm SAT}, m_{\rm SAT}, I_{\rm SAT,rol}, I_{\rm SAT,pit}, I_{\rm SAT,yaw})$ are the mass matrices ($m_{\rm TM(SAT)}$ is the mass of the test mass (satellite) and $I_{\rm TM[SAT],rol(pit,yaw)}$ is the moment of inertia along $x(y,z)$-axis) of the test mass and the satellite, respectively, and $\boldsymbol{\gamma}_{\rm TM} \equiv \gamma_{\rm TM}\boldsymbol{I}_6$ and $\boldsymbol{\gamma}_{\rm SAT} \equiv \gamma_{\rm SAT}\boldsymbol{I}_6$ ($\boldsymbol{I}_6$ is a 6-by-6 identity matrix) are the damping matrices of the test mass and the satellite, respectively. $\gamma_{\rm TM(SAT)}$ is a damping ratio of the test mass (satellite). By performing Laplace transformation (for detail, see Appendix B), equations (5.1) and (5.2) are denoted as

$$\boldsymbol{M}_{\rm TM}(-\omega^2\boldsymbol{I}_6 + i\omega\boldsymbol{\gamma}_{\rm TM})\tilde{\boldsymbol{x}}_{i\alpha} \equiv \boldsymbol{M}'_{\rm TM}\tilde{\boldsymbol{x}}_{i\alpha} = \tilde{\boldsymbol{F}}_{i\alpha}, \tag{5.3}$$

$$\boldsymbol{M}_{\rm SAT}(-\omega^2\boldsymbol{I}_6 + i\omega\boldsymbol{\gamma}_{\rm SAT})\tilde{\boldsymbol{x}}_{{\rm SAT}i} \equiv \boldsymbol{M}'_{\rm SAT}\tilde{\boldsymbol{x}}_{{\rm SAT}i} = \tilde{\boldsymbol{F}}_{{\rm SAT}i}, \tag{5.4}$$

where the tilde indicates the frequency domain parameters.

Table 5.1: Mechanical property of test masses and satellites. In the parentheses, B-DECIGO parameters are shown if they are different from DECIGO one.

	Test mass	Satellite
Mass [kg]	100 (30)	1000
Diameter [m]	1.66 (0.70)	1.6
Thickness [m]	0.02 (0.04)	2.0
Moment of inertia [kg·m^2]		
along x-axis (Roll)	36 (1.8)	490
along y-axis (Pitch)	18 (0.90)	490
along z-axis (Yaw)	18 (0.90)	320
Damping ratio [Hz]	10^{-11}	10^{-11}

The satellite motion is coupled to the acceleration of the test mass. The relationship is given by

$$\ddot{\boldsymbol{x}}_{1\mathrm{b(2c,3a)}} = K\boldsymbol{R}_{\mathrm{SAT_{to}M1}}\boldsymbol{x}_{\mathrm{SAT1(2,3)}}, \tag{5.5}$$

$$\ddot{\boldsymbol{x}}_{1\mathrm{c(2a,3b)}} = K\boldsymbol{R}_{\mathrm{SAT_{to}M2}}\boldsymbol{x}_{\mathrm{SAT1(2,3)}}, \tag{5.6}$$

where

$$\boldsymbol{R}_{\mathrm{SAT_{to}M1}} \equiv \begin{pmatrix} \cos\left(\frac{\pi}{6}\right) & \sin\left(\frac{\pi}{6}\right) & 0 & 0 & 0 & 0 \\ -\sin\left(\frac{\pi}{6}\right) & \cos\left(\frac{\pi}{6}\right) & 0 & 0 & 0 & a \\ 0 & 0 & 1 & a\sin\left(\frac{\pi}{6}\right) & -a\cos\left(\frac{\pi}{6}\right) & 0 \\ 0 & 0 & 0 & \cos\left(\frac{\pi}{6}\right) & \sin\left(\frac{\pi}{6}\right) & 0 \\ 0 & 0 & 0 & -\sin\left(\frac{\pi}{6}\right) & \cos\left(\frac{\pi}{6}\right) & 0 \\ 0 & 0 & 0 & 0 & 0 & 1 \end{pmatrix}, \tag{5.7}$$

$$\boldsymbol{R}_{\mathrm{SAT_{to}M2}} \equiv \begin{pmatrix} \cos\left(-\frac{\pi}{6}\right) & \sin\left(-\frac{\pi}{6}\right) & 0 & 0 & 0 & 0 \\ -\sin\left(-\frac{\pi}{6}\right) & \cos\left(-\frac{\pi}{6}\right) & 0 & 0 & 0 & a \\ 0 & 0 & 1 & a\sin\left(-\frac{\pi}{6}\right) & -a\cos\left(-\frac{\pi}{6}\right) & 0 \\ 0 & 0 & 0 & \cos\left(-\frac{\pi}{6}\right) & \sin\left(-\frac{\pi}{6}\right) & 0 \\ 0 & 0 & 0 & -\sin\left(-\frac{\pi}{6}\right) & \cos\left(-\frac{\pi}{6}\right) & 0 \\ 0 & 0 & 0 & 0 & 0 & 1 \end{pmatrix}, \tag{5.8}$$

are rotation matrices from the satellite position and angle to the mass position and angle.

5.2.2 Opto-mechanical property

The test masses for the Fabry–Pérot cavity are coupled via radiation pressure of the laser. This coupling is called opto-mechanical coupling. The angular opto-mechanical coupling, known as Sidles–Sigg effect [168], affects the cavity stability since one opto-mechanical mode behaves as an anti-spring. Also, translational opto-mechanical couplings are considered [192]. These couplings are represented

as

$$\begin{pmatrix} F_{y,1} \\ F_{y,2} \\ T_{\theta_{\mathrm{yaw},1}} \\ T_{\theta_{\mathrm{yaw},2}} \end{pmatrix} = \begin{pmatrix} -\frac{2P^{\mathrm{cav}}}{c} & 0 & \frac{2P^{\mathrm{cav}}}{cR_c} & 0 \\ 0 & -\frac{2P^{\mathrm{cav}}}{c} & 0 & \frac{2P^{\mathrm{cav}}}{cR_c} \\ 0 & 0 & \frac{2P^{\mathrm{cav}}}{c} & 0 \\ 0 & 0 & 0 & \frac{2P^{\mathrm{cav}}}{c} \end{pmatrix} \begin{pmatrix} \theta_{\mathrm{yaw},1} \\ \theta_{\mathrm{yaw},2} \\ y_1^{\mathrm{mc}} \\ y_2^{\mathrm{mc}} \end{pmatrix}, \tag{5.9}$$

$$\begin{pmatrix} F_{z,1} \\ F_{z,2} \\ T_{\theta_{\mathrm{pit},1}} \\ T_{\theta_{\mathrm{pit},2}} \end{pmatrix} = \begin{pmatrix} \frac{2P^{\mathrm{cav}}}{c} & 0 & \frac{2P^{\mathrm{cav}}}{cR_c} & 0 \\ 0 & \frac{2P^{\mathrm{cav}}}{c} & 0 & \frac{2P^{\mathrm{cav}}}{cR_c} \\ 0 & 0 & -\frac{2P^{\mathrm{cav}}}{c} & 0 \\ 0 & 0 & 0 & -\frac{2P^{\mathrm{cav}}}{c} \end{pmatrix} \begin{pmatrix} \theta_{\mathrm{pit},1} \\ \theta_{\mathrm{pit},2} \\ z_1^{\mathrm{mc}} \\ z_2^{\mathrm{mc}} \end{pmatrix}, \tag{5.10}$$

where P^{cav} is intracavity power,

$$(F_{y(z),1}, F_{y(z),2}) = (F_{y(z)_{1\mathrm{b}}}, F_{y(z)_{3\mathrm{b}}}), (F_{y(z)_{2\mathrm{c}}}, F_{y(z)_{1\mathrm{c}}}), (F_{y(z)_{3\mathrm{a}}}, F_{y(z)_{2\mathrm{a}}}), \tag{5.11}$$

$$(T_{\theta_{\mathrm{yaw(pit)},1}}, T_{\theta_{\mathrm{yaw(pit)},2}}) = (T_{\theta_{\mathrm{yaw(pit)},1\mathrm{b}}}, T_{\theta_{\mathrm{yaw(pit)},3\mathrm{b}}}), (T_{\theta_{\mathrm{yaw(pit)},2\mathrm{c}}}, T_{\theta_{\mathrm{yaw(pit)},1\mathrm{c}}}), (T_{\theta_{\mathrm{yaw(pit)},3\mathrm{a}}}, T_{\theta_{\mathrm{yaw(pit)},2\mathrm{a}}}), \tag{5.12}$$

$$(\theta_{\mathrm{yaw(pit)},1}, \theta_{\mathrm{yaw(pit)},2}) = (\theta_{\mathrm{yaw(pit)},1\mathrm{b}}, \theta_{\mathrm{yaw(pit)},3\mathrm{b}}), (\theta_{\mathrm{yaw(pit)},2\mathrm{c}}, \theta_{\mathrm{yaw(pit)},1\mathrm{c}}), (\theta_{\mathrm{yaw(pit)},3\mathrm{a}}, \theta_{\mathrm{yaw(pit)},2\mathrm{a}}), \tag{5.13}$$

and $y(z)^{\mathrm{mc}}_{1(2)}$ is the mis-centering on the test mass and defined as $(y(z)^{\mathrm{mc}}_1, y(z)^{\mathrm{mc}}_2) \equiv (y(z)^{\mathrm{mc}}_{1\mathrm{b}}, y(z)^{\mathrm{mc}}_{3\mathrm{b}}), (y(z)^{\mathrm{mc}}_{2\mathrm{c}}, y(z)^{\mathrm{mc}}_{1\mathrm{c}}), (y(z)^{\mathrm{mc}}_{3\mathrm{a}}, y(z)^{\mathrm{mc}}_{2\mathrm{a}})$. The mis-centering on each test mass is denoted as

$$\begin{aligned} y^{\mathrm{mc}}_{1\mathrm{b}(2\mathrm{c},3\mathrm{a})} &= -\frac{L}{2}\theta^{\mathrm{cavb(c,a)}}_{\mathrm{yaw}} + y^{\mathrm{cavb(c,a)}}, \quad & y^{\mathrm{mc}}_{3\mathrm{b}(1\mathrm{c},2\mathrm{a})} &= -\frac{L}{2}\theta^{\mathrm{cavb(c,a)}}_{\mathrm{yaw}} - y^{\mathrm{cavb(c,a)}}, \\ z^{\mathrm{mc}}_{1\mathrm{b}(2\mathrm{c},3\mathrm{a})} &= \frac{L}{2}\theta^{\mathrm{cavb(c,a)}}_{\mathrm{pit}} + z^{\mathrm{cavb(c,a)}}, & z^{\mathrm{mc}}_{3\mathrm{b}(1\mathrm{c},2\mathrm{a})} &= -\frac{L}{2}\theta^{\mathrm{cavb(c,a)}}_{\mathrm{pit}} + z^{\mathrm{cavb(c,a)}}. \end{aligned} \tag{5.14}$$

5.3 Sensing method

Hereafter, for simplicity, we use sensing efficiency normalized with its DC value. This treatment does not lose generality.

5.3.1 Interferometer longitudinal sensing

In each cavity, its longitudinal fluctuation signal is taken with the Pound–Drever–Hall technique. As discussed in Section 3.3.4, each photodetector measures the phase fluctuation of the cavity. When we measure the phase in terms of length,

the measured signals at photodetectors are each written as

$$
\begin{aligned}
s_{\mathrm{PD}_{1\mathrm{b}(1\mathrm{c})}} &= \frac{H_{\mathrm{FP}}^{(L)}(\omega)}{H_{\mathrm{FP}}^{(L)}(0)}\left(-\delta x_{3\mathrm{b}(2\mathrm{c})} - \delta x_{1\mathrm{b}(1\mathrm{c})} + L\frac{\delta f_1}{f_1}\right),\\
s_{\mathrm{PD}_{2\mathrm{c}(2\mathrm{a})}} &= \frac{H_{\mathrm{FP}}^{(L)}(\omega)}{H_{\mathrm{FP}}^{(L)}(0)}\left(-\delta x_{1\mathrm{c}(3\mathrm{a})} - \delta x_{2\mathrm{c}(2\mathrm{a})} + L\frac{\delta f_2}{f_2}\right),\\
s_{\mathrm{PD}_{3\mathrm{a}(3\mathrm{c})}} &= \frac{H_{\mathrm{FP}}^{(L)}(\omega)}{H_{\mathrm{FP}}^{(L)}(0)}\left(-\delta x_{2\mathrm{a}(1\mathrm{c})} - \delta x_{3\mathrm{a}(3\mathrm{c})} + L\frac{\delta f_3}{f_3}\right).
\end{aligned}
\tag{5.15}
$$

Moreover, the absolute length of each cavity can be measured as

$$
\begin{aligned}
s_{\mathrm{PD}_{1L_{\mathrm{b}}(3L_{\mathrm{b}})}} &= L_{\mathrm{b}},\\
s_{\mathrm{PD}_{2L_{\mathrm{c}}(1L_{\mathrm{c}})}} &= L_{\mathrm{c}},\\
s_{\mathrm{PD}_{3L_{\mathrm{a}}(2L_{\mathrm{a}})}} &= L_{\mathrm{a}}.
\end{aligned}
\tag{5.16}
$$

5.3.2 Alignment sensing

In the alignment sensing of DECIGO and B-DECIGO, the wavefront sensing and the dithering method are used. Using the wavefront sensing method [133,134], we can measure the difference between the alignment of the incident beam ($y(z)^{\mathrm{inc}}$ and $\theta^{\mathrm{inc}}_{\mathrm{yaw(pit)}}$) and the cavity axis ($y(z)^{\mathrm{cav}}$ and $\theta^{\mathrm{cav}}_{\mathrm{yaw(pit)}}$). The signal is expressed as

$$
\begin{aligned}
s_{\mathrm{QPD}_{1\mathrm{b}},y(z)} &= y(z)^{\mathrm{cavb}} - y(z)^{\mathrm{inc1b}}, & s_{\mathrm{QPD}_{1\mathrm{b}},\mathrm{yaw(pit)}} &= \theta^{\mathrm{cavb}}_{\mathrm{yaw(pit)}} - \theta^{\mathrm{inc1b}}_{\mathrm{yaw(pit)}},\\
s_{\mathrm{QPD}_{1\mathrm{c}},y(z)} &= y(z)^{\mathrm{cavc}} - y(z)^{\mathrm{inc1c}}, & s_{\mathrm{QPD}_{1\mathrm{c}},\mathrm{yaw(pit)}} &= \theta^{\mathrm{cavc}}_{\mathrm{yaw(pit)}} - \theta^{\mathrm{inc1c}}_{\mathrm{yaw(pit)}},\\
s_{\mathrm{QPD}_{2\mathrm{c}},y(z)} &= y(z)^{\mathrm{cavc}} - y(z)^{\mathrm{inc2c}}, & s_{\mathrm{QPD}_{2\mathrm{c}},\mathrm{yaw(pit)}} &= \theta^{\mathrm{cavc}}_{\mathrm{yaw(pit)}} - \theta^{\mathrm{inc2c}}_{\mathrm{yaw(pit)}},\\
s_{\mathrm{QPD}_{2\mathrm{a}},y(z)} &= y(z)^{\mathrm{cava}} - y(z)^{\mathrm{inc2a}}, & s_{\mathrm{QPD}_{2\mathrm{a}},\mathrm{yaw(pit)}} &= \theta^{\mathrm{cava}}_{\mathrm{yaw(pit)}} - \theta^{\mathrm{inc2a}}_{\mathrm{yaw(pit)}},\\
s_{\mathrm{QPD}_{3\mathrm{a}},y(z)} &= y(z)^{\mathrm{cava}} - y(z)^{\mathrm{inc3a}}, & s_{\mathrm{QPD}_{3\mathrm{a}},\mathrm{yaw(pit)}} &= \theta^{\mathrm{cava}}_{\mathrm{yaw(pit)}} - \theta^{\mathrm{inc3a}}_{\mathrm{yaw(pit)}},\\
s_{\mathrm{QPD}_{3\mathrm{b}},y(z)} &= y(z)^{\mathrm{cavb}} - y(z)^{\mathrm{inc3b}}, & s_{\mathrm{QPD}_{3\mathrm{b}},\mathrm{yaw(pit)}} &= \theta^{\mathrm{cavb}}_{\mathrm{yaw(pit)}} - \theta^{\mathrm{inc3b}}_{\mathrm{yaw(pit)}},
\end{aligned}
\tag{5.17}
$$

where the cavity axis can be written with the position and angle of the test mass as

$$
\begin{aligned}
y^{\mathrm{cavb(c,a)}} &= \frac{y_{1\mathrm{b}(2\mathrm{c},3\mathrm{a})} - y_{3\mathrm{b}(1\mathrm{c},2\mathrm{a})}}{2} + R_c\frac{\theta_{\mathrm{yaw},1\mathrm{b}(2\mathrm{c},3\mathrm{a})} - \theta_{\mathrm{yaw},3\mathrm{b}(1\mathrm{c},2\mathrm{a})}}{2},\\
\theta^{\mathrm{cavb(c,a)}}_{\mathrm{yaw}} &= \frac{1}{R_c - \frac{L}{2}}\frac{y_{1\mathrm{b}(2\mathrm{c},3\mathrm{a})} + y_{3\mathrm{b}(1\mathrm{c},2\mathrm{a})}}{2} + \frac{R_c}{R_c - \frac{L}{2}}\frac{\theta_{\mathrm{yaw},1\mathrm{b}(2\mathrm{c},3\mathrm{a})} + \theta_{\mathrm{yaw},3\mathrm{b}(1\mathrm{c},2\mathrm{a})}}{2},\\
z^{\mathrm{cavb(c,a)}} &= \frac{z_{1\mathrm{b}(2\mathrm{c},3\mathrm{a})} + z_{3\mathrm{b}(1\mathrm{c},2\mathrm{a})}}{2} - R_c\frac{\theta_{\mathrm{pit},1\mathrm{b}(2\mathrm{c},3\mathrm{a})} + \theta_{\mathrm{pit},3\mathrm{b}(1\mathrm{c},2\mathrm{a})}}{2},\\
\theta^{\mathrm{cavb(c,a)}}_{\mathrm{pit}} &= -\frac{1}{R_c - \frac{L}{2}}\frac{z_{1\mathrm{b}(2\mathrm{c},3\mathrm{a})} - z_{3\mathrm{b}(1\mathrm{c},2\mathrm{a})}}{2} + \frac{R_c}{R_c - \frac{L}{2}}\frac{\theta_{\mathrm{pit},1\mathrm{b}(2\mathrm{c},3\mathrm{a})} - \theta_{\mathrm{pit},3\mathrm{b}(1\mathrm{c},2\mathrm{a})}}{2}.
\end{aligned}
\tag{5.18}
$$

Here, we assume $\frac{L}{2} < R_c < L$. Note that the quadrant photodetectors are located in the photodetector that has the same index.

With the dither sensing method [131], we can measure the mis-centering of the beam spot on each test mass in the longitudinal signal. Note that the beam mis-centering is denoted with the same basis as each test mass. The beam mis-centering on each test mass can be distinguished with the dithering frequency. For example, when we dither TM1b and TM3b at 1.03 Hz and 1.39 Hz, the mis-centering signals on TM1b and TM3b appear at 1.03 Hz and 1.39 Hz, respectively. The signals that we can measure are expressed as

$$\begin{aligned}
s_{\mathrm{PD}_{\mathrm{1b[3b]}},y^{\mathrm{mc}}_{\mathrm{1b(3b)}}} &= y^{\mathrm{mc}}_{\mathrm{1b(3b)}} - y_{\mathrm{1b(3b)}}, \quad & s_{\mathrm{PD}_{\mathrm{1b[3b]}},z^{\mathrm{mc}}_{\mathrm{1b(3b)}}} &= z^{\mathrm{mc}}_{\mathrm{1b(3b)}} - z_{\mathrm{1b(3b)}}, \\
s_{\mathrm{PD}_{\mathrm{2c[1c]}},y^{\mathrm{mc}}_{\mathrm{2c(1c)}}} &= y^{\mathrm{mc}}_{\mathrm{2c(1c)}} - y_{\mathrm{2c(1c)}}, \quad & s_{\mathrm{PD}_{\mathrm{2c[1c]}},z^{\mathrm{mc}}_{\mathrm{2c(1c)}}} &= z^{\mathrm{mc}}_{\mathrm{2c(1c)}} - z_{\mathrm{2c(1c)}}, \\
s_{\mathrm{PD}_{\mathrm{3a[2a]}},y^{\mathrm{mc}}_{\mathrm{3a(2a)}}} &= y^{\mathrm{mc}}_{\mathrm{3a(2a)}} - y_{\mathrm{3a(2a)}}, \quad & s_{\mathrm{PD}_{\mathrm{3a[2a]}},z^{\mathrm{mc}}_{\mathrm{3a(2a)}}} &= z^{\mathrm{mc}}_{\mathrm{3a(2a)}} - z_{\mathrm{3a(2a)}}.
\end{aligned} \tag{5.19}$$

In addition to the above single cavity alignment signal, the difference of the two cavity axes can be measured with QPD1bc(2ca, 3ab) similarly to the wave front sensing as

$$\begin{aligned}
s_{\mathrm{QPD}_{\mathrm{1bc(2ca,3ab)}},y} &= y^{\mathrm{cavb(c,a)}} + y^{\mathrm{cavc(a,b)}}, \\
s_{\mathrm{QPD}_{\mathrm{1bc(2ca,3ab)}},\mathrm{yaw}} &= \theta^{\mathrm{cavb(c,a)}}_{\mathrm{yaw}} - \theta^{\mathrm{cavc(a,b)}}_{\mathrm{yaw}}, \\
s_{\mathrm{QPD}_{\mathrm{1bc(2ca,3ab)}},z} &= z^{\mathrm{cavb(c,a)}} - z^{\mathrm{cavc(a,b)}}, \\
s_{\mathrm{QPD}_{\mathrm{1bc(2ca,3ab)}},\mathrm{pit}} &= \theta^{\mathrm{cavb(c,a)}}_{\mathrm{pit}} + \theta^{\mathrm{cavc(a,b)}}_{\mathrm{pit}}.
\end{aligned} \tag{5.20}$$

5.3.3 Local sensing

Using local sensors, i.e. interferometric sensors, the test mass positions from the satellite can be measured. The obtained signal is written as

$$\begin{aligned}
\boldsymbol{s}_{\mathrm{LS,1b(2c,3a)}} &= \boldsymbol{x}_{\mathrm{1b(2c,3a)}} - \boldsymbol{R}_{\mathrm{SAT_{to}M1}}\boldsymbol{x}_{\mathrm{SAT1(2,3)}}, \\
\boldsymbol{s}_{\mathrm{LS,1c(2a,3b)}} &= \boldsymbol{x}_{\mathrm{1c(2a,3b)}} - \boldsymbol{R}_{\mathrm{SAT_{to}M2}}\boldsymbol{x}_{\mathrm{SAT1(2,3)}},
\end{aligned} \tag{5.21}$$

where $\boldsymbol{s}_{\mathrm{LS},i\alpha} \equiv (s_{\mathrm{LS},x_{i\alpha}}, s_{\mathrm{LS},y_{i\alpha}}, s_{\mathrm{LS},\theta_{\mathrm{rol},i\alpha}}, s_{\mathrm{LS},\theta_{\mathrm{pit},i\alpha}}, s_{\mathrm{LS},\theta_{\mathrm{yaw},i\alpha}})^\top$ is the obtained signal.

5.4 Actuation method

Hereafter, for simplicity, we use actuation efficiency normalized with its DC value. This treatment does not lose generality. Note that we assume that the test masses and the satellites float in free space though they rotate around the center object (Sun or Earth) in reality. In other words, we neglect the centrifugal force applied to the test mass and the satellite due to the actuation. In heliocentric orbit, the additional centrifugal force applied to the test mass (satellite) due to the actuation is ~ 0.1 (1) nN and it is much smaller than the other forces. In geocentric orbit, the additional centrifugal force applied to the test mass

(satellite) due to the actuation is $\sim$ 30 (1000) μN. Although these values are comparable with the other forces that should be compensated, this is just a problem of the actuator diagonalization.

5.4.1 Frequency actuation

The laser frequency can be actuated by applying the voltage to the laser source. When the voltage, $v_{f_{1(2,3)}}$, is applied to the laser source, the frequency is varied as

$$\delta f_{1(2,3)} = v_{f_{1(2,3)}}. \tag{5.22}$$

5.4.2 Test mass actuation

The test mass position and angle are actuated with the test mass actuator, i.e. electro-static drive. By applying the voltage, $\boldsymbol{v}_{i\alpha}$, we can apply the force and torque $\delta\boldsymbol{F}_{i\alpha}$ to the test mass as

$$\delta\boldsymbol{F}_{i\alpha} = \boldsymbol{v}_{i\alpha}, \tag{5.23}$$

where

$$\boldsymbol{v}_{i\alpha} \equiv (v_{x_{i\alpha}}, v_{y_{i\alpha}}, v_{z_{i\alpha}}, v_{\theta_{\mathrm{rol},i\alpha}}, v_{\theta_{\mathrm{pit},i\alpha}}, v_{\theta_{\mathrm{yaw},i\alpha}})^\top, \tag{5.24}$$

$$\delta\boldsymbol{F}_{i\alpha} \equiv (\delta F_{x_{i\alpha}}, \delta F_{y_{i\alpha}}, \delta F_{z_{i\alpha}}, \delta T_{\theta_{\mathrm{rol},i\alpha}}, \delta T_{\theta_{\mathrm{pit},i\alpha}}, \delta T_{\theta_{\mathrm{yaw},i\alpha}})^\top. \tag{5.25}$$

Here, $\delta F_{x(y,z)_{i\alpha}}$ and $\delta T_{\theta_{\mathrm{rol(pit,yaw)},i\alpha}}$ are the force along $x(y,z)$-axis and the torque along roll (pitch, yaw) angle applied to the test mass.

Notice that when the force and torque are applied to the test mass, its back reaction, $\delta\boldsymbol{F}^{\mathrm{br}}_{\mathrm{SAT1(2,3)}}$ is applied to the satellite as

$$\delta\boldsymbol{F}^{\mathrm{br}}_{\mathrm{SAT1(2,3)}} = -\boldsymbol{R}_{\mathrm{M1_{to}SAT}}\delta\boldsymbol{F}_{\mathrm{1b(2c,3a)}}, \tag{5.26}$$

$$\delta\boldsymbol{F}^{\mathrm{br}}_{\mathrm{SAT1(2,3)}} = -\boldsymbol{R}_{\mathrm{M2_{to}SAT}}\delta\boldsymbol{F}_{\mathrm{1c(2a,3b)}}, \tag{5.27}$$

where

$$\boldsymbol{R}_{\mathrm{M1_{to}SAT}} \equiv \begin{pmatrix} \cos\left(\frac{\pi}{6}\right) & -\sin\left(\frac{\pi}{6}\right) & 0 & 0 & 0 & 0 \\ \sin\left(\frac{\pi}{6}\right) & \cos\left(\frac{\pi}{6}\right) & 0 & 0 & 0 & 0 \\ 0 & 0 & 1 & 0 & 0 & 0 \\ 0 & 0 & a\sin\left(\frac{\pi}{6}\right) & \cos\left(\frac{\pi}{6}\right) & -\sin\left(\frac{\pi}{6}\right) & 0 \\ 0 & 0 & -a\cos\left(\frac{\pi}{6}\right) & \sin\left(\frac{\pi}{6}\right) & \cos\left(\frac{\pi}{6}\right) & 0 \\ 0 & a & 0 & 0 & 0 & 1 \end{pmatrix}, \tag{5.28}$$

$$\boldsymbol{R}_{\mathrm{M2_{to}SAT}} \equiv \begin{pmatrix} \cos\left(-\frac{\pi}{6}\right) & -\sin\left(-\frac{\pi}{6}\right) & 0 & 0 & 0 & 0 \\ \sin\left(-\frac{\pi}{6}\right) & \cos\left(-\frac{\pi}{6}\right) & 0 & 0 & 0 & 0 \\ 0 & 0 & 1 & 0 & 0 & 0 \\ 0 & 0 & a\sin\left(-\frac{\pi}{6}\right) & \cos\left(-\frac{\pi}{6}\right) & -\sin\left(-\frac{\pi}{6}\right) & 0 \\ 0 & 0 & -a\cos\left(-\frac{\pi}{6}\right) & \sin\left(-\frac{\pi}{6}\right) & \cos\left(-\frac{\pi}{6}\right) & 0 \\ 0 & a & 0 & 0 & 0 & 1 \end{pmatrix}. \tag{5.29}$$

are rotation matrices from the satellite position and angle to the test mass position and angle.

5.4.3 Satellite actuation

The satellite is actuated with low noise thrusters. With the applying voltage, $\boldsymbol{v}_{\mathrm{SAT}i}$, the force and torque applied to the satellite are expressed as

$$\delta \boldsymbol{F}_{\mathrm{SAT}i} = \boldsymbol{v}_{\mathrm{SAT}i}, \tag{5.30}$$

where

$$\boldsymbol{v}_{\mathrm{SAT}i} \equiv (v_{x_{\mathrm{SAT}i}}, v_{y_{\mathrm{SAT}i}}, v_{z_{\mathrm{SAT}i}}, v_{\theta_{\mathrm{rol,SAT}i}}, v_{\theta_{\mathrm{pit,SAT}i}}, v_{\theta_{\mathrm{yaw,SAT}i}})^\top, \tag{5.31}$$

$$\delta \boldsymbol{F}_{\mathrm{SAT}i} \equiv (\delta F_{x_{\mathrm{SAT}i}}, \delta F_{y_{\mathrm{SAT}i}}, \delta F_{z_{\mathrm{SAT}i}}, \delta T_{\theta_{\mathrm{rol,SAT}i}}, \delta T_{\theta_{\mathrm{pit,SAT}i}}, \delta T_{\theta_{\mathrm{yaw,SAT}i}})^\top. \tag{5.32}$$

5.4.4 Incident beam alignment

The incident beam to the cavity is aligned with the satellite and steering mirrors on the satellite. The incident beam is given by

$$\boldsymbol{x}^{\mathrm{inc1b(2c,3a)}} = \boldsymbol{R}_{\mathrm{SAT_{to}Inc1}} \boldsymbol{x}_{\mathrm{SAT1(2,3)}} + \boldsymbol{x}^{\mathrm{STM_{1b(2c,3a)}}}, \tag{5.33}$$

$$\boldsymbol{x}^{\mathrm{inc1c(2a,3b)}} = \boldsymbol{R}_{\mathrm{SAT_{to}Inc2}} \boldsymbol{x}_{\mathrm{SAT1(2,3)}} + \boldsymbol{x}^{\mathrm{STM_{1c(2a,3b)}}}, \tag{5.34}$$

where $\boldsymbol{x}^{\mathrm{STM}_{i\alpha}} \equiv (x^{\mathrm{STM}_{i\alpha}}, y^{\mathrm{STM}_{i\alpha}}, z^{\mathrm{STM}_{i\alpha}}, \theta^{\mathrm{STM}_{i\alpha}}_{\mathrm{rol}}, \theta^{\mathrm{STM}_{i\alpha}}_{\mathrm{pit}}, \theta^{\mathrm{STM}_{i\alpha}}_{\mathrm{yaw}})^\top$ denotes the steering mirror position and angle, which are defined in the basis of the incident beam, and

$$\boldsymbol{R}_{\mathrm{SAT_{to}Inc1}} \equiv \begin{pmatrix} \cos\left(\frac{\pi}{6}\right) & \sin\left(\frac{\pi}{6}\right) & 0 & 0 & 0 & 0 \\ -\sin\left(\frac{\pi}{6}\right) & \cos\left(\frac{\pi}{6}\right) & 0 & 0 & 0 & \frac{L}{2} \\ 0 & 0 & 1 & \frac{L}{2}\sin\left(\frac{\pi}{6}\right) & -\frac{L}{2}\cos\left(\frac{\pi}{6}\right) & 0 \\ 0 & 0 & 0 & \cos\left(\frac{\pi}{6}\right) & \sin\left(\frac{\pi}{6}\right) & 0 \\ 0 & 0 & 0 & -\sin\left(\frac{\pi}{6}\right) & \cos\left(\frac{\pi}{6}\right) & 0 \\ 0 & 0 & 0 & 0 & 0 & 1 \end{pmatrix}, \tag{5.35}$$

$$\boldsymbol{R}_{\mathrm{SAT_{to}Inc2}} \equiv \begin{pmatrix} \cos\left(\frac{5\pi}{6}\right) & \sin\left(\frac{5\pi}{6}\right) & 0 & 0 & 0 & 0 \\ -\sin\left(\frac{5\pi}{6}\right) & \cos\left(\frac{5\pi}{6}\right) & 0 & 0 & 0 & -\frac{L}{2} \\ 0 & 0 & 1 & -\frac{L}{2}\sin\left(\frac{5\pi}{6}\right) & \frac{L}{2}\cos\left(\frac{5\pi}{6}\right) & 0 \\ 0 & 0 & 0 & \cos\left(\frac{5\pi}{6}\right) & \sin\left(\frac{5\pi}{6}\right) & 0 \\ 0 & 0 & 0 & -\sin\left(\frac{5\pi}{6}\right) & \cos\left(\frac{5\pi}{6}\right) & 0 \\ 0 & 0 & 0 & 0 & 0 & 1 \end{pmatrix}, \tag{5.36}$$

are rotation matrices from the satellite position and angle to the incident beam position and angle.

5.5 Sources of the noise

In order to estimate the noise level, the sources of noise in DECIGO and B-DECIGO are listed here. The listed noise sources are also used to estimate the actuator loading. Noises not shown here are discussed in Appendix C and they are negligible for the investigation of the control.

5.5.1 Interferometer noise

Quantum noise

As discussed in Appendix C, the most fundamental limit of the laser interferometer is determined by quantum noise due to the quantumness of photon. The quantum noise is divided into two components: shot noise and radiation pressure noise. They are given by [115]

$$x_{\mathrm{shot}}(f) = \frac{1}{4\mathcal{F}}\sqrt{\frac{\pi\hbar c\lambda}{2P_{\mathrm{inc}}}\left[1+\left(\frac{f}{\nu_{1/2}}\right)^2\right]}, \tag{5.37}$$

$$x_{\mathrm{rad}}(f) = \frac{16\mathcal{F}}{\pi(2\pi f)^2 m_{\mathrm{TM}}}\sqrt{\frac{2\pi\hbar P_{\mathrm{inc}}}{c\lambda}\frac{1}{1+\left(\frac{f}{\nu_{1/2}}\right)^2}}, \tag{5.38}$$

where m is the mass of the test mass, $\hbar$ is reduced Planck constant, and λ is the wavelength of the laser. Note that this is equivalent to the differential cavity length fluctuation, i.e. not to one test mass fluctuation.

Frequency noise

Equation (3.69) indicates that the laser frequency fluctuation is a noise source of the laser interferometer. The frequency noise of the laser source in DECIGO and B-DECIGO is given by

$$\delta f_{1(2,3)} = 1\ \mathrm{Hz}/\sqrt{\mathrm{Hz}} \tag{5.39}$$

Intensity noise

According to equation (3.70), there is a kind of sensing noise due to the intensity fluctuation coupled with the cavity detuning, which is written as

$$x_{\mathrm{int}} = \Delta x\frac{\delta P}{P_0}, \tag{5.40}$$

where Δx is the cavity detuning in terms of length.

Alignment sensing noise

The noises of the wave front sensing for shift and tilt of the optical axis are given by [193]

$$\begin{cases} \delta y_{\mathrm{WFS}} = \delta z_{\mathrm{WFS}} \simeq 2 \times 10^{-10}\ \mathrm{m}/\sqrt{\mathrm{Hz}}, \\ \delta\theta_{\mathrm{pit,WFS}} = \delta\theta_{\mathrm{yaw,WFS}} \simeq 8 \times 10^{-16}\ \mathrm{rad}/\sqrt{\mathrm{Hz}}, \end{cases} \quad \text{(DECIGO)} \tag{5.41}$$

$$\begin{cases} \delta y_{\mathrm{WFS}} = \delta z_{\mathrm{WFS}} \simeq 1 \times 10^{-9}\ \mathrm{m}/\sqrt{\mathrm{Hz}}, \\ \delta\theta_{\mathrm{pit,WFS}} = \delta\theta_{\mathrm{yaw,WFS}} \simeq 5 \times 10^{-14}\ \mathrm{rad}/\sqrt{\mathrm{Hz}}. \end{cases} \quad \text{(B-DECIGO)} \tag{5.42}$$

For the global attitude sensing, we assume the same noise level as the wave front sensing.

The noises for the dithering method for beam spot shift measurement are given by [194]

$$\delta y_{\mathrm{dith}} = \delta z_{\mathrm{dith}} \simeq \begin{cases} 3 \times 10^{-8}\ \mathrm{m}/\sqrt{\mathrm{Hz}}, & \text{(DECIGO)} \\ 5 \times 10^{-9}\ \mathrm{m}/\sqrt{\mathrm{Hz}}. & \text{(B-DECIGO)} \end{cases} \tag{5.43}$$

Here, we assume that dithering frequency is 1 Hz and applied force is 0.06 μN. This leads to the root-mean-square of the beam spot fluctuation of about 0.1 mm.

Test mass tilt coupling

The tilt motion of the test mass causes length noise through the beam spot mis-centering on the test mass. This tilt coupling noise is approximately given by [195]

$$\delta x_{\mathrm{tilt}} = \delta\theta_{\mathrm{yaw(pit)}} \Delta y(z)_{\mathrm{RMS}}, \tag{5.44}$$

where $\delta\theta_{\mathrm{yaw(pit)}}$ is yaw (pitch) motion of the test mass and $\Delta y(z)_{\mathrm{RMS}}$ is the root-mean-square of the beam mis-centering along $y(z)$-axis.

Absolute length sensing noise

The absolute length sensing is more noisy than sensing with the Pound–Drever–Hall technique. We assume the absolute length sensing noise is to be

$$\delta x_{\mathrm{AbsL}} = 1 \times 10^{-13}\ \mathrm{m}/\sqrt{\mathrm{Hz}}. \tag{5.45}$$

5.5.2 Force noise on test masses

The major force noise on the test mass is caused by electrostatic actuator, thermal radiation pressure, and the gravity. To investigate the force noise effect on the control scheme, it is enough to consider these noises since they are the dominant noise sources.

Actuator noise

The actuator noise is important above 0.001 Hz. The actuator of DECIGO and B-DECIGO is planned to be electrostatic actuator. The force noise is assumed to be

$$\delta F_{\rm act} \simeq 2 \times 10^{-17}\ {\rm N}/\sqrt{\rm Hz}, \tag{5.46}$$

$$\delta T_{\rm act} \simeq 2 \times 10^{-17}\ {\rm Nm}/\sqrt{\rm Hz}. \tag{5.47}$$

Note that the force noise level depends on the required actuator range [176].

Thermal radiation pressure

When temperature of the housing around test mass fluctuates, the thermal radiation pressure applied to the test mass causes force noise. The thermal radiation pressure force fluctuation, $\delta F_{\rm Trad}$, is given by [140]

$$\delta F_{\rm Trad} = \epsilon_{\rm Trad} \frac{4\sigma_{\rm SB} S_{\rm TM} T^3 \delta T}{c}, \tag{5.48}$$

where $\sigma_{\rm SB}$ is Stefan–Boltzmann constant, $S_{\rm TM}$ is the cross section of the test mass, δT is temperature fluctuation of housing, and $\epsilon_{\rm Trad}$ is common mode rejection ratio. When the temperature fluctuations in front and back of the test mass are correlated, the thermal radiation pressure is reduced. When we assume $\epsilon_{\rm Trad} = 0.1$, $S_{\rm TM} = 2\ {\rm m}^2$, $T = 300\ {\rm K}$, $\delta T = 10^{-8}(0.1\ {\rm Hz}/f)^{1/3}\ {\rm K}/\sqrt{\rm Hz}$, and typical scale of temperature fluctuation is 0.5 m, the force and torque noises due to the thermal radiation pressure are written as

$$\delta F_{\rm Trad} \simeq 4 \times 10^{-17} \left(\frac{0.1\ {\rm Hz}}{f}\right)^{1/3}\ {\rm N}/\sqrt{\rm Hz}, \tag{5.49}$$

$$\delta T_{\rm Trad} \simeq 2 \times 10^{-17} \left(\frac{0.1\ {\rm Hz}}{f}\right)^{1/3}\ {\rm Nm}/\sqrt{\rm Hz}. \tag{5.50}$$

Gravity

The gravity force is significant in the low frequency. In heliocentric orbit, the gravity field caused by the satellite applies static force of 20 nN according to equation (4.2). In geocentric orbit, the gravity of the Earth J_2 term is $\sim 0.6\ \mu$N at $\sim 10^{-5}$ Hz ($\sim$ /1 day). We need to confirm that this force is successfully suppressed with the feedback control. This point is discussed in the end of Section 5.8.2

5.5.3 Force noise on satellites

About the force noise on the satellite, solar radiation force and thruster noise should be considered. In the geocentric orbit, we also need to consider gravity from the Earth.

Solar radiation pressure

The solar radiation pressure and its fluctuation are given by [140, 142, 144]

$$F_{\rm Srad} = \frac{W_{\rm Sun} S_{\rm SAT}}{c} = 9 \times 10^{-6}\ {\rm N}, \tag{5.51}$$

$$\delta F_{\rm Srad} = \frac{\delta W_{\rm Sun} S_{\rm SAT}}{c} = 3 \times 10^{-9} \left(\frac{0.1\ {\rm Hz}}{f}\right)^{\frac{1}{3}}\ {\rm N}/\sqrt{\rm Hz}, \tag{5.52}$$

where $W_{\rm Sun} = 1360\ {\rm W/m^2}$ and $\delta W_{\rm Sun} = 0.2 \left(\frac{0.1\ {\rm Hz}}{f}\right)^{\frac{1}{3}}\ {\rm W/m^2}/\sqrt{\rm Hz}$ are the solar radiation power density and its fluctuation, respectively. The solar radiation pressure torque depends on the satellite shape. When we assume the typical scale of the satellite of 1 m and 10% coupling from the force to torque, the solar radiation torque is denoted as

$$T_{\rm Srad} = \frac{1}{10} F_{\rm Srad} = 9 \times 10^{-7}\ {\rm Nm}, \tag{5.53}$$

$$\delta T_{\rm Srad} = \frac{1}{10} \delta F_{\rm Srad} = 3 \times 10^{-8} \left(\frac{0.1\ {\rm Hz}}{f}\right)^{\frac{1}{3}}\ {\rm Nm}/\sqrt{\rm Hz}. \tag{5.54}$$

Thruster noise

In DECIGO and B-DECIGO, 100-μN class thrusters are planned to be used. Their force and torque noises are approximately given by [177]

$$\delta F_{\rm thr} = 1 \times 10^{-7}\ {\rm N}/\sqrt{\rm Hz}, \tag{5.55}$$

$$\delta T_{\rm thr} = 1 \times 10^{-7}\ {\rm Nm}/\sqrt{\rm Hz}. \tag{5.56}$$

Here, we assumed that the two thrusters are placed at a distance of 1 m.

Gravity of the Earth

In B-DECIGO with the geocentric orbit, the gravity of the Earth makes some amount of force and torque at $\sim 10^{-5}$ Hz in the same manner as the gravity on the test masses. They are written as

$$F_{\rm GrE} \sim 2 \times 10^{-5}\ {\rm N}, \tag{5.57}$$

$$T_{\rm GrE} \sim 3 \times 10^{-7}\ {\rm Nm}. \tag{5.58}$$

5.5.4 Sensing noise of local sensors

As a local sensor, interferometric sensors are planned to be used. The sensitivity is given by [185]

$$\delta x_{\rm LS} = 1 \times 10^{-12}\ {\rm m}/\sqrt{\rm Hz}. \tag{5.59}$$

By putting six local sensors to measure the six mechanical degrees of freedom of the test mass, we measure the tilt of the test mass. Approximately, the tilt sensing sensitivity is written as

$$\delta\theta_{\rm LS} = 3 \times 10^{-12}\ {\rm rad}/\sqrt{\rm Hz}. \tag{5.60}$$

Here, the distance of the local sensors are assumed to be ~ 0.5 m.

The noise of the star tracker is assumed to be

$$\delta\theta_{\rm STT} = 2 \times 10^{-6}\ {\rm rad}/\sqrt{\rm Hz}. \tag{5.61}$$

5.6 Control topology

Here, we show the basic control topology of length, alignment, drag-free, and local control of DECIGO and B-DECIGO. In this section, the coupling between the satellite and the test mass, back reaction, and opto-mechanical coupling are not considered for simplicity. The effects of these couplings can be suppressed when the control gain is enough. Note that they considered in the constructed model shown in Section 5.7 to quantitatively evaluate the effects of the couplings. For more description about the feedback control, such as Laplace transformation, the block diagram, and stability analysis, see Appendix B. Note also that there is no inter-satellite communication in terms of the data processing in the following design since the precise control with the inter-satellite communication is challenging.

5.6.1 Length control

The block diagram of the length control is shown in figure 5.2. The signals obtained from Cavity c with PD1c and PD2c, i.e. $s_{\rm PD_{1c}}$ and $s_{\rm PD_{2c}}$ are fed back to Laser 1 and Laser 2, respectively. The output of PD3a, i.e. $s_{\rm PD_{3a}}$ is fed back to Laser 3. Signals from PD1b and PD2a are fed back to TM1b and TM2a (longitudinal motion), respectively. The longitudinal motion of TM1c is controlled with the absolute length measurement of Cavity c, i.e. $s_{{\rm PD}_{1L_c}}$. The gravitational wave signal is taken from PD1b, PD2a, and PD3b.

It is worth noting that PD3b can measure the signal of Cavity b even without the feedback of any signal. This is achieved by adjusting the length of Cavity a and Cavity b in the dual-pass differential Fabry–Pérot interferometer as shown in Chapter 6.

5.6.2 Alignment control

Since the alignment control having the same topology is implemented to all the cavities, we focus on one cavity, Cavity b, first. In the alignment control, the position of the test mass is set as a reference of the alignment control. In other words, these two parameters are regarded as parameters external to the control

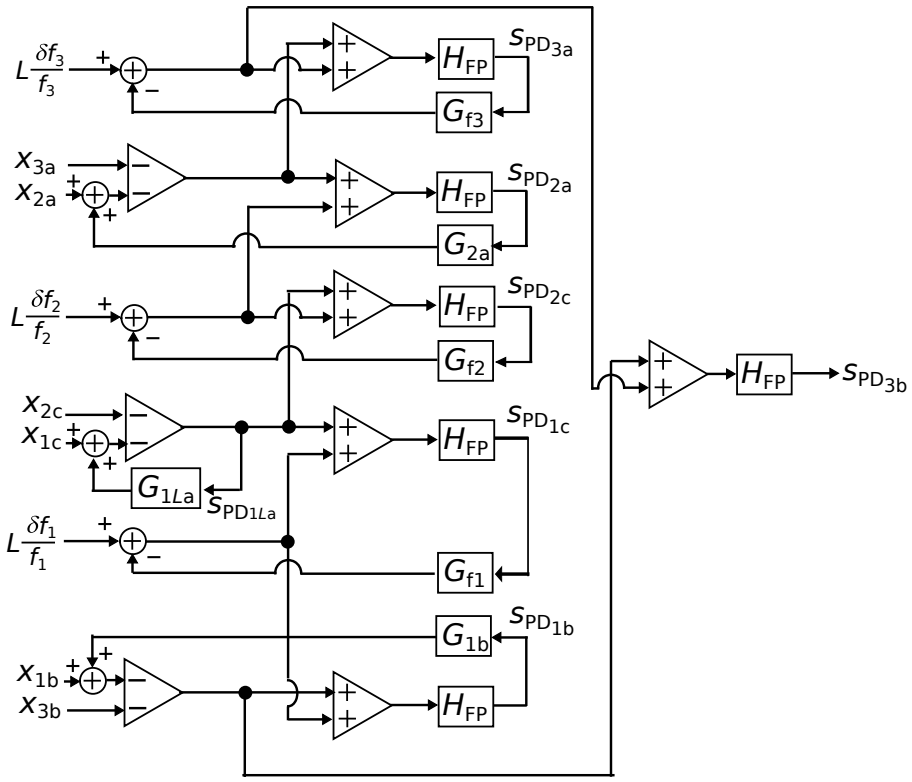

Figure 5.2: Block diagram of length control. We define $H_{\mathrm{FP}} \equiv H_{\mathrm{FP}}^{(L)}(\omega)/H_{\mathrm{FP}}^{(L)}(0)$. $G_{f_{1(2,3)}}$ and $G_{1\mathrm{b}(2\mathrm{a})}$ are the control gains of each control loop.

loop. From this point of view, the alignment sensing vector is denoted as

$$\boldsymbol{s}_{\mathrm{ASC1b(3b)},y} \equiv \begin{pmatrix} s_{\mathrm{QPD}_{1\mathrm{b(3b)}},y} \\ s_{\mathrm{QPD}_{1\mathrm{b(3b)}},\mathrm{yaw}} \\ s_{\mathrm{PD}_{1\mathrm{b(3b)}},y_{1\mathrm{b}}^{\mathrm{mc}}} \\ s_{\mathrm{PD}_{1\mathrm{b(3b)}},y_{3\mathrm{b}}^{\mathrm{mc}}} \end{pmatrix} = \boldsymbol{R}_y \begin{pmatrix} \theta_{\mathrm{yaw,1b}} \\ \theta_{\mathrm{yaw,3b}} \\ y^{\mathrm{STM}_{1\mathrm{b(3b)}}} \\ \theta_{\mathrm{yaw}}^{\mathrm{STM}_{1\mathrm{b(3b)}}} \end{pmatrix} + \boldsymbol{R}'_y \begin{pmatrix} y_{1\mathrm{b}} \\ y_{3\mathrm{b}} \end{pmatrix} + \boldsymbol{R}''_y \begin{pmatrix} \boldsymbol{x}_{\mathrm{SAT1}} \\ \boldsymbol{x}_{\mathrm{SAT3}} \end{pmatrix}, \tag{5.62}$$

$$\boldsymbol{s}_{\mathrm{ASC1b(3b)},z} \equiv \begin{pmatrix} s_{\mathrm{QPD}_{1\mathrm{b(3b)}},z} \\ s_{\mathrm{QPD}_{1\mathrm{b(3b)}},\mathrm{pit}} \\ s_{\mathrm{PD}_{1\mathrm{b(3b)}},z_{1\mathrm{b}}^{\mathrm{mc}}} \\ s_{\mathrm{PD}_{1\mathrm{b(3b)}},z_{3\mathrm{b}}^{\mathrm{mc}}} \end{pmatrix} = \boldsymbol{R}_z \begin{pmatrix} \theta_{\mathrm{pit,1b}} \\ \theta_{\mathrm{pit,3b}} \\ z^{\mathrm{STM}_{1\mathrm{b(3b)}}} \\ \theta_{\mathrm{pit}}^{\mathrm{STM}_{1\mathrm{b(3b)}}} \end{pmatrix} + \boldsymbol{R}'_z \begin{pmatrix} z_{1\mathrm{b}} \\ z_{3\mathrm{b}} \end{pmatrix} + \boldsymbol{R}''_z \begin{pmatrix} \boldsymbol{x}_{\mathrm{SAT1}} \\ \boldsymbol{x}_{\mathrm{SAT3}} \end{pmatrix}, \tag{5.63}$$

where $\boldsymbol{R}_{y(z)}$, $\boldsymbol{R}'_{y(z)}$ and $\boldsymbol{R}''_{y(z)}$ are the transfer matrices from each component to the measured signals. Among these matrices, $\boldsymbol{R}_y$ and $\boldsymbol{R}_z$ are important to

design the control topology and written as

$$\boldsymbol{R}_y = \begin{pmatrix} \frac{R_c}{2} & -\frac{R_c}{2} & -1 & 0 \\ \frac{R_c}{2\left(R_c-\frac{L}{2}\right)} & \frac{R_c}{2\left(R_c-\frac{L}{2}\right)} & 0 & -1 \\ -\frac{R_c(L-R_c)}{2\left(R_c-\frac{L}{2}\right)} & -\frac{R_c^2}{2\left(R_c-\frac{L}{2}\right)} & 0 & 0 \\ -\frac{R_c^2}{2\left(R_c-\frac{L}{2}\right)} & -\frac{R_c(L-R_c)}{2\left(R_c-\frac{L}{2}\right)} & 0 & 0 \end{pmatrix}, \tag{5.64}$$

$$\boldsymbol{R}_z = \begin{pmatrix} -\frac{R_c}{2} & -\frac{R_c}{2} & -1 & 0 \\ \frac{R_c}{2\left(R_c-\frac{L}{2}\right)} & -\frac{R_c}{2\left(R_c-\frac{L}{2}\right)} & 0 & -1 \\ \frac{R_c(L-R_c)}{2\left(R_c-\frac{L}{2}\right)} & -\frac{R_c^2}{2\left(R_c-\frac{L}{2}\right)} & 0 & 0 \\ -\frac{R_c^2}{2\left(R_c-\frac{L}{2}\right)} & \frac{R_c(L-R_c)}{2\left(R_c-\frac{L}{2}\right)} & 0 & 0 \end{pmatrix}. \tag{5.65}$$

The processed signals are fed back to the test mass angles and incident beam alignments. The relation between them and the feedback voltages is written as

$$\begin{aligned} \begin{pmatrix} \theta_{\mathrm{yaw,1b}} \\ \theta_{\mathrm{yaw,3b}} \\ y^{\mathrm{STM_{1b(3b)}}} \\ \theta_{\mathrm{yaw}}^{\mathrm{STM_{1b(3b)}}} \end{pmatrix} &= \mathrm{diag}\left(\frac{1}{I_{\mathrm{TM,yaw}}(-\omega^2+i\gamma\omega)}, \frac{1}{I_{\mathrm{TM,yaw}}(-\omega^2+i\gamma\omega)}, 1, 1 \right) \\ &\quad \cdot \left(v_{\theta_{\mathrm{yaw,1b}}}, v_{\theta_{\mathrm{yaw,3b}}}, v_{y^{\mathrm{STM_{1b(3b)}}}}, v_{\theta_{\mathrm{yaw}}^{\mathrm{STM_{1b(3b)}}}} \right)^{\top} \\ &\equiv (\boldsymbol{M}_{\mathrm{ASC}y})^{-1} \boldsymbol{v}_{\mathrm{ASC}y,\mathrm{1b(3b)}}, \end{aligned} \tag{5.66}$$

$$\begin{aligned} \begin{pmatrix} \theta_{\mathrm{pit,1b}} \\ \theta_{\mathrm{pit,3b}} \\ z^{\mathrm{STM_{1b(3b)}}} \\ \theta_{\mathrm{pit}}^{\mathrm{STM_{1b(3b)}}} \end{pmatrix} &= \mathrm{diag}\left(\frac{1}{I_{\mathrm{TM,pit}}(-\omega^2+i\gamma\omega)}, \frac{1}{I_{\mathrm{TM,pit}}(-\omega^2+i\gamma\omega)}, 1, 1 \right) \\ &\quad \cdot \left(v_{\theta_{\mathrm{pit,1b}}}, v_{\theta_{\mathrm{pit,3b}}}, v_{z^{\mathrm{STM_{1b(3b)}}}}, v_{\theta_{\mathrm{pit}}^{\mathrm{STM_{1b(3b)}}}} \right)^{\top} \\ &\equiv (\boldsymbol{M}_{\mathrm{ASC}z})^{-1} \boldsymbol{v}_{\mathrm{ASC}z,\mathrm{1b(3b)}}, \end{aligned} \tag{5.67}$$

where $v_{y(z)^{\mathrm{inc1b(3b)}}}$ and $v_{\theta_{\mathrm{yaw(pit)}}^{\mathrm{inc1b(3b)}}}$ are the voltages fed back to the steering mirror 1b(3b).

Figure 5.3 shows the block diagram of alignment control of one cavity. According to the discussion in Appendix B, the control matrix needs to meet the following condition:

$$(\boldsymbol{M}_{\mathrm{ASC}y})^{-1} \boldsymbol{G}_y \boldsymbol{R}_y = (\text{diagonal matrix}), \tag{5.68}$$

$$(\boldsymbol{M}_{\mathrm{ASC}z})^{-1} \boldsymbol{G}_z \boldsymbol{R}_z = (\text{diagonal matrix}). \tag{5.69}$$

The simple choice of the control gain, $\boldsymbol{G}_{y(z)}$, is [57]

$$\boldsymbol{G}_y = \boldsymbol{M}_{\mathrm{ASC}y}\mathrm{diag}\left(G_{\theta_{\mathrm{yaw,1b}}}, G_{\theta_{\mathrm{yaw,3b}}}, G_{y^{\mathrm{inc1b(3b)}}}, G_{\theta^{\mathrm{inc1b(3b)}}_{\mathrm{yaw}}}\right)\boldsymbol{R}_y^{-1}, \tag{5.70}$$

$$\boldsymbol{G}_z = \boldsymbol{M}_{\mathrm{ASC}z}\mathrm{diag}\left(G_{\theta_{\mathrm{pit,1b}}}, G_{\theta_{\mathrm{pit,3b}}}, G_{z^{\mathrm{inc1b(3b)}}}, G_{\theta^{\mathrm{inc1b(3b)}}_{\mathrm{pit}}}\right)\boldsymbol{R}_z^{-1}, \tag{5.71}$$

where $G_{\theta_{\mathrm{yaw(pit),1b(3b)}}}$, $G_{y(z)^{\mathrm{inc1b(3b)}}}$, and $G_{\theta^{\mathrm{inc1b(3b)}}_{\mathrm{yaw(pit)}}}$ are the control open loop gains of each loop. The above discussion in this section including equations (5.62)-(5.71) is valid for Cavity b and Cavity a by replacing (1b, 3b, SAT1, SAT3) to (2c, 1c, SAT2, SAT1) and (3a, 2a, SAT3, SAT2) in equations (5.62)-(5.71).

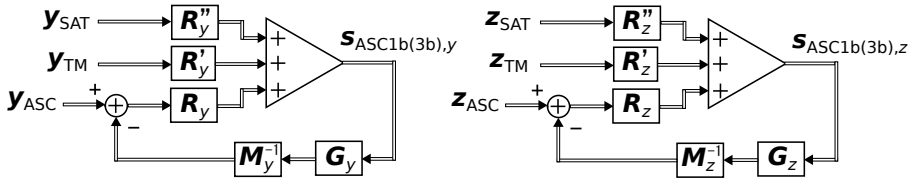

Figure 5.3: Block diagram of alignement control. We define $\boldsymbol{y}_{\mathrm{ASC}} \equiv (\theta_{\mathrm{yaw,1b}}, \theta_{\mathrm{yaw,3b}}, y^{\mathrm{STM}_{\mathrm{1b(3b)}}}, \theta^{\mathrm{STM}_{\mathrm{1b(3b)}}}_{\mathrm{yaw}})^\top$, $\boldsymbol{z}_{\mathrm{ASC}} \equiv (\theta_{\mathrm{pit,1b}}, \theta_{\mathrm{pit,3b}}, z^{\mathrm{STM}_{\mathrm{1b(3b)}}}, \theta^{\mathrm{STM}_{\mathrm{1b(3b)}}}_{\mathrm{pit}})^\top$, $\boldsymbol{y}_{\mathrm{TM}} \equiv (y_{\mathrm{1b}}, y_{\mathrm{3b}})^\top$, $\boldsymbol{z}_{\mathrm{TM}} \equiv (z_{\mathrm{1b}}, z_{\mathrm{3b}})^\top$, and $\boldsymbol{y}(\boldsymbol{z})_{\mathrm{SAT}} \equiv (\boldsymbol{x}_{\mathrm{SAT1}}, \boldsymbol{x}_{\mathrm{SAT3}})^\top$.

5.6.3 Drag-free and local control

In the drag-free control, TM1c, TM2a, and TM3a are used as references for SAT1, SAT2, and SAT3, respectively. The obtained signals are fed back to the thruster of the satellite. The block diagram for these controls is shown in figure 5.4. With the similar discussion in the previous section, we choose the gain matrix, $\boldsymbol{G}_{\mathrm{DF1(2,3)}}$, as

$$\begin{aligned}\boldsymbol{G}_{\mathrm{DF1}} &= (\boldsymbol{R}_{\mathrm{SAT_{to}M2}})^{-1} \\ &\quad \cdot \mathrm{diag}(G_{x_{\mathrm{SAT1}}}, G_{y_{\mathrm{SAT1}}}, G_{z_{\mathrm{SAT1}}}, G_{\theta_{\mathrm{rol,SAT1}}}, G_{\theta_{\mathrm{pit,SAT1}}}, G_{\theta_{\mathrm{yaw,SAT1}}})\boldsymbol{M}'_{\mathrm{SAT}},\end{aligned} \tag{5.72}$$

$$\begin{aligned}\boldsymbol{G}_{\mathrm{DF2}} &= (\boldsymbol{R}_{\mathrm{SAT_{to}M2}})^{-1} \\ &\quad \cdot \mathrm{diag}(G_{x_{\mathrm{SAT2}}}, G_{y_{\mathrm{SAT2}}}, G_{z_{\mathrm{SAT2}}}, G_{\theta_{\mathrm{rol,SAT2}}}, G_{\theta_{\mathrm{pit,SAT2}}}, G_{\theta_{\mathrm{yaw,SAT2}}})\boldsymbol{M}'_{\mathrm{SAT}},\end{aligned} \tag{5.73}$$

$$\begin{aligned}\boldsymbol{G}_{\mathrm{DF3}} &= (\boldsymbol{R}_{\mathrm{SAT_{to}M1}})^{-1} \\ &\quad \cdot \mathrm{diag}(G_{x_{\mathrm{SAT3}}}, G_{y_{\mathrm{SAT3}}}, G_{z_{\mathrm{SAT3}}}, G_{\theta_{\mathrm{rol,SAT3}}}, G_{\theta_{\mathrm{pit,SAT3}}}, G_{\theta_{\mathrm{yaw,SAT3}}})\boldsymbol{M}'_{\mathrm{SAT}},\end{aligned} \tag{5.74}$$

where $G_{x_{\mathrm{SAT1(2,3)}}}$, $G_{y_{\mathrm{SAT1(2,3)}}}$, $G_{z_{\mathrm{SAT1(2,3)}}}$, $G_{\theta_{\mathrm{rol,SAT1(2,3)}}}$, $G_{\theta_{\mathrm{pit,SAT(2,3)1}}}$, and $G_{\theta_{\mathrm{yaw,SAT1(2,3)}}}$ are the open loop gains of each degree of freedom.

The test masses other than the reference of the drag-free control are locally controlled with local sensors partially. Specifically, the positions and rolls of

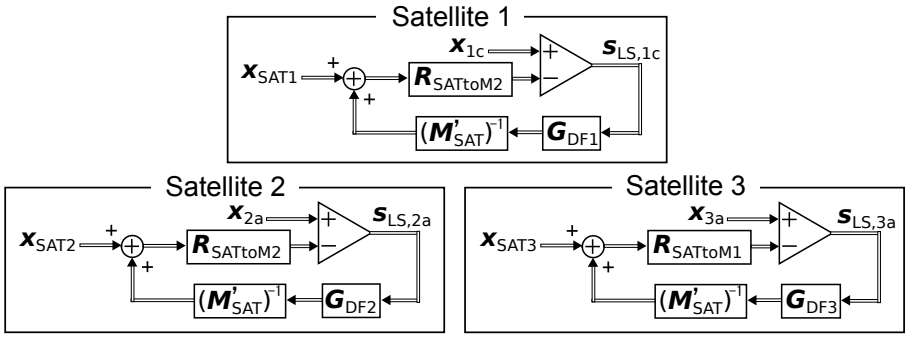

Figure 5.4: Block diagram of the drag-free control.

TM2c and TM3b are controlled and the positions only along y- and z-axes and roll of TM1b are controlled. The block diagram of this control is shown in figure 5.5. The control gain is designed as

$$\boldsymbol{G}_{\mathrm{LS,1b}} = \mathrm{diag}(0, G_{\mathrm{LS}y,\mathrm{1b}}, G_{\mathrm{LS}z,\mathrm{1b}}, G_{\mathrm{LS}\theta_{\mathrm{roll}},\mathrm{1b}}, 0, 0), \tag{5.75}$$

$$\boldsymbol{G}_{\mathrm{LS,2c}} = \mathrm{diag}(G_{\mathrm{LS}x,\mathrm{2c}}, G_{\mathrm{LS}y,\mathrm{2c}}, G_{\mathrm{LS}z,\mathrm{2c}}, G_{\mathrm{LS}\theta_{\mathrm{roll}},\mathrm{2c}}, 0, 0), \tag{5.76}$$

$$\boldsymbol{G}_{\mathrm{LS,3b}} = \mathrm{diag}(G_{\mathrm{LS}x,\mathrm{3b}}, G_{\mathrm{LS}y,\mathrm{3b}}, G_{\mathrm{LS}z,\mathrm{3b}}, G_{\mathrm{LS}\theta_{\mathrm{roll}},\mathrm{3b}}, 0, 0), \tag{5.77}$$

where $G_{\mathrm{LS}x,\mathrm{2c(3b)}}$, $G_{\mathrm{LS}y,\mathrm{1b(2c,3b)}}$, and $G_{\mathrm{LS}z,\mathrm{1b(2c,3b)}}$ are the open loop gains of each degree of freedom.

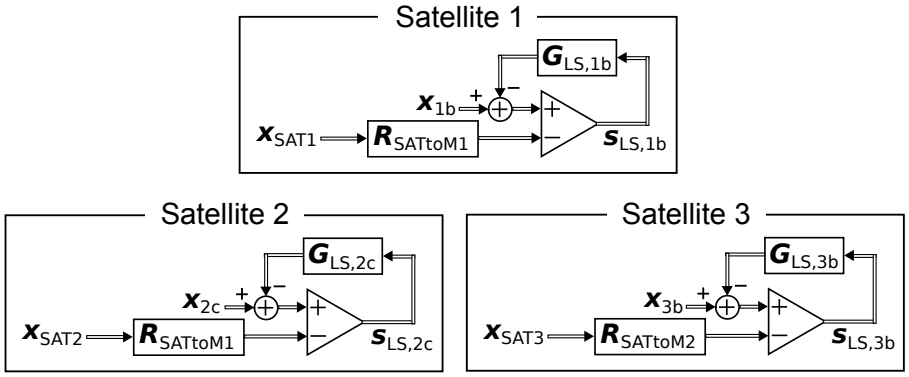

Figure 5.5: Block diagram of the local control.

5.6.4 Global attitude control of satellite formation

In addition to the above control, global attitude of satellite formation needs to be controlled. For this purpose, the cavity axis difference in yaw motion of Cavity b and c is fed back to y-axis motion of TM1c. The cavity axis difference in pitch motion of Cavity c and a (a and b) is fed back to the z-axis motion of TM2a

(TM3a). The obtained signal, $s_{\mathrm{QPD}_{1\mathrm{bc}},y(z)}$, is denoted as

$$s_{\mathrm{QPD}_{1\mathrm{bc}},y} = -\frac{1}{2\left(R_c - \frac{L}{2}\right)} y_{1\mathrm{c}} + f(y_{1\mathrm{b}}, y_{3\mathrm{b}}, y_{2\mathrm{c}}, \theta_{\mathrm{yaw},1\mathrm{b}}, \theta_{\mathrm{yaw},3\mathrm{b}}, \theta_{\mathrm{yaw},2\mathrm{c}}, \theta_{\mathrm{yaw},1\mathrm{c}}), \tag{5.78}$$

$$s_{\mathrm{QPD}_{2\mathrm{ca}},z} = -\frac{1}{2\left(R_c - \frac{L}{2}\right)} z_{2\mathrm{a}} + f'(z_{2\mathrm{c}}, z_{1\mathrm{c}}, z_{3\mathrm{a}}, \theta_{\mathrm{pit},2\mathrm{c}}, \theta_{\mathrm{pit},1\mathrm{c}}, \theta_{\mathrm{pit},2\mathrm{a}}, \theta_{\mathrm{pit},3\mathrm{a}}), \tag{5.79}$$

$$s_{\mathrm{QPD}_{3\mathrm{ab}},z} = \frac{1}{2\left(R_c - \frac{L}{2}\right)} z_{3\mathrm{a}} + f''(z_{3\mathrm{b}}, z_{2\mathrm{a}}, z_{1\mathrm{b}}, \theta_{\mathrm{pit},3\mathrm{a}}, \theta_{\mathrm{pit},2\mathrm{a}}, \theta_{\mathrm{pit},3\mathrm{b}}, \theta_{\mathrm{pit},1\mathrm{b}}). \tag{5.80}$$

In addition, the roll motion of the drag-free control reference masses, i.e. TM1c, TM2a, and TM3a, is controlled with the star trackers.

5.6.5 Summary of control

In the end of this section, the summary of control topology is shown in table 5.2. Note that x and the roll of incident beam alignment do not need to be controlled and x- and y-axis motion of TM3a, y-axis motion of TM2a, and z-axis motion of TM1c define the reference frame of the control. In other words, the attitude of the triangular interferometer can be changed by actuating these test masses. This topology is implemented in the model constructed in Section 5.7.

5.7 Control model construction

In order to analyze the control of DECIGO and B-DECIGO, we construct a control model with Matlab and Simulink. In this model, mechanical and opto-mechanical properties (Section 5.2), sensing and actuation method (Section 5.3 and 5.4), and control topology (Section 5.6) are implemented with graphically coding using block diagrams of Simulink. The constructed model is shown in Appendix H. We named this model a *full DECIGO interferometer model*. We used the parameters that we considered in this chapter and shown in table 4.1. With the model, we can calculate the transfer function from each excitation port to each sensing port and noise spectrum based on the calculated transfer function (for more details of the noise estimation method, see Appendix B). Therefore, whether the controls of all degrees of freedom shown in table 5.2 are stable and the requirements of noises and their root-mean-square for the sensitivity and stability are met can be investigated.

Table 5.2: Summary of control topology. Used signal name to control each degree freedom is shown. Align, alignment control; Global, global attitude control; DF, drag free control; STT, star tracker.

	TM1b	TM1c	TM2c	TM2a	TM3a	TM3b
x	Length	Length	Local	Length (Abs.)	Ref	Local
y	Local	Global	Local	Ref	Ref	Local
z	Local	Ref	Local	Global	Global	Local
Roll	Local	STT	Local	STT	STT	Local
Pitch	Align	Align	Align	Align	Align	Align
Yaw	Align	Align	Align	Align	Align	Align

	Inc1b	Inc1b	Inc1b	Inc1b	Inc1b	Inc1b
y	Align	Align	Align	Align	Align	Align
z	Align	Align	Align	Align	Align	Align
Pitch	Align	Align	Align	Align	Align	Align
Yaw	Align	Align	Align	Align	Align	Align

	SAT1	SAT2	SAT3
x	DF	DF	DF
y	DF	DF	DF
z	DF	DF	DF
Roll	DF	DF	DF
Pitch	DF	DF	DF
Yaw	DF	DF	DF

	LAS1	LAS2	LAS3
f	Length	Length	Length

5.8 Investigation of the control system with the control model

5.8.1 Open loop transfer function

Using the full DECIGO interferometer model, we designed the open loop gains of each loop described in Section 5.6. Figures 5.6-5.12 show the designed open loop gains for DECIGO. The figures indicate that all degrees of freedom of each component are stably controlled (the stability can be checked with the phase at the unity gain frequency as discussed in Appendix B). The peaks around 10^{-4} Hz, which appear in figures 5.7, 5.10, and 5.11, are caused by the coupling, K, between the satellite and the test masses. Below the peak frequency, we cannot increase the gain of the control loop. For B-DECIGO, the control gains are designed in the same way and all controls are made to be stable.

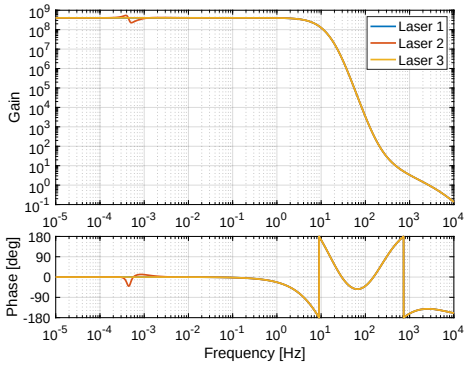

Figure 5.6: Open loop transfer function of frequency control loop. The open loop gain for Laser 1 is overlapped by that for Laser 2.

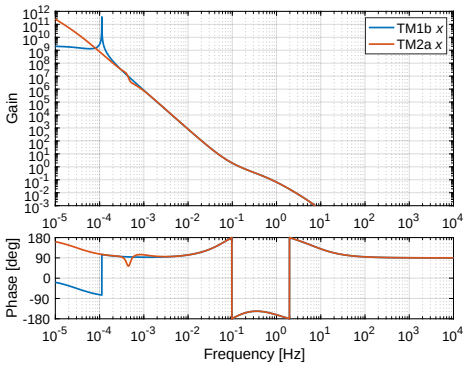

Figure 5.7: Open loop transfer function of x-axis motion of TM1b and TM2a.

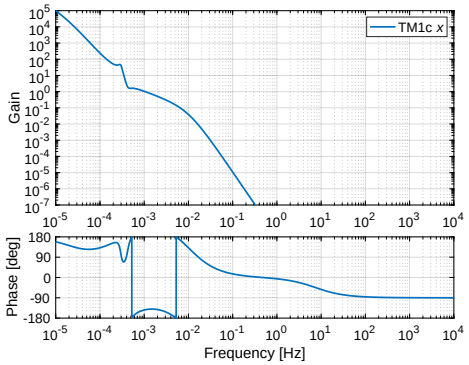

Figure 5.8: Open loop transfer function of x-axis motion of TM1c.

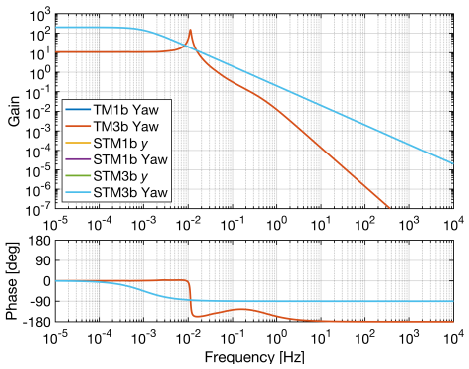

Figure 5.9: Open loop transfer function of alignment control. The open loop gain for TM1b Yaw is overlapped by that for TM3b Yaw. Also the open loop gain for STM1b (y and Yaw) and STM3b (y) is overlapped by that for STM3b Yaw.

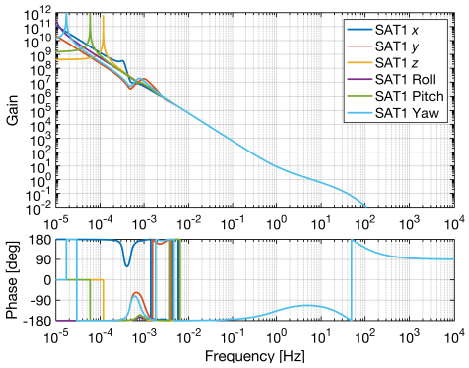

Figure 5.10: Open loop transfer function of the drag-free control of Satellite 1.

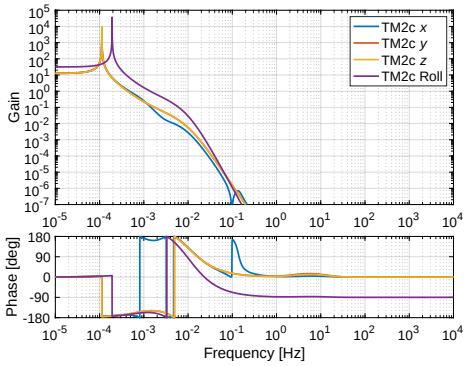

Figure 5.11: Open loop transfer function of local control of TM2c. The open loop gain for y-axis motion is overlapped by that for z-axis.

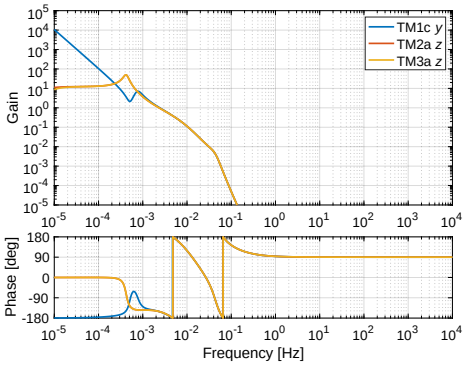

Figure 5.12: Open loop transfer function of the global attitude control.

5.8.2 Noise suppression performance

We investigate the noise suppression performance of the designed control system. Specifically, the residual motion between each mass and satellite and the residual cavity fluctuation are estimated. If the former is large, the actuator response could be non-linear. If the latter is large, the intensity noise coupling could be so large that the sensitivity can be degraded. Figures 5.13 and 5.14 show the residual displacement and tilt between each test mass and the satellite for DECIGO case, respectively. They meet the requirement for obtaining the linear response of the electro-static actuator (displacement, 0.1 mm; tilt, 10^{-4} rad). In B-DECIGO case, it is confirmed that the requirement is met. Figures 5.15 and 5.16 show the residual cavity fluctuation of DECIGO and B-DECIGO, respectively. In DECIGO and B-DECIGO, the root-mean-square values of the residual fluctuation, i.e. cavity detuning, are 5×10^{-10} m and 1×10^{-10} m, respectively. The intensity noise with this cavity detuning is estimated in the next subsection.

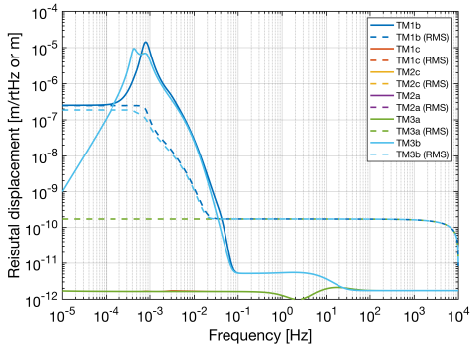

Figure 5.13: Residual displacement between each test mass and the satellite in DECIGO.

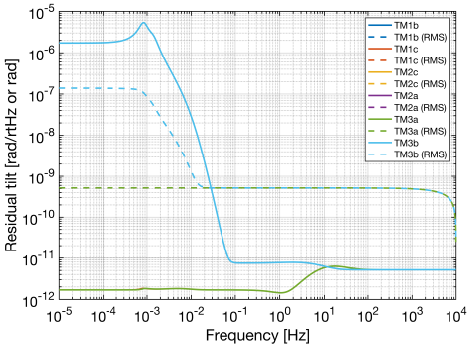

Figure 5.14: Residual tilt between each test mass and the satellite in DECIGO.

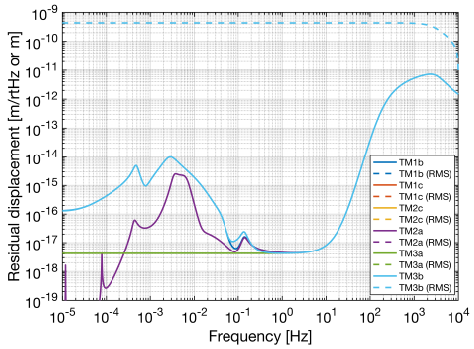

Figure 5.15: Residual cavity fluctuation of DECIGO.

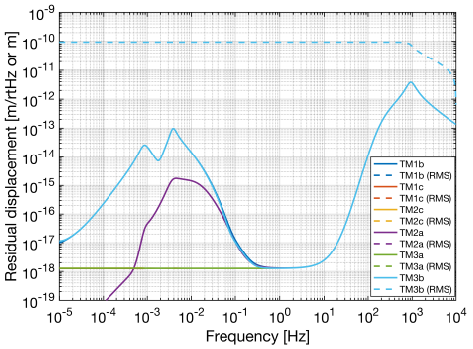

Figure 5.16: Residual cavity fluctuation of B-DECIGO.

For B-DECIGO in geocentric orbit, the largest fluctuation of the cavity is caused by the gravity of the Earth. As mentioned in Section 5.5.2, we need to confirm the fluctuation caused by the gravity of the Earth is suppressed by the control system. In order to keep the longitudinal cavity fluctuation to be less than 10^{-10} m, i.e. not to make the gravity of the Earth affect the cavity detuning, the transfer function from the force applied to the test mass to the longitudinal cavity fluctuation should be less than 10^{-5} m/N at around 10^{-5} Hz ($\simeq$ /1 day). According to the estimation with the constructed full mode, the transfer function is less than 10^{-5} m/N in each cavity requirement.

5.8.3 Actuator range

In Chapter 4, we estimate the required actuator range considering the external force that should be compensated. However, the sensing noise also takes a part of the actuator range through the feedback system. Thus, we investigate the amount of the applied force and torque for control as shown in figures 5.17 and 5.18 for DECIGO and figures 5.19 and 5.20 for B-DECIGO. The range required

to each actuator of the test mass is 2×10^{-7} N in DECIGO and 8×10^{-7} N in DECIGO.

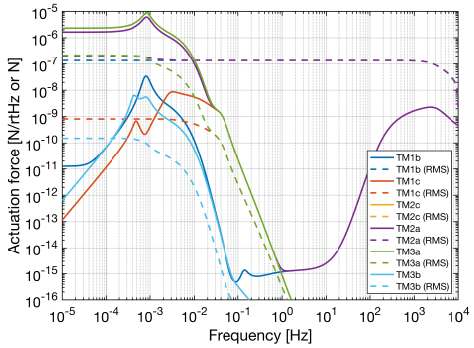

Figure 5.17: Amount of the applied force for control of DECIGO.

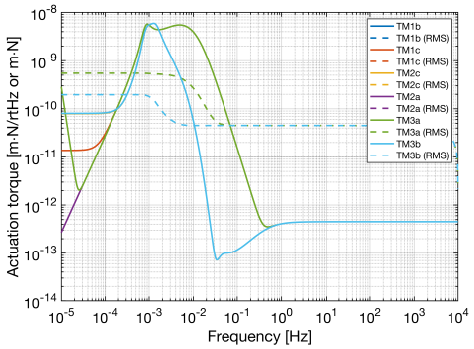

Figure 5.18: Amount of the applied torque for control of DECIGO.

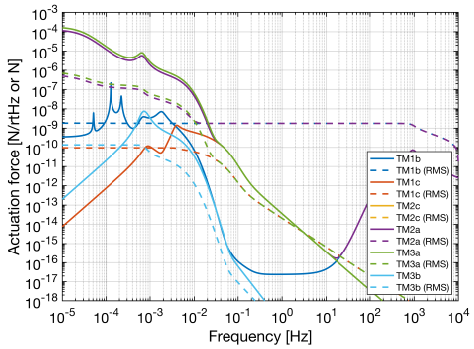

Figure 5.19: Amount of the applied force for control of B-DECIGO.

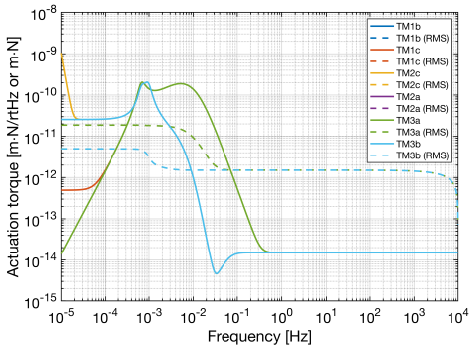

Figure 5.20: Amount of the applied torque for control of B-DECIGO.

5.8.4 Noise budget of DECIGO and B-DECIGO

Using the full DECIGO interferometer model with the designed control loop, we estimate the expected noise budget of DECIGO and B-DECIGO. Figures 5.21-5.23 show DECIGO cases and figures 5.24-5.26 show B-DECIGO cases. Note that, in figures 5.21-5.26, L-shaped interferometer equivalent sensitivities are shown. Here, we consider the noise sources described in Section 5.5. We assumed the cavity detuning of 5×10^{-10} m for DECIGO and 1×10^{-10} m for B-DECIGO as shown in figures 5.15 and 5.16 and the root-mean-square of the beam spot mis-centering of 0.1 mm. The latter is mainly caused by the dithering. In these figures, the curves labeled 'ASC' and 'Global ASC' mean the noises equivalent to the strain that issues from the sensing noise of the alignment control and global attitude control, respectively. For the frequency noise of DECIGO, we assume the noise cancellation by a factor of 10 with post processing.

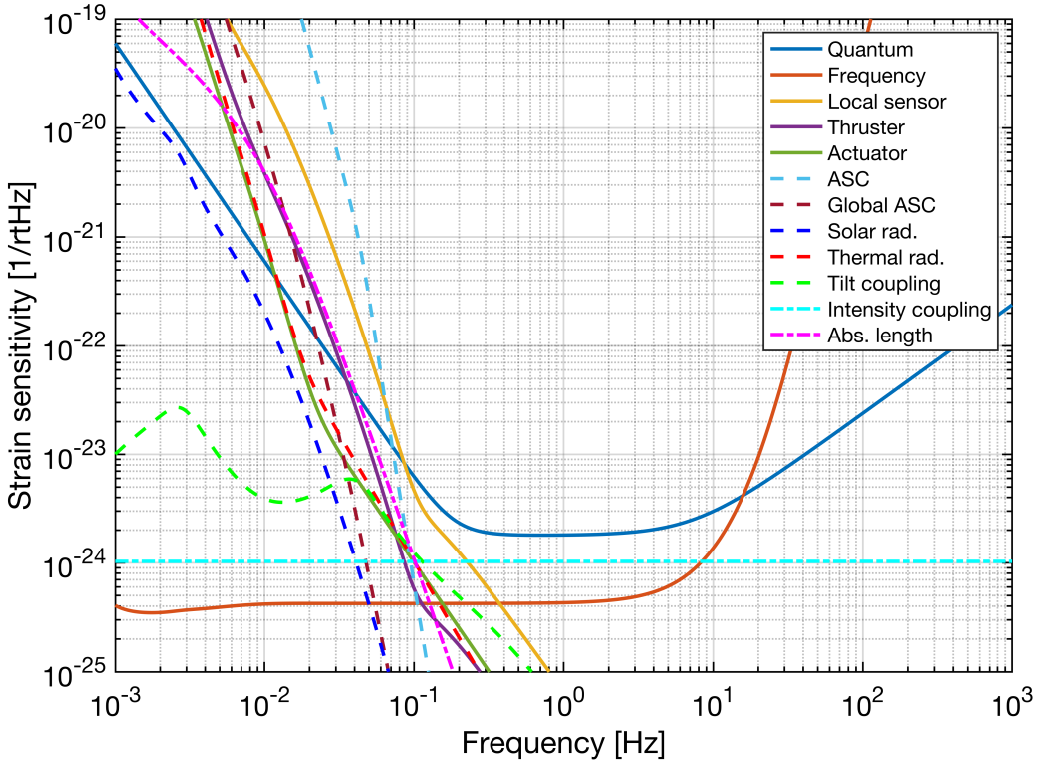

Figure 5.21: DECIGO noise budget (interferometer 1) with the full control implementation.

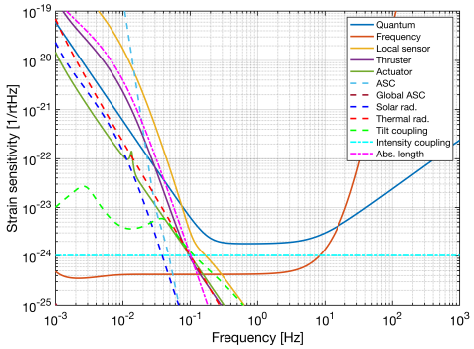

Figure 5.22: DECIGO noise budget (interferometer 2) with the full control implementation.

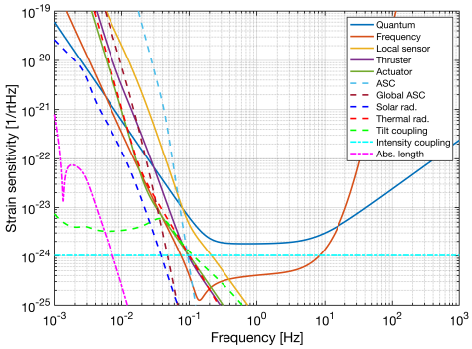

Figure 5.23: DECIGO noise budget (interferometer 3) with the full control implementation.

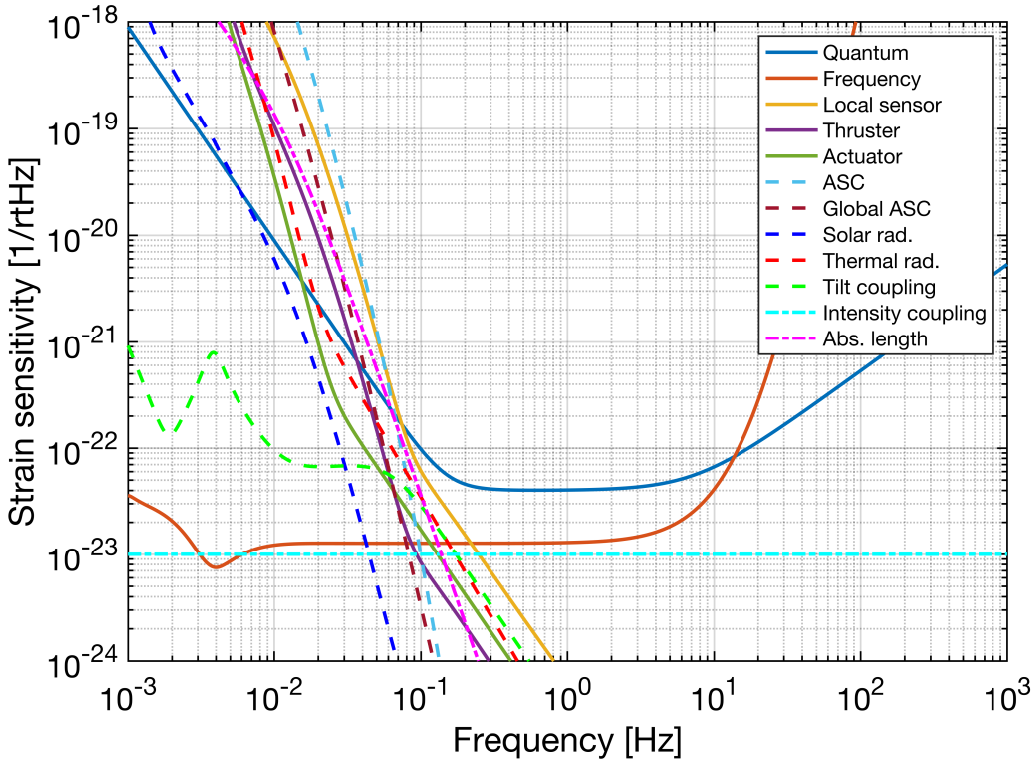

Figure 5.24: B-DECIGO noise budget (interferometer 1) with the full control implementation.

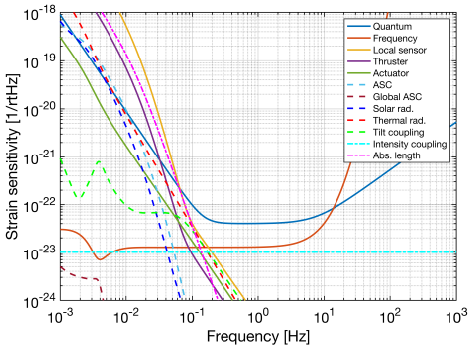

Figure 5.25: B-DECIGO noise budget (interferometer 2) with the full control implementation.

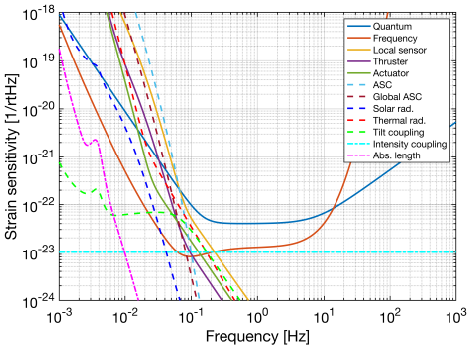

Figure 5.26: B-DECIGO noise budget (interferometer 3) with the full control implementation.

5.9 Discussion

5.9.1 Control filter in the real detector

In order to design the control filter, we should know the interferometer responses while, in the constructed model, they are known in advance as described in Section 5.2-5.4. In the real detector, the interferometer response should be diagonalized in orbit after launch. Similar investigation was performed in the ground-based detectors, especially, for suspension systems after their construction. This kind of work is known as commissioning. By using the auxiliary sensors including the local interferometric sensors, the commissioning can also be performed in space.

As shown in figure 5.6, the unity gain frequency of the control loop for the frequency control loop in DECIGO is about 2 kHz that is higher than the free spectral range of the arm cavity, 150 Hz. Such a high unity gain frequency is necessary to reduce the residual cavity fluctuation shown in figure 5.15. The source of the residual motion is the laser frequency fluctuation. At the frequencies of multiple of the free spectral range, the gain of the cavity response goes zero and the phase is delayed by 90 deg. Therefore, compensation of the phase delay is necessary to obtain the unity gain frequency above the free spectral range.

5.9.2 Actuator range

The required actuator range for the developed control system is 2×10^{-7} N in DECIGO. This is within the range considered in terms of the external force in Chapter 4. To obtain the dynamic range of the actuator in DECIGO, new techniques, such as frequency-dependent actuators, are necessary. The required actuator range for the control system in B-DECIGO is 8×10^{-7} N, which is mainly for the noise of the star tracker for the global attitude control. The actuator range is larger than that of the heliocentric-orbit case mentioned in Chapter 4. This result indicates that the frequency-dependent actuators or other improved actuator are necessary for B-DECIGO even in the heliocentric orbit. Another solution to save the actuator range is the development of the low noise star tracker or compatible sensors.

5.9.3 Dominant technical noise source

Figures 5.21-5.26 indicate that the noise performance of the feedback control meets the sensitivity requirement of DECIGO and B-DECIGO. As shown in figures 5.21-5.26, the dominant noise sources are coupling noise from the sensing noise of the local sensor in 0.1-0.2 Hz and the alignment sensing noise below 0.1 Hz. Local sensing noise is mainly coupled from the x-axis local control shown in equations (5.76) and (5.77). As shown in figure 5.11, although the control gain is rolled off at 0.1 Hz, we can improve the shape of control filters by considering the measured open loop gain in actual operation. Notice that above 0.1 Hz,

the sensitivity is limited by the residual motion of the satellites due to the local sensing noise. Alignment sensing coupling is caused by the global attitude control in equation (5.78). Cavity c can be mis-aligned by the motion of TM1c and the y-axis motion of TM1c can couple with the x-axis motion through the motion of Satellite 1. Thus, the global attitude control can make a spurious large coupling from the alignment sensing noise to the length of Cavity b which is included in Interferometer 1 and 3. This coupling can be reduced by improving the shape of the control filter shown in figure 5.12, if necessary. These discussions also support the qualitative reliability of the full DECIGO interferometer model.

5.9.4 Effect of the technical noise source on the gravitational-wave observation.

As shown in figures 5.21-5.26, the sensitivity of DECIGO and B-DECIGO is limited not only by the fundamental noise, i.e. quantum noise, but also by the technical noise. We investigate the effect of the sensitivity degradation from that only with quantum noise that is considered in the pre-conceptual design of DECIGO [54]. Here the detection range (sometimes called inspiral range) of the compact binary coalescence is investigated. The detection range is a kind of measure of the detectability of the compact binary coalescence and is defined as the luminosity distance for the binary detected at a certain signal-to-noise

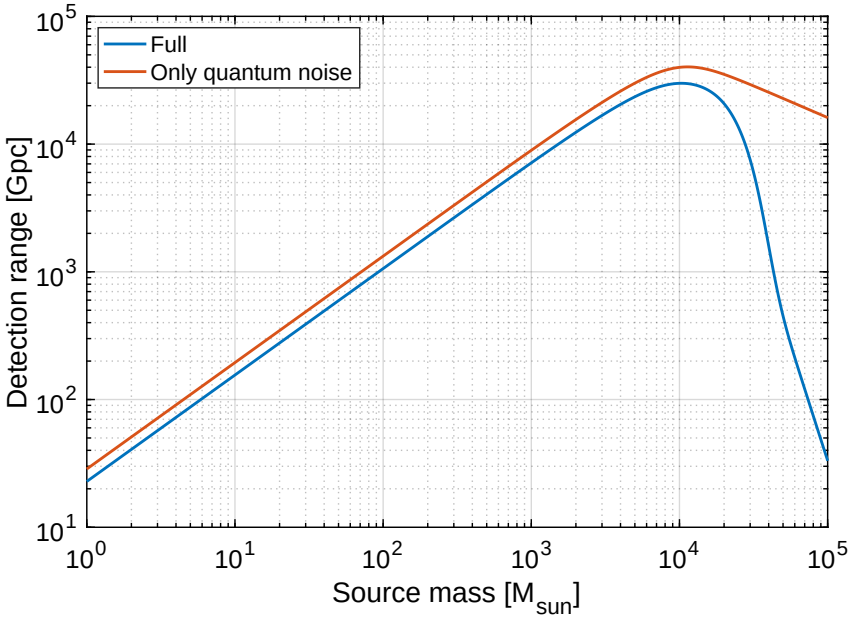

Figure 5.27: Comparison of DECIGO detection ranges with all noises and only with quantum noise. Note that the source mass is represented in the detector frame.

ratio, typically eight.[*1] Using the equations (2.35) and (B.4), we calculate the detection range of the sensitivity with the full noise sources and that only with quantum noise shown in figure 5.21. The result is shown in figure 5.27. Note that the integration band is between 0.01 Hz and the frequency of the innermost stable circular orbit (equation (2.36)). Figure 5.27 indicates that the detection range is degraded by about 30% below 10^4 $M_\odot$ and is decreased steeply above 10^4 $M_\odot$. The degradation below 10^4 $M_\odot$ is caused by the intensity noise. The detection range above 10^4 $M_\odot$ is decreased since the heavy binary merges below the sensitivity band, which is 0.06 Hz or so. In spite of the degradation of the detection range due to the technical noises, most of the scientific targets discussed in Chapter 4 are still within the reach of DECIGO and B-DECIGO. Especially, the detection range longer than 200 Gpc is enough to observe the compact binaries since the first star of the Universe is thought to be formed at a luminosity distance of 200 Gpc [196]. Actually, the probability of the detection of the light white-dwarf binaries, which are estimated to merge at around 0.05 Hz, is relatively low. For investigating the wide mass range distribution of the black holes (1-10^6 $M_\odot$), multi-band observation with the detectors that are sensitive below 0.01 Hz, such as LISA, is important.

[*1] The signal-to-noise ratio of eight is a kind of gravitational wave detection threshold in the gravitational wave research field. The signal-to-noise ratio of eight corresponds to the false detection probability of $\sim 10^{-15}$ [63].

Chapter 6

Demonstration of the dual-pass differential Fabry–Pérot interferometer

In this chapter, we show the result of the demonstration of the dual-pass differential Fabry–Pérot interferometer in the ground laboratory.

6.1 Objective

The dual-pass differential Fabry–Pérot interferometer is a new interferometer configuration for DECIGO and B-DECIGO. In the dual-pass differential Fabry–Pérot interferometer, its longitudinal signals cannot be obtained with the same way as the conventional differential Fabry–Pérot interferometer since, in general, all the cavities cannot meet the resonance condition simultaneously as explained in Section 6.2.1. In order to obtain the signal of the dual-pass differential Fabry–Pérot interferometer, the length of each cavity has to be adjusted to be similarly (quantitative discussion is in the next section). By adjusting the cavity lengths, the offset of the laser frequency from the cavity resonant frequency, known as cavity detuning, can be reduced. This is an essential feature of the dual-pass differential Fabry–Pérot interferometer not only for signal extraction but also for noise reduction to the gravitational wave observation. When there is cavity detuning, intensity fluctuation of the laser couples with the detuning and can be a dominant noise source of DECIGO and B-DECIGO. Therefore, we develop the dual-pass differential Fabry–Pérot interferometer to demonstrate its operation and to investigate its behavior. In particular, the dependence of the cavity detuning on the cavity length is investigated. This time, in order to focus on the operation of one dual-pass differential Fabry–Pérot interferometer, the setup constructed in the ground loboratory has two arm cavities with two laser sources.

6.2 Formulation and behavior of the dual-pass differential Fabry–Pérot interferometer

6.2.1 Dependence of the cavity detuning on the cavity length difference

Here, we explain the behavior of the dual-pass differential Fabry–Pérot interferometer in DECIGO and B-DECIGO. In the dual-pass differential Fabry–Pérot interferometer, one cavity is composed of two lasers, which have different frequency in order to reduce interference effect of them. Even in this case, two of the three arm cavities in DECIGO and B-DECIGO can be resonant for both lasers with feedback control as shown in figure 6.1. Laser 1 and Laser 2 are controlled to follow the resonant frequency of Cavity c. The length of Cavity a and b are controlled to follow Laser 2 and 1, respectively. The frequency of Laser 3 is controlled to use Cavity a as a reference. Thanks to these feedback control, Cavity a (c) is resonant for Laser 2 and 3 (1 and 2) and Cavity b is resonant for Laser 1. However, Cavity b cannot be resonant for Laser 3 using feedback control in general. This is because, if there is the additional feedback control loop, the feedback control is cancelled out due to the other control loops. Therefore, without a new technique, we cannot obtain the longitudinal signal of Cavity b with Laser 3.

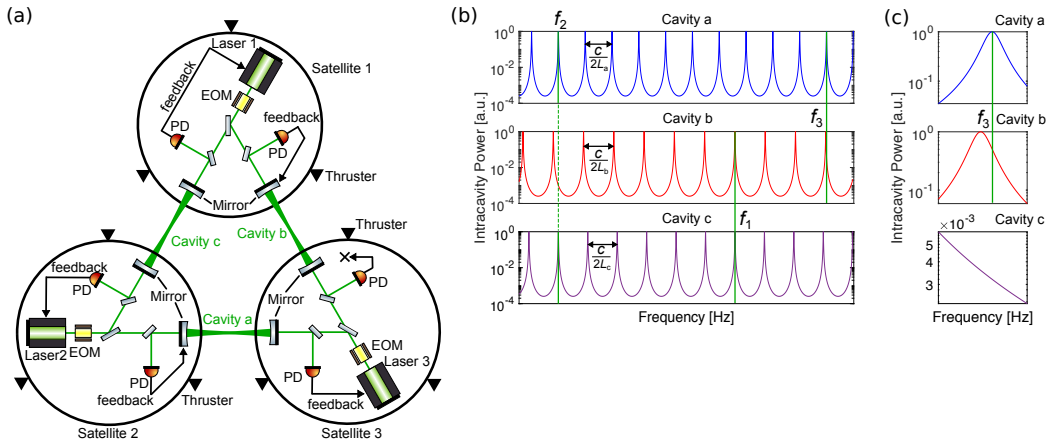

Figure 6.1: (a) Schematic of the dual-pass differential Fabry–Pérot interferometer length control topology. (b) Relation between the cavity resonant frequency and laser frequency. f_i $(i = 1, 2, 3)$ is the frequency of each laser. (c) Enlarged figure of (b) around f_3.

In order to make the cavity resonant for both lasers without feedback control, it is found that we need to adjust the absolute cavity length. The frequency difference of the frequency of Laser 3, f_3, from the resonant frequency of Cavity b, f_b, is written as

$$\Delta f_3 \equiv f_3 - f_\mathrm{b} = f_3 - N\frac{c}{2L_\mathrm{b}}. \quad (N \in \mathbb{N}) \tag{6.1}$$

Since Laser 3 is controlled to resonate with Cavity a, the frequency of Laser 3 is denoted as $f_3 = N' \frac{c}{2L_\mathrm{a}}$ ($N' \in \mathbb{N}$). Consequently, Δf_3 is written as

$$\Delta f_3 = N' \frac{c}{2L_\mathrm{a}} - N \frac{c}{2L_\mathrm{b}}. \tag{6.2}$$

We can choose N' in $0.995N \lesssim N' \lesssim 1.005N$. This range corresponds to the actuation range of the laser source. Obviously, when $N' = N$ and $L_\mathrm{a} = L_\mathrm{b}$, the frequency difference Δf_3 is zero, i.e. Cavity a is resonant with Laser 3. When $N' = N + \Delta N$ ($\Delta N \in \mathbb{N}$) and $L_\mathrm{a} = L_\mathrm{b} + \Delta L$ ($|\Delta L|/L_\mathrm{b} \ll 1$), Δf_3 is denoted as

$$\Delta f_3 \simeq \frac{c}{2L_\mathrm{b}} \left(\Delta N + N \frac{\Delta L}{L_\mathrm{b}} \right). \tag{6.3}$$

When $|\Delta L|/L_\mathrm{b} \lesssim 0.005$ (this level can be achieved with auxiliary sensors such as microwave ranging system), we can choose ΔN to be the nearest integer to $-N\frac{\Delta L}{L_\mathrm{b}}$. As a result, the frequency difference Δf_3 is within,

$$|\Delta f_3| \leq \frac{c|\Delta L|}{2L_\mathrm{b}^2}. \tag{6.4}$$

The frequency difference corresponds to the cavity detuning. When the cavity detuning is smaller than the resonant width of the cavity, i.e. $2\nu_{1/2}$, the longitudinal and alignment signal of the cavity can be obtained in the same manner as the conventional cavity. The stringent requirement for the cavity detuning is determined by the intensity noise coupling (equation (3.70)) to be $|\Delta f_3| \leq 0.6$ Hz for B-DECIGO ($|\Delta f_3| \leq 0.3$ Hz for DECIGO). This leads to the length adjustment requirement of $|\Delta L| \leq 40$ m for B-DECIGO ($|\Delta L| \leq 2$ km for DECIGO). This precision can be achieved with the auxiliary ranging instruments such as micro-wave ranging system [189]. The dependence of the cavity detuning on the cavity length is a representative feature of the dual-pass differential Fabry–Pérot interferometer and should be confirmed in the experiment.

6.2.2 Optical spring effect

Here, we discuss the effect of the optical spring due to the cavity detuning. When there is detuning in a cavity, the circulating power of the cavity varies depending on the mirror motion. As a result, the radiation pressure of the circulating laser behaves as a spring. This effect is called the optical spring [197]. The spring constant of the optical spring is given by [198]

$$K^\mathrm{opt} \equiv k^\mathrm{opt} + i\omega\gamma^\mathrm{opt}, \tag{6.5}$$

$$k^\mathrm{opt} \equiv \frac{4P_\mathrm{circ}\omega_\mathrm{l}}{Lc} \frac{\Delta f}{2\pi[(\Delta f)^2 + \nu_{1/2}^2]}, \tag{6.6}$$

$$\gamma^\mathrm{opt} \equiv -\frac{8P_\mathrm{circ}\omega_\mathrm{l}}{Lc} \frac{\nu_{1/2}(\Delta f)}{4\pi^2[(\Delta f)^2 + \nu_{1/2}^2]^2}, \tag{6.7}$$

where $P_{\rm circ}$ is the circulating power in the cavity and Δf is the cavity detuning in terms of frequency. Equations (6.5)-(6.7) indicate that the optical spring provides the positive and anti-damping spring (or the negative and damping spring) depending on the detuning. In the dual-path differential Fabry–Pérot interferometer shown in Chapter 5, the optical spring exists in Cavity c since there is cavity detuning due to the different length of the cavity as discussed in Section 6.2. In other words, TM1b and TM3b are considered to be connected with the optical spring.

One way to deal with the optical spring effect due to the different length of the cavity is detuning the resonance of Cavity c from f_1. When the resonance of Cavity c is detuned from f_1, the laser beam from Satellite 1 behaves as the optical spring, too. When the amount of the detuning of the resonance of Cavity c from f_1 is the same as that from f_3 but the sign is reversed, the optical spring effect is cancelled. Notice that the optical spring by detuning the cavity has been demonstrated [199, 200] and the amount of the detuning can be adjusted. Therefore, the results in Chapter 5 are valid when the optical spring effect is cancelled by adjusting the detuning of the resonance of Cavity c from f_1.

Actually, even without detuning the resonance of Cavity c from f_1, the optical spring effect due to the different length of the cavity can be dealt with using the control discussed in Chapter 5. If we assume $\Delta f = \Delta f_3 = 0.3$ Hz for DECIGO and $\Delta f = \Delta f_3 = 0.6$ Hz for B-DECIGO, the spring constants of the optical spring between TM1b and TM3b for DECIGO and B-DECIGO are given by, according to equations (6.5)-(6.7),

$$\begin{cases} k^{\rm opt} = 0.63 \text{ N/m}, \\ \gamma^{\rm opt} = -2.7 \times 10^{-2} \text{ N/(m/s)}, \end{cases} \qquad \text{(DECIGO)} \tag{6.8}$$

$$\begin{cases} k^{\rm opt} = 0.25 \text{ N/m}, \\ \gamma^{\rm opt} = -1.1 \times 10^{-2} \text{ N/(m/s)}. \end{cases} \qquad \text{(B-DECIGO)} \tag{6.9}$$

Here, we also use the parameters shown in table 4.1. Note that, in the dual-path differential Fabry–Pérot interferometer, we can choose the positive and anti-damping optical spring by adjusting f_3. In the condition with the positive and anti-damping optical spring, we discuss the optical spring effect. The resonant frequency of the optical spring in Cavity c is 0.017 Hz for DECIGO and 0.020 Hz for B-DECIGO. These resonant frequencies are smaller than the unity gain frequency of the control of the x-motion of TM1b according to figure 5.7. Since the optical spring affects the control system below the resonant frequency, the optical spring effect can be suppressed with the control system considered in Chapter 5. We also confirmed the above discussion using the full DECIGO interferometer model including the optical spring effect, and could obtain the stable control system and the sensitivity better than the target sensitivity between 0.1 Hz and 10 Hz.

6.3 Experimental setup

Figure 6.2 shows the schematic of the dual-pass differential Fabry–Pérot interferometer experiment. A photograph of the main dual-pass Fabry–Pérot cavities is shown in figure 6.3. We use single-frequency distributed-feedback fiber lasers with a wavelength of 1550 nm (Laser1, Koheras AdjustiK C15; Laser 2, Koheras BASIK X15). The powers of output of Laser 1 and Laser 2 are about 10 mW and 30 mW, respectively. Each of their outputs is a polarization-maintaining single-mode optical fiber. The single-mode optical fiber is the optical fiber that is designed to transmit only the fundamental spacial mode of the laser beam [127] (about the spacial mode of the laser beam, see Appdendix F). The emitted lasers go to the fiber coupled Faraday isolators (Thorlabs IO-G-1550-APC for both lasers, not shown in figure 6.2) and electro-optic modulators (EO Space PM-0K5-00-PFA-PFA-UL-S for Laser 1 and PM-0S5-00-PFA-PFA-NT for Laser 2). The phase modulation frequencies for Laser 1 and Laser 2 are 14.7 MHz and 15.3 MHz, respectively. We use the different modulation frequencies for signal decoupling of the two lasers. After the electro-optic modulator, the laser is splitted with the fiber coupled beam splitter: one goes to the main dual-pass interferometer (main beam) and the other goes to the monitoring system for absolute cavity length measurement as explained later. The main beams are introduced to free space through collimators (Newport F-COL-9-15-FCAPC) and splitted with the beam splitter for the two arm cavities. After adjusting the mode matching and alignment, the beam is incident to the cavity from both sides. This is the main dual-pass Fabry–Pérot cavity. The cavity is 55-cm-long and its finesse is designed to be 210. The radius of curvature of the mirrors is 2 m and their amplitude reflectivity is 0.992 (Lattice Electro Optics, Inc. BS-1550-R98.5-UF-MPC-0525-2000). These cavity mirrors are placed on the two optical benches isolated with rubber stacks. The reflected light and the transmitted light from the other side are received by each photodetector. Note that the two beams have orthogonal linear polarization to avoid interference effect. The cavity longitudinal signals are obtained with the Pound–Drever–Hall technique.

The block diagram of the control in this experiment is shown in figure 6.4. Signals from PD1a and PD2a are fed back to the frequencies of Laser 1 and Laser 2, respectively. With the signal from PD2b, the position of M2b is controlled using a piezoelectric transducer. We defined open loop transfer functions of each feedback loop as

$$G_{1a} \equiv S_{1a} E_{1a} A_{1a}, \tag{6.10}$$

$$G_{2a} \equiv S_{2a} E_{2a} A_{2a}, \tag{6.11}$$

$$G_{2b} \equiv \frac{f_{las}}{L} S_{2b} E_{2b} A_{2b}. \tag{6.12}$$

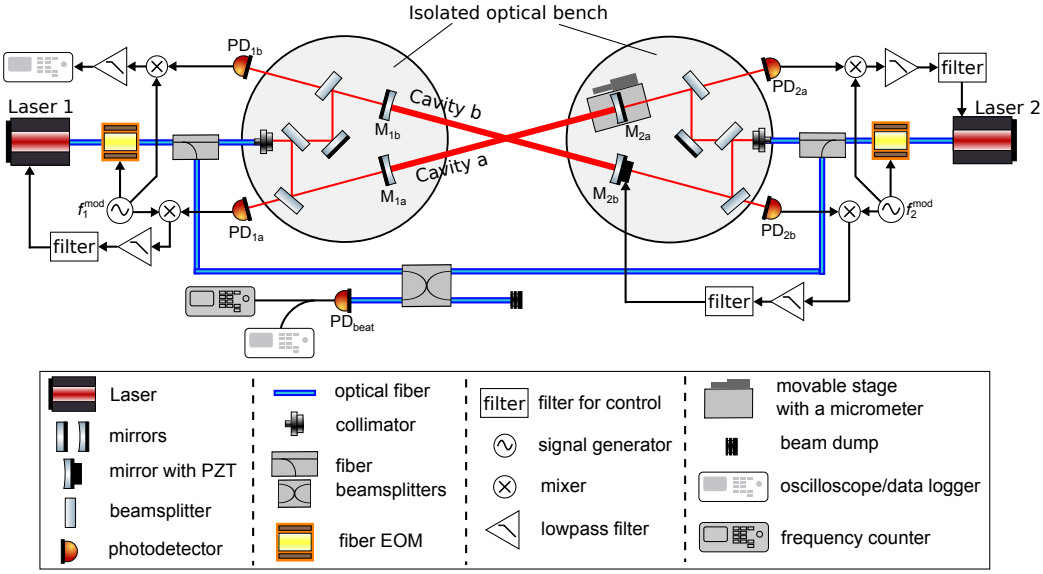

Figure 6.2: Schematic of the dual-pass differential Fabry–Pérot interferometer experiment.

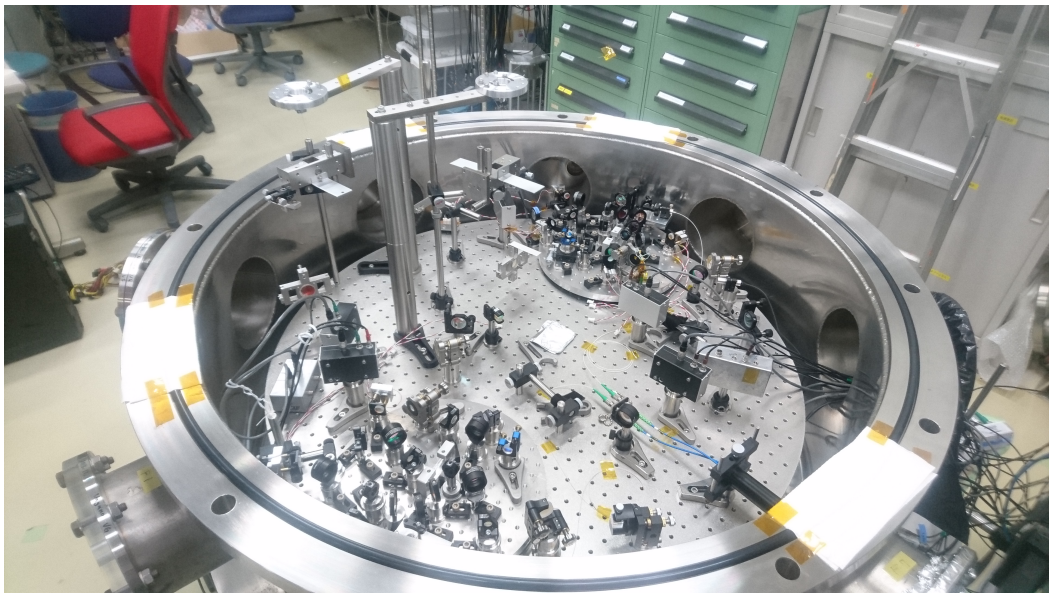

Figure 6.3: Photograph of the main dual-pass Fabry–Pérot cavities.

Each error signal (about the notation, see Appendix B) is denoted as

$$e_{1a} = \frac{S_{1a}}{1+G_{1a}} \frac{f_{las}}{L} (x_{1a} - x_{2a}) + \frac{S_{1a}}{1+G_{1a}} f_1, \tag{6.13}$$

$$e_{2a} = \frac{S_{2a}}{1+G_{2a}} \frac{f_{las}}{L} (x_{1a} - x_{2a}) + \frac{S_{2a}}{1+G_{2a}} f_2, \tag{6.14}$$

$$e_{1\mathrm{b}} = \left(\frac{G_{2\mathrm{a}}}{1+G_{2\mathrm{a}}} \frac{G_{2\mathrm{b}}}{1+G_{2\mathrm{b}}} - \frac{G_{1\mathrm{a}}}{1+G_{1\mathrm{a}}} \right) \frac{f_{\mathrm{las}}}{L} S_{1\mathrm{b}} \left(x_{1\mathrm{a}} - x_{2\mathrm{a}} \right) + \frac{1}{1+G_{2\mathrm{b}}} \frac{f_{\mathrm{las}}}{L} S_{1\mathrm{b}} \left(x_{1\mathrm{b}} - x_{2\mathrm{b}} \right) + \frac{1}{1+G_{1\mathrm{a}}} S_{1\mathrm{b}} f_1 - \frac{1}{1+G_{2\mathrm{a}}} \frac{G_{2\mathrm{b}}}{1+G_{2\mathrm{b}}} S_{1\mathrm{b}} f_2, \tag{6.15}$$

$$e_{2\mathrm{b}} = -\frac{G_{2\mathrm{a}}}{1+G_{2\mathrm{a}}} \frac{1}{1+G_{2\mathrm{b}}} \frac{f_{\mathrm{las}}}{L} S_{2\mathrm{b}} \left(x_{1\mathrm{a}} - x_{2\mathrm{a}} \right) + \frac{1}{1+G_{2\mathrm{b}}} \frac{f_{\mathrm{las}}}{L} S_{2\mathrm{b}} \left(x_{1\mathrm{b}} - x_{2\mathrm{b}} \right) + \frac{1}{1+G_{2\mathrm{a}}} \frac{1}{1+G_{2\mathrm{b}}} S_{2\mathrm{b}} f_2. \tag{6.16}$$

When $|G_{1\mathrm{a}}| \gg 1$ and $|G_{2\mathrm{a}}| \gg 1$, we can write $e_{1\mathrm{b}}$ and $e_{2\mathrm{b}}$ as

$$e_{1\mathrm{b}} = -\frac{1}{1+G_{2\mathrm{b}}} \frac{f_{\mathrm{las}}}{L} S_{1\mathrm{b}} \left(x_{1\mathrm{a}} - x_{2\mathrm{a}} \right) + \frac{1}{1+G_{2\mathrm{b}}} \frac{f_{\mathrm{las}}}{L} S_{1\mathrm{b}} \left(x_{1\mathrm{b}} - x_{2\mathrm{b}} \right), \tag{6.17}$$

$$e_{2\mathrm{b}} = -\frac{1}{1+G_{2\mathrm{b}}} \frac{f_{\mathrm{las}}}{L} S_{1\mathrm{b}} \left(x_{1\mathrm{a}} - x_{2\mathrm{a}} \right) + \frac{1}{1+G_{2\mathrm{b}}} \frac{f_{\mathrm{las}}}{L} S_{1\mathrm{b}} \left(x_{1\mathrm{b}} - x_{2\mathrm{b}} \right), \tag{6.18}$$

so that the same signal should be measured at the two ports.

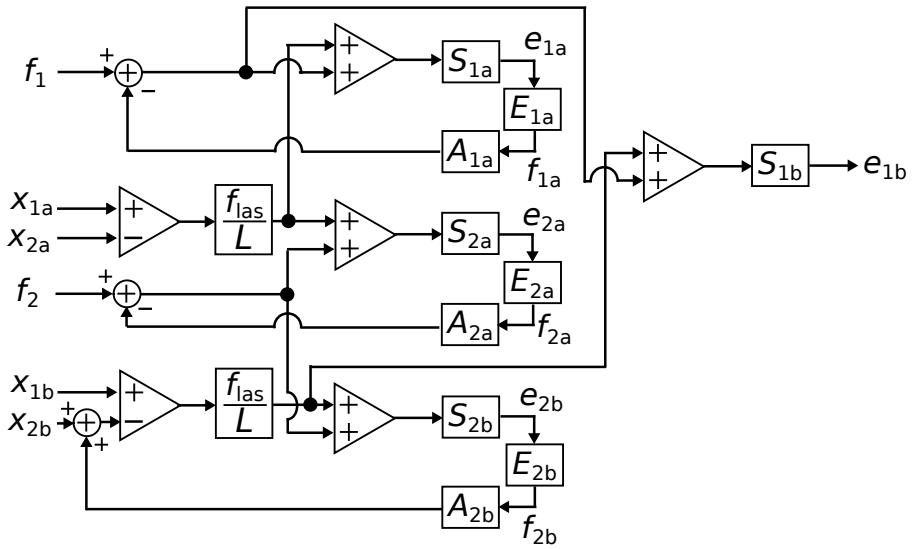

Figure 6.4: Block diagram of the dual-pass differential Fabry–Pérot interferometer experiment. $e_{i\alpha}$ and $f_{i\alpha}$ are the error signal and feedback signal of each port, respectively, $S_{i\alpha}$ is the sensing efficiency, $E_{i\alpha}$ is the control electric filter, $A_{i\alpha}$ is the actuator efficiency ($i = 1, 2$ and $\alpha = \mathrm{a}, \mathrm{b}$), $f_{\mathrm{las}} = 5.8 \times 10^{14}$ Hz is the laser frequency, and L is the cavity length.

6.4 Characterization of each component

After the setup was constructed, the finesse of the cavities, the actuation efficiencies, the sensing efficiencies, the control filters, and the cavity lengths were evaluated.

6.4.1 Finesse of the cavity

The finesse of the cavity was measured by taking the ratio of the free spectral range to the resonance peak full width at half maximum by sweeping the frequency of Laser 2. This method is called cavity scanning. Since Laser 2 has larger power than Laser 1, the measurement with better signal-to-noise ratio can be performed with Laser 2. We scanned Cavity a and Cavity b and saw several pairs of the resonant peaks next to each other for each cavity. One pair of the resonant peaks is shown in figures 6.5 and 6.6 as an example. The largest peak in figures 6.5 is the fundamental Hermite–Gaussian mode (about Hermite–Gaussian mode, see Appendix F). The finesse is measured with the following equation:

$$\mathcal{F} = \frac{\Delta t_{\mathrm{FSR}}}{\Delta t_{\mathrm{FWHM}}}, \tag{6.19}$$

where Δt_{FSR} is the temporal difference of the peaks and Δt_{FWHM} is the full width at half maximum of the peak in terms of time. As a result, the finesses of Cavity a and b were measured to be,

$$\text{Cavity a:} \quad 290 \pm 70, \tag{6.20}$$

$$\text{Cavity b:} \quad 270 \pm 80, \tag{6.21}$$

where statistical errors are shown. The measured finesses of the two cavities are the same within error ranges. Although the measured finesse of Cavity a does not agree with the designed value within the error range, it does not significantly affect the whole result in this chapter.

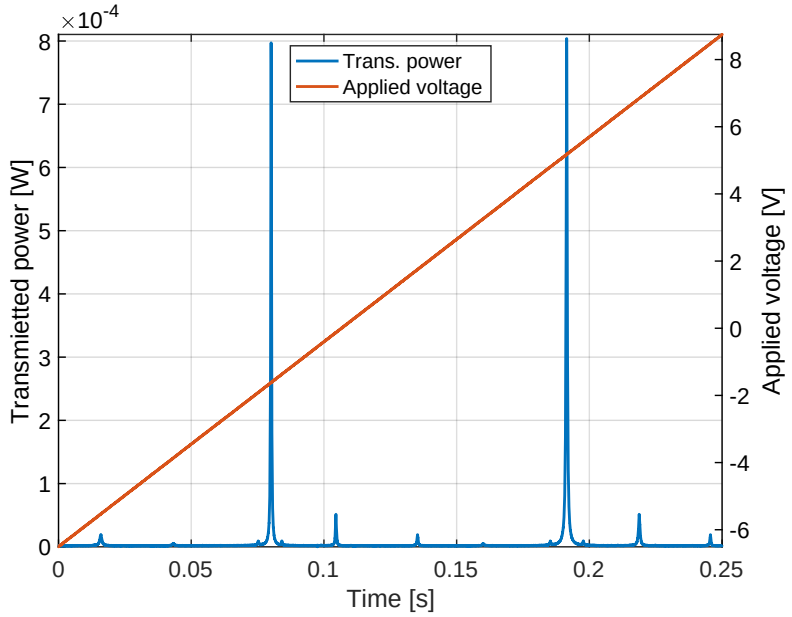

Figure 6.5: Example of the result for cavity scanning to measure actuation efficiency. In this plot, the applied voltage to Laser 2 for scanning its frequency and transmitted power measured with PD1b is shown. During this measurement, the beam from Laser 1 was blocked.

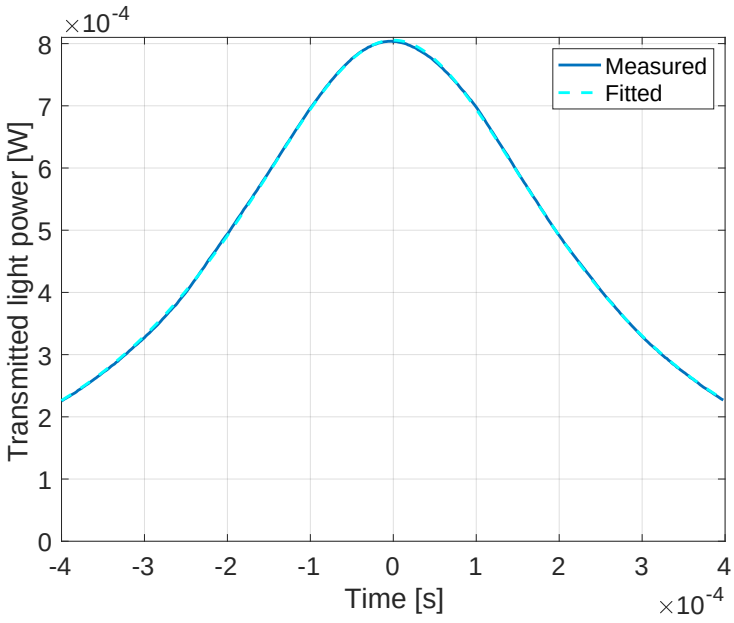

Figure 6.6: Enlarged plot of figure 6.5 around 0.08 s. We can see the peak of the fundamental mode. The origin of the horizontal axis (i.e. 0 s) is set to be the peak point.

6.4.2 Actuator efficiency

Actuator efficiencies, i.e. laser frequency change of Laser 1 (Laser 2) when 1 V is applied to Laser 1 (Laser 2) and the efficiency of piezoelectric transducer on M2b, were measured with two methods. The first one is cavity scanning again for overall efficiency measurement and the second one is frequency response measurement. The cavity has a peak at every half of the wavelength, which is a precise length reference. Thus, by comparing the voltage difference between the two cavity peaks during cavity scanning with each actuator to the half of the wavelength, we can measure the overall efficiency of the actuator. If we scan the cavity with the piezoelectric transducer on M2b, the efficiency of the cavity is measured. The frequency response can be measured with the transfer function measurement from the input of the actuator to the sensor output when the cavity is locked with each actuator. As a result, the actuator efficiencies were measured to be

$$\text{Laser 1 (freqency): } A_{1\mathrm{a}}(f) = A_1 \exp\left(-if/f_1\right), \tag{6.22}$$
$$A_1 = (1.31 \pm 0.04) \times 10^8 \text{ [Hz/V]}, \ f_1 = 5500 \pm 20 \text{ [Hz]},$$

$$\text{Laser 2 (freqency): } A_{2\mathrm{a}}(f) = A_2 \frac{1}{1+if/f_2} \frac{1}{1+if/f_2'} \exp\left(-if/f_2''\right), \tag{6.23}$$
$$A_2 = (3.89 \pm 0.08) \times 10^7 \text{ [Hz/V]}, \ f_2 = 328 \pm 3 \text{ [Hz]},$$
$$f_2' = 5250 \pm 40, \text{[Hz]}, \ f_2'' = 17.0 \pm 0.2 \text{ [kHz]},$$

$$\text{Piezoelectric transducer: } A_{2\mathrm{b}}(f) = A_{\mathrm{PZT}} \frac{1}{1+if/f_{\mathrm{PZT}}} \exp\left(-if/f_{\mathrm{PZT}}'\right), \tag{6.24}$$
$$A_{\mathrm{PZT}} = (4.7 \pm 0.4) \times 10^{-7} \text{ [m/V]},$$
$$f_{\mathrm{PZT}} = 2500 \pm 700 \text{ [Hz]}, \ f_{\mathrm{PZT}}' = 5500 \pm 20 \text{ [Hz]}.$$

6.4.3 Sensing efficiency

In the cavity experiment, the laser frequency difference from the resonant frequency of the cavity can be measured with the Pound–Drever–Hall technique as explained in Chapter 3. The efficiency of the measurement of the frequency difference between the laser frequency and the resonant frequency of the cavity can be represented by sensing efficiency, which is the transfer function from the difference of the resonant frequency to the output voltage. The sensing efficiency can be measured from the measurement of the transfer function from the input of the actuator to the sensor output if the actuator efficiency is known. In this dual-pass differential Fabry–Pérot interferometer experiment, sensing efficiency is assumed to have a flat response since $\nu_{1/2}$ is ~ 500 kHz, which is much larger

than the frequency that is considered in this experiment, e.g. at most 10 kHz (see also Section 3.3.2). The measured sensing efficiencies are

$$\text{PD1a} : S_{1\text{a}} = (2.64 \pm 0.01) \times 10^{-8} \text{ [V/Hz]}, \tag{6.25}$$

$$\text{PD1b} : S_{1\text{b}} = (1.655 \pm 0.006) \times 10^{-8} \text{ [V/Hz]}, \tag{6.26}$$

$$\text{PD2a} : S_{2\text{a}} = (8.76 \pm 0.03) \times 10^{-8} \text{ [V/Hz]}, \tag{6.27}$$

$$\text{PD2b} : S_{2\text{b}} = (1.40 \pm 0.03) \times 10^{-7} \text{ [V/Hz]}. \tag{6.28}$$

Note that these results are expressed in terms of the cavity resonant frequency.

6.4.4 Control electric filter

The control electric filter is designed to obtain stable control. The measured transfer functions are

$$\text{Laser 1 loop: } E_{1\text{a}}(f) = E_{1\text{a}} \frac{1 + if/f''_{1\text{a}}}{1 + if/f_{1\text{a}}} \frac{1 + if'''/f_{1\text{a}}}{1 + if/f'_{1\text{a}}} \tag{6.29}$$

$$E_{1\text{a}} = 3598 \pm 2,\ f_{1\text{a}} = 2.80 \pm 0.01 \text{ [Hz]},\ f'_{1\text{a}} = 32.6 \pm 0.2 \text{ [Hz]},$$
$$f''_{1\text{a}} = 310 \pm 2 \text{ [Hz]},\ f'''_{1\text{a}} = 1.1 \pm 0.4 \text{ [kHz]},$$

$$\text{Laser 2 loop: } E_{2\text{a}}(f) = E_{2\text{a}} \frac{1 + if''/f_{2\text{a}}}{1 + if/f_{2\text{a}}} \frac{1 + if'''/f_{2\text{a}}}{1 + if/f'_{2\text{a}}} \frac{1}{1 + if/f''''_{2\text{a}}}, \tag{6.30}$$

$$E_{2\text{a}} = 94830 \pm 60,\ f_{2\text{a}} = 0.390 \pm 0.008 \text{ [Hz]},\ f'_{2\text{a}} = 34.1 \pm 0.3 \text{ [Hz]},$$
$$f''_{2\text{a}} = 286 \pm 3 \text{ [Hz]},\ f'''_{2\text{a}} = 1.67 \pm 0.03 \text{ [kHz]},\ f''''_{2\text{a}} = 9.7 \pm 0.2 \text{ [kHz]},$$

$$\text{M}_{2\text{b}} \text{ loop: } E_{2\text{b}}(f) = E_{2\text{b}} \frac{1 + if/f''_{2\text{b}}}{1 + if/f_{2\text{b}}} \frac{1 + if'''/f_{2\text{b}}}{1 + if/f'_{2\text{b}}}, \tag{6.31}$$

$$E_{2\text{b}} = 55.32 \pm 0.01,\ f_{2\text{a}} = 2.76 \pm 0.02 \text{ [Hz]},\ f'_{2\text{b}} = 31.9 \pm 0.4 \text{ [Hz]},$$
$$f''_{2\text{b}} = 353 \pm 6 \text{ [Hz]},\ f'''_{2\text{b}} = 1.434 \pm 0.002 \text{ [kHz]}.$$

6.4.5 Absolute cavity length

The absolute cavity length can be determined if the cavity free spectral range is measured according to equation (3.31). In this experiment, the free spectral range can be measured by observing the beatnote frequency with PDbeat and a frequency counter when the two lasers are made to resonate at the next resonance of the cavity. The measured lengths of Cavity a and b are

$$\text{Cavity a: } L_{\text{a}} = 0.55340 \pm 0.00001 \text{ [m]}, \tag{6.32}$$

$$\text{Cavity b: } L_{\text{b}} = 0.55340 \pm 0.00001 \text{ [m]}. \tag{6.33}$$

Note that the length of Cavity a can be changed with the stage on which M2a is located and the value of L_{a} shown in equation (6.32) is the length of Cavity a after the adjustment to be the same as the length of Cavity b.

6.5 Results of the dual-pass differential Fabry–Pérot interferometer experiment

6.5.1 Lock sequence

Figure 6.7 shows the lock sequence of the dual-pass differential Fabry–Pérot interferometer. At 11 s, the frequency of Laser 1 is controlled to be the resonant frequency of Cavity a. Then, at 19 s, the frequency of Laser 2 is controlled to be the resonant frequency of Cavity a. Finally, at 32 s, the length of the cavity b is controlled with the signal obtained with PD2b. The error signal from the PD1b can be observed although it is not fed back to any actuator. Note that at 7 s, Cavity a is held in the non-intended higher order mode.

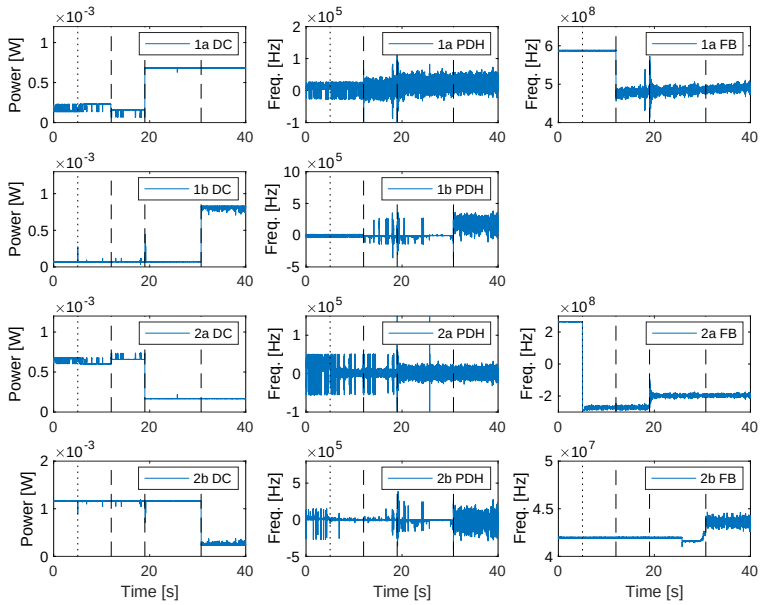

Figure 6.7: Lock sequence of the dual-pass differential Fabry–Pérot interferometer. Left panels show the laser power received by each photodetector, center panels show the error signals of each cavity, and right panels show the feedback signals in each control loop. The error and feedback signals are written in terms of the resonant frequency, which is the origin of these signals. At the timings indicated by the dashed lines, each control servo was engaged successively.

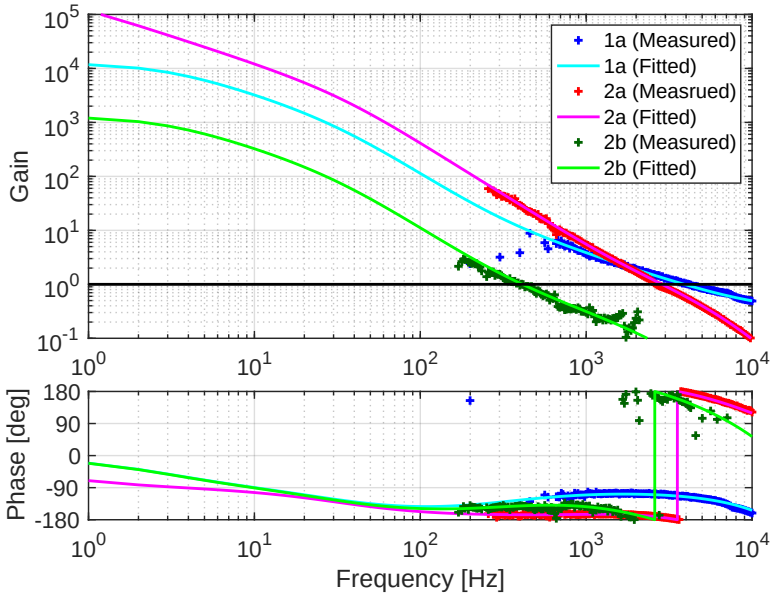

Figure 6.8: Measured open loop gain of each control loop. The upper and lower panels show the gain and phase, respectively. The solid lines are the open loop gains predicted by the characterization of each component in Section 6.5.

6.5.2 Open loop transfer function

We measured open loop transfer functions of the two frequency servos and piezoelectric transducer servo as shown in figure 6.8. The open loop transfer functions predicted by the characterization of each component described in Section 6.5 are also shown. Here, we used the mean values. The measured gain and predicted gain agree with each other around their unity gain frequency.

6.5.3 Detuning dependence on the cavity length

We measured the dependence of the error signal offset from the resonant frequency on the cavity length with the Pound–Drever–Hall technique. The error signals correspond to the cavity detuning. The cavity length was adjusted by moving the stage with a micro meter where M2a is placed. Two examples of the time series data of the error signals when the two cavity lengths are off and adjusted are shown in figures 6.9 and 6.10. We measured the error signal offsets with five different positions of M2a as shown in figure 6.11. During this measurement, the cavity alignment is kept to be almost the same. We determined the error signal offset dependence of the mirror position by fitting the result in figure 6.11 to be $(-5.1 \pm 0.5) \times 10^8$ Hz/m.

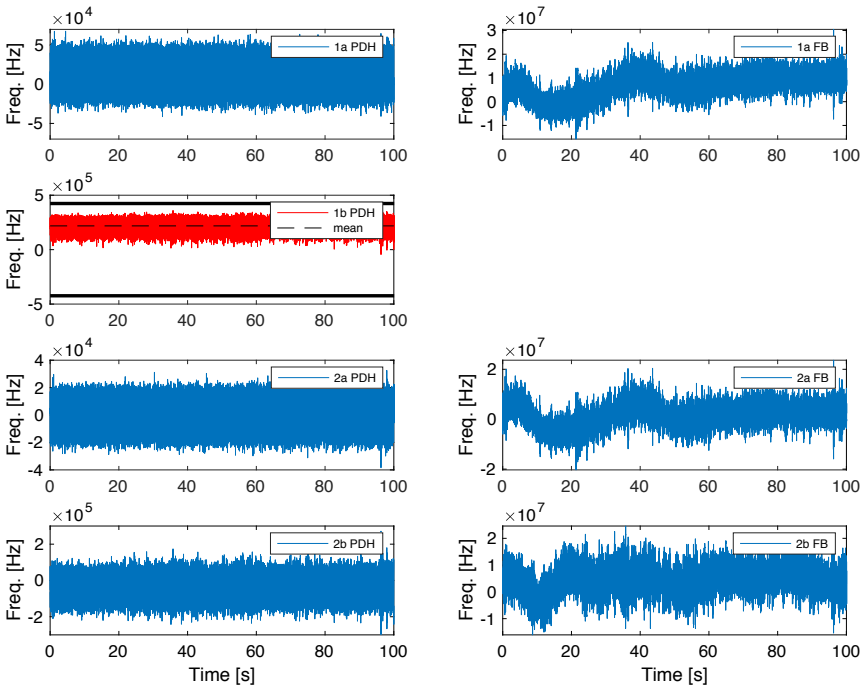

Figure 6.9: Error and feedback signals when two cavity lengths are shifted.

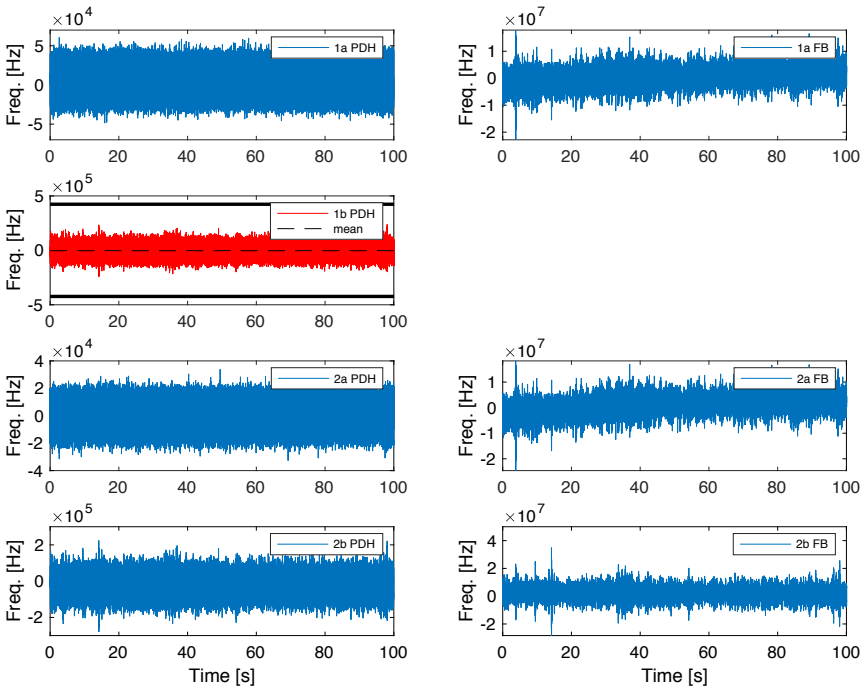

Figure 6.10: Error and feedback signals when two cavity lengths are adjusted by moving the position of M2a as described in Section 6.4.5.

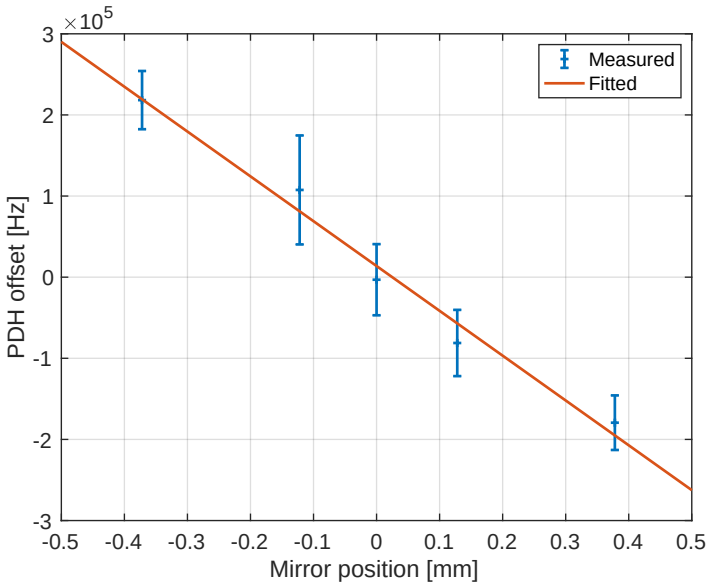

Figure 6.11: Measured offsets of the Pound–Drever–Hall signal, i.e. error signals, at the five different cavity lengths. The offset of the Pound–Drever–Hall signal corresponds to the cavity detuning.

6.5.4 Noise spectrum measurement

We measured noise spectra of the dual-pass differential Fabry–Pérot interferometer. The result is shown in figure 6.12. The '1a' and '2a' curves are calibrated from the feedback signal and the '2b' curve is calibrated from the error signal. The '1b' and '2b' curves represent the differential length fluctuations of Cavity a and b. The spectra of '1a' and '1b' indicate that the frequency noise is successfully stabilized by the frequency servo and they work as a differential Fabry–Pérot interferometer effectively without feeding back the signal of PD1b.

6.6 Discussion

When the dual-pass differential Fabry–Pérot interferometer works well, the same signal, i.e. the differential length fluctuation of the two cavities, is obtained in the two interferometer. To show that, we calculated the coherence of $e_{1\mathrm{b}}$ and $e_{2\mathrm{b}}$ as shown in figure 6.13. Since the average number is 100, the two signals are regarded as coherent when the coherence is larger than 0.06 [201]. Figure 6.13 indicates that the two signals are coherent between 1 and 1500 Hz. The coherence below 10 Hz decreases since the noise is large. The main noise source is considered to be the differential component of the seismic motion. The coherence above 1500 Hz is small since the gain of the frequency feedback loop is small. In this case, the independent frequency noise affects the measurement according to equations (6.15) and (6.16). The discussion in this paragraph indicates that the

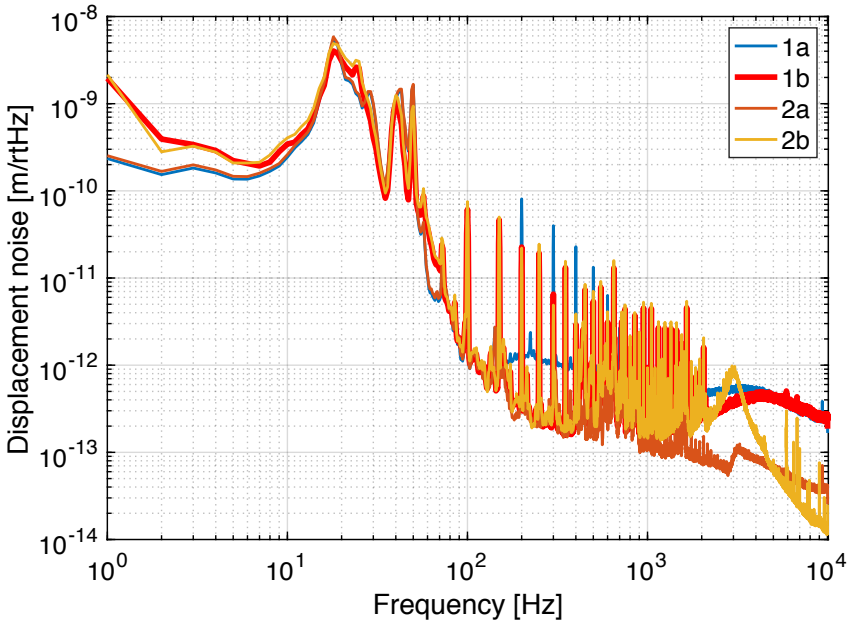

Figure 6.12: Calibrated noise spectra of the dual-pass differential Fabry–Pérot interferometer measured with PD1a, PD1b, PD2a, and PD2b.

dual-pass differential Fabry–Pérot interferometer is considered to be successfully operated.

In order to see the behavior of the dual-pass differential Fabry–Pérot interferometer with another way, we also check if the common motion can be subtracted by taking the difference between the output signals of PD1b and PD2b. Since there could be relative calibration error between PD1b and PD2b, we need to apply a factor to the output signal of PD2b for the subtraction of the output of PD2b from the output of PD1b. We survey the optimal factor of the subtraction with 1D-grid searching. The best subtracted signal is shown in figure 6.14. This figure suggests that the two interferometers measure the same signal, i.e. the differential cavity length fluctuation. The optimal factor for the subtraction of the output of PD2b from the output of PD1b was 0.89. This indicates that there is relative calibration error of 11% between the two interferometers. The 11% calibration error can be explained by the sensing efficiency error estimated in Section 6.5.

It is worth noting that the procedure mentioned above for the subtraction from the signal of PD1b with the signal of PD2b is a kind of way to make a null-stream and can also be used for the relative calibration of each sensing port even in DECIGO and B-DECIGO. Since the mass and volume of the instrument are limited in the space mission, this kind of in-situ scheme is beneficial.

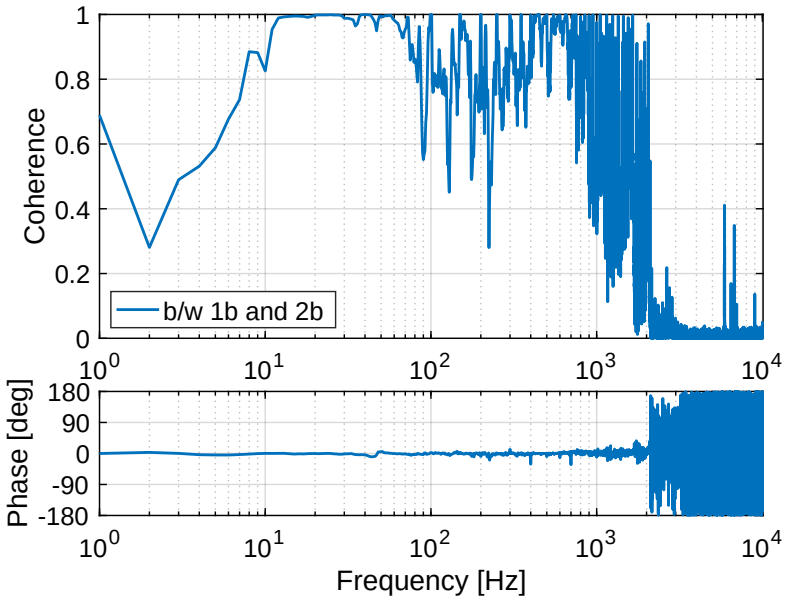

Figure 6.13: Measured magnitude-squared amplitude (upper panel) and phase (lower panel) of coherence of the error signal from PD1b and PD2b.

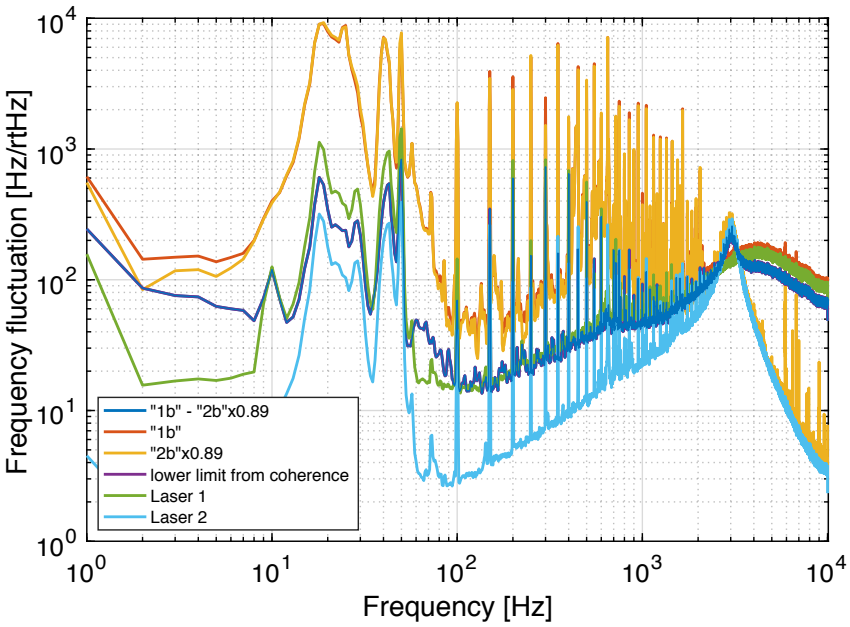

Figure 6.14: Noise spectra with common noise subtraction (blue curve). '1b' and '2b' are measured error signals with PD1b and PD2b, respectively. 'Laser 1' and 'Laser 2' are estimated frequency noises of Laser 1 and Laser 2, respectively. The purple line indicates the lower limit of the noise subtraction estimated from the coherence measurement as shown in figure 6.13. The curves of the subtracted signal and 'lower limit from coherence' are overlapped.

Here, the result in Section 6.5.3 is discussed to see the dependence of the cavity detuning on the cavity length. The fitting result of the relation between mirror position and cavity detuning from figure 6.11 is $(-5.1 \pm 0.5) \times 10^8$ Hz/m. Our formulation and the cavity length measurement in Section 6.4.5 predict that the dependence of the detuning of Cavity b to the position of TM2a is to be $(-4.8976 \pm 0.0002) \times 10^8$ Hz/m. They are consistent within the error ranges. This discussion indicates that, by adjusting the cavity length, the longitudinal signal of the dual-pass differential Fabry–Pérot interferometer can be obtained. Moreover, there is the position of TM2a where the cavity detuning is zero as shown in figure 6.11. Therefore, intensity noise coupling explained in Section 3.3.5 can be reduced in the dual-pass differential Fabry–Pérot interferometer.

Chapter 7

Conclusion

7.1 Summary

In this thesis, the control scheme of the Fabry–Pérot type space gravitational wave antenna is studied. First, the control topology is considered with the numerical model of the Fabry–Pérot type antenna including a mechanical and opto-mechanical response, a sensing and actuation scheme, external disturbances, and sensing noises. The new model is named a *full DECIGO interferometer model*. This new model reveals that the interferometer control and drag-free control can be engaged at the same time by separating the degrees of freedom controlled by the control system: one mirror in the satellite is used as the reference of the drag-free control and the other mirror is used for the interferometer control and the local control. The model also reveals that the mirror position can be used as a reference of the control to obtain the stable control system. Using the model, a solution of DECIGO parameters with interferometer control achieving the target strain sensitivity of 10^{-23} $/\sqrt{\mathrm{Hz}}$ is also found as shown in figure 5.21. In addition, more than one-day stability was also achieved. Second, the dual-pass differential Fabry–Pérot interferometer is formulated and is constructed in a ground laboratory as shown in figure 6.2. The operation of the dual-pass differential Fabry–Pérot interferometer is demonstrated for the first time. Moreover, it is confirmed that cavity detuning can be reduced by the cavity length adjustment as predicted by the formulation as shown in figure 6.11. The cavity detuning reduction is essential to minimize a noise coupled with the laser intensity fluctuation, which would be a major noise source in DECIGO. These results indicate that the dual-pass differential Fabry–Pérot interferometer is correctly understood with the new formulation.

7.2 DECIGO and B-DECIGO design

In this thesis, control topology and the dual-pass differential Fabry–Pérot interferometer are developed. These two components are essential for DECIGO and B-DECIGO. Here, including the obtained results, we summarize the design of DECIGO and B-DECIGO as shown in table 7.1. The dual-pass differential Fabry–Pérot interferometer is utilized. The sensing method for the longitudinal signal is the Pound–Drever–Hall method. The methods for the alignment signal

are the wavefront sensing method and the dithering method. With these sensing methods, the interferometer is controlled stably with almost shot-noise-limited sensitivity between 0.1 and 10 Hz. We can implement the drag-free control to control the satellite motion at the same time as the interferometer control with control scheme developed in this thesis. The degrees of freedom of the test mass that is not controlled with the interferometer control is controlled with the local sensors and the star trackers. In this design, the dominant technical noise is caused by the noise of the local sensor and the significant part of the actuator range is taken by the star tracker noise. The local sensors and the star trackers should be more sensitive than 1×10^{-12} m/$\sqrt{\text{Hz}}$ above 0.1 Hz (for interferometer sensitivity), and 2×10^{-6} rad/$\sqrt{\text{Hz}}$ below 0.01 Hz (for interferometer stability), respectively. The test mass actuators should have the maximum range of 2×10^{-6} N and the noise level of 2×10^{-17} N/$\sqrt{\text{Hz}}$ above 0.1 Hz. The dynamic range of the actuator is $\sim 10^{-11}$ /$\sqrt{\text{Hz}}$, which is greater than that of the conventional simple actuators, so that we need to develop a new actuator. One candidate is the frequency-dependent actuator that has the large range (larger than 2×10^{-6} N with the safety factor of 10) outside the observation band, and is low noise (better than 2×10^{-17} N/$\sqrt{\text{Hz}}$) in the observation band. The coupling from the satellite motion to the test mass acceleration should be less than 5×10^{-7} /s^2 not only for the sensitivity but also for the stability below 10^{-4} Hz. Using these components and control scheme developed in this thesis, we achieved the target sensitivity of DECIGO (10^{-23} /$\sqrt{\text{Hz}}$) and B-DECIGO (10^{-22} /$\sqrt{\text{Hz}}$) between 0.1 and 10 Hz and one-day-long stability in the simulation.

Table 7.1: Summary of the design of DECIGO and B-DECIGO considered in this thesis. In the brackets, the achieved values in the previous works are shown.

Interferometer configuration	Dual-pass differential Fabry–Pérot interferometer
Sensing method longitudinal alignment	 Pound–Drever–Hall method Wavefront sensing and dithering
Control topology	Combined control of the interferometer control with the drag-free control
Local sensor sensitivity	1×10^{-12} m/$\sqrt{\text{Hz}}$ (> 0.1 Hz) [2×10^{-9} m/$\sqrt{\text{Hz}}$ (in space) [182], 1×10^{-12} m/$\sqrt{\text{Hz}}$ (ground) [185]]
Star tracker sensitivity	2×10^{-6} rad/$\sqrt{\text{Hz}}$ (< 0.01 Hz) [2×10^{-6} rad/$\sqrt{\text{Hz}}$ [182]]
Actuator range noise	 2×10^{-6} N 2×10^{-17} N/$\sqrt{\text{Hz}}$ (> 0.1 Hz) [$\sim 5 \times 10^{-6}$ N, $\sim 5 \times 10^{-15}$ N/$\sqrt{\text{Hz}}$ [176]]
Coupling between satellite and test mass	5×10^{-7} /s^2 [4×10^{-7} /s^2 [140]]

7.3 Conclusion

The observation frequency of the ground-based gravitational wave observatory, such as aLIGO, is limited between $\sim$ 10 Hz and a few kHz. The lower frequency limit is mainly determined by the seismic motion. Some observational targets below 10 Hz are predicted. One target is the coalescence of the intermediate-mass black holes with masses in the range between $\sim 10^3\ M_\odot$ and $\sim 10^6\ M_\odot$. The intermediate-mass black holes typically emit the gravitational waves in the frequency range between $\sim 10^{-3}$ Hz and $\sim$ 1 Hz. The coalescence of the intermediate-mass black holes is considered to be a candidate of the origin of the super massive black hole that has been discovered at the galactic center. Another target is the early Universe. The quantum fluctuation is considered to cause the gravitational waves in the wide frequency range, for example, between $\sim 10^{-17}$ Hz and $\sim 10^4$ Hz. Therefore, some space gravitational wave observatories are proposed to avoid the seismic motion.

DECIGO and B-DECIGO are the planned Fabry–Pérot type interferometric space gravitational wave antennas to observe the gravitational waves between 0.1 Hz and 10 Hz. The design sensitivity of DECIGO is better than $10^{-23}\ /\sqrt{\text{Hz}}$ so that the stochastic gravitational wave background generated by the quantum fluctuation in the early Universe could be observed. These space antennas have two unique features: the precise interferometer control system including the Fabry–Pérot cavity and drag-free satellite, and the dual-pass differential Fabry–Pérot interferometer.

The Fabry–Pérot cavity is necessary to achieve high shot-noise-limited sensitivity. The drag-free satellite is also necessary to isolate the test masses from the extra-satellite noise sources. Although these two techniques have been demonstrated independently, there was a concern about the simultaneous operation of them, especially in terms of control method. Thus, we numerically modeled the full control system of DECIGO and B-DECIGO. The model is named the full DECIGO interferometer model. This numerical model reveals that the interferometer control and drag-free control can be engaged at the same time by separating the degrees of freedom controlled by the control system; one mirror in the satellite is used as the reference of the drag-free control and the other mirror is used for the interferometer control and the local control. Using the model, we also considered the detailed requirement including control design for DECIGO and B-DECIGO. As a result, we found a solution of interferometer control with target strain sensitivity of DECIGO, which is $10^{-23}\ /\sqrt{\text{Hz}}$, and more than one-day stability. If we achieve the sensitivity of $10^{-23}\ /\sqrt{\text{Hz}}$ at 0.1 Hz, some features at the early Universe can be tested, for example the phase transition at the electroweak scale [113] and the cosmic strings [114].

The dual-pass differential Fabry–Pérot interferometer is a totally new interferometer configuration. We formulated the dual-pass differential Fabry–Pérot interferometer and found that absolute length adjustment is needed to obtain all interferometer signals. For the demonstration, the ground-based dual-pass differential Fabry–Pérot interferometer was constructed. In the actual experi-

ment performed in the ground-base laboratory with the 0.55-m-long dual-pass Fabry–Pérot cavities, we succeeded in operating the dual-pass differential Fabry–Pérot interferometer and confirmed that adjustment of the absolute arm length reduced the cavity detuning as expected with our formulation. This leads to the reduction of the laser intensity noise coupling. These results indicate that the behavior of the dual-pass differential Fabry–Pérot interferometer is correctly understood. In future, the constructed interferometer can be expanded for the experimental demonstration of the full control scheme, which we developed with the full DECIGO interferometer model.

We conclude that the sensing and control scheme of the interferometer in Fabry–Pérot type interferometric space gravitational wave antenna, especially DECIGO and B-DECIGO, has been demonstrated theoretically and experimentally. We hope that this work provides an essential basis for opening the window of gravitational wave physics and astronomy in the decihertz band.

7.4 Future prospect

In this section, we describe the future prospect towards the actual DECIGO and B-DECIGO observation and further expansion of gravitational wave physics and astronomy. Specifically, further investigation of interferometer simulation, construction of ground-based DECIGO and B-DECIGO prototype, and space demonstration are shown.

7.4.1 Further investigation of interferometer simulation

In the simulation expressed in this thesis, the orbital motion is incorporated as a typical external force noise. However, the actual behavior of the orbital motion varies depending on the orbital parameters, such as semi-major orbital axis, orbital inclination, longitude of the ascending node, launch date, and so on. For more realistic simulation, orbital simulation should be combined with the interferometer simulation.

Moreover, though we showed one solution to achieve shot noise limited sensitivity of DECIGO and B-DECIGO, there are other possibilities to achieve the similar sensitivity. For example, interferometer configuration could be changed to the interferometer with two laser sources in one satellite while the configuration requires new research and development. If it is confirmed in future that the new interferometer configuration can achieve the shot noise limited sensitivity, we need to perform a trade-off study between the scheme studied in this thesis and the newly developed configuration.

7.4.2 Construction of ground-based DECIGO and B-DECIGO prototype

The dual-pass differential Fabry–Pérot interferometer experiment constructed in this work can be expanded into the future small-scale ground-base prototype of DECIGO and B-DECIGO. The prototype will have the following two features:

the same control topology including interferometer of sensors and actuators and soft suspension systems. The latter is necessary to mimic the situation of space. About the control topology, the alignment sensing system will be implemented in addition to the main dual-pass differential Fabry–Pérot interferometer demonstrated in this thesis. Since the alignment sensing method was demonstrated in the previous work [133], just an implementation is necessary. About the soft suspension system, we will use torsion pendulums. The conceptual design has been done as shown in Appendix D. By using the prototype, the control scheme discussed in this thesis can be experimentally demonstrated. After the principal demonstration, the integrated test with the actual components such as test mass actuators, local sensors, thrusters and so on, should be performed. This integration test can also be performed with the modification of the prototype.

7.4.3 Space demonstration

Towards DECIGO and B-DECIGO, even small scale demonstration in space, if any, is very beneficial. The implementation of the control scheme discussed in this thesis including the interferometer characterization leads to an essential milestone for DECIGO and B-DECIGO. Another thing which would be tested in space is noise characterization. Using the measured data in space , the accuracy of the performance estimation in this thesis can be improved. In addition, it is important to demonstrate the end-to-end test of the gravitational wave observation, i.e. initial alignment, detector operation, data transfer from the satellite to the Earth, and data analysis.

Appendix A

Axion dark matter search with the Fabry–Pérot cavity

The Fabry–Pérot cavity is a very precise measurement instrument which is used even to detect gravitational waves. In addition to the gravitational wave observation, there are many applications of precision measurements, for example, axion dark matter search. Here, we explain the new approach for the axion dark matter search with interferometric gravitational wave detectors. This work is reported in K. Nagano *et al.* [155]. In this chapter, the natural unit $\hbar = c = 1$ is used.

Axion dark matter and its probe technique

The axion is a pseudo-scalar field which is originally proposed a half-century ago by Roberto Daniele Peccei and Helen Rhoda Quinn to solve the strong Charge-conjugation Parity problem in quantum chromodynamics physics, known as "quantum chromodynamics axion" [202]. Recently, high energy physics, e.g. string theory, also predicts manifold of axion-like particles from the compactification of extra dimensions [203–206]. Typically, the axion is considered to have a light mass $m \ll 1$ eV. Also, it behaves like non-relativistic fluid in the current universe because of its oscillatory feature. Therefore, from cosmological point of view, the axion or axion-like particle is considered to be a candidate of dark matter. Hereafter, they are jointly called "axion".

In general prediction of high energy physics, the axion has a weak but finite coupling to gauge bosons, such as photons. This feature allows us to search for axion dark matter with optical techniques. Conventionally, many experiments and observations have tried to detect axions under the magnetic field background, where axions are converted to photons (and vise versa) [207–213]. For example, in the solar axion observation such as CERN Axion Solar Telescope (CAST) [214, 215], the axion that is generated in the Sun is converted to X-ray with magnets and then the axion could be observed by the X-ray detector. Another example is the observation of the axion generated in the supernova such as SN1987A [216]. The axion generated in SN1987A is considered to be converted to gamma ray by the galactic magnetic field. Thus the axion could be observed

with the gamma-ray observation. Note that the result of the axion observation using SN1987A depends on the model of the galactic magnetic field. Although the various observations explained above were performed, no characteristic signal of axion dark matter has been detected and a new method to search for axion dark matter is needed.

Lately, a number of new approaches to search for axion dark matter using optical cavity have been proposed [217–220]. These proposals do not need a strong magnet which could be a noise source (or make an experiment expensive), while they utilize phase velocity variation between two circular-polarized lights caused by axion dark matter [221–225]. Inspired by these experimental proposals, we propose a new scheme to search for axion dark matter by using a Fabry–Pérot cavity, especially the arm cavity of the interferometric gravitational wave detectors.

Phase velocity modulation caused by axion dark matter

In this section, how the dispersion relations of two circular-polarized lights are modified in the axion background field. The axion-photon coupling constant, $g_{a\gamma}$, which is the characteristic parameter of axion's coupling to photons is denoted as Chern-Simons interaction

$$\frac{g_{a\gamma}}{4} a(t) F_{\mu\nu}\tilde{F}^{\mu\nu} = g_{a\gamma}\dot{a}(t)\epsilon_{ijk}A_i\partial_j A_k + (\text{total derivative}), \tag{A.1}$$

where $a(t)$ is the value of the axion field, the dot is the time derivative, ϵ_{ijk} is the three-dimentional Levi-Civita tensor, and A_μ is the vector potential obtained from a curl of the electromagnetic field strength tensor. The electromagnetic field strength tensor is defined as $F_{\mu\nu} \equiv \partial_\mu A_\nu - \partial_\nu A_\mu$. The Hodge dual of $F_{\mu\nu}$ is defined as $\tilde{F}^{\mu\nu} \equiv \epsilon^{\mu\nu\rho\sigma}F_{\rho\sigma}/2$, where $\epsilon^{\mu\nu\rho\sigma}$ is the four-dimentional Levi-Civita tensor. Here, cosmic expansion is ignored and the Coulomb gauge, $\partial_i A_i = 0$ and the temporal gauge, $A_0 = 0$ are adopted. By the Fourier transformation of A_i, they are decomposed to the two circular-polarized photons,

$$A_i(t,\boldsymbol{x}) = \sum_{\lambda=\mathrm{L,R}} \int \frac{\mathrm{d}^3k}{(2\pi)^3} A_\lambda(t,\boldsymbol{k})\, e_i^\lambda(\hat{\boldsymbol{k}})\, e^{i\boldsymbol{k}\cdot\boldsymbol{x}} \ , \tag{A.2}$$

where $\boldsymbol{k}$ is the vector of the wave number ($k \equiv |\boldsymbol{k}|$), and the circular-polarization vectors meet

$$e_i^\lambda(\hat{\boldsymbol{k}}) = e_i^{\lambda *}(-\hat{\boldsymbol{k}}),\ e_i^\lambda(\hat{\boldsymbol{k}})e_i^{\lambda' *}(\hat{\boldsymbol{k}}) = \delta^{\lambda\lambda'},\ i\epsilon_{ijm}k_j e_m^{\mathrm{L/R}}(\hat{\boldsymbol{k}}) = \pm k e_i^{\mathrm{L/R}}(\hat{\boldsymbol{k}}). \tag{A.3}$$

Here the indices of L and R mean the left- and right-handed circular lights, respectively. The upper and lower signs of the double sign in equation (A.3) correspond to the left- and right-handed circular lights, respectively. Hereafter, the same notation for the double sign is used as equation (A.3). The equation of motion for electromagnetic field, $\ddot{A}_{\mathrm{L/R}} + \omega_{\mathrm{L/R}}^2 A_{\mathrm{L/R}} = 0$, needs the modification of the dispersion relation because of the axion field,

$$\omega_{\mathrm{L/R}}^2 = k^2\left(1 \mp g_{a\gamma}\dot{a}/k\right), \tag{A.4}$$

where $\omega_{\mathrm{L/R}}$ is the angular frequency of the left- and right-handed polarized light. Equation (A.4) also modifies the phase velocity of the two circular polarized lights,

$$c_{\mathrm{L/R}}^2 = 1 \mp \frac{g_{\mathrm{a}\gamma}\dot{a}}{k} \ . \tag{A.5}$$

Notice that, since axion dark matter is non-relativistic, its momentum is ignored. The field of the axion dark matter is written as

$$a(t) = a_0 \cos[mt + \delta_\tau(t)], \tag{A.6}$$

where m is the axion mass which corresponds to the oscillation frequency, $f = m/(2\pi) \simeq 2.4$ Hz $(m/10^{-14}$ eV), and $\delta_\tau(t)$ is a phase factor of the axion oscillation. The phase factor, $\delta_\tau(t)$, can be considered to be constant within the time scale of the coherent axion oscillation, $\tau = 2\pi/(mv_{\mathrm{a}}^2)$, where v_{a} is the velocity of the axion dark matter. Plugging the local dark matter velocity, $\sim 10^{-3}$, we obtain

$$\tau \sim 1 \left(\frac{10^{-16} \text{ eV}}{m}\right) \text{ years.} \tag{A.7}$$

According to equations (A.6) and (A.5), the phase velocity of the left- and right-handed light is written as

$$c_{\mathrm{L/R}}(t) \simeq 1 \pm \delta c(t) \equiv 1 \pm \delta c_0 \sin[mt + \delta_\tau(t)], \tag{A.8}$$

where $\delta c_0 \ll 1$ is assumed and

$$\delta c_0 \equiv \frac{g_{\mathrm{a}\gamma} a_0 m}{2k} \simeq 1.3 \times 10^{-24} \left(\frac{\lambda}{1550 \text{ nm}}\right) \left(\frac{g_{\mathrm{a}\gamma}}{10^{-12} \text{ GeV}^{-1}}\right). \tag{A.9}$$

Here the present energy density value of axion dark matter around the Earth, $\rho_a = a_0^2 m^2/2 \simeq 0.3$ GeV/cm^3 is used. By measuring the phase velocity modulation, i.e. δc_0, we can search for axion dark matter.

Axion search with a Fabry–Pérot cavity

Figure A.1 shows the schematic of the experiment with a Fabry–Pérot cavity that we propose. The cavity is kept on resonance with Pound–Drever–Hall technique [129] and increases the phase velocity difference, δc, as explained later. The linearly-polarized laser with the wavelength of λ is injected. Here, p-polarized incident laser can be considered without loosing generality. The cavity is composed of the input and output mirrors with amplitude reflectivities and transmissivities of (r_1, t_1) and (r_2, t_2). Hereafter, the axion is regarded as oscillating coherently while the laser circulating in the cavity interacts with axion dark matter unless otherwise mentioned. In other words, $\delta_\tau(t)$ is treated as a constant. This is valid for the light axion mass range where $\tau > 4\pi L\sqrt{r_1 r_2}/(1 - r_1 r_2)$.

The signal of axion dark matter is detected as polarization modulation since it is generated by the phase velocity modulation of the circular polarized lights. The modulation is detected in the detection ports (a) and (b) using polarizing

optics. Specifically, interference between p-polarized light (incident light) and s-polarized light (generated by axion dark matter) which are mixed by the half-wave plate (in port (a)) or non-ideal birefringence of the input mirror (in port (b)) is detected. Note that detection ports (a) and (b) can be installed without changing the rest part of the interferometer.

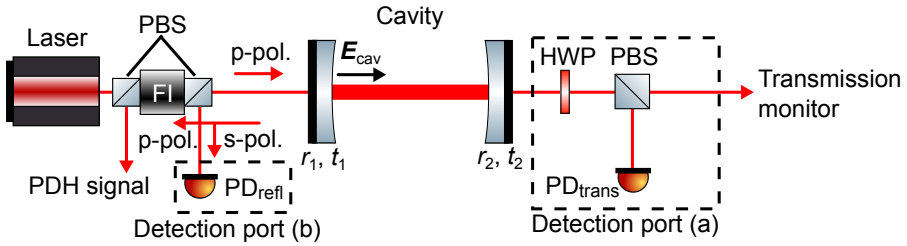

Figure A.1: Schematic of the experimental setup for axion dark matter search with a Fabry–Pérot cavity [155]. FI is the Faraday isolator, PBS is the polarizing beam splitter, HWP is the half wave plate, and PD is the photodetector. The detection instrument for Pound–Drever–Hall method is not shown.

Here, the way to enhance, δc, is explained. The incident light with p-polarization is given by

$$\boldsymbol{E}_{\rm in}(t) = \boldsymbol{E}^{\rm p}(t) = E_0 e^{ikt} \begin{pmatrix} \boldsymbol{e}^{\rm L} & \boldsymbol{e}^{\rm R} \end{pmatrix} \frac{1}{\sqrt{2}} \begin{pmatrix} 1 \\ 1 \end{pmatrix}, \tag{A.10}$$

where $\boldsymbol{E}^{\rm p}(t)$ is the vector of the electric field of the p-polarized laser, $\boldsymbol{e}^{\rm L}$ and $\boldsymbol{e}^{\rm R}$ are basis vectors of left- and right-handed lights, respectively. In the axion background field, the vector of the electric field in the cavity in front of the front mirror is written as

$$\boldsymbol{E}_{\rm cav}(t) = t_1 E_0 e^{ikt} \begin{pmatrix} \boldsymbol{e}^{\rm L} & \boldsymbol{e}^{\rm R} \end{pmatrix} \left[\sum_{n=1}^{\infty} A_n(t) \right] \frac{1}{\sqrt{2}} \begin{pmatrix} 1 \\ 1 \end{pmatrix}, \tag{A.11}$$

$$\begin{cases} A_{n+1}(t) \equiv A_n(t) R_1 T[t - 2L(n-1)] R_2 T[t - 2L(n-1/2)] (n \geq 1) \\ A_1 = 1 \end{cases}, \tag{A.12}$$

where L is the length of the cavity, $T(t)$ is transfer matrix for one-way translation,

$$T(t) \equiv \begin{pmatrix} e^{-i\phi^{\rm L}(t)} & 0 \\ 0 & e^{-i\phi^{\rm R}(t)} \end{pmatrix}, \tag{A.13}$$

$$\phi^{\rm L/R}(t) \equiv kL \mp k \int_{t-L}^{t} \delta c(t') dt', \tag{A.14}$$

and R_i is the matrix for the reflection of the circularly-polarized lights,

$$R_i \equiv \begin{pmatrix} 0 & -r_i \\ -r_i & 0 \end{pmatrix} \quad (i = 1, 2). \tag{A.15}$$

By calculating the summation of equation (A.11), we obtain

$$\boldsymbol{E}_{\rm cav}(t) = \frac{t_1 E_0 e^{ikt}}{1-r_1 r_2} \begin{pmatrix} \boldsymbol{e}^{\rm L} & \boldsymbol{e}^{\rm R} \end{pmatrix} \begin{pmatrix} 1+i\delta\phi(t) & 0 \\ 0 & 1-i\delta\phi(t) \end{pmatrix} \frac{1}{\sqrt{2}} \begin{pmatrix} 1 \\ 1 \end{pmatrix} \tag{A.16}$$

$$= \frac{t_1}{1-r_1 r_2} \left[\boldsymbol{E}^{\rm p}(t) - \delta\phi(t) \boldsymbol{E}^{\rm s}(t) \right], \tag{A.17}$$

where $\boldsymbol{E}^{\rm s}$ is the vector of the electric field of the s-polarized laser

$$\delta\phi(t) \equiv \int_{-\infty}^{\infty} \tilde{\delta c}(m) H_{\rm a}(m) e^{imt} \frac{dm}{2\pi} \quad \left(\tilde{\delta c}(m) = \int_{-\infty}^{\infty} \delta c(t) e^{-imt} dt \right), \tag{A.18}$$

and $H_{\rm a}(m)$ is the cavity response function to the phaser velocity modulation,

$$H_{\rm a}(m) \equiv i \frac{k}{m} \frac{4 r_1 r_2 \sin^2\left(\frac{mL}{2}\right)}{1 - r_1 r_2 e^{-i2mL}} \left(-e^{-imL} \right). \tag{A.19}$$

Here, we assumed that the cavity is on resonance, i.e. $2kL = 2\pi n$ ($n \in \mathbb{N}$). Equation (A.19) shows that the signal of the axion dark matter is enhanced to be proportional to the finesse, i.e. $\pi\sqrt{r_1 r_2}/(1-r_1 r_2)$, and resonates at odd multiple of the free spectral range of the cavity, i.e. $m = \pi(2N-1)/L$ ($N \in \mathbb{N}$).

Sensitivity of gravitational wave detectors to the axion-photon coupling

Here, we estimate the sensitivity of the gravitational wave detectors to the axion dark matter by considering just a quantum noise. Actually, the proposed method is not affected by the displacement noise such as the radiation pressure noise, or the gravitational wave. Thus, it is enough just to consider a shot noise. In each detection port, the electric field received by the photodetector is written as

$$\boldsymbol{E}_{\rm PD}(t) = \left\{ \sqrt{\mathcal{T}_j} \left[\theta_{\rm p} - \delta\phi(t) \right] + \frac{E_{\rm vac}(t)}{E_0} \right\} \boldsymbol{E}^{\rm s}(t) \quad (j = 1, 2), \tag{A.20}$$

$$\sqrt{\mathcal{T}_j} \equiv \frac{t_1 t_j}{1 - r_1 r_2}, \tag{A.21}$$

where $E_{\rm vac}(t)$ is the electric field of vacuum fluctuation, and $\theta_{\rm p}$ ($|\theta_{\rm p}| \ll 1$, $|\theta_{\rm p}| \gg |\delta\phi(t)|$, $|\theta_{\rm p}| \gg |E_{\rm vac}(t)|$) is the mixing angle of the polarization. Here, the second (or higher) order of $|\theta_{\rm p}|$ is ignored. The power received by the photodetector is written as

$$P_{\rm PD}(t) \propto |\boldsymbol{E}_{\rm PD}(t)|^2$$

$$\simeq \theta_{\rm p} \sqrt{\mathcal{T}_j} E_0^2 \left[\theta_{\rm p} \sqrt{\mathcal{T}_j} - 2\sqrt{\mathcal{T}_j} \delta\phi(t) + 2 \frac{E_{\rm vac}(t)}{E_0} \right], \tag{A.22}$$

where we neglect the second order terms of $\delta\phi(t)$ and $E_{\rm vac}(t)$ and their cross term since $|\delta\phi(t)| \ll 1$ and $|E_{\rm vac}(t)| \ll E_0$. We can evaluate the sensitivity by

Table A.1: Sets of parameters of the considered detectors. The incident power, P_0, is enhanced by the power recycling technique for CE-, KAGRA-, and aLIGO-like detectors [21].

Similar detector	L [m]	P_0 [W]	λ [$\times 10^{-9}$ m]	(r_1^2, r_2^2)
DECIGO [54]	10^6	5	515	(0.69, 0.69)
CE [48]	4×10^4	600	1550	(0.9988, 0.999995)
KAGRA [27, 28]	3×10^3	335	1064	(0.996, 0.999995)
aLIGO [22]	4×10^3	2600	1064	(0.986, 0.999995)

comparing the signal term (second term) and noise term (third term) of equation (A.22). The one-sided amplitude spectrum density of shot noise equivalent to $\tilde{\delta c}(m)$ is denoted as,

$$\sqrt{S_{\rm shot}(m)} = \frac{\sqrt{\frac{k}{2P_0}}}{\sqrt{\mathcal{T}_j}|H_{\rm a}(m)|}, \tag{A.23}$$

where $P_0 = kE_0^2/2$ is the incident power. Here, the one-sided spectrum of $E_{\rm vac}(t)$ is unity [115]. Equation (A.23) indicates that, if $r_1 < r_2$, the detection port (b) has better sensitivity than the detection port (a). On the other hand, the detection port (a) is better when $r_1 = r_2$. Equation (A.23) can be translated into the sensitivity to the axion dark matter, i.e. the axion-photon coupling $g_{\rm a\gamma}$, as

$$g_{\rm a\gamma}(m) \simeq 1.5 \times 10^{12}\,{\rm GeV}^{-1} \left(\frac{1550\ {\rm nm}}{\lambda}\right) \times \begin{cases} \sqrt{\frac{S_{\rm shot}(m)}{T_{\rm obs}}} & (T_{\rm obs} \lesssim \tau) \\ \sqrt{\frac{S_{\rm shot}(m)}{\sqrt{T_{\rm obs}\tau}}} & (T_{\rm obs} \gtrsim \tau) \end{cases}, \tag{A.24}$$

where $T_{\rm obs}$ is the measurement time. The sensitivity improvement depends on if $T_{\rm obs}$ is larger than the axion coherent oscillation time, τ, or not [226].

Figure A.2 shows the sensitivities of the gravitational wave detectors to $g_{\rm a\gamma}$ with the method that we propose. Here, we set the experimental parameters similar to the gravitational wave detectors in operation or planned (specifically, DECIGO [54], Cosmic Explorer (CE) [48], KAGRA [27, 28] and aLIGO [22]) as shown in table A.1. We assume $T_{\rm obs} = 1$ year and a lossless cavity, i.e. $r_i^2 + t_i^2 = 1$ $(i = 1, 2)$. For DECIGO-like detector, the detection port (a) is adopted, and for CE-, KAGRA-, and aLIGO-like detectors the detection port (b) is adopted. All detectors overcome the upper limit provided by CAST [214, 215].

We can apply the proposed method to the gravitational wave detectors by installing polarizing optics in detection ports without replacing optics in the main interferometer, e.g. main test masses, and so on. Although it is not so simple to realize the detection port (b) due to the existing apparatuses, such as a signal recycling mirror [135, 227], the axion dark matter signal, in principle, can be obtained from the detection port behind the signal recycling mirror as with the gravitational wave signal readout [228].

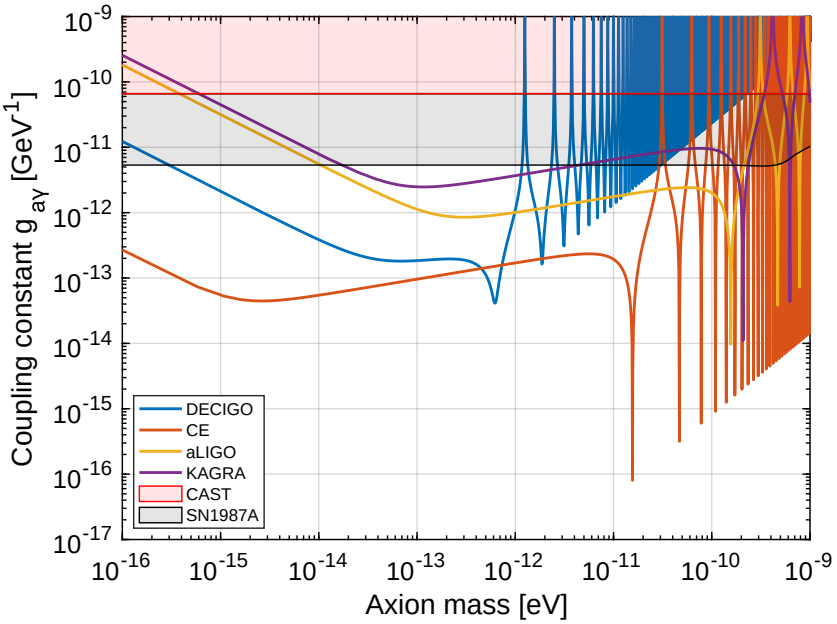

Figure A.2: Sensitivity comparison of the detectors of which parameters are shown in table A.1. The sensitivity in higher mass range is peaky at the axion mass of $m = \pi(2N-1)/L$ ($N \in \mathbb{N}$). The red and gray regions express the current limit set by CAST [214, 215] and the cosmic ray observations of SN1987A [216], respectevely.

Summary

Axion dark matter modulates the phase velocities of the circular polarized lights. The effect in the Fabry-Pérot cavity is modeled and its response is formulated. With this model, we propose a new scheme to search for axion dark matter with the Fabry–Pérot cavity in the arm of gravitational wave detectors. Their potential sensitivity to the axion-photon coupling constant, $g_{a\gamma}$, is evaluated to be so sensitive that the current limit of CAST [214, 215] can be improved with 1 year observation. Remarkably, these sensitivities can be realized by installing the additional polarizing optics without changing the main gravitational wave interferometer.

Appendix B

Power spectral density and feedback control

Here, we review power spectral density and feedback control. In this appendix, only linear system is considered.

Power spectral density

Power spectral density is a measure of the noise/sensitivity of the system in frequency domain. The (single-sided) power spectral density for a random fluctuation, $x(t)$, is defined as

$$S_x(f) \equiv \lim_{T\to\infty} \frac{1}{T} \left\langle x_T^\dagger(f) x_T(f) + x_T(f) x_T^\dagger(f) \right\rangle, \tag{B.1}$$

$$x_T(f) \equiv \int_{-T/2}^{T/2} x(t) e^{-2i\pi f t} dt, \tag{B.2}$$

where $\langle \cdots \rangle$ means the ensemble average. Physically, the power spectral density, $S_x(f)$, means the contribution of $x(t)$ to its variance in a frequency band around f. Sometimes, linear spectral density (or amplitude spectral density) defined as $\sqrt{S_x(f)}$ is useful to consider noise effect.

Here, how to calculate signal-to-noise ratio is shown. We consider the detector that has noise level of the power spectral density $S(f)$ and signal $h(f)$, which is Fourier space representation of $h(t)$. In this setup, the squared signal-to-noise ratio, ρ^2, is estimated by [63],

$$\rho^2 = 4 \int_0^\infty \frac{|h(f)|^2}{S(f)} df \tag{B.3}$$

$$= 4 \int_0^\infty \frac{|\sqrt{f} h(f)|^2}{S(f)} d(\log f). \tag{B.4}$$

The cross spectral density and the magnitude-squared coherence are also introduced here. The cross spectral density and the magnitude-squared coherence are measures of the correlation of the two systems. The (single-sided) cross spectral

density for two random fluctuation, $x(t)$ and $y(t)$, is defined as

$$S_{xy}(f) \equiv \lim_{T\to\infty} \frac{1}{T} \left\langle x_T^\dagger(f) y_T(f) + x_T(f) y_T^\dagger(f) \right\rangle, \tag{B.5}$$

$$x_T(f) \equiv \int_{-T/2}^{T/2} x(t) e^{-2i\pi ft} dt, \quad y_T(f) \equiv \int_{-T/2}^{T/2} y(t) e^{-2i\pi ft} dt. \tag{B.6}$$

The magnitude-squared coherence is defined as

$$C_{xy}^2(f) \equiv \frac{S_{xy}^2(f)}{S_x(f) S_y(f)}. \tag{B.7}$$

Feedback control

Laplace transformation

Feedback control is often considered in frequency domain. The frequency response of the linear system can be easily understood with Laplace transformation. Laplace transformation of time-domain function $f(t)$ is defined as

$$\tilde{f}(s) \equiv \int_0^\infty f(t) e^{-st} dt, \tag{B.8}$$

where $s \equiv i\omega$. In this thesis, tilde of the function in frequency domain is sometimes omitted if there is no confusion.

Transfer function

The frequency response of the linear system is characterized with the transfer function. When the input and output of the system are $\tilde{X}(s)$ and $\tilde{Y}(s)$, respectively, the transfer function, $G(s)$, is defined as

$$G(s) \equiv \frac{\tilde{Y}(s)}{\tilde{X}(s)}. \tag{B.9}$$

The absolute value and angle of the transfer function, i.e. $|G(s)|$ and $\angle G(s)$, are called the gain and phase, respectively. This system is illustrated as shown in figure B.1 which is called a block diagram.

Figure B.1: Block diagram of a single-input single-output system.

For example, let's consider the equation of motion of a mass. The equation of motion in time-domain can be written as

$$m\ddot{x}(t) = F(t), \tag{B.10}$$

where, m is the mass, x is the position of the mass, and F is the force applied to the mass. By performing Laplace transformation, the equation of motion is written as

$$-m\omega^2\tilde{x}(\omega) = \tilde{F}(\omega). \tag{B.11}$$

Here, we use $s = i\omega$. As a result, the transfer function from the force to the position is written as

$$\frac{\tilde{x}(\omega)}{\tilde{F}(\omega)} = \frac{1}{-m\omega^2}. \tag{B.12}$$

This equation indicates that the frequency response of the equation of motion from the force to the position is proportional to ω^{-2} with phase delay of π rad (or 180 deg).

Open loop transfer function

Feedback control is composed of a sensor, filter, and actuator. The block diagram of the feedback controlled system is shown in figure B.2. $H(s)$, $F(s)$, and $A(s)$ are transfer functions of the sensor, filter, and actuator, respectively. In this system, the output of each port is written as

$$\Delta\tilde{x}(s) = \frac{1}{1 + H(s)F(s)A(s)}\tilde{x}_{\mathrm{ext}}(s), \tag{B.13}$$

$$\tilde{y}(s) = \frac{H(s)}{1 + H(s)F(s)A(s)}\tilde{x}_{\mathrm{ext}}(s), \tag{B.14}$$

$$\tilde{z}(s) = \frac{H(s)F(s)}{1 + H(s)F(s)A(s)}\tilde{x}_{\mathrm{ext}}(s). \tag{B.15}$$

Here, we assumed $z_{\mathrm{inj}} = 0$. Sometimes, $\tilde{y}(s)$ and $\tilde{z}(s)$ are called error signal and feedback signal, respectively. The feedback control is characterized with the open loop transfer function defined as $G_{\mathrm{o}}(s) \equiv H(s)F(s)A(s)$ which we can measure by injecting a large signal from the injection port and taking the ratio of $\tilde{z}'(s)$ to $\tilde{z}(s)$ as

$$-\frac{\tilde{z}'(s)}{\tilde{z}(s)} = H(s)F(s)A(s) = G_{\mathrm{o}}(s), \tag{B.16}$$

$$\left(\tilde{z}(s) = \frac{1}{1 + H(s)F(s)A(s)}\tilde{z}_{\mathrm{inj}}(s),\ \tilde{z}'(s) = -\frac{H(s)F(s)A(s)}{1 + H(s)F(s)A(s)}\tilde{z}_{\mathrm{inj}}(s)\right),$$

where $\tilde{z}_{\mathrm{inj}}$ is the injection signal from the injection port shown in figure B.2.

One important feature of the feedback control is the suppression of the external fluctuation. Equation (B.13) shows that, when $|G_{\mathrm{o}}(s)| \gg 1$, the residual motion is suppressed to be $\tilde{x}_0(s) \simeq \tilde{x}_{\mathrm{ext}}(s)/G_{\mathrm{o}}(s)$. On the other hand, when $|G_{\mathrm{o}}(s)| \ll 1$, the external motion is not suppressed, i.e. $\tilde{x}_0(s) \simeq \tilde{x}_{\mathrm{ext}}(s)$. The above discussion about the fluctuation suppression is also valid when we change $\tilde{x}_{\mathrm{ext}}(s)$ and $\tilde{x}_0(s)$ into the linear spectral density.

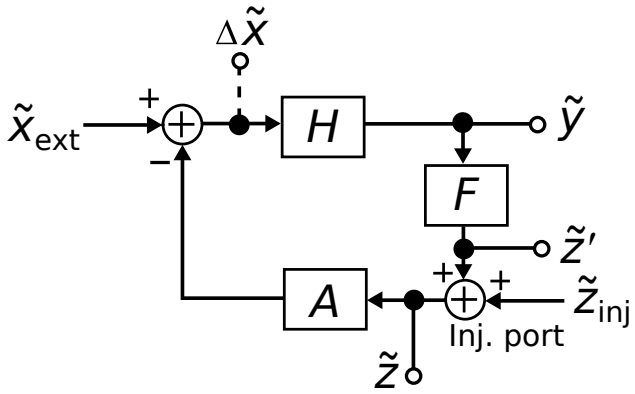

Figure B.2: Block diagram of the feedback control system.

Signal equivalent noise estimation

In the feedback control system, we can estimate the effect of noise equivalent to the signal. For example, if $\tilde{x}(s)$ is the signal, the effect of the measured noise, $\tilde{n}(s)$, injected from the injection port in figure B.2 is estimated as follows: first, we calculate the transfer function from the signal and the noise to the sensing port. If we use error signal, the transfer functions are written as $\frac{y(s)}{x_{\mathrm{ext}}(s)} \equiv G_{\mathrm{s}}(s)$ and $\frac{y(s)}{z_{\mathrm{inj}}(s)} \equiv G_{\mathrm{n}}(s)$. Then, using these transfer functions, the signal equivalent noise is estimated to be

$$\tilde{x}_{\mathrm{n}}(s) = \frac{G_{\mathrm{n}}(s)}{G_{\mathrm{s}}(s)}\tilde{n}(s). \tag{B.17}$$

The discussion in this subsection is also valid for the linear spectral density.

Stability of feedback control

For the stable operation of the system, the feedback control should be stable. The stability of the feedback control can be checked with the open loop transfer function. Although there are several ways to check the stability [229], we focus on the scheme with a Bode plot here. The Bode plot is a plot set of the gain and phase of the open loop transfer functions as shown in figure B.3. The frequency where the gain is unity is called unity gain frequency. Equation (B.13) indicates that, if the open loop transfer function at the unity gain frequency is -1 (gain is 1 and phase is $-\pi$), the residual motion, $\tilde{x}_0(s)$, goes to infinity, i.e. the feedback control is unstable. Thus, the open loop transfer function should be designed to have phase delay less than π at the unity gain frequency. In practice, the phase delay at the unity gain frequency is designed to be less than $5\pi/6$ to obtain the robust system. The phase delay can be checked with the Bode plot intuitively as shown in figure B.3.

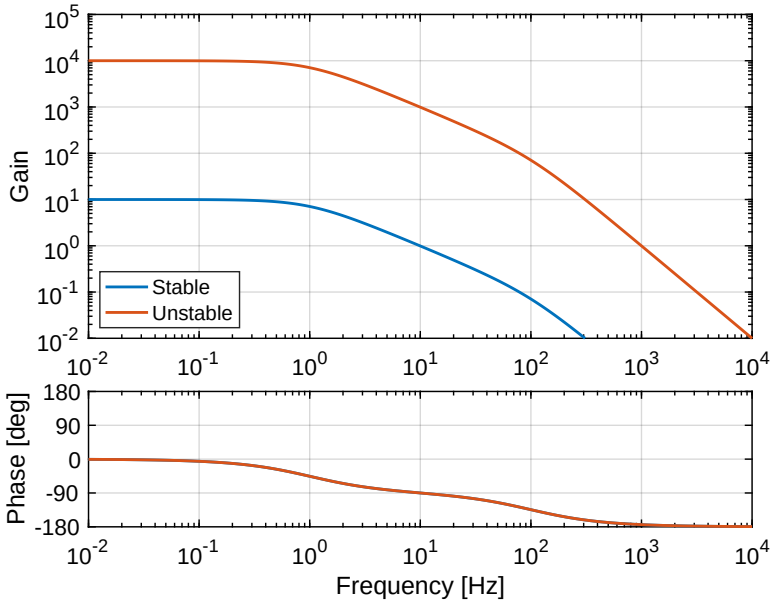

Figure B.3: Example of the Bode plot of open loop transfer functions of stable and unstable feedback control. Phase plots for both cases are overlapped. The unity gain frequencies in the stable and unstable cases are 10 Hz and 1000 Hz, respectively.

Multivariable control system

Up to here, we considered a single-input single-output system. Hereafter, we will expand the above discussion to a multi-input multi-output system. When the inputs and outputs of the system are n- and m-dimensional, respectively, the transfer function can be denotes with $m \times n$ matrix as

$$\tilde{\boldsymbol{Y}}(s) = \boldsymbol{G}(s)\tilde{\boldsymbol{X}}(s), \tag{B.18}$$

where, $\tilde{\boldsymbol{X}}(s)$ and $\tilde{\boldsymbol{Y}}(s)$ are the n-dimensional input column vector and the m-dimensional output column vector, respectively.

The block diagram of the feedback control system with multi variables is represented in figure B.4. In order to control the n-dimensional system, we need the n-dimensional sensors, at least. Here, we consider the n-dimensional system. If we choose the filter matrix as $\boldsymbol{F}(s) = \boldsymbol{A}^{-1}(s)\boldsymbol{G}(s)\boldsymbol{H}^{-1}(s)$ ($\boldsymbol{G}(s) \equiv \mathrm{diag}(G_1(s), ..., G_n(s))$), the open loop transfer function is written as $\boldsymbol{A}(s)\boldsymbol{F}(s)\boldsymbol{H}(s) = \boldsymbol{G}(s)$. In this condition, the n-dimensional system is decomposed into the n feedback loops of the single-input single-output system and the discussion up to the previous section can be applied independently to each loop (for more detailed discussion, see [229, 230]).

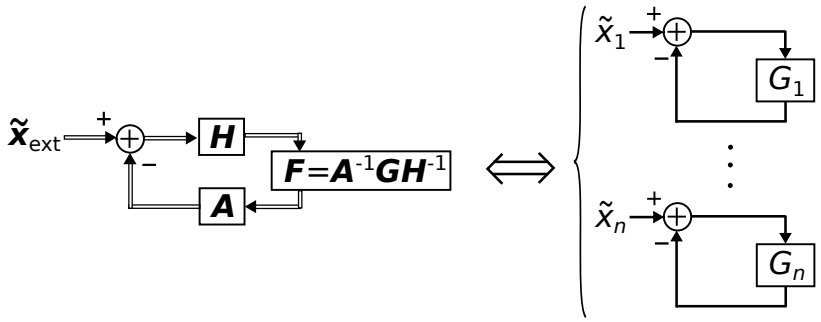

Figure B.4: Block diagram of the multi-input multi-output feedback control system and equivalent set of the single-input single-output feedback control systems. $\tilde{\boldsymbol{x}}_{\rm ext} \equiv (\tilde{x}_1, ..., \tilde{x}_n)^\top$ is an input vector, and $\boldsymbol{H}$, $\boldsymbol{F}$, and $\boldsymbol{A}$ are sensing, filter, and actuation matrices $(n \times n)$, respectively.

Appendix C

Noise sources of laser interferometer

In order to detect gravitational waves, we need to reduce many noises. For example, quantum noise of the laser light, Brownian motion of the mirror, seismic motion, and Newtonian force caused by the density fluctuation of the ground are considered to be major noise sources for the ground based detectors. The latter two can be mitigated in the space detectors. Here, major noise sources are reviewed. In this appendix, we considered one differential Fabry–Pérot interferometer as shown in figure C.1. For simplicity, we assume $|G_{\mathrm{freq}}| \gg 1$ and $|G_x| \ll 1$ in the observation frequency range. In this condition, the gravitational wave signal is obtained at the error signal of the cavity length control loop. Note that the amplitude spectral density of the noise equivalent to the length fluctuation, $x_{\mathrm{noise}}(f)$ $[\mathrm{m}/\sqrt{\mathrm{Hz}}]$, is shown and it can be converted to the amplitude spectral density of the stain equivalent noise, $h_{\mathrm{noise}}(f)$ $[/\sqrt{\mathrm{Hz}}]$, with the relation

$$h_{\mathrm{noise}}(f) = \frac{1}{L} x_{\mathrm{noise}}(f), \tag{C.1}$$

where f is the frequency and we assume that the mirrors are free.

General noises

Quantum noise

Quantum noise is caused by the quantumness of the laser light. Since the laser is intrinsic to the laser interferometers, quantum noise is the most principal noise for the interferometers. Quantum noise can be divided into two parts: shot noise and radiation pressure noise. Shot noise is the sensing noise and radiation pressure noise is the force noise. With the classical measurement, shot noise and

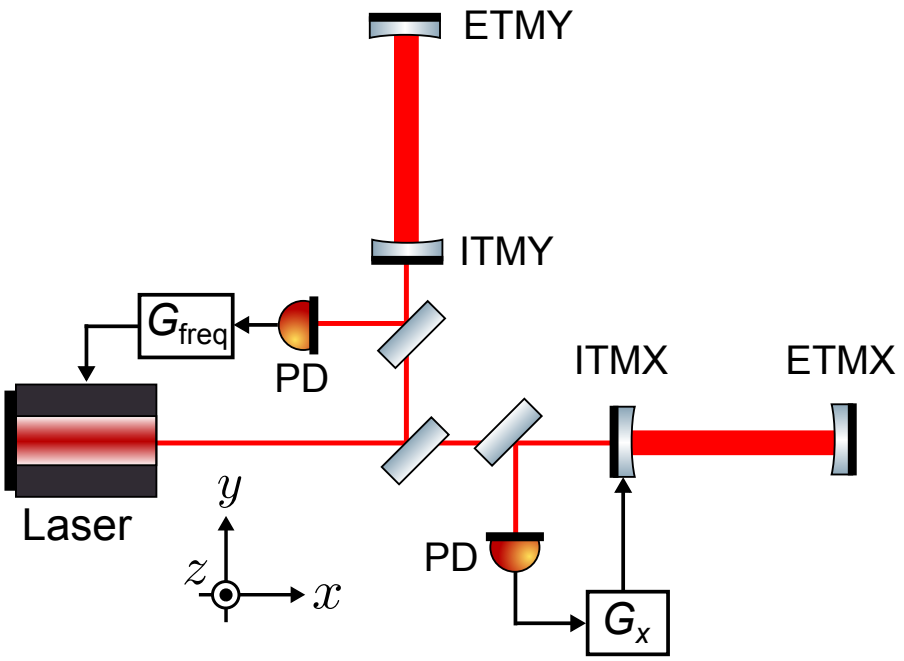

Figure C.1: Considered differential Fabry–Pérot interferometer. The open loop transfer functions of the frequency and the cavity length control loop are G_{freq} and G_x, respectively.

radiation pressure noise can be written as [115]

$$x_{\mathrm{shot}}(f) = \frac{1}{4\mathcal{F}}\sqrt{\frac{\pi\hbar c\lambda}{2P_{\mathrm{inc}}}\left[1+\left(\frac{f}{\nu_{1/2}}\right)^2\right]}, \tag{C.2}$$

$$x_{\mathrm{rad}}(f) = \frac{16\mathcal{F}}{\pi(2\pi f)^2 m_{\mathrm{TM}}}\sqrt{\frac{2\pi\hbar P_{\mathrm{inc}}}{c\lambda}\frac{1}{1+\left(\frac{f}{\nu_{1/2}}\right)^2}}, \tag{C.3}$$

where m_{TM} is the mass of the mirror, $\hbar$ is the reduced Planck constant, and λ is the wavelength of the laser. According to equaitons (C.2) and (C.3), shot noise and radiation pressure noise inversely depend on $\sqrt{P_{\mathrm{inc}}}$. This means that, by changing the input power, the root mean square of the shot noise and radiation pressure noise, i.e. the power spectral density of the quantum noise, cannot be less than,

$$x_{\mathrm{SQL}}(f) = \sqrt{\frac{4\hbar}{m_{\mathrm{TM}}(2\pi f)^2}}. \tag{C.4}$$

$x_{\mathrm{SQL}}(f)$ is called standard quantum limit and means the lower limit of the quantum noise in the classical measurement. To beat the standard quantum limit, quantum measurement, so called quantum-non-demolition measurement, is necessary [115,116,231]. The quantum-non-demolition measurement is the measurement scheme using the quantum correlation of the system to reduce the quantum noise.

Thermal noise

Since mirrors (its supporting system, if any) have finite temperature, they fluctuate due to their Brownian motion. This motion is the source of the thermal noise. The main thermal noise source is the mirror substrate and coating (and its suspension system).

The thermal noise is estimated with the fluctuation-dissipation theorem. According to the fluctuation-dissipation theorem, the fluctuation force is given by [117]

$$F_{\mathrm{th}}(f) = \sqrt{4k_{\mathrm{B}}TR(f)}, \tag{C.5}$$

where k_{B} is the Boltzmann constant, T is the temperature of the mirror, and $R(f)$ is the mechanical resistance. By applying the mechanical transfer function from the force at the dissipation point to the longitudinal motion of the mirror, the thermal noise is obtained.

The thermal noises of the mirror substrate and coating are classified into two types according to the dissipation mechanism: Brownian noise and thermoelastic noise. The substrate brownian noise, $x_{\mathrm{SB}}(f)$, and thermoelastic noise, $x_{\mathrm{STE}}(f)$ are represented as [118–120]

$$x_{\mathrm{SB}}(f) = \sqrt{\frac{16k_{\mathrm{B}}T}{(2\pi f)}\frac{1-{\sigma_{\mathrm{s}}}^2}{\sqrt{\pi}E_{\mathrm{s}}w_0}\phi_{\mathrm{s}}\left(1+\frac{2}{\sqrt{\pi}}\frac{1-2\sigma_{\mathrm{s}}}{1-\sigma_{\mathrm{s}}}\frac{\phi_{\mathrm{c}}}{\phi_{\mathrm{s}}}\frac{d_{\mathrm{c}}}{w_0}\right)}, \tag{C.6}$$

$$x_{\mathrm{STE}}(f) = \sqrt{\frac{64}{\sqrt{\pi}}\frac{{\alpha_{\mathrm{s}}}^2\left(1+\sigma_{\mathrm{s}}\right)^2 k_{\mathrm{B}}T^2}{{\rho_{\mathrm{s}}}^2{C_{\mathrm{s}}}^2}\frac{k_{\mathrm{s}}}{{w_0}^3}\frac{1}{(2\pi f)^2}}, \tag{C.7}$$

where σ_{s} is the Poisson's ratio of the substrate, E_{s} is Young's modulus of the substrate, w_0 is the laser radius on the mirror, $\phi_{\mathrm{s(c)}}$ is the loss angle of the substrate (coating), and d_{c} is the depth of the coating, α_{s} is the coefficient of thermal expansion of the substrate, ρ_{s} is the mass density of the substrate, C_{s} is the heat capacity of the substrate, and k_{s} is the thermal conductivity.

Coating brownian noise, $x_{\mathrm{CB}}(f)$, and thermoelastic noise, $x_{\mathrm{CTE}}(f)$, are given by [122]

$$x_{\mathrm{CB}}(f) = \sqrt{\frac{16k_{\mathrm{B}}T}{(2\pi f)}\frac{d_{\mathrm{c}}}{\pi{w_0}^2}\phi_{\mathrm{c}}\frac{E_{\mathrm{c}}\left(1+\sigma_{\mathrm{s}}\right)^2\left(1-2\sigma_{\mathrm{s}}\right)^2+{E_{\mathrm{s}}}^2\left(1+\sigma_{\mathrm{c}}\right)^2\left(1-2\sigma_{\mathrm{c}}\right)}{{E_{\mathrm{s}}}^2E_{\mathrm{c}}\left(1-{\sigma_{\mathrm{c}}}^2\right)}}, \tag{C.8}$$

$$x_{\mathrm{CTE}}(f) = \sqrt{\frac{64k_{\mathrm{B}}T\left(1+\sigma_{\mathrm{s}}\right)^2{\alpha_{\mathrm{s}}}^2\kappa_{\mathrm{s}}}{\sqrt{\pi}\rho_{\mathrm{s}}C_{\mathrm{s}}{w_0}^3(2\pi f)^2}}, \tag{C.9}$$

where E_{c} is Young's modulus of the coating, σ_{c} is the Poisson's ratio of the coating, and κ_{s} ($\equiv k_{\mathrm{s}}/\rho_{\mathrm{s}}/C_{\mathrm{s}}$) is the thermal diffusion coefficient of the substrate.

In addition to the mirror thermal noise, the residual gas could introduce non-negligible thermal noise, so called residual gas thermal noise, even if the mirror

is placed in the vacuum system. The residual gas thermal noise is given by

$$x_{\rm gas}(f) = \frac{1}{m_{\rm TM}(2\pi f)^2}\sqrt{16\frac{S_{\rm mir}P_{\rm gas}T}{C_{\rm gas}}\sqrt{\frac{3m_{\rm gas}k_{\rm B}}{T_{\rm gas}}}}, \tag{C.10}$$

where $S_{\rm mir}$ is the cross section of the mirror along the longitudinal axis, $P_{\rm gas}$ is the pressure around the mirror, $C_{\rm gas}$ is the shape factor which is almost unity for the cylinder-shaped mirror, $m_{\rm gas}$ is the mass of the residual gas molecular, and $T_{\rm gas}$ is the temperature of the residual gas.

Seismic noise

The ground always fluctuates even when the earthquake does not occur. The surface ground motion in quiet site above 10 Hz is approximately written as [232]

$$x'_{\rm seis}(f) = 1\times10^{-10}\left(\frac{10\ {\rm Hz}}{f}\right)^2\ \left[{\rm m}/\sqrt{\rm Hz}\right]. \tag{C.11}$$

Note that the actual seismic motion is different from place to place. This seismic motion is much larger than the expected fluctuation caused by the gravitational wave. Thus, we need to isolate the test mass from the ground motion. One way to do this is to float the mirror in space. Another way which is done in the ground based detectors is suspending the mirror by pendulums. When the mirror is suspended by the n-fold pendulum which has the resonant frequency of $f_{\rm pend}$ and the damping value $\gamma_{\rm pend}$, the transfer function from the seismic motion to the mirror motion is approximately denoted as

$$T_{\rm pend}(f) \simeq \left[\frac{f_{\rm pend}^2}{-f^2+f_{\rm pend}^2+if\gamma_{\rm pend}/(2\pi)}\right]^n. \tag{C.12}$$

As a result, the cavity length fluctuation with seismic motion is written as

$$x_{\rm seis}(f) = x'_{\rm seis}|T_{\rm pend}(f)|. \tag{C.13}$$

For example, when we use 9-fold pendulums with $f_{\rm pend} = 2.5$ Hz and $\gamma_{\rm pend} = 2\pi$ rad·Hz, the seismic noise above 10 Hz is approximately written as

$$x_{\rm seis}(f) = 1.5\times10^{-21}\left(\frac{10\ {\rm Hz}}{f}\right)^{20}\ \left[{\rm m}/\sqrt{\rm Hz}\right]. \tag{C.14}$$

Newtonian noise

When the environmental Newtonian gravity field around the test mass fluctuates, the gravitational force jiggles the test mass even without gravitational wave. This force fluctuation is a source of noise called Newtonian noise. The environmental Newtonian gravity can vary due to the mass density fluctuation of the ground,

atmosphere, water, space craft, planets, and so on. For example, the seismic Newtonian noise is modeled as [55]

$$x_{\mathrm{SNN}}(f) = 2 \times 10^{-20} \begin{cases} \left(\frac{10\ \mathrm{Hz}}{f}\right)^2 & (3\ \mathrm{Hz} \lesssim f \lesssim 10\ \mathrm{Hz}) \\ \left(\frac{10\ \mathrm{Hz}}{f}\right)^4 & (10\ \mathrm{Hz} \lesssim f \lesssim 30\ \mathrm{Hz}) \end{cases} \left[\mathrm{m}/\sqrt{\mathrm{Hz}}\right], \quad \text{(C.15)}$$

while modeling most types of the Newtonian noises is still on going.

Interferometer noises

Frequency noise

As explained in Section 3.3.5, the laser frequency fluctuation is a noise source. Considering the frequency stabilization with y-arm, the frequency noise is denoted as

$$x_{\mathrm{freq}} = \frac{1}{1 + G_{\mathrm{freq}}} \frac{L}{\nu} \delta f, \quad \text{(C.16)}$$

where δf is the laser frequency fluctuation of the laser source before the stabilization.

It is worth noting the frequency noise can be subtracted with the frequency fluctuation measured in the frequency control loop. In the frequency control loop, the dominant signal is frequency fluctuation. Thus, if we know the transfer function from the laser frequency fluctuation to the gravitational wave signal, the frequency noise can be subtracted as follows:

$$h(t) = h_{\mathrm{gw}}(t) + n_{\mathrm{freq}}(t) - T'_{\mathrm{freq}} \delta f(t) + n_{\mathrm{others}}(t), \quad \text{(C.17)}$$

$$n_{\mathrm{freq}}(t) = T_{\mathrm{freq}} \delta f(t) \quad \text{(C.18)}$$

where $h(t)$ is the measured signal equivalent to the gravitational wave strain, $h_{\mathrm{gw}}(t)$ is the gravitational wave signal, $n_{\mathrm{freq}}(t)$ is the noise due to the laser frequency fluctuation, T is the transfer function from the laser frequency fluctuation to the measured signal equivalent to the gravitational wave strain, $\delta f(t)$ is the laser frequency fluctuation, and $n_{\mathrm{others}}(t)$ is the noise other than the frequency noise. If we can estimate T'_{freq} ideally, i.e. $T_{\mathrm{freq}} = T'_{\mathrm{freq}}$, the frequency noise can be totally subtracted. However, when there is an error, ΔT_{freq}, in the estimation of T'_{freq}, i.e. $T'_{\mathrm{freq}} = T_{\mathrm{freq}} + \Delta T_{\mathrm{freq}}$, the frequency noise after the subtraction becomes $\Delta T_{\mathrm{freq}} \delta f(t)$. For example, when the precision of the transfer function measurement is 10%, i.e. $\Delta T_{\mathrm{freq}} = 0.1 T_{\mathrm{freq}}$, the frequency noise is subtracted by a factor of 10, i.e. the frequency noise after the subtraction becomes $0.1 n_{\mathrm{freq}}(t)$.

Intensity coupled noise

As explained in Section 3.3.5, the laser intensity fluctuation is a noise source through the cavity detuning. According to equation (3.70), the intensity coupled

noise is written as

$$x_{\mathrm{int}} = \sqrt{(\Delta x_{\mathrm{rms}})^2 + (\Delta y_{\mathrm{rms}})^2}\frac{\delta P}{P_{\mathrm{inc}}}, \tag{C.19}$$

where $\Delta x(y)_{\mathrm{rms}}$ is the root-mean-square of the cavity detuning of $x(y)$-arm, δP is the intensity fluctuation, and P_{inc} is the incident power to the first beamsplitter.

Classical radiation pressure noise

In addition to the intensity coupled noise, the intensity fluctuation of the laser light causes the classical radiation pressure noise due to the radiation pressure fluctuation applied to the test masses. The classical radiation pressure noise is denoted as

$$x_{\mathrm{CRP}} = \frac{8\mathcal{F}\delta P}{\pi c m_{\mathrm{TM}}\omega^2}, \tag{C.20}$$

where m is the mass of each test mass, and $\mathcal{F}$ is the finesse of the cavity.

It is worth noting that the classical radiation pressure noise can totally be subtracted with the measured intensity fluctuation. For example, if the cavity is critically coupled, the intensity fluctuation can be measured at the transmission port of the cavity.

Phase noise after the beam splitter

In the differential Fabry–Pérot interferometer, the phase noise between the first beamsplitter and the input test mass affect the interferometer sensitivity to the gravitational waves since the phase noise corresponds to the differential frequency fluctuation. The phase noise is expressed as

$$x_{\mathrm{phase}} = \frac{2x_{\mathrm{diff}}\omega}{c}L, \tag{C.21}$$

where x_{diff} is the displacement fluctuation between the first beam splitter and each test mass.

Test mass actuator noise

The actuator on the test mass is essential part if we actuate the test mass to keep the cavity resonance.[*1] The force noises of the actuators are not distinguished from the gravitational wave. The force noise is written as

$$x_{\mathrm{act}} = \frac{2\delta f_{\mathrm{act}}}{m_{\mathrm{TM}}\omega^2}, \tag{C.22}$$

where δf_{act} is the force fluctuation of the actuator.

[*1] In some interferometer configuration where the cavity resonance is kept with the frequency control, the test mass actuator is not necessary.

Noise sources in space detectors

Here, we show the specific noise sources in space detectors, especially in DECIGO and B-DECIGO. Specifically, force noises applied to the test masses and satellites are explained. Although the other noises, such as local sensor noises and so on, are noise sources as discussed in Chapter 5, their effects vary depending on the detector configuration. Thus they are not discussed here.

Force noise applied on test masses

Gravitational force

The gravitational force is a noise source especially in the geocentric orbit. The main source is the higher order mode of the eccentricity of the Earth gravity. Currently, the effect of the higher order modes up to the 2190th order is considered [233]. However, in high orbital radius, such as the geostationary orbit, the gravitational force noise can be negligible.

Electro-magnetic force

One of the electro-magnetic force noise is caused by the magnetic fluctuation. Since there is magnetic field in the satellite, the test mass is magnetized. Thus, the magnetic field fluctuation couples the test mass motion. The magnetic fluctuation noise is written as [140]

$$x_{\rm mag} = \frac{2\chi_{\rm TM} V_{\rm TM}}{m_{\rm TM}\mu_0\omega^2} B'\delta B, \tag{C.23}$$

where $\chi_{\rm TM}$ is magnetic susceptibility of the test mass, $V_{\rm TM}$ is the volume of the test mass, μ_0 is magnetic permeability of vacuum, B' is a local gradient of the magnetic field, and δB is the fluctuation of the local magnetic field. In DECIGO and B-DECIGO case, the largest magnetic field is caused by the satellite, e.g. $B' = 3\times10^{-8}$ T/m and $\delta B = 1\times10^{-9}$ T/$\sqrt{\rm Hz}$ [140]. Here we assume shielding by a factor of 100 around the test mass.

The Lorentz force also makes a force noise applied to the test mass [140]. The largest noise of Lorentz force is caused by the velocity fluctuation coupled with the static magnetic field of the Earth [234] (in the geocentric orbit) or in the inter-planet [140] (in the heliocentric orbit). However, the Lorentz force effect can be negligible.

Thermal radiation

When there is a temperature fluctuation, the thermal radiation makes a force noise on the test mass. As explained in Section 5.5, the thermal radiation noise is denoted as [140]

$$x_{\rm Trad} = \epsilon_{\rm Trad}\frac{8\sigma_{\rm SB}S_{\rm TM}T^3\delta T}{m_{\rm TM}c\omega^2}. \tag{C.24}$$

Cosmic ray collision

Cosmic rays occasionally collides with the test mass. The momentum transfer from a cosmic ray makes a force noise on the test mass. However, the effect can be negligible [140].

Force noise of applied on satellites

Solar radiation pressure

The major force noise applied on the satellite is caused by the solar radiation pressure fluctuation. As explained in Section 5.5, the solar radiation pressure fluctuation is estimated to be [140, 142]

$$\delta F_{\mathrm{Srad}} = \frac{\delta W_{\mathrm{Sun}} S_{\mathrm{SAT}}}{c} = 3 \times 10^{-9} \left(\frac{0.1 \text{ Hz}}{f} \right)^{\frac{1}{3}} \text{ N}/\sqrt{\text{Hz}}. \tag{C.25}$$

Gravitational force

The gravity force is also applied to the satellite in the same way as the test mass. However, the gravity force can be negligible in the observation frequency band.

Other practical noises

In addition to the principal noises explained above, there are many practical noise sources. Since these practical noise sources vary from detector to detector, they should be considered in each case. The possible noise sources are scattered light, electrical circuit noise and so on.

Appendix D

Suspension system for ground-based DECIGO prototype

Before the launch of DECIGO and B-DECIGO, the ground-based prototype should be constructed. However, it is impossible to make a free mass on the Earth. One way to mimic the situation in space on the Earth is using a soft suspension system. Here, we show the suspension design study for the future prototype construction.

Suspension design

The schematic of the suspension system is shown in figure D.1. The ground base prototype consists of the cavity mirror suspension and the optical bench suspension. In the design, we aimed to obtain almost all the considered eigenmodes of the suspensions to be $\lesssim 1$ Hz.

The cavity mirror is suspended from the frame with a double pendulum. The intermediate beam stage is made of copper and its dimensions are $10 \times 2 \times 2$ cm^3. The mass of the beam is ~ 360 g. As the suspension wire, the 10-cm-long and 120-μm-diameter tungsten wire is utilized. From one edge of the intermediate beam, the mirror holder made of aluminum is suspended with two tungsten wires. The cavity mirror is attached to the mirror holder. The mirror holder weighs ~ 220 g and the two tungsten suspension wires are 40 μm in diameter. The mirror holder is designed to be a plus shape to obtain a large moment of inertia for pitch and roll rotations. On the other edge of the intermediate beam, the counter weight is attached to compensate the mass of the mirror holder.

The optical bench that mimics the satellite is suspended with a single piano wire. The piano wire has the diameter of 150 μm and the length of 25 cm. In order to decrease the resonant frequency of the vertical motion, a coil spring of a spring constant of $\sim 10^3$ N/m is inserted between the frame of the suspension system of the optical bench and the suspension wire. The optical bench is made of aluminum plate of which thickness is 1.5 cm and diameter is 30 cm. On the optical bench, some optics are fixed and the total mass of the optical bench and the optics is estimated to be ~ 15 kg.

We estimate the resonant frequencies of the cavity mirror suspension and the

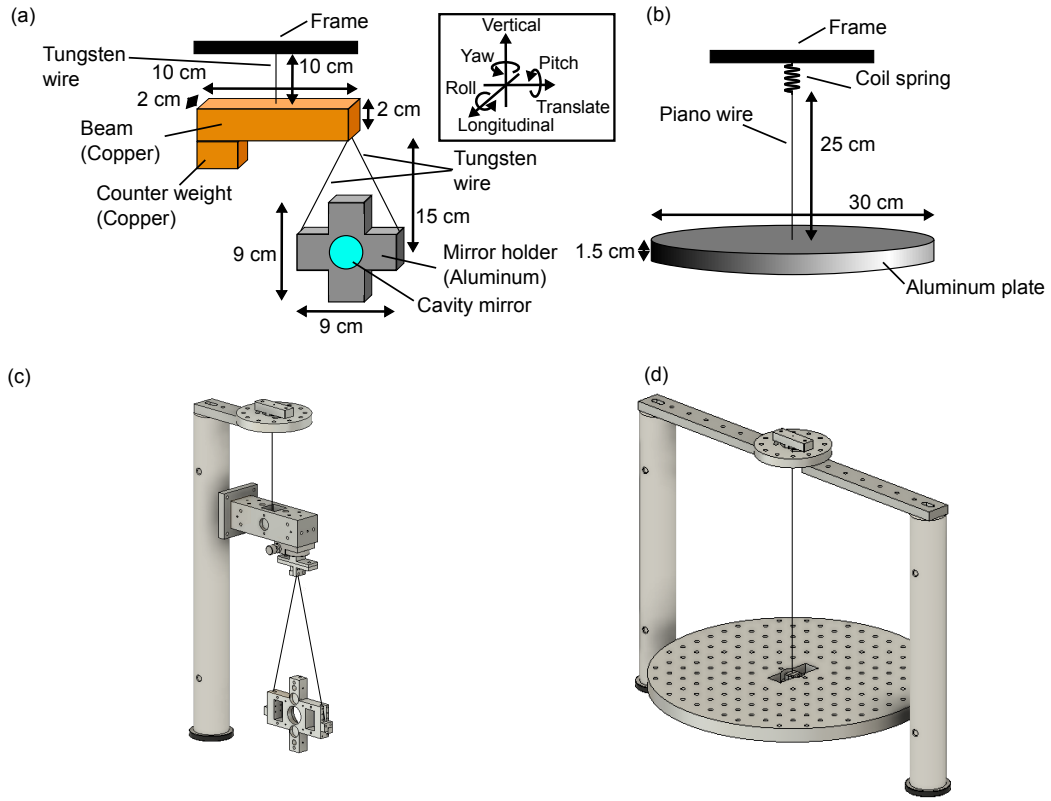

Figure D.1: Schematic (upper panel) and CAD image (lower panel) of the suspension system of the prototype. The left panel shows the cavity mirror system and the right panel shows the optical bench system. Notice that the coil spring is not shown in the CAD image of the optical bench.

optical bench suspension in terms of the center of the mirror and aluminum plate, respectively. We use a toolkit of three-dimensional rigid-body modeling coded in Mathematica® [235, 236]. The results are shown in table D.1. As a result, almost all the resonant frequencies are designed to be lower than ~ 1 Hz. Since the roll mode of the mirror is less important due to the symmetry of the mirror, its resonant frequency is designed to be relatively high. The roll resonant frequency can be reduced using a spring system.

Table D.1: Resonant frequencies for each mode of two suspension types. Mode name: (L, T, V, R, P, Y) indicates (Longitudinal, Translation, Vertical, Roll, Pitch, Yaw). Since the roll mode of the mirror is less important due to the symmetry of the mirror, its resonant frequency is designed relatively higher.

Suspension type	L	T	V	R	P	Y
Cavity Mirror	0.02 Hz	1 Hz	0.5 Hz	(30 Hz)	0.05 Hz	0.1 Hz
Optical Bench	1 Hz	1 Hz	1.4 Hz	0.09 Hz	0.09 Hz	0.01 Hz

Local sensors and actuators

For the ground-based prototype of DECIGO and B-DECIGO, not only the mechanical part, i.e. the suspension, but also the sensor/actuator for control is necessary. As the sensor and actuator of the first prototype, the reflective photosensor and the coil-magnet actuator are planned to be used, respectively. The photosensor imitates the local sensor and satellite attitude sensor in DECIGO and B-DECIGO. The coil-magnet actuator imitates the test mass actuator and the thruster of the satellite. Although the sensor and the actuator are not the same as those of DECIGO and B-DECIGO, we can demonstrate the control scheme that is developed in this thesis.

Appendix E

Electronic circuit

Here, we show the electronic circuit diagram used in the experiment in Chapter 6.

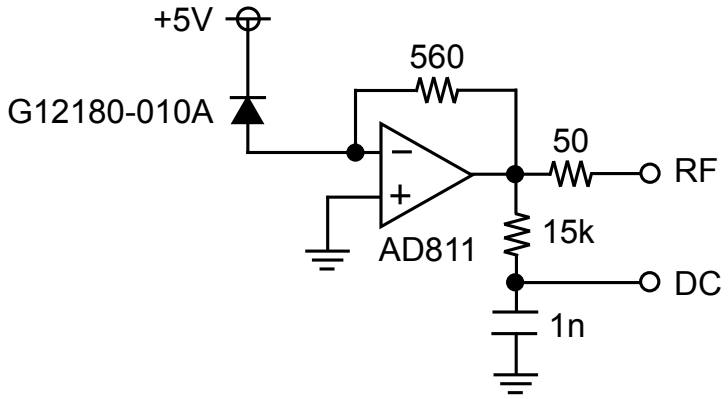

Figure E.1: Circuit diagram of the photodetectors.

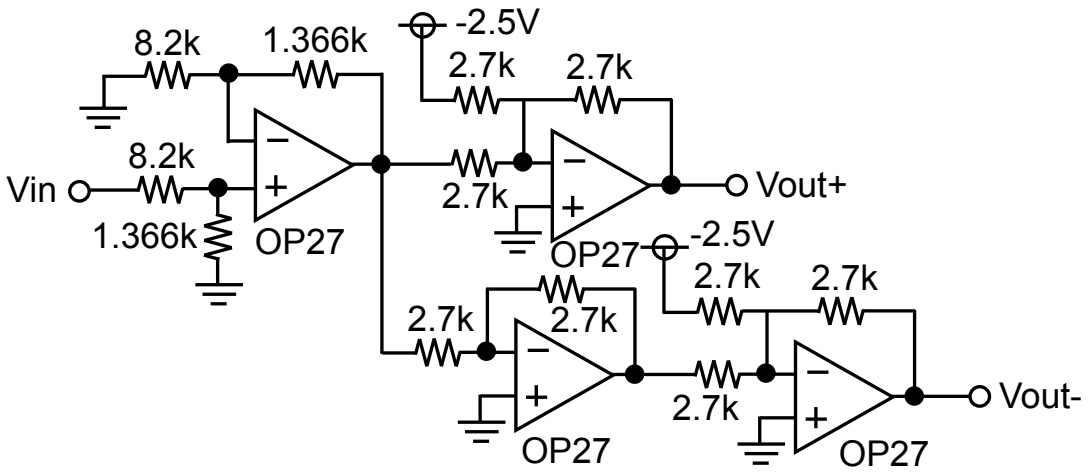

Figure E.2: Circuit diagram of the driver for the laser frequency (Koheras BASIK X15).

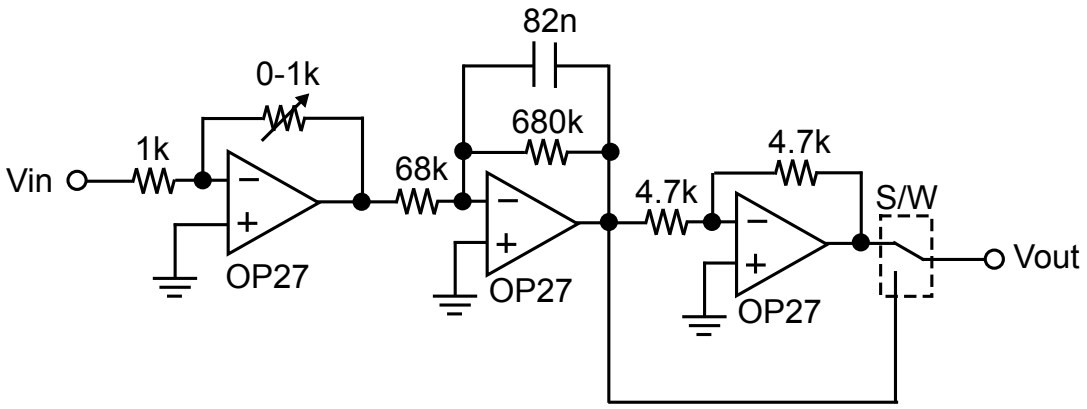

Figure E.3: Circuit diagram of the filter of a length loop.

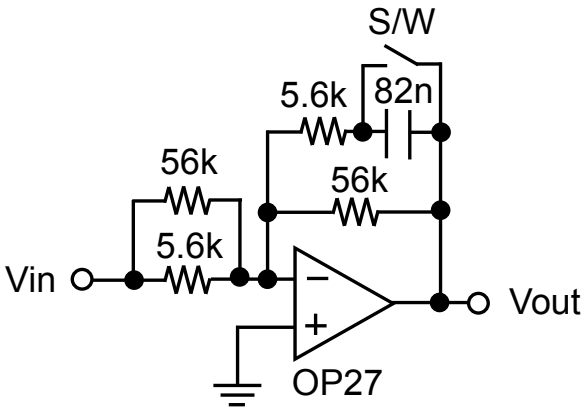

Figure E.4: Circuit diagram of the filter of a DC boost.

Appendix F

Hermite–Gaussian mode of the electric field

Here, we show the brief review of the spacial mode of the laser beam and the laser alignment sensing. For comprehensive explanation, see [127]. In this appendix, we consider electric and magnetic field in vacuum.

Hermite–Gaussian mode

From Maxwell equations, the electric field propagating along z-axis, $\boldsymbol{E}$, meets the following equation,

$$\nabla \times (\nabla \times \boldsymbol{E}) + \mu_0 \epsilon_0 \frac{\partial^2}{\partial t^2} \boldsymbol{E} = 0. \tag{F.1}$$

This equation is denoted as

$$\nabla^2 \boldsymbol{E} - \mu_0 \epsilon_0 \boldsymbol{E} = -\nabla \left(\frac{1}{\epsilon_0} \boldsymbol{E} \cdot \nabla \epsilon_0 \right). \tag{F.2}$$

Since $\nabla \epsilon_0 = 0$ and the electric field can be denoted as $\boldsymbol{E} = \boldsymbol{E}_0 e^{i(\omega_1 t - 2\pi z/\lambda)}$, we can rewrite the equation as

$$\nabla^2 \boldsymbol{E} + \omega_1 \mu_0 \epsilon_0 \boldsymbol{E} = 0. \tag{F.3}$$

When we set the origin of the spacial coordinates at the beam waist, i.e. the position where the beam radius becomes smallest, the general solution of equation (F.3) is given by

$$\begin{aligned} E_{l,m}(x,y,z,t) =& E_0 \frac{w_0}{w(z)} H_l \left(\frac{\sqrt{2}x}{w(z)} \right) H_m \left(\frac{\sqrt{2}y}{w(z)} \right) e^{i\omega_1 t} \\ & \times \exp \left[-\frac{x^2+y^2}{w^2(z)} - i\frac{\pi(x^2+y^2)}{R(z)} - i\frac{2\pi z}{\lambda} + i(l+m+1)\eta \right], \end{aligned} \tag{F.4}$$

where $H_l(\cdots)$ is the l-th Hermite polynomial, w_0 and $w(z) = w_0\sqrt{1+\frac{z^2}{z_0^2}}$ are the spot sizes of the laser beam at waist ($z = 0$) and z, $z_0 = \frac{\pi w_0^2}{\lambda}$ is Rayleigh length, $R(z) = z\left(1+\frac{z_0^2}{z^2}\right)$ is the radius of curvature of the electric field at z, and $\eta = \tan^{-1}\left(\frac{z}{z_0}\right)$ is Gouy phase at z. Here, we assume rotationally symmetric beam along z-axis. The electric field modes represented in equation (F.4) are called Hermite–Gausssian modes. Hermite–Gaussian mode with $l = m = 0$ is called the fundamental mode. In addition, Hermite–Gaussian modes with $(l = 1, m = 0)$ and $(l = 0, m = 1)$ are sometimes called 10 and 01 modes, respectively.

Beam translation and tilt

In laser interferometric gravitational wave detectors, the fundamental mode laser is mainly used. The small translation and tilt of the beam can be expressed by the combination of the fundamental mode and 10/01 modes [130]. The translated $(x \to x+\delta x)$ and tilted $((x,z) \to (x' = x\cos\delta\theta - z\sin\delta\theta, z' = x\sin\delta\theta + z\cos\delta\theta))$ beams are given by

$$\text{Translation } (\delta x):\ E_{0,0}(x+\delta x, y, z, t) \simeq E_{0,0}(x, y, z, t) + \frac{\delta x}{w_0} E_{1,0}(x, y, z, t), \tag{F.5}$$

$$\text{Tilt } (\delta\theta):\ E_{0,0}(x', y, z', t) \simeq E_{0,0}(x, y, z, t) + i\frac{\delta\theta}{\theta_{\mathrm{D}}} E_{1,0}(x, y, z, t), \tag{F.6}$$

where $\theta_{\mathrm{D}} = \frac{\lambda}{\pi w_0}$ $(w_0 \gg \lambda)$ is the beam divergence angle. Here, we assume $|\delta x| \ll w_0$ and $|\delta\theta| \ll \theta_{\mathrm{D}}$.

We can measure the translation and tilt of the laser beam by measuring the amplitude of the 10/01 modes. There are some schemes to measure the 10/01 modes. One example for Fabry–Pérot cavity alignment is the wavefront sensing method [133,134] where the 10/01 modes generated in the cavity due to the cavity axis translation/tilt are measured by taking the beatnote with the fundamental mode reflected by the input mirror. Note that the optical axis of the Fabry–Pérot cavity is determined by the centers of curvature of the cavity mirrors.

Appendix G

Antenna pattern

Here, we show the brief review of the antenna pattern of interferometric gravitational wave detectors, i.e. angular response. Especially, we compared the pattern of the L-shaped detector and the pattern of the triangular-shaped detector.

The output signal of the gravitational wave detectors are given by [63]

$$h(\hat{\boldsymbol{n}}, t) = \sum_A F_A(\hat{\boldsymbol{n}}, t) h_A(t), \tag{G.1}$$

where $\hat{\boldsymbol{n}}$ is the unit vector along the traveling gravitational wave direction, $F^A(\hat{\boldsymbol{n}}, t)$ is the antenna pattern function of the gravitational wave detector, and $h_A(t)$ is the gravitational wave form. Here, A indicates the existing mode of the gravitational wave in the theory. As discussed in Chapter 2, in general relativity the allowed modes are two tensor modes, i.e. plus and cross modes ($A = +, \times$). In some modified gravity theories, two vector modes and two scalar modes are allowed in addition to the tensor modes. The two additional vector modes are called vector-x and vector-y modes ($A = x, y$). Also, the two additional scalar modes are called breathing and longitudinal modes ($A = \mathrm{b}, \mathrm{l}$). The gravitational waves of each mode are given by [84]

$$\text{Plus mode: } h_+(t) e^+_{ij}(\hat{\boldsymbol{n}}), \quad e^+_{ij}(\hat{\boldsymbol{n}}) \equiv \hat{\boldsymbol{e}}'_x \otimes \hat{\boldsymbol{e}}'_x - \hat{\boldsymbol{e}}'_y \otimes \hat{\boldsymbol{e}}'_y, \tag{G.2}$$

$$\text{Cross mode: } h_\times(t) e^\times_{ij}(\hat{\boldsymbol{n}}), \quad e^\times_{ij}(\hat{\boldsymbol{n}}) \equiv \hat{\boldsymbol{e}}'_x \otimes \hat{\boldsymbol{e}}'_y + \hat{\boldsymbol{e}}'_y \otimes \hat{\boldsymbol{e}}'_x, \tag{G.3}$$

$$\text{Vector-}x\text{ mode: } h_x(t) e^x_{ij}(\hat{\boldsymbol{n}}), \quad e^x_{ij}(\hat{\boldsymbol{n}}) \equiv \hat{\boldsymbol{e}}'_x \otimes \hat{\boldsymbol{e}}'_z + \hat{\boldsymbol{e}}'_z \otimes \hat{\boldsymbol{e}}'_x, \tag{G.4}$$

$$\text{Vector-}y\text{ mode: } h_y(t) e^y_{ij}(\hat{\boldsymbol{n}}), \quad e^y_{ij}(\hat{\boldsymbol{n}}) \equiv \hat{\boldsymbol{e}}'_y \otimes \hat{\boldsymbol{e}}'_z + \hat{\boldsymbol{e}}'_z \otimes \hat{\boldsymbol{e}}'_y, \tag{G.5}$$

$$\text{Breathing mode: } h_\mathrm{b}(t) e^\mathrm{b}_{ij}(\hat{\boldsymbol{n}}), \quad e^\mathrm{b}_{ij}(\hat{\boldsymbol{n}}) \equiv \hat{\boldsymbol{e}}'_x \otimes \hat{\boldsymbol{e}}'_x + \hat{\boldsymbol{e}}'_y \otimes \hat{\boldsymbol{e}}'_y, \tag{G.6}$$

$$\text{Longitudinal mode: } h_\mathrm{l}(t) e^\mathrm{l}_{ij}(\hat{\boldsymbol{n}}), \quad e^\mathrm{l}_{ij}(\hat{\boldsymbol{n}}) \equiv \sqrt{2}\hat{\boldsymbol{e}}'_z \otimes \hat{\boldsymbol{e}}'_z, \tag{G.7}$$

where the set of the three unit vector, $\{\hat{\boldsymbol{e}}'_x, \hat{\boldsymbol{e}}'_y, \hat{\boldsymbol{e}}'_z\}$ ($\hat{\boldsymbol{e}}'_x = (\cos\theta\cos\phi, \cos\theta\sin\phi, -\sin\theta)$, $\hat{\boldsymbol{e}}'_y = (-\sin\phi, \cos\phi, 0)$, $\hat{\boldsymbol{e}}'_z = (\sin\theta\cos\phi, \sin\theta\sin\phi, \cos\theta) = -\hat{\boldsymbol{n}}$), and the coordinates of the traveling gravitational wave are defined in figure G.1-(a). Here, $\otimes$ is the Kronecker product. The detection of the non-tensor mode is an important milestone for the test of the modified gravity theory.

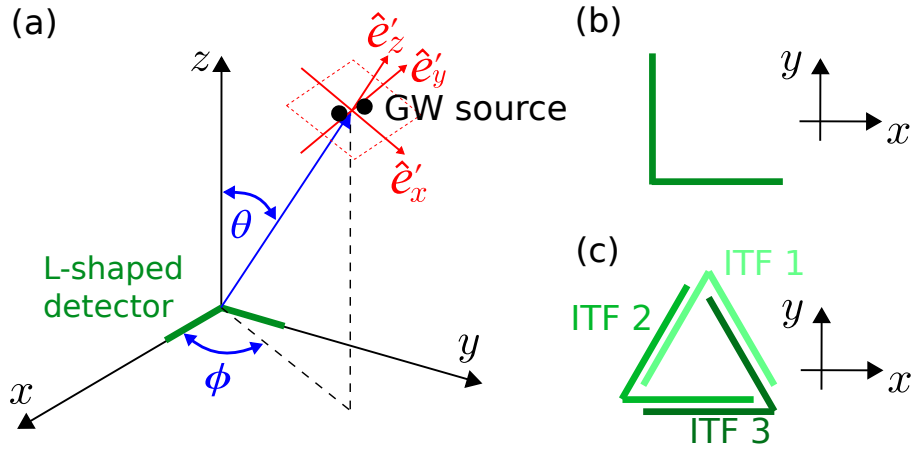

Figure G.1: Some definitions for antenna pattern calculation: (a) the coordinates (b) L-shaped detector orientation, and (c) triangular-shaped detector orientation.

The antenna pattern function is calculated as

$$F_A(\hat{\boldsymbol{n}}) = D^{ij} e^A_{ij}(\hat{\boldsymbol{n}}), \tag{G.8}$$

$$D^{ij} \equiv \frac{1}{2}(\hat{\boldsymbol{u}} \otimes \hat{\boldsymbol{u}} - \hat{\boldsymbol{v}} \otimes \hat{\boldsymbol{v}}), \tag{G.9}$$

where D^{ij} is the detector tensor, and $\hat{\boldsymbol{u}}$ and $\hat{\boldsymbol{v}}$ are the unit vectors along the arm direction of the detector. Here and hereafter, we ignore the time dependence of the antenna pattern function. When we set the coordinate as shown in figure G.1, $\hat{\boldsymbol{u}}$ and $\hat{\boldsymbol{v}}$ are given by

$$\text{L-shaped: } \hat{\boldsymbol{u}} = (1,0,0),\ \hat{\boldsymbol{v}} = (0,1,0), \tag{G.10}$$

$$\text{Triangular-shaped (1): } \hat{\boldsymbol{u}} = \left(-\cos\left(\frac{\pi}{3}\right), -\sin\left(\frac{\pi}{3}\right), 0\right),$$

$$\hat{\boldsymbol{v}} = \left(\cos\left(\frac{\pi}{3}\right), -\sin\left(\frac{\pi}{3}\right), 0\right), \tag{G.11}$$

$$\text{Triangular-shaped (2): } \hat{\boldsymbol{u}} = (1,0,0),\ \hat{\boldsymbol{v}} = \left(\cos\left(\frac{\pi}{3}\right), \sin\left(\frac{\pi}{3}\right), 0\right), \tag{G.12}$$

$$\text{Triangular-shaped (3): } \hat{\boldsymbol{u}} = \left(-\cos\left(\frac{\pi}{3}\right), \sin\left(\frac{\pi}{3}\right), 0\right),\ \hat{\boldsymbol{v}} = (-1,0,0). \tag{G.13}$$

Consequently, the antenna pattern functions for the L-shaped detector are calculated as

$$\begin{aligned}
F_+^{(\mathrm{L})} &= \frac{1}{2}(1+\cos^2\theta)\cos 2\phi,\ F_\times^{(\mathrm{L})} = -\cos\theta \sin 2\phi, \\
F_x^{(\mathrm{L})} &= \sin\theta\cos\theta\cos 2\phi,\ F_y^{(\mathrm{L})} = -\sin\theta\sin 2\phi, \\
F_{\mathrm{b}}^{(\mathrm{L})} &= -\frac{1}{2}\sin^2\theta\cos 2\phi,\ F_{\mathrm{l}}^{(\mathrm{L})} = \frac{1}{\sqrt{2}}\sin^2\theta\cos 2\phi.
\end{aligned} \tag{G.14}$$

The antenna pattern functions for the triangular shape detectors are calculated

as

$$\text{ITF1:}\begin{cases} F_{+}^{(\mathrm{T1})} = \frac{\sqrt{3}}{4}(1+\cos^2\theta)\sin 2\phi, \;\; F_{\times}^{(\mathrm{T1})} = -\frac{\sqrt{3}}{2}\cos\theta\cos 2\phi, \\ F_{x}^{(\mathrm{T1})} = \frac{\sqrt{3}}{2}\sin\theta\cos\theta\sin 2\phi, \;\; F_{y}^{(\mathrm{T1})} = \frac{\sqrt{3}}{2}\sin\theta\cos 2\phi, \\ F_{\mathrm{b}}^{(\mathrm{T1})} = -\frac{\sqrt{3}}{4}\sin^2\theta\sin 2\phi, \;\; F_{\mathrm{l}}^{(\mathrm{T1})} = \frac{1}{2}\sqrt{\frac{3}{2}}\sin^2\theta\cos 2\phi. \end{cases} \tag{G.15}$$

$$\text{ITF2:}\begin{cases} F_{+}^{(\mathrm{T2})} = \frac{1}{8}(1+\cos^2\theta)(3\cos 2\phi - \sqrt{3}\sin 2\phi), \\ F_{\times}^{(\mathrm{T2})} = -\frac{1}{4}\cos\theta(\sqrt{3}\cos 2\phi + 3\sin 2\phi), \\ F_{x}^{(\mathrm{T2})} = \frac{1}{4}\sin\theta\cos\theta(3\cos 2\phi - \sqrt{3}\sin 2\phi), \\ F_{y}^{(\mathrm{T2})} = -\frac{1}{4}\sin\theta(\sqrt{3}\cos 2\phi + 3\sin 2\phi), \\ F_{\mathrm{b}}^{(\mathrm{T2})} = -\frac{1}{8}\sin^2\theta(3\cos 2\phi - \sqrt{3}\sin 2\phi), \\ F_{\mathrm{l}}^{(\mathrm{T2})} = \frac{1}{4\sqrt{2}}\sin^2\theta(3\cos 2\phi - \sqrt{3}\sin 2\phi). \end{cases} \tag{G.16}$$

$$\text{ITF3:}\begin{cases} F_{+}^{(\mathrm{T3})} = -\frac{1}{8}(1+\cos^2\theta)(3\cos 2\phi + \sqrt{3}\sin 2\phi), \\ F_{\times}^{(\mathrm{T3})} = -\frac{1}{4}\cos\theta(\sqrt{3}\cos 2\phi - 3\sin 2\phi), \\ F_{x}^{(\mathrm{T3})} = -\frac{1}{4}\sin\theta\cos\theta(3\cos 2\phi + \sqrt{3}\sin 2\phi), \\ F_{y}^{(\mathrm{T3})} = -\frac{1}{4}\sin\theta(\sqrt{3}\cos 2\phi - 3\sin 2\phi), \\ F_{\mathrm{b}}^{(\mathrm{T3})} = \frac{1}{8}\sin^2\theta(3\cos 2\phi + \sqrt{3}\sin 2\phi), \\ F_{\mathrm{l}}^{(\mathrm{T3})} = -\frac{1}{4\sqrt{2}}\sin^2\theta(3\cos 2\phi + \sqrt{3}\sin 2\phi). \end{cases} \tag{G.17}$$

The results are illustrated in figures G.2-G.5.

For non-tensor mode detection, we need the interferometers which have independent antenna patterns. If we utilize a triangular-shaped geometry, there is one pair of the interferometer. Therefore, when the number of satellites is three, the triangular geometry is better than the L-shaped geometry for the test of the modified gravity theory even though the single L-shaped interferometer has a good response to each mode.

It is worth noting two things. First, although there are three interferometers in the triangular geometry, we can obtain only two independent signals. This is because the third interferometer signal can be constructed ideally from the signals of the other two interferometers. However, the third interferometer is still very useful for constructing null-streams, which are time-series data where the gravitational wave signals are cancelled. The null-stream is useful for the test of general relativity [61]. The second is the time dependence of the antenna pattern. Although it is not ignored in the above discussion, we can obtain more information from the observation data considering the time dependence of the antenna pattern. This is because, when the antenna pattern varies during the observation, the detector can be regarded as multiple detectors effectively. Especially in DECIGO and B-DECIGO, the observation duration of a single event lasts more than one month. Thus, time dependence of the antenna pattern is useful.

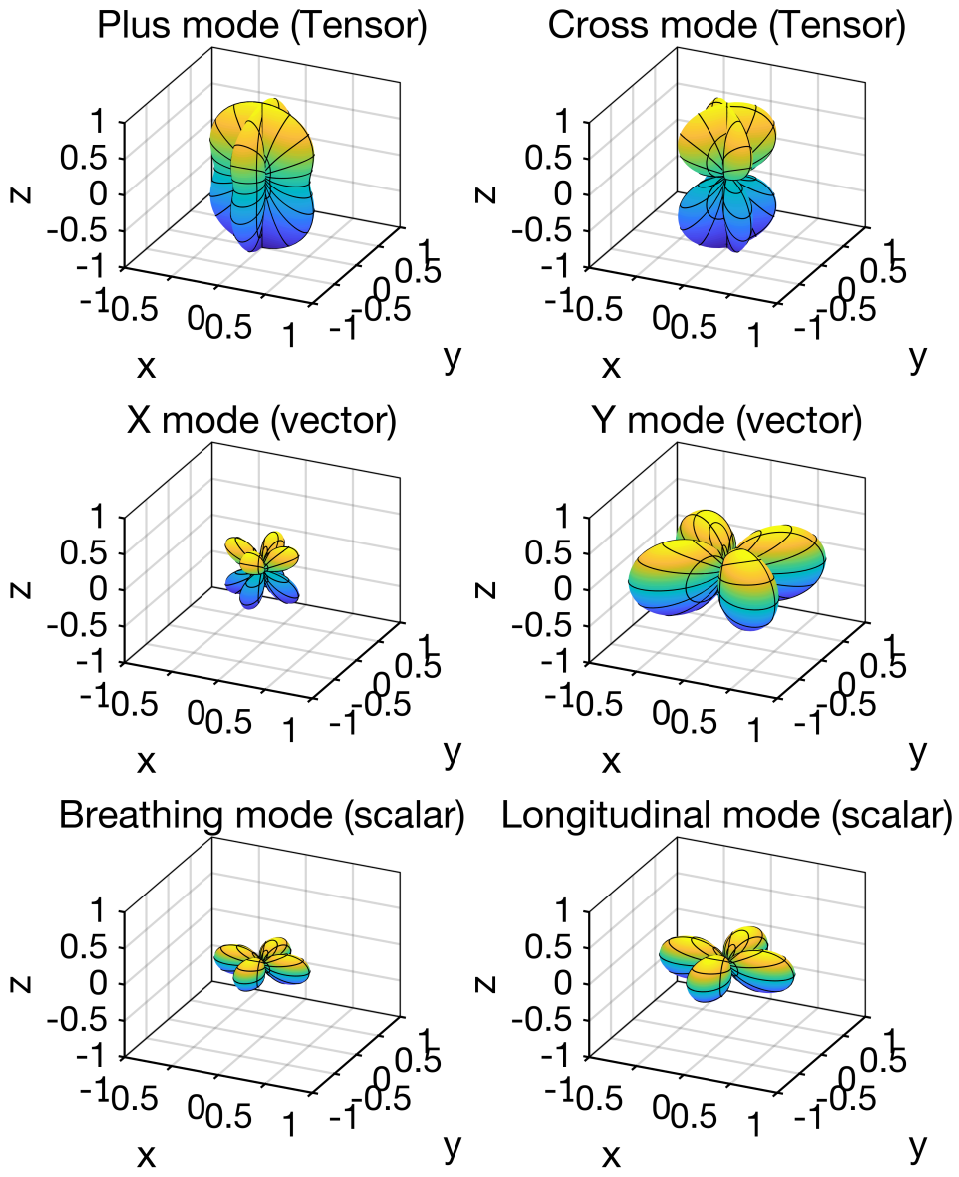

Figure G.2: Antenna pattern functions for the L-shaped interferometer.

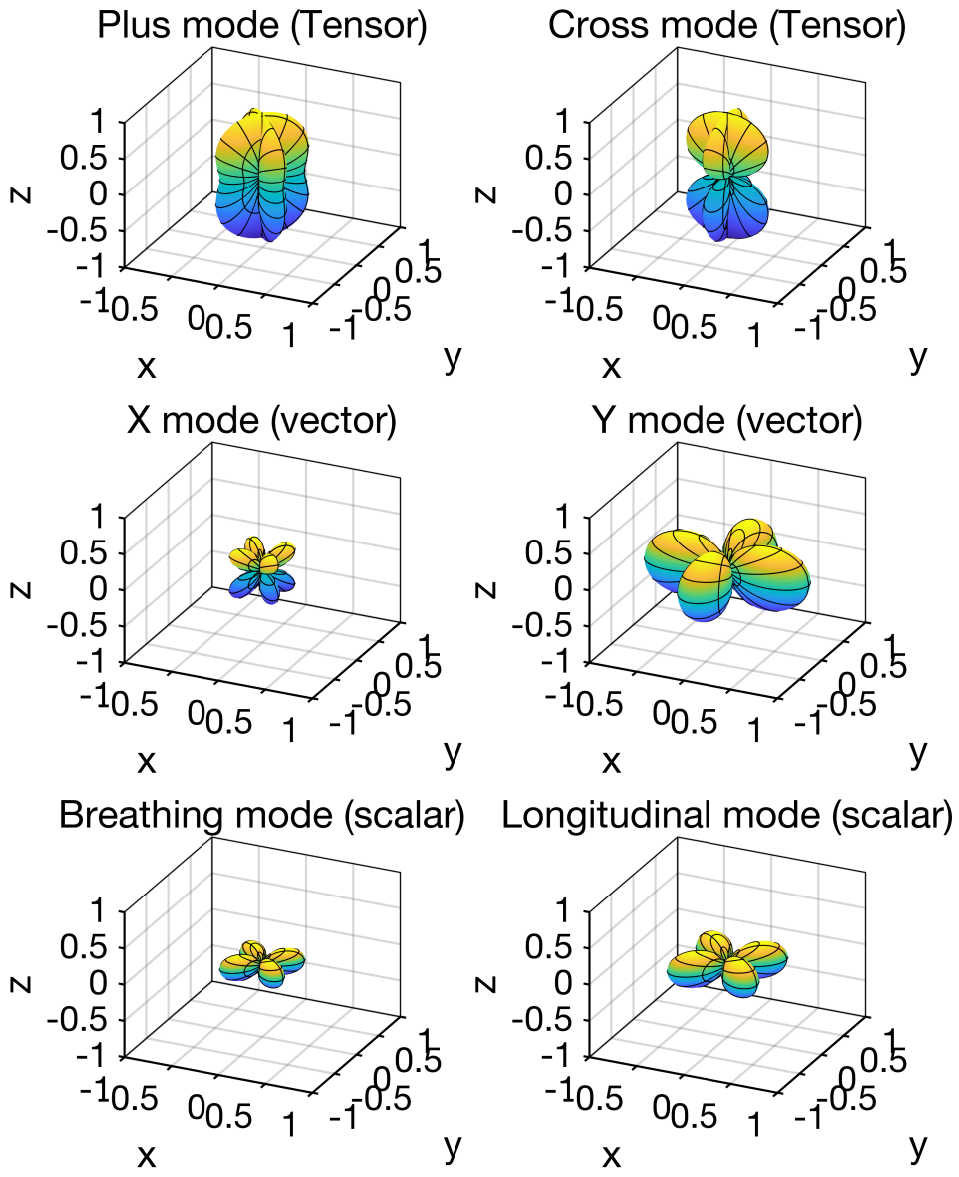

Figure G.3: Antenna pattern functions for triangular-shaped interferometer 1.

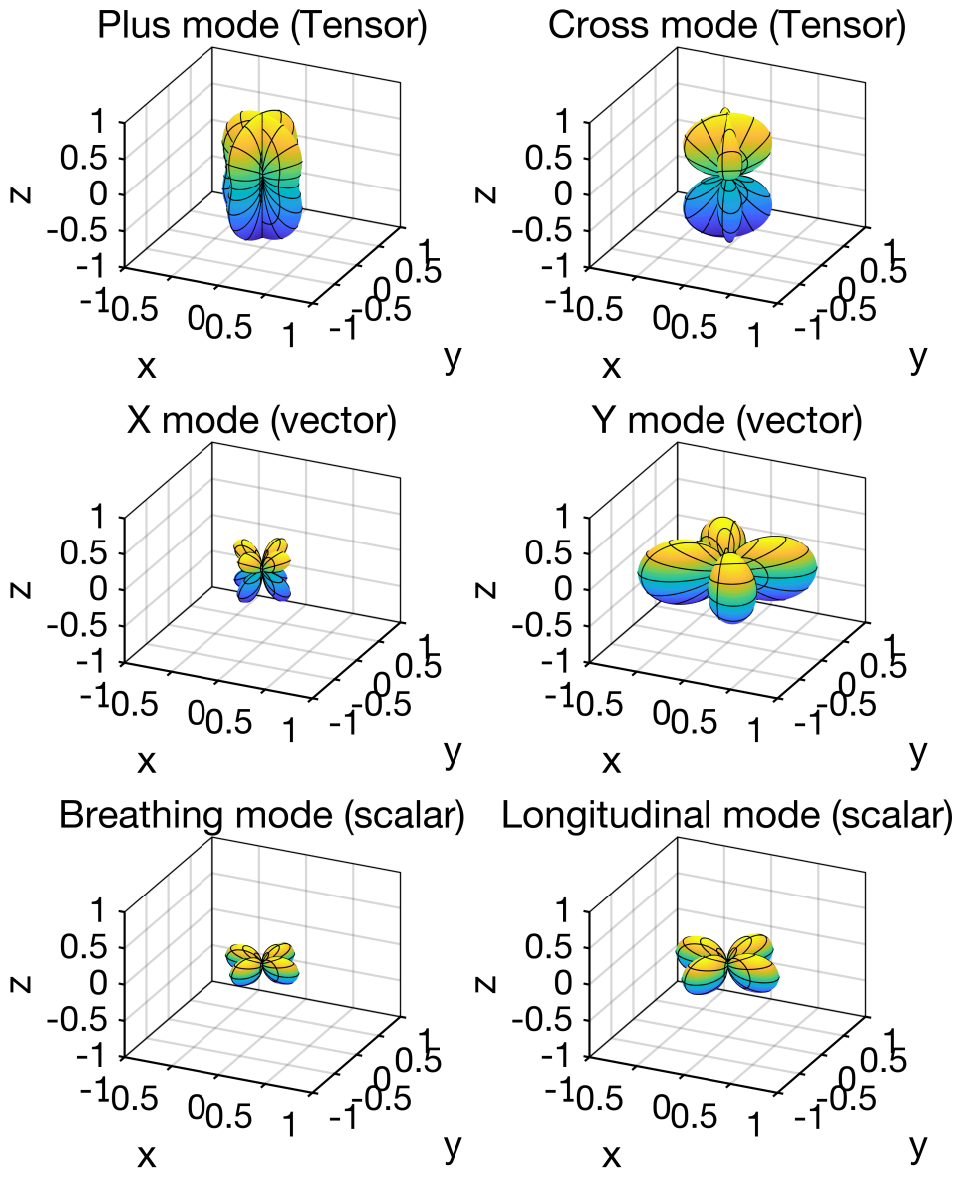

Figure G.4: Antenna pattern functions for triangular-shaped interferometer 2.

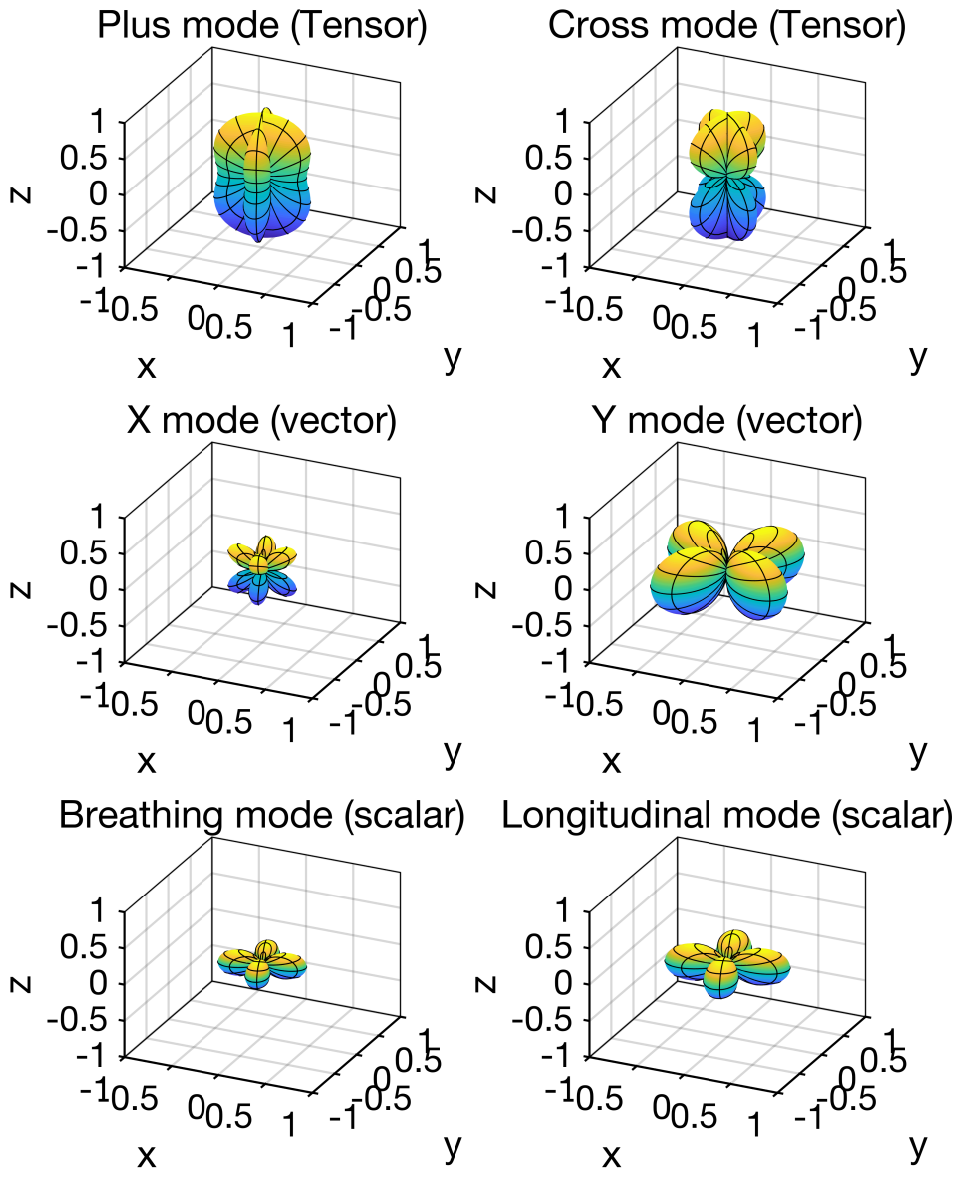

Figure G.5: Antenna pattern functions for triangular-shaped interferometer 3.

Appendix H

Full DECIGO interferometer model

Here, we show the Simulink system of the full DECIGO interferometer model. The model is organized as follows: Figure H.1 shows the top layer of the full DECIGO interferometer model, which is mainly for defining the name of the ports. From these ports, the noise explained in Section 5.5 or the excitation signal to measure the open loop transfer functions can be injected and the sensor signals can be obtained. Note that virtual sensors to measure parameters that cannot be measured in the real detector (e.g. a global position of the mirror) can also be used. Figure H.2 is the main system of the full DECIGO interferometer model included in the top system (represented as 'DECIGO'). This main system represents the behavior of the whole DECIGO. In the orange blocks, the longitudinal and alignment sensing methods explained in Section 5.3 are coded. In the magenta blocks, control topology explained in Section 5.6 is coded. The gravitational wave can be injected in the cavity length to estimate the noise performance. Figure H.3 shows the plant system of the mechanical and opto-mechanical system of the full DECIGO interferometer model, which includes the test masses and the satellites. In the subsystems of the plant model, the mechanical property (in Section 5.2), the actuation system (except for the frequency actuation in Section 5.4) and the local sensors (in Subsection 5.3.3) are coded. The opto-mechanical coupling is also coded in this plant block.

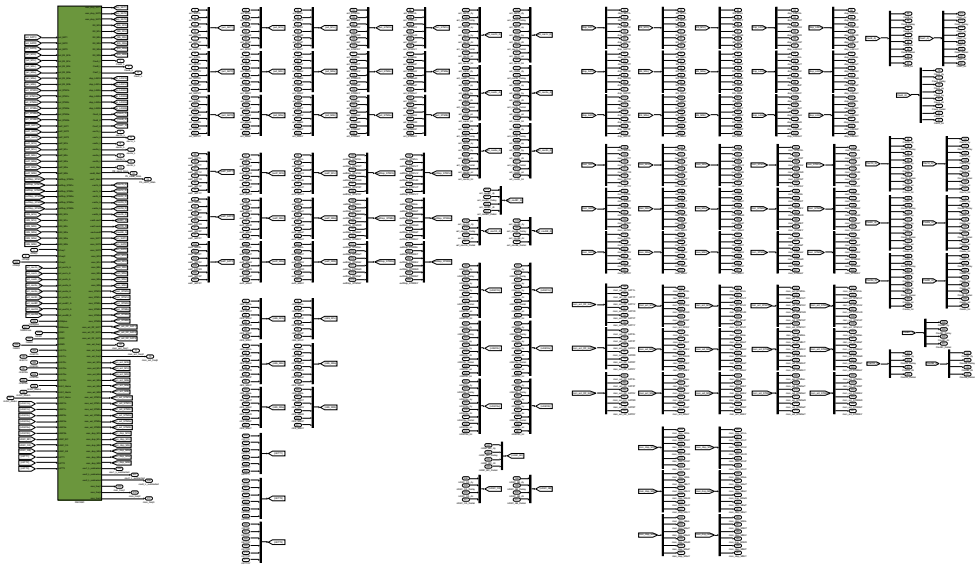

Figure H.1: Top layer of the full DECIGO interferometer model.

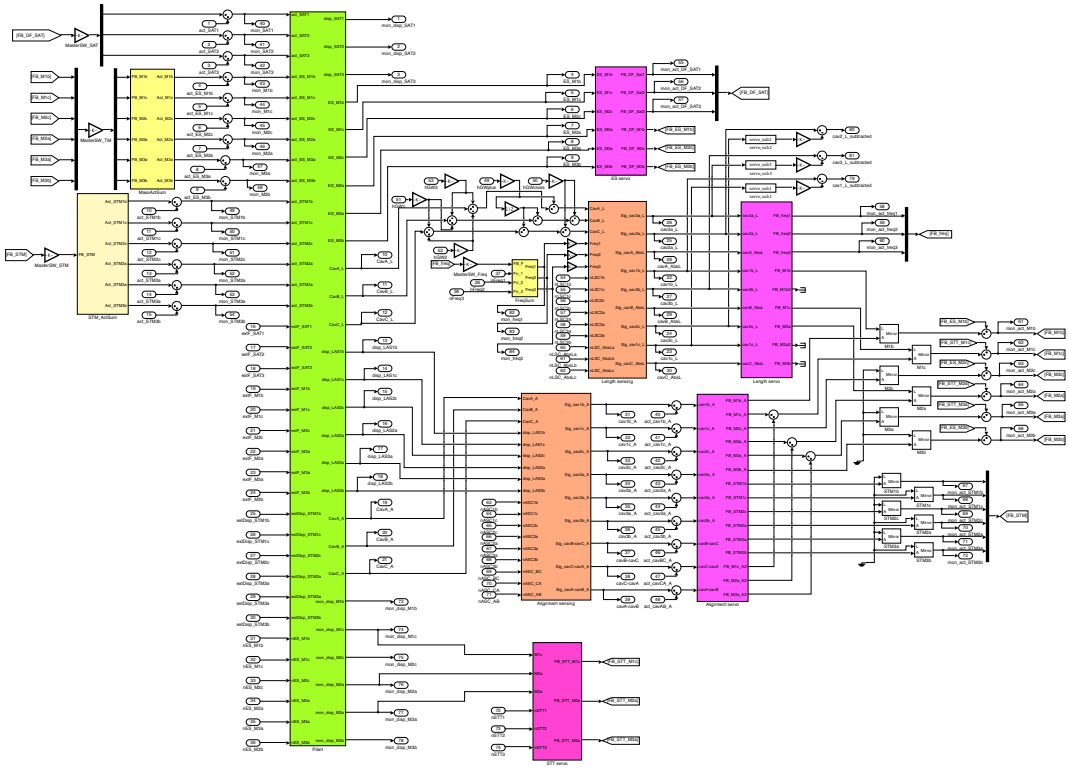

Figure H.2: Main system of the full DECIGO interferometer model.

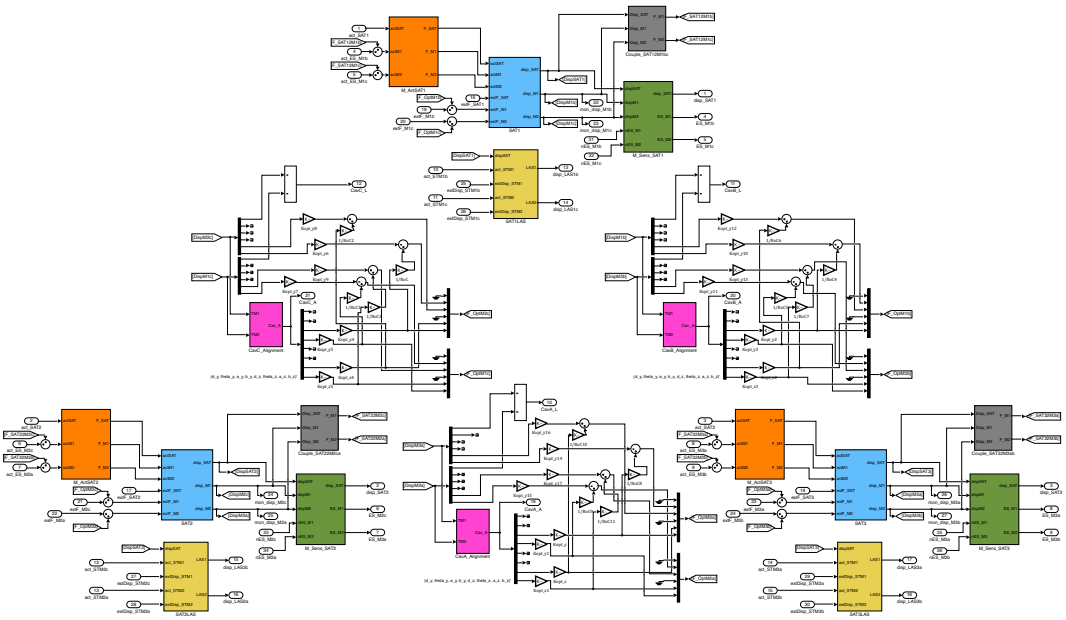

Figure H.3: Plant system of the mechanical and opto-mechanical system of the full DECIGO interferometer model.

Bibliography

[1] A. Einstein, "Approximative Integration of the Field Equations of Gravitation", Sitzungsber.Preuss.Akad.Wiss.Berlin (Math.Phys.) **1916**, 688 (1916).

[2] G. M. Clemence, "The Relativity Effect in Planetary Motions", Reviews of Modern Physics **19**, 361 (1947).

[3] F. W. Dyson, A. S. Eddington, and C. Davidson, "A Determination of the Deflection of Light by the Sun's Gravitational Field, from Observations Made at the Total Eclipse of May 29, 1919", Philosophical Transactions of the Royal Society A: Mathematical, Physical and Engineering Sciences **220**, 291 (1920).

[4] A. Einstein, "LENS-LIKE ACTION OF A STAR BY THE DEVIATION OF LIGHT IN THE GRAVITATIONAL FIELD", Science **84**, 506 (1936).

[5] D. Walsh, R. F. Carswell, and R. J. Weymann, "0957 + 561 A, B: twin quasistellar objects or gravitational lens?", Nature **279**, 381 (1979).

[6] M. D. Kruskal, "Maximal Extension of Schwarzschild Metric", Physical Review **119**, 1743 (1960).

[7] S. W. Hawking, "Black Holes in General Relativity", Communications in Mathematical Physics **25**, 152 (1972).

[8] J. Weber, "Detection and Generation of Gravitational Waves", Physical Review **117**, 306 (1960).

[9] H. Hirakawa and K. Narihara, "Search for Gravitational Radiation at 145 Hz", Physical Review Letters **35**, 330 (1975).

[10] P. Astone *et al.*, "IGEC2: A 17-month search for gravitational wave bursts in 2005–2007", Physical Review D **82**, 022003 (2010).

[11] N. Yunes and X. Siemens, "Gravitational-Wave Tests of General Relativity with Ground-Based Detectors and Pulsar-Timing Arrays", Living Reviews in Relativity **16**, 9 (2013).

[12] C. M. Will, "The Confrontation between General Relativity and Experiment", Living Reviews in Relativity **17**, 4 (2014).

[13] W. H. Press and K. S. Thorne, "Gravitational-Wave Astronomy", Annual Review of Astronomy and Astrophysics **10**, 335 (1972).

[14] B. F. Schutz, "Gravitational wave astronomy", Classical and Quantum Gravity **16**, A131 (1999).

[15] S. Kobayashi and P. Meszaros, "Gravitational Radiation from Gamma-Ray Burst Progenitors", The Astrophysical Journal **589**, 861 (2003).

[16] E. Muller, M. Rampp, R. Buras, H.-T. Janka, and D. H. Shoemaker, "Toward Gravitational Wave Signals from Realistic Core-Collapse Supernova Models", The Astrophysical Journal **603**, 221 (2004).

[17] C. D. Ott, A. Burrows, L. Dessart, and E. Livne, "A New Mechanism for Gravitational-Wave Emission in Core-Collapse Supernovae", Physical Review Letters **96**, 201102 (2006).

[18] R. A. Hulse and J. H. Taylor, "Discovery of a pulsar in a binary system", The Astrophysical Journal **195**, L51 (1975).

[19] A. A. Michelson and E. W. Morley, "On the Relative Motion of the Earth and the Luminiferous Ether", American Journal of Science **s3-34**, 333 (1887).

[20] A. Perot and C. Fabry, "On the Application of Interference Phenomena to the Solution of Various Problems of Spectroscopy and Metrology", The Astrophysical Journal **9**, 87 (1899).

[21] R. W. P. Drever *et al.*, "Gravitational Wave Detectors Using Laser Interferometers and Optical Cavities: Ideas, Principles and Prospects", in *Quantum Optics, Experimental Gravity, and Measurement Theory*, edited by P. Meystre and M. O. Scully, NATO Advanced Science Institutes Series, pages 503–514, Springer US, Boston, MA, 1983.

[22] A. J. Aasi *et al.*, "Advanced LIGO", Classical and Quantum Gravity **32**, 074001 (2015).

[23] F. Acernese *et al.*, "Advanced Virgo: a second-generation interferometric gravitational wave detector", Classical and Quantum Gravity **32**, 024001 (2014).

[24] H. Grote and LIGO Scientific Collaboration, "The status of GEO 600", Classical and Quantum Gravity **25**, 114043 (2008).

[25] H. Grote and the LIGO Scientific Collaboration, "The GEO 600 status", Classical and Quantum Gravity **27**, 084003 (2010).

[26] K. L. Dooley *et al.*, "GEO 600 and the GEO-HF upgrade program: successes and challenges", Classical and Quantum Gravity **33**, 075009 (2016).

[27] K. Somiya, "Detector configuration of KAGRA–the Japanese cryogenic gravitational-wave detector", Classical and Quantum Gravity **29**, 124007 (2012).

[28] Y. Aso *et al.*, "Interferometer design of the KAGRA gravitational wave detector", Physical Review D **88**, 043007 (2013).

[29] B. P. Abbott *et al.*, "Observation of Gravitational Waves from a Binary Black Hole Merger", Physical Review Letters **116**, 061102 (2016).

[30] B. P. Abbott *et al.*, "GWTC-1: A Gravitational-Wave Transient Catalog of Compact Binary Mergers Observed by LIGO and Virgo during the First and Second Observing Runs", Physical Review X **9**, 031040 (2019).

[31] B. P. Abbott *et al.*, "Tests of General Relativity with GW150914", Physical Review Letters **116**, 221101 (2016).

[32] B. P. Abbott *et al.*, "Tests of General Relativity with GW170817", Physical Review Letters **123**, 011102 (2019).

[33] B. P. Abbott *et al.*, "GW170817: Observation of Gravitational Waves from a Binary Neutron Star Inspiral", Physical Review Letters **119**, 161101 (2017).

[34] B. P. Abbott *et al.*, "Multi-messenger Observations of a Binary Neutron Star Merger", The Astrophysical Journal **848**, L12 (2017).

[35] B. P. Abbott *et al.*, "Gravitational Waves and Gamma-Rays from a Binary Neutron Star Merger: GW170817 and GRB 170817A", The Astrophysical Journal **848**, L13 (2017).

[36] T. Matsubayashi, H. Shinkai, and T. Ebisuzaki, "Gravitational Waves from Merging Intermediate-Mass Black Holes", The Astrophysical Journal **614**, 864 (2004).

[37] C. Reisswig *et al.*, "Formation and Coalescence of Cosmological Supermassive-Black-Hole Binaries in Supermassive-Star Collapse", Physical Review Letters **111**, 151101 (2013).

[38] B. Allen, "The stochastic gravity-wave background: sources and detection", arXiv:gr-qc/9604033 (1996).

[39] D. Langlois, R. Maartens, and D. Wands, "Gravitational waves from inflation on the brane", Physics Letters B **489**, 259 (2000).

[40] T. L. Smith, M. Kamionkowski, and A. Cooray, "Direct detection of the inflationary gravitational-wave background", Physical Review D **73**, 023504 (2006).

[41] J. R. Gair, M. Vallisneri, S. L. Larson, and J. G. Baker, "Testing General Relativity with Low-Frequency, Space-Based Gravitational-Wave Detectors", Living Reviews in Relativity **16**, 7 (2013).

[42] A. Stroeer and A. Vecchio, "The LISA verification binaries", Classical and Quantum Gravity **23**, S809 (2006).

[43] B. F. Schutz, "Fundamental physics with LISA", Classical and Quantum Gravity **26**, 094020 (2009).

[44] K. Yagi and T. Tanaka, "DECIGO/BBO as a Probe to Constrain Alternative Theories of Gravity", Progress of Theoretical Physics **123**, 1069

(2010).

[45] J. García-Bellido, D. G. Figueroa, and A. Sastre, "Gravitational wave background from reheating after hybrid inflation", Physical Review D **77**, 043517 (2008).

[46] L. Alabidi, K. Kohri, M. Sasaki, and Y. Sendouda, "Observable spectra of induced gravitational waves from inflation", Journal of Cosmology and Astroparticle Physics **2012**, 017 (2012).

[47] M. Punturo *et al.*, "The Einstein Telescope: a third-generation gravitational wave observatory", Classical and Quantum Gravity **27**, 194002 (2010).

[48] B. P. Abbott *et al.*, "Exploring the sensitivity of next generation gravitational wave detectors", Classical and Quantum Gravity **34**, 044001 (2017).

[49] P. Amaro-Seoane *et al.*, "Laser Interferometer Space Antenna", arXiv:1702.00786 [astro-ph] (2017).

[50] G. M. Harry, P. Fritschel, D. A. Shaddock, W. Folkner, and E. S. Phinney, "Laser interferometry for the Big Bang Observer", Classical and Quantum Gravity **23**, 4887 (2006).

[51] J. Luo *et al.*, "TianQin: a space-borne gravitational wave detector", Classical and Quantum Gravity **33**, 035010 (2016).

[52] W.-R. Hu and Y.-L. Wu, "The Taiji Program in Space for gravitational wave physics and the nature of gravity", National Science Review **4**, 685 (2017).

[53] K. A. Kuns, H. Yu, Y. Chen, and R. X. Adhikari, "Astrophysics and cosmology with a deci-hertz gravitational-wave detector: TianGO", arXiv:1908.06004 [astro-ph, physics:gr-qc] (2019).

[54] S. Kawamura *et al.*, "The Japanese space gravitational wave antenna: DECIGO", Classical and Quantum Gravity **28**, 094011 (2011).

[55] S. A. Hughes and K. S. Thorne, "Seismic gravity-gradient noise in interferometric gravitational-wave detectors", Physical Review D **58**, 122002 (1998).

[56] R. Abbott *et al.*, "Seismic isolation enhancements for initial and advanced LIGO", Classical and Quantum Gravity **21**, S915 (2004).

[57] W. Fichter, P. Gath, S. Vitale, and D. Bortoluzzi, "LISA Pathfinder drag-free control and system implications", Classical and Quantum Gravity **22**, S139 (2005).

[58] F. Acernese *et al.*, "Performances of the Virgo interferometer longitudinal control system", Astroparticle Physics **33**, 75 (2010).

[59] L. Barsotti, M. Evans, and P. Fritschel, "Alignment sensing and control in advanced LIGO", Classical and Quantum Gravity **27**, 084026 (2010).

[60] C. Cutler, "Angular resolution of the LISA gravitational wave detector", Physical Review D **57**, 7089 (1998).

[61] A. Freise *et al.*, "Triple Michelson interferometer for a third-generation gravitational wave detector", Classical and Quantum Gravity **26**, 085012 (2009).

[62] L. D. Landau and E. M. Lifshits, *The classical theory of fields*, Number v. 2 in Course of theoretical physics, Pergamon Press, Oxford ; New York, 4th rev. english ed edition, 1975.

[63] M. Maggiore, *Gravitational Waves*, Oxford University Press, Oxford, 2008.

[64] H.-T. Janka, T. Eberl, M. Ruffert, and C. L. Fryer, "Black Hole–Neutron Star Mergers as Central Engines of Gamma-Ray Bursts", The Astrophysical Journal **527**, L39 (1999).

[65] S. Rosswog, "Mergers of Neutron Star–Black Hole Binaries with Small Mass Ratios: Nucleosynthesis, Gamma-Ray Bursts, and Electromagnetic Transients", The Astrophysical Journal **634**, 1202 (2005).

[66] G. Nelemans, L. R. Yungelson, and S. F. Portegies Zwart, "The gravitational wave signal from the Galactic disk population of binaries containing two compact objects", Astronomy & Astrophysics **375**, 890 (2001).

[67] E. García-Berro *et al.*, "The merging of white dwarf and neutron star systems: gravitational radiation", Journal of Physics: Conference Series **66**, 012040 (2007).

[68] C. L. Fryer, S. E. Woosley, M. Herant, and M. B. Davies, "Merging White Dwarf/Black Hole Binaries and Gamma-Ray Bursts", The Astrophysical Journal **520**, 650 (1999).

[69] K. N. Yakunin *et al.*, "Gravitational waves from core collapse supernovae", Classical and Quantum Gravity **27**, 194005 (2010).

[70] C. Grupen, *Astroparticle Physics*, Springer, Berlin ; New York, 2005.

[71] P. Jaranowski, A. Królak, and B. F. Schutz, "Data analysis of gravitational-wave signals from spinning neutron stars: The signal and its detection", Physical Review D **58**, 063001 (1998).

[72] A. Vilenkin, "Gravitational radiation from cosmic strings", Physics Letters B **107**, 47 (1981).

[73] T. Damour and A. Vilenkin, "Gravitational radiation from cosmic (super)strings: Bursts, stochastic background, and observational windows", Physical Review D **71**, 063510 (2005).

[74] A. Kosowsky, M. S. Turner, and R. Watkins, "Gravitational waves from first-order cosmological phase transitions", Physical Review Letters **69**, 2026 (1992).

[75] M. Gleiser and R. Roberts, "Gravitational Waves from Collapsing Vacuum

Domains", Physical Review Letters **81**, 5497 (1998).

[76] R. Easther and E. A. Lim, "Stochastic gravitational wave production after inflation", Journal of Cosmology and Astroparticle Physics **2006**, 010 (2006).

[77] N. Yunes and F. Pretorius, "Fundamental theoretical bias in gravitational wave astrophysics and the parametrized post-Einsteinian framework", Physical Review D **80**, 122003 (2009).

[78] T. G. F. Li *et al.*, "Towards a generic test of the strong field dynamics of general relativity using compact binary coalescence", Physical Review D **85**, 082003 (2012).

[79] M. Isi, M. Giesler, W. M. Farr, M. A. Scheel, and S. A. Teukolsky, "Testing the No-Hair Theorem with GW150914", Physical Review Letters **123**, 111102 (2019).

[80] C. Brans and R. H. Dicke, "Mach's Principle and a Relativistic Theory of Gravitation", Physical Review **124**, 925 (1961).

[81] H. A. Buchdahl, "Non-Linear Lagrangians and Cosmological Theory", Monthly Notices of the Royal Astronomical Society **150**, 1 (1970).

[82] M. Visser, "Mass for the Graviton", General Relativity and Gravitation **30**, 1717 (1998).

[83] D. M. Eardley, D. L. Lee, A. P. Lightman, R. V. Wagoner, and C. M. Will, "Gravitational-Wave Observations as a Tool for Testing Relativistic Gravity", Physical Review Letters **30**, 884 (1973).

[84] A. Nishizawa, A. Taruya, K. Hayama, S. Kawamura, and M.-a. Sakagami, "Probing nontensorial polarizations of stochastic gravitational-wave backgrounds with ground-based laser interferometers", Physical Review D **79**, 082002 (2009).

[85] K. Hayama and A. Nishizawa, "Model-independent test of gravity with a network of ground-based gravitational-wave detectors", Physical Review D **87**, 062003 (2013).

[86] P. S. Cowperthwaite *et al.*, "The Electromagnetic Counterpart of the Binary Neutron Star Merger LIGO/Virgo GW170817. II. UV, Optical, and Near-infrared Light Curves and Comparison to Kilonova Models", The Astrophysical Journal **848**, L17 (2017).

[87] R. W. Klebesadel, I. B. Strong, and R. A. Olson, "Observations of Gamma-Ray Bursts of Cosmic Origin", The Astrophysical Journal **182**, L85 (1973).

[88] J. van Paradijs, C. Kouveliotou, and R. A. M. J. Wijers, "Gamma-Ray Burst Afterglows", Annual Review of Astronomy and Astrophysics **38**, 379 (2000).

[89] C. S. Kochanek and T. Piran, "Gravitational Waves and γ-Ray Bursts", The Astrophysical Journal **417**, L17 (1993).

[90] M. Tanaka *et al.*, "Kilonova from post-merger ejecta as an optical and near-Infrared counterpart of GW170817", Publications of the Astronomical Society of Japan **69** (2017).

[91] K. Sato, "First-order phase transition of a vacuum and the expansion of the Universe", Monthly Notices of the Royal Astronomical Society **195**, 467 (1981).

[92] A. H. Guth, "Inflationary universe: A possible solution to the horizon and flatness problems", Physical Review D **23**, 347 (1981).

[93] P. A. R. Ade *et al.*, "Joint Analysis of BICEP2/*Keck Array* and *Planck* Data", Physical Review Letters **114**, 101301 (2015).

[94] Planck Collaboration, "Planck 2018 results. X. Constraints on inflation", Astronomy & Astrophysics (2019).

[95] F. A. Jenet *et al.*, "Upper Bounds on the Low-Frequency Stochastic Gravitational Wave Background from Pulsar Timing Observations: Current Limits and Future Prospects", The Astrophysical Journal **653**, 1571 (2006).

[96] R. van Haasteren *et al.*, "Placing limits on the stochastic gravitational-wave background using European Pulsar Timing Array data: EPTA GWB limit", Monthly Notices of the Royal Astronomical Society **414**, 3117 (2011).

[97] Z. Arzoumanian *et al.*, "The NANOGrav 11 Year Data Set: Pulsar-timing Constraints on the Stochastic Gravitational-wave Background", The Astrophysical Journal **859**, 47 (2018).

[98] J. W. Armstrong, L. Iess, P. Tortora, and B. Bertotti, "Stochastic Gravitational Wave Background: Upper Limits in the 10^{-6} to 10^{-3} Hz Band", The Astrophysical Journal **599**, 806 (2003).

[99] K. Ishidoshiro *et al.*, "Upper Limit on Gravitational Wave Backgrounds at 0.2 Hz with a Torsion-Bar Antenna", Physical Review Letters **106**, 161101 (2011).

[100] Y. Kuwahara, A. Shoda, K. Eda, and M. Ando, "Search for a stochastic gravitational wave background at 1–5 Hz with a torsion-bar antenna", Physical Review D **94**, 042003 (2016).

[101] B. P. Abbott *et al.*, "Upper Limits on the Stochastic Gravitational-Wave Background from Advanced LIGO's First Observing Run", Physical Review Letters **118**, 121101 (2017).

[102] A. Nishizawa *et al.*, "Laser-interferometric detectors for gravitational wave backgrounds at 100 MHz: Detector design and sensitivity", Physical Review D **77**, 022002 (2008).

[103] T. Akutsu *et al.*, "Search for a Stochastic Background of 100-MHz Gravitational Waves with Laser Interferometers", Physical Review Letters **101**, 101101 (2008).

[104] A. Ito, T. Ikeda, K. Miuchi, and J. Soda, "Probing GHz Gravitational Waves with Graviton-magnon Resonance", arXiv:1903.04843 [astro-ph, physics:gr-qc, physics:hep-ph] (2019).

[105] S. Kuroyanagi, S. Tsujikawa, T. Chiba, and N. Sugiyama, "Implications of the B -mode polarization measurement for direct detection of inflationary gravitational waves", Physical Review D **90**, 063513 (2014).

[106] A. Sesana, "Prospects for Multiband Gravitational-Wave Astronomy after GW150914", Physical Review Letters **116**, 231102 (2016).

[107] S. Vitale, "Multiband Gravitational-Wave Astronomy: Parameter Estimation and Tests of General Relativity with Space- and Ground-Based Detectors", Physical Review Letters **117**, 051102 (2016).

[108] S. Isoyama, H. Nakano, and T. Nakamura, "Multiband gravitational-wave astronomy: Observing binary inspirals with a decihertz detector, B-DECIGO", Progress of Theoretical and Experimental Physics **2018** (2018).

[109] N. Seto and J. Yokoyama, "Probing the Equation of State of the Early Universe with a Space Laser Interferometer", Journal of the Physical Society of Japan **72**, 3082 (2003).

[110] A. Albrecht, P. J. Steinhardt, M. S. Turner, and F. Wilczek, "Reheating an Inflationary Universe", Physical Review Letters **48**, 1437 (1982).

[111] K. Nakayama, S. Saito, Y. Suwa, and J. Yokoyama, "Space-based gravitational-wave detectors can determine the thermal history of the early Universe", Physical Review D **77**, 124001 (2008).

[112] S. Kuroyanagi, T. Chiba, and N. Sugiyama, "Precision calculations of the gravitational wave background spectrum from inflation", Physical Review D **79**, 103501 (2009).

[113] C. Grojean and G. Servant, "Gravitational waves from phase transitions at the electroweak scale and beyond", Physical Review D **75**, 043507 (2007).

[114] J. J. Blanco-Pillado, K. D. Olum, and X. Siemens, "New limits on cosmic strings from gravitational wave observation", Physics Letters B **778**, 392 (2018).

[115] H. J. Kimble, Y. Levin, A. B. Matsko, K. S. Thorne, and S. P. Vyatchanin, "Conversion of conventional gravitational-wave interferometers into quantum nondemolition interferometers by modifying their input and/or output optics", Physical Review D **65**, 022002 (2001).

[116] A. Buonanno and Y. Chen, "Quantum noise in second generation, signal-recycled laser interferometric gravitational-wave detectors", Physical Review D **64**, 042006 (2001).

[117] P. R. Saulson, "Thermal noise in mechanical experiments", Physical Review D **42**, 2437 (1990).

[118] V. Braginsky, M. Gorodetsky, and S. Vyatchanin, "Thermodynamical fluc-

tuations and photo-thermal shot noise in gravitational wave antennae", Physics Letters A **264**, 1 (1999).

[119] M. Cerdonio, L. Conti, A. Heidmann, and M. Pinard, "Thermoelastic effects at low temperatures and quantum limits in displacement measurements", Physical Review D **63**, 082003 (2001).

[120] N. Nakagawa, A. M. Gretarsson, E. K. Gustafson, and M. M. Fejer, "Thermal noise in half-infinite mirrors with nonuniform loss: A slab of excess loss in a half-infinite mirror", Physical Review D **65**, 102001 (2002).

[121] G. M. Harry *et al.*, "Titania-doped tantala/silica coatings for gravitational-wave detection", Classical and Quantum Gravity **24**, 405 (2007).

[122] K. Somiya and K. Yamamoto, "Coating thermal noise of a finite-size cylindrical mirror", Physical Review D **79**, 102004 (2009).

[123] R. Del Fabbro *et al.*, "Low frequency behaviour of the Pisa seismic noise super-attenuator for gravitational wave detection", Physics Letters A **133**, 471 (1988).

[124] T. Sekiguchi, *A Study of Low Frequency Vibration Isolation System for Large Scale Gravitational Wave Detectors*, Ph.D. thesis, The University of Tokyo, 2016.

[125] P. R. Saulson, "Terrestrial gravitational noise on a gravitational wave antenna", Physical Review D **30**, 732 (1984).

[126] D. Fiorucci, J. Harms, M. Barsuglia, I. Fiori, and F. Paoletti, "Impact of infrasound atmospheric noise on gravity detectors used for astrophysical and geophysical applications", Physical Review D **97**, 062003 (2018).

[127] A. Yariv and P. Yeh, *Photonics: Optical Electronics in Modern Communications*, Oxford University Press, 2007.

[128] D. H. Reitze, P. R. Saulson, and H. Grote, editors, *Advanced interferometric gravitational-wave detectors*, World Scientific, New Jersey, 2019.

[129] R. W. P. Drever *et al.*, "Laser phase and frequency stabilization using an optical resonator", Applied Physics B **31**, 97 (1983).

[130] D. Z. Anderson, "Alignment of resonant optical cavities", Applied Optics **23**, 2944 (1984).

[131] S. Solimeno *et al.*, "Fabry-Pérot resonators with oscillating mirrors", Physical Review A **43**, 6227 (1991).

[132] N. M. Sampas and D. Z. Anderson, "Stabilization of laser beam alignment to an optical resonator by heterodyne detection of off-axis modes", Applied Optics **29**, 394 (1990).

[133] E. Morrison, B. J. Meers, D. I. Robertson, and H. Ward, "Experimental demonstration of an automatic alignment system for optical interferometers", Applied Optics **33**, 5037 (1994).

[134] E. Morrison, B. J. Meers, D. I. Robertson, and H. Ward, "Automatic alignment of optical interferometers", Applied Optics **33**, 5041 (1994).

[135] J. Mizuno *et al.*, "Resonant sideband extraction: a new configuration for interferometric gravitational wave detectors", Physics Letters A **175**, 273 (1993).

[136] T. Robson, N. Cornish, and C. Liu, "The construction and use of LISA sensitivity curves", Classical and Quantum Gravity **36**, 105011 (2019).

[137] L. Barsotti, S. Gras, M. Evans, and P. Fritschel, "The updated Advanced LIGO design curve", LIGO Document T1800044-v5, 2018.

[138] D. Bortoluzzi *et al.*, "Testing LISA drag-free control with the LISA technology package flight experiment", Classical and Quantum Gravity **20**, S89 (2003).

[139] A. Schleicher *et al.*, "In-orbit performance of the LISA Pathfinder drag-free and attitude control system", CEAS Space Journal **10**, 471 (2018).

[140] B. L. Schumaker, "Disturbance reduction requirements for LISA", Classical and Quantum Gravity **20**, S239 (2003).

[141] G. Noci *et al.*, "Cold Gas Micro Propulsion System for Scientific Satellite Fine Pointing: Review of Development and Qualification Activities at Thales Alenia Space Italia", in *45th AIAA/ASME/SAE/ASEE Joint Propulsion Conference & Exhibit*, Denver, Colorado, 2009, American Institute of Aeronautics and Astronautics.

[142] G. Anderson *et al.*, "Experimental results from the ST7 mission on LISA Pathfinder", Physical Review D **98**, 102005 (2018).

[143] M. Armano *et al.*, "LISA Pathfinder micronewton cold gas thrusters: In-flight characterization", Physical Review D **99**, 122003 (2019).

[144] J. Pap *et al.*, "Variations in total solar and spectral irradiance as measured by the VIRGO experiment on SOHO", Advances in Space Research **24**, 215 (1999).

[145] S. Kuroyanagi, K. Nakayama, and S. Saito, "Prospects for determination of thermal history after inflation with future gravitational wave detectors", Physical Review D **84**, 123513 (2011).

[146] P. L. Bender and D. Hils, "Confusion noise level due to galactic and extragalactic binaries", Classical and Quantum Gravity **14**, 1439 (1997).

[147] M. R. Adams and N. J. Cornish, "Detecting a stochastic gravitational wave background in the presence of a galactic foreground and instrument noise", Physical Review D **89**, 022001 (2014).

[148] A. J. Farmer and E. S. Phinney, "The gravitational wave background from cosmological compact binaries", Monthly Notices of the Royal Astronomical Society **346**, 1197 (2003).

[149] C. C. Yancey *et al.*, "MULTI-MESSENGER ASTRONOMY OF GRAVITATIONAL-WAVE SOURCES WITH FLEXIBLE WIDE-AREA RADIO TRANSIENT SURVEYS", The Astrophysical Journal **812**, 168 (2015).

[150] A. Nishizawa, A. Taruya, and S. Saito, "Tracing the redshift evolution of Hubble parameter with gravitational-wave standard sirens", Physical Review D **83**, 084045 (2011).

[151] N. Seto, S. Kawamura, and T. Nakamura, "Possibility of Direct Measurement of the Acceleration of the Universe Using 0.1 Hz Band Laser Interferometer Gravitational Wave Antenna in Space", Physical Review Letters **87**, 221103 (2001).

[152] S. Hawking, "Gravitationally Collapsed Objects of Very Low Mass", Monthly Notices of the Royal Astronomical Society **152**, 75 (1971).

[153] R. Saito and J. Yokoyama, "Gravitational-Wave Background as a Probe of the Primordial Black-Hole Abundance", Physical Review Letters **102**, 161101 (2009).

[154] H. Niikura *et al.*, "Microlensing constraints on primordial black holes with the Subaru/HSC Andromeda observation", Nature Astronomy **3**, 524 (2019).

[155] K. Nagano, T. Fujita, Y. Michimura, and I. Obata, "Axion Dark Matter Search with Interferometric Gravitational Wave Detectors", Physical Review Letters **123**, 111301 (2019).

[156] T. Nakamura *et al.*, "Pre-DECIGO can get the smoking gun to decide the astrophysical or cosmological origin of GW150914-like binary black holes", Progress of Theoretical and Experimental Physics **2016**, 093E01 (2016).

[157] B. Bertotti, L. Iess, and P. Tortora, "A test of general relativity using radio links with the Cassini spacecraft", Nature **425**, 374 (2003).

[158] K. Yagi, N. Yunes, and T. Tanaka, "Gravitational Waves from Quasicircular Black-Hole Binaries in Dynamical Chern-Simons Gravity", Physical Review Letters **109**, 251105 (2012).

[159] K. Yagi, "SCIENTIFIC POTENTIAL OF DECIGO PATHFINDER AND TESTING GR WITH SPACE-BORNE GRAVITATIONAL WAVE INTERFEROMETERS", International Journal of Modern Physics D **22**, 1341013 (2013).

[160] G. Gnocchi, A. Maselli, T. Abdelsalhin, N. Giacobbo, and M. Mapelli, "Bounding alternative theories of gravity with multiband GW observations", Physical Review D **100**, 064024 (2019).

[161] T. Kinugawa, H. Takeda, and H. Yamaguchi, "Probe for Type Ia supernova progenitor in decihertz gravitational wave astronomy", arXiv:1910.01063 [astro-ph] (2019).

[162] D. Shaddock, B. Ware, P. G. Halverson, R. E. Spero, and B. Klipstein, "Overview of the LISA Phasemeter", in *AIP Conference Proceedings*, volume 873, pages 654–660, Greenbelt, Maryland (USA), 2006, AIP.

[163] I. Bykov, J. J. E. Delgado, A. F. G. Marín, G. Heinzel, and K. Danzmann, "LISA phasemeter development: Advanced prototyping", Journal of Physics: Conference Series **154**, 012017 (2009).

[164] B. P. Abbott *et al.*, "LIGO: the Laser Interferometer Gravitational-Wave Observatory", Reports on Progress in Physics **72**, 076901 (2009).

[165] D. V. Martynov *et al.*, "Sensitivity of the Advanced LIGO detectors at the beginning of gravitational wave astronomy", Physical Review D **93**, 112004 (2016).

[166] A. Abramovici *et al.*, "Improved sensitivity in a gravitational wave interferometer and implications for LIGO", Physics Letters A **218**, 157 (1996).

[167] M. Ohashi *et al.*, "Design and construction status of CLIO", Classical and Quantum Gravity **20**, S599 (2003).

[168] J. A. Sidles and D. Sigg, "Optical torques in suspended Fabry–Perot interferometers", Physics Letters A **354**, 167 (2006).

[169] A. Suemasa, A. Shimo-oku, K. Nakagawa, and M. Musha, "Developments of high frequency and intensity stabilized lasers for space gravitational wave detector DECIGO/B-DECIGO", CEAS Space Journal **9**, 485 (2017).

[170] M. Musha, T. Kanaya, K. Nakagawa, and K.-I. Ueda, "Intensity and frequency noise characteristics of two coherently-added injection-locked Nd:YAG lasers", Applied Physics B **73**, 209 (2001).

[171] L.-W. Wei, F. Cleva, and C. N. Man, "Coherently combined master oscillator fiber power amplifiers for Advanced Virgo", Optics Letters **41**, 5817 (2016).

[172] E. A. Donley, T. P. Heavner, F. Levi, M. O. Tataw, and S. R. Jefferts, "Double-pass acousto-optic modulator system", Review of Scientific Instruments **76**, 063112 (2005).

[173] G. P. Barwood, P. Gill, and W. R. C. Rowley, "High-accuracy length metrology using multiple-stage swept-frequency interferometry with laser diodes", Measurement Science and Technology **9**, 1036 (1998).

[174] A. Araya *et al.*, "Absolute-length determination of a long-baseline Fabry–Perot cavity by means of resonating modulation sidebands", Applied Optics **38**, 2848 (1999).

[175] A. Stochino, K. Arai, and R. X. Adhikari, "Technique for in situ measurement of free spectral range and transverse mode spacing of optical cavities", Applied Optics **51**, 6571 (2012).

[176] K. A. Strain, "Electrostatic drive (ESD) results from GEO and application in Advanced LIGO", LIGO Document T060015-x0, 2006.

[177] O. Jennrich, "*LISA* technology and instrumentation", Classical and Quantum Gravity **26**, 153001 (2009).

[178] D. I. Robertson *et al.*, "Construction and testing of the optical bench for LISA Pathfinder", Classical and Quantum Gravity **30**, 085006 (2013).

[179] M. Musha (private communication).

[180] F. Wei *et al.*, "Subkilohertz linewidth reduction of a DFB diode laser using self-injection locking with a fiber Bragg grating Fabry-Perot cavity", Optics Express **24**, 17406 (2016).

[181] E. Canuto, A. Molano, and L. Massotti, "Drag-Free Control of the GOCE Satellite: Noise and Observer Design", IEEE Transactions on Control Systems Technology **18**, 501 (2010).

[182] M. Armano *et al.*, "LISA Pathfinder platform stability and drag-free performance", Physical Review D **99**, 082001 (2019).

[183] W. J. Weber *et al.*, "Position sensors for flight testing of LISA drag-free control", in *Astronomical Telescopes and Instrumentation*, edited by M. Cruise and P. Saulson, page 31, Waikoloa, Hawai'i, United States, 2003.

[184] C. C. Speake and S. M. Aston, "An interferometric sensor for satellite drag-free control", Classical and Quantum Gravity **22**, S269 (2005).

[185] S. J. Cooper *et al.*, "A compact, large-range interferometer for precision measurement and inertial sensing", Classical and Quantum Gravity **35**, 095007 (2018).

[186] I. Funaki, Y. Nakayama, H. Horisawa, and M. Ando, "Micro-thruster Options for the Japanese Space Gravitational Wave Observatory Missions", International Electric Propulsion Conference, IEPC-2011-308 (2011).

[187] P. J. Wass *et al.*, "Testing of the UV discharge system for LISA Pathfinder", in *AIP Conference Proceedings*, volume 873, pages 220–224, Greenbelt, Maryland (USA), 2006, AIP.

[188] K. Yagi and N. Seto, "Detector configuration of DECIGO/BBO and identification of cosmological neutron-star binaries", Physical Review D **83**, 044011 (2011).

[189] D. G. Enzer, R. T. Wang, and W. M. Klipstein, "GRAIL – A microwave ranging instrument to map out the lunar gravity field", in *2010 IEEE International Frequency Control Symposium*, pages 572–577, Newport Beach, CA, USA, 2010, IEEE.

[190] F. Cirillo and P. F. Gath, "Control system design for the constellation acquisition phase of the LISA mission", Journal of Physics: Conference Series **154**, 012014 (2009).

[191] P. G. Maghami and T. T. Hyde, "Laser interferometer space antenna dynamics and controls model", Classical and Quantum Gravity **20**, S273 (2003).

[192] Y. Michimura, Y. Kuwahara, T. Ushiba, N. Matsumoto, and M. Ando, "Optical levitation of a mirror for reaching the standard quantum limit", Optics Express **25**, 13799 (2017).

[193] P. Fritschel *et al.*, "Alignment of an interferometric gravitational wave detector", Applied Optics **37**, 6734 (1998).

[194] N. Smith-Lefebvre *et al.*, "Optimal alignment sensing of a readout mode cleaner cavity", Optics Letters **36**, 4365 (2011).

[195] S. Kawamura and M. E. Zucker, "Mirror-orientation noise in a Fabry–Perot interferometer gravitational wave detector", Applied Optics **33**, 3912 (1994).

[196] T. Abel, G. L. Bryan, and M. L. Norman, "The Formation of the First Star in the Universe", Science **295**, 93 (2002).

[197] A. Buonanno and Y. Chen, "Signal recycled laser-interferometer gravitational-wave detectors as optical springs", Physical Review D **65**, 042001 (2002).

[198] H. Rehbein *et al.*, "Double optical spring enhancement for gravitational-wave detectors", Physical Review D **78**, 062003 (2008).

[199] K. Somiya *et al.*, "Development of a frequency-detuned interferometer as a prototype experiment for next-generation gravitational-wave detectors", Applied Optics **44**, 3179 (2005).

[200] O. Miyakawa *et al.*, "Measurement of optical response of a detuned resonant sideband extraction gravitational wave detector", Physical Review D **74**, 022001 (2006).

[201] R. O. R. Y. Thompson, "Coherence Significance Levels", Journal of Atmospheric Sciences **36**, 2020 (1979).

[202] R. D. Peccei and H. R. Quinn, "CP Conservation in the Presence of Pseudoparticles", Physical Review Letters **38**, 1440 (1977).

[203] P. Svrcek and E. Witten, "Axions in string theory", Journal of High Energy Physics **06**, 051 (2006).

[204] A. Arvanitaki, S. Dimopoulos, S. Dubovsky, N. Kaloper, and J. March-Russell, "String axiverse", Physical Review D **81**, 123530 (2010).

[205] L. Visinelli and S. Vagnozzi, "Cosmological window onto the string axiverse and the supersymmetry breaking scale", Physical Review D **99**, 063517 (2019).

[206] J. P. Conlon, "The QCD Axion and Moduli Stabilisation", Journal of High Energy Physics **2006**, 078 (2006).

[207] P. Sikivie, "Experimental Tests of the "Invisible" Axion", Physical Review Letters **51**, 1415 (1983).

[208] M. B. Schneider, F. P. Calaprice, A. L. Hallin, D. W. MacArthur, and

D. F. Schreiber, "Limit on Im (C S C A *) from a Test of T Invariance in Ne 19 Beta Decay", Physical Review Letters **51**, 1239 (1983).

[209] G. Raffelt and L. Stodolsky, "Mixing of the photon with low-mass particles", Physical Review D **37**, 1237 (1988).

[210] A. G. Dias, A. C. B. Machado, C. C. Nishi, A. Ringwald, and P. Vaudrevange, "The quest for an intermediate-scale accidental axion and further ALPs", Journal of High Energy Physics **2014**, 37 (2014).

[211] P. W. Graham, I. G. Irastorza, S. K. Lamoreaux, A. Lindner, and K. A. van Bibber, "Experimental Searches for the Axion and Axion-Like Particles", Annual Review of Nuclear and Particle Science **65**, 485 (2015).

[212] I. G. Irastorza and J. Redondo, "New experimental approaches in the search for axion-like particles", Progress in Particle and Nuclear Physics **102**, 89 (2018).

[213] M. Y. Khlopov, "Probes for dark matter physics", International Journal of Modern Physics D **27**, 1841013 (2018).

[214] K. Zioutas *et al.*, "First Results from the CERN Axion Solar Telescope", Physical Review Letters **94**, 121301 (2005).

[215] V. Anastassopoulos *et al.*, "New CAST limit on the axion–photon interaction", Nature Physics **13**, 584 (2017).

[216] A. Payez *et al.*, "Revisiting the SN1987A gamma-ray limit on ultralight axion-like particles", Journal of Cosmology and Astroparticle Physics **02**, 006 (2015).

[217] A. C. Melissinos, "Search for Cosmic Axions using an Optical Interferometer", Physical Review Letters **102**, 202001 (2009).

[218] W. DeRocco and A. Hook, "Axion interferometry", Physical Review D **98**, 035021 (2018).

[219] I. Obata, T. Fujita, and Y. Michimura, "Optical Ring Cavity Search for Axion Dark Matter", Physical Review Letters **121**, 161301 (2018).

[220] H. Liu, B. D. Elwood, M. Evans, and J. Thaler, "Searching for axion dark matter with birefringent cavities", Physical Review D **100**, 023548 (2019).

[221] S. M. Carroll, G. B. Field, and R. Jackiw, "Limits on a Lorentz- and parity-violating modification of electrodynamics", Physical Review D **41**, 1231 (1990).

[222] S. M. Carroll, "Quintessence and the Rest of the World: Suppressing Long-Range Interactions", Physical Review Letters **81**, 3067 (1998).

[223] A. Andrianov, D. Espriu, F. Mescia, and A. Renau, "The axion shield", Physics Letters B **684**, 101 (2010).

[224] D. Espriu and A. Renau, "Photon propagation in a cold axion background with and without magnetic field", Physical Review D **85**, 025010 (2012).

[225] T. Fujita, R. Tazaki, and K. Toma, "Hunting Axion Dark Matter with Protoplanetary Disk Polarimetry", Physical Review Letters **122**, 191101 (2019).

[226] D. Budker, P. W. Graham, M. Ledbetter, S. Rajendran, and A. O. Sushkov, "Proposal for a Cosmic Axion Spin Precession Experiment (CASPEr)", Physical Review X **4**, 021030 (2014).

[227] B. J. Meers, "Recycling in laser-interferometric gravitational-wave detectors", Physical Review D **38**, 2317 (1988).

[228] T. T. Fricke *et al.*, "DC readout experiment in Enhanced LIGO", Classical and Quantum Gravity **29**, 065005 (2012).

[229] 久村 富持, **『制御システム論の基礎』**, 共立出版, 1988.

[230] M. Araki, B. Kondo, and K. Yamamoto, "GG-Pseudo-Band Method for the Design of Multivariable Control Systems", IFAC Proceedings Volumes **14**, 393 (1981).

[231] C. M. Caves, "Quantum-mechanical noise in an interferometer", Physical Review D **23**, 1693 (1981).

[232] K. Aki and P. G. Richards, *Quantitative Seismology*, Univ. Science Books, Sausalito, Calif, 2. ed., corr. print edition, 2009.

[233] N. K. Pavlis, S. A. Holmes, S. C. Kenyon, and J. K. Factor, "The development and evaluation of the Earth Gravitational Model 2008 (EGM2008): THE EGM2008 EARTH GRAVITATIONAL MODEL", Journal of Geophysical Research: Solid Earth **117**, n/a (2012).

[234] E. Thébault *et al.*, "International Geomagnetic Reference Field: the 12th generation", Earth, Planets and Space **67**, 79 (2015).

[235] M. A. Barton, "Models of the Advanced LIGO Suspensions in Mathematica", LIGO Document T020205-v1, 2014.

[236] T. Sekiguchi, "Suspension rigid-body modeling tool in Mathematica", JGW-T1503729-v2, 2015.

Acknowledgement

This work is supported by a large number of people. Here, I want to express my appreciation for their supports.

Takashi Uchiyama, who is my supervisor, told me that enjoying research is important. Also he let me do what I wanted to do. Thanks to him, I was able to concentrate on and enjoy my research. Actually, one of my most favorite events during my Ph.D. course is Extended Uchiyama Group Meeting in a 'proper' place.

Masaki Ando gave me many insightful advices for my research based on his wide knowledge and experience. From him, I learned various research related things, such as planning of an experiment, interpretation of the obtained results, how to present the experimental output, and so on. They will help me in my future research life.

Yuta Michimura is the most familiar professional staff to me. I can consult him on everything without any hesitation. When I asked something, he mostly gave me appropriate answers.

Ayaka Shoda gave me important suggestions related to the simulation. She kindly told me how to make a model in Matlab, Simulink. Especially, I really appreciate her comment on the way to calculate open loop transfer function with the constructed model. The stating point of the full interferometer model in this thesis is her prototype model.

Kiwamu Izumi gave me important suggestions on the interferometer control when I considered the control topology of the dual-pass differential Fabry–Pérot interferometer. He also encouraged me in my experiment occasionally.

Tomofumi Shimoda helped me with the design of the suspension system based on his deep knowledge on the suspension system with torsion pendulum. In addition, I discussed many things with him in our group office. He also gave me insightful comments on the manuscript of this thesis.

Hiroki Takeda helped me with the construction of the dual-pass differential Fabry–Pérot interferometer. Moreover, from him, I learned not only experimental thing but also theoretical thing.

Kunihiko Hasegawa and Takaharu Shishido kindly washed the mechanical parts.

Shuichi Sato and Mitsuru Musha gave me valuable comments about the formation flying and laser at occasional DECIGO-related meetings, respectively.

Isao Kawano, Takahiro Ito, Satoshi Ikari, Shuhei Matsushita, and Sho Ishiwata

gave me various knowledge from engineering aspect.

Tomohiro Fujita, and Ippei Obata told me many theoretical things, especially axion dark matter and related topics. Without them, I could not perform a research on the axion dark matter search.

From Kazuhiro Hayama, Atsushi Nishizawa, and Sachiko Kuroyanagi, I learned theoretical point of view of the gravitational wave physics, astronomy, and cosmology in occasional meetings.
From Tomotada Akutsu, I learned scientific attitude for research.

Kentaro Komori gave me wide knowledge on gravitational wave physics and precision measurement.
Yutaro Enomoto gave me various knowledge on laser interferometric gravitational wave detectors. I enjoyed the discussion with him during my master and doctoral courses. He also gave me valuable comments on the manuscript of this thesis.
Ching Pin Ooi proofread this thesis. With him, I also discussed some topics of thermal noise. Also, he taught me that tempura is a steamed dish.
Discussion with Naoki Aritomi, Takuya Kawasaki, Satoru Takano, Naoki Kita, and Yuki Miyazaki made me improve my understanding on the gravitational wave and quantum mechanics.

Shigemi Otsuka, and Togo Shimozawa made most mechanical parts of my experiment in the machine shop. Also, I learned how to design mechanical parts and drawing from them.

Rie Kikuchi, Mayuko Niwata, and Naomi Kudo helped me with office works, such as application of the business trip. Thanks to them, I can concentrate on my research.

Hiroyuki Sagawa, Junji Yumoto, Katsuaki Asano, Shinji Miyoki, and Takuro Ideguchi were referees of this thesis. I would like to thank their insightful comments.

Some of the illustrations in this thesis are drawn using the component library prepared by Alexander Franzen.

This work is financially supported by JSPS Grant-in-Aid for Scientific Research (A) No. 15H02087 and JSPS KAKENHI Grant No. JP17J01176.

In the end, I am greatly obliged to Seiji Kawamura. He is a researcher who I respect the most. If I had not met him, my research life would not be so exciting as it is now. Without what he taught me, this work could not be completed.

最後の最後に、ここまで私を支えてくれた両親に感謝します。